THERMALLY EVAPORATED SILICON PHTHALOCYANINE AND THIOXANTHENE BENZANTHRONE BASED ORGANIC THIN-FILM TRANSISTORS

BY

OWEN ALFRED MELVILLE

A THESIS

SUBMITTED TO THE UNIVERSITY OF OTTAWA

IN PARTIAL FULFILMENT OF THE REQUIREMENTS FOR THE

DOCTORATE OF PHILOSOPHY DEGREE

IN CHEMICAL ENGINEERING

DEPARTMENT OF CHEMICAL AND BIOLOGICAL ENGINEERING

UNIVERSITY OF OTTAWA

© Owen Alfred Melville, Ottawa, Canada, 2020

All Rights Reserved

PhD in Chemical Engineering (2020) University of Ottawa

Chemical and Biological Engineering Ottawa, Ontario, Canada

TITLE:	Thermally Evaporated Silicon Phthalocyanine and Thioxanthene Benzanthrone Based Organic Thin-Film Transistors
AUTHOR:	Owen Alfred Melville
	B.ASc, (Engineering Science)
	M.Eng, (Chemical Engineering)
	University of Toronto (Toronto, Ontario, Canada)
SUPERVISOR:	Professor Benoît Lessard
NUMBER OF PAGES:	xx, 180

Abstract

Since their infancy began approximately 50 years ago, carbon-based ‘organic’ semiconductors (OSCs) have redefined the possibilities of electronics through their unique material properties such as solubility, chemical sensitivity, sublimability and flexibility. The enormous amount of organic synthetic tools available can produce a nearly endless number of tailor-made OSCs for a wide variety of applications, including already established technology such as organic light-emitting diodes (OLEDs). An increasing demand for smart-technology and data creates a particular need for low-cost electronic communication tools, sensors, and processors. In this area, organic thin-film transistors (OTFTs) excel, demonstrating potential for chemical and biological sensing, large area and printed electronics, artificial skin and smart packaging. Despite this potential, OTFT technology is still developing, with a number of consistent issues hampering widespread commercial utilization. Lack of available OSCs with good performance and low synthetic complexity is one such problem, especially for electron conducting OSCs required for complex circuit components such as inverters. Although metal phthalocyanines (MPcs) are well-known, stable molecules demonstrated in high-performance OTFTs, few are successful as n-type or ambipolar OSCs that transport electrons. The work presented in this thesis documents the first use of silicon phthalocyanines (SiPcs) in n-type OTFTs along with a thioxanthene benzanthrone, 14H-anthra[2,1,9-mna]thioxanthen-14-one (Red GG), a simple base molecule in a relatively unexplored class of compounds never before characterized for p-type OTFTs. The report within documents a number of strategies aimed at understanding and improving the performance of these molecules for this application. In particular, the chapters examine dielectric, architectural and contact modification as part of the OTFT fabrication process, while considering characterization environment, bias stress and contact resistance in their analysis. The results serve as a basis for continued development of SiPcs and Red GG derivatives for OTFT-based applications.

Abstrait

Depuis leur plus jeune âge, il y a environ 50 ans, les semi-conducteurs «organiques» à base de carbone (OSC) ont redéfini les possibilités de l'électronique grâce à leurs propriétés de matériaux uniques telles que la solubilité, la sensibilité chimique, la sublimabilité et la flexibilité. L'énorme quantité d'outils de synthèse organique disponibles peut produire une quantité presque infinie d'OSC sur mesure pour une grande variété d'applications, y compris des technologies déjà bien établies telles que les diodes électroluminescentes organiques (OLED). La demande croissante de technologies intelligentes et de données crée un besoin particulier d'outils de communication électroniques, de capteurs et de processeurs peu coûteux. Dans ce domaine, les transistors organiques à couche mince (OTFT) sont excellents et démontrent un potentiel de détection chimique et biologique, de produits électroniques de grande surface et imprimés, de peaux artificielles et d'emballages intelligents. Malgré ce potentiel, la technologie OTFT continue de se développer et de nombreux problèmes persistants entravent une utilisation généralisée. Le manque de composants OSC disponibles offrant de bonnes performances sans synthèse complexe est un problème, en particulier pour les composants OSC de type n requis pour les composants de circuit complexes tels que les inverseurs. Bien que les phtalocyanines métalliques (MPcs) soient des molécules bien connues et stables démontrées dans les OTFT à haute performance, peu réussissent en tant que OSC de type n qui transportent des électrons. Le travail présenté dans cette thèse démontre la première utilisation de phtalocyanines de silicium (SiPcs) en tant que OSC de type n dans des OTFT aussi qu'un OSC de type p, 14H-anthra [2,1,9-mna] thioxanthen-14-one (Red GG), qui représente la molécule de base d'une classe de composés relativement inexplorée encore jamais caractérisée dans les OTFT. Le rapport décrit plusieurs stratégies visant à comprendre et à améliorer les performances de ces molécules pour cette application. Les chapitres examinent en particulier les modifications du diélectrique, de l'architecture et des contacts dans le processus de fabrication d'OTFT, tout en prenant en compte l'environnement de caractérisation, les contraintes de polarisation et la résistance de contact. Les résultats servent de base au développement continu des dérivés SiPcs et Red GG pour les applications basées sur OTFT.

Acknowledgements

Without the help of many other people, my work on this project would not have been possible. I would like to thank Dr. Benoît Lessard for giving me the opportunity to join his new research group. Thank you for your trust, guidance, patience and understanding. I have no doubt the group will continue to develop, grow and discover under your supervision.

I would like to thank Dr. Timothy Bender at the University of Toronto for inviting me to work with him and for introducing me to Dr. Lessard. The prior and ongoing work of his research group was important to the development of this project.

I would like to thank the staff at the University of Ottawa Department of Chemical and Biological Engineering for their administrative and technical support. Special thanks to Louis Tremblay and Franco Ziroldo for their help in setting up the lab when our research group was small, to James Macdermid for designing and machining components for our fabrication process, and to Gerrard Nina for helping with electrical issues.

I would like to thank former and present employees at Angstrom Engineering for their ongoing assistance with the glove boxes and thermal evaporation system. Thank you to Shoji Kanamori and Dr. Yan Pennec from Element Instrumentation and Kreus Design Incorporated for designing and helping to troubleshoot the probe station. Thank you to Ian Myers working on the auto-tester. Thank you to Dr. Bulat Gabidullin for your assistance and training with x-ray diffraction.

I would like to thank my colleagues in the Lessard Research Group (LRG) for their collaboration and for helping to maintain a positive research environment. Special thanks to Trevor Grant for collaborating from the beginning and for synthesizing many semiconductors that I used in these projects. Special thanks to Dr. Nicole Rice for providing guidance for this thesis report.

I would like to express my heartfelt gratitude to my parents, Catherine and Thomas Melville, for their lifelong support and incredible kindness. I would also like to thank my wonderful siblings William Melville, Rebecca Melville, Christopher Melville, Matthew James, and Katja Linher-Melville.

Thank you to the thesis committee for your consideration of this report.

List of Abbreviations

246F-SiPc	Bis(2,4,6-trifluorophenoxy) silicon phthalocyanine
246F-SnPc	Bis(2,4,6-trifluorophenoxy) tin phthalocyanine
AFM	Atomic Force Microscopy
BC	Bottom Contact
BG	Bottom Gate
C_i	Capacitance Density
Cl_2-SiPc	Silicon phthalocyanine dichloride
DFT	Density Functional Theory
ΔV_T	Change in Threshold Voltage
E_G	Band Gap
F_{10}-SiPc	Bis(pentafluorophenoxy) silicon phthalocyanine
F_{10}-SnPc	Bis(pentafluorophenoxy) tin phthalocyanine
FOTS	Figure 1.16A **35**
HMDS	Hexamethyldisilazane
HOMO	Highest Occupied Molecular Orbital
I_{DS}	Source-Drain Current
I_{OFF}	Off Current
I_{ON}	On Current
$I_{ON/OFF}$	On/Off Current Ratio
L	Channel Length
LUMO	Lower Unoccupied Molecular Orbital
μ_e	Electron Mobility
μ_h	Hole Mobility
MOSFET	Metal Oxide Semiconductor Field-Effect Transistor
MPc	Metal Phthalocyanine
mTLM	Modified Transmission Line Method
NDI	Napthalene Diimide
ODTS	Octadecyltrichlorosilane
OECT	Organic Electrochemical Transistor

OLED	Organic Light-Emitting Diode
OPV	Organic Photovoltaic
OSC	Organic Semiconductor
OTFT	Organic Thin-Film Transistor
OTS	Octyltrichlorosilane
Pc	Phthalocyanine
PIL	Polymer Interlayer
PTS	Phenyltrichlorosilane
PVD	Physical Vapor Deposition
PXRD	Powder X-Ray Diffraction
R_C	Contact Resistance
RFID	Radio Frequency Identification
SAM	Self-assembled Monolayer
SCOFET	Single Crystal Organic Field-Effect Transistor
SD	Source-Drain
SiPc	Silicon Phthalocyanine
SMIL	Small Molecule Interlayer
SnPc	Tin Phthalocyanine
SS	Subthreshold Slope
TC	Top Contact
TG	Top Gate
TGA	Thermogravitational Analysis
TLM	Transmission Line Method
UPS	Ultraviolet Photoelectron Spectroscopy
UV-Vis	Ultraviolet-Visible
V_{DS}	Source-Drain Voltage
V_{GS}	Gate Voltage
V_T	Threshold Voltage
W	Channel Width
XRD	X-Ray Diffraction
YFM	Y-Function Method

Table of Contents

List of Figures

Note - Figure titles have been abbreviated for clarity. Please refer to actual figures for full titles.

List of Tables

Note - Table titles have been abbreviated for clarity. Please refer to actual tables for full titles.

Chapter 1: Device Engineering for Organic Thin-Film Transistors (OTFTs)

1.1 Overview

1.1.1 Organic Electronic and Thin-Film Transistor Technology

Organic electronic devices using carbon-based semiconductors (OSCs) continue to evolve and demonstrate incredible potential for low-cost consumer, medical and industrial applications. Organic light-emitting diodes (OLEDs) are an all but ubiquitous component of smart phone screens used by companies like Samsung, LG, Sony, Apple, Nokia and Panasonic in order to reduce power consumption, decrease screen thickness, and increase brightness. Organic photovoltaics (OPVs) have demonstrated power conversion efficiencies of 17.3% in tandem cells[1] and up to 17% in single junction cells,[2] within the realm of commercial silicon photovoltaics but with the potential for vastly lower production costs. Organic thin-film transistors (OTFTs), despite somewhat less attention, have demonstrated the widest array of potential applications amongst organic electronic devices. RFID tags,[3] printed electronics,[4] backplanes for active displays[5] and flexible[6] or printed[7] memory devices are just a few developing technologies potentially on the verge of commercialization. The chemically responsive and potentially biocompatible nature of OSCs makes OTFTs ideal sensors for a smart, sustainable world. Applications incorporating OTFTs into electronic paper for LED arrays[8] or smart packaging,[9] pressure[10] and temperature[11] sensors and artificial skin[12,13] are all in development. Chemical and biological sensors using OTFTs have demonstrated great promise in the detection of NH_3,[14] DNA[15] and other analytes.[16] Organic electrochemical transistors (OECTs), which are structurally similar to OTFTs, have been utilized in ion and enzymatic sensing[17] as well as electrocardiographic recording.[18] This long list of incredible applications is built upon a large base of fundamental research on OTFTs that continues to broaden. Issues with performance and availability of n-type OSCs, operational stability, processing/fabrication consistency, contact resistance, power requirements and synthetic complexity continue to hamper the widespread adoption of OTFT-based technology. As these issues and others are systematically addressed, it will assist the development of OTFTs and their contribution to a smart, sustainable future.

1.1.2 Scope of Thesis and Literature Review

This report will focus on the fabrication and characterization of OTFTs using novel small molecule organic semiconductors (OSCs) based on tin phthalocyanine (SnPc), silicon phthlocyanine (SiPc), or 14H-anthra[2,1,9-mna]thioxanthen-14-one, also known as Red GG. These molecules are suitable for OTFT fabrication using physical vapor deposition (PVD), described in Section 1.2.2, because they are relatively insoluble and thermally stable. Fabrication of OTFTs using PVD is a complex chemical engineering process involving many steps and careful control. The characterization of OTFTs involves examining the OSC film, as described in Section 1.2.3, and the OTFT electrical polarization and transport properties as described in Section 1.3.1 & 1.3.2. As required, the reported chapters utilize concepts from electrical, materials science, and chemical engineering. This section will briefly overview areas of research focus covered in Chapters 2 – 5, before they are explained in more detail later in this chapter. Notably, chemical synthesis of OSCs is not covered within the scope of this report.

While RedGG, examined in Chapter 2, was chosen because it is a commercially available dye molecule never before used in OTFTs, the phthalocyanines (Chapters 3 – 5) were chosen because of their electron conducting properties, simple synthesis, and synthetic versatility. The latter refers to the axial position of SiPc and SnPcs, illustrated in Figure 1.1, substitution of which changes the solid-state packing and energetic properties of the molecules.[19–22] Because this class of di-substituted Group XIV phthalocyanines has not been previously studied in OTFTs, Section 1.3.3 covers both the existing published research on these molecules and also how changes in molecular structure have been related to OTFT performance in other classes of molecules. The results presented in Chapters 3 – 5 find some patterns relating SiPc/SnPc structure and properties to OTFT performance, with ongoing research still warranted.

In Chapter 2 and 3, the effect of dielectric modification with a self-assembled monolayer (SAM) is examined. As explained in Section 1.3.4, the dielectric-OSC interface is critical for device operation, and there is considerable existing research on modifying the dielectric using SAMs and other techniques. As all reported devices in Chapters 2 – 5 used silicon dioxide (SiO_2) dielectrics, the focus in this report will be on dielectric modification, not the dielectric material itself. Although novel techniques for dielectric modification were not used for these studies, the

effect of dielectric modification is different for different materials and warranted investigation in this context of developing new OSCs for OTFTs.

For the OTFTs presented in this report, I focused on two device architectures: bottom-gate, bottom-contact (BGBC, Chapters 2 – 4) and bottom-gate, top-contact (BGTC, Chapter 5). Contact resistance (R_C), as described in Section 1.3.5, is a significant contemporary concern in OTFT research because it distorts characterization data and has a parasitic effect on performance.[23,24] The move to BGTC was an attempt to address obvious concerns with R_C in the devices reported in Chapters 2 – 4 by controlling the electrode-OSC interface. The use of interlayers to reduce R_C is well documented, but the technique presented in Chapter 5 uses novel interlayer materials on n-type OSCs (SiPcs/SnPcs). This is significant because reducing R_C with interlayers for p-type materials has received more attention.

As discussed in Section 1.3.6, the operational stability of OTFTs based on environmental and electrical stress continues to be an issue in the field, in particular for n-type OSCs. Chapter 4 explores this issue for ambipolar SiPcs, and the devices presented in Chapters 3 – 5 do not have a high degree of ambient operational stability. Although only one chapter in this report focuses on this issue, it is an important concern for ongoing research, research I contributed to as a secondary author, and research I did not publish.

Chapter 6 summarizes the research presented in Chapters 2 – 5 and describes both ongoing work and potential future investigations related to the topics explored in the thesis. Chapter 7 provides abstracts to papers I have contributed to as a secondary author during my PhD and describes those contributions.

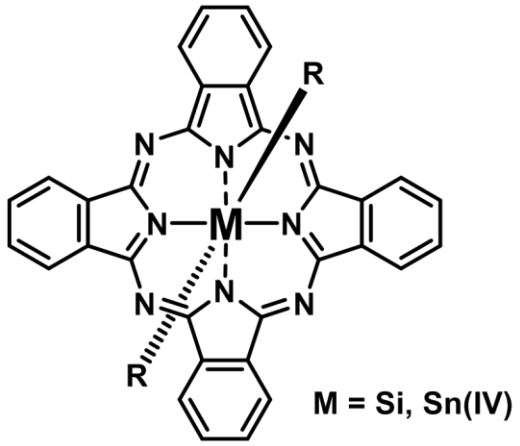

Figure 1.1: Illustration of the chemical structure of silicon and tin (IV) phthalocyanines, with two axial substituents in the R positions.

1.2 Thin Films of Organic Semiconductors (OSCs)

1.2.1 Charge Transport in OSCs

Organic materials composed of chains and rings of carbon that incorporate H, N, O, S and other atoms were long considered to be electrical insulators, justifying the modern development of electronics focused on inorganic semiconducting materials such as silicon. A few advances between the 1950s and 1970s, including the Nobel-prize winning discovery of conductive doped polyacetylene by Hideki Shirakawa and others in 1977,[25] indicated that certain organic molecules could have non-insulating electrical properties. These non-insulating organic materials all share variations of a chemical bonding motif, known as π-conjugation, where carbon atoms alternate between double and single bonds in rings or chains of rings that sometimes incorporate heteroatoms such as S, N or O. These conjugated structures cause delocalization of the π electrons held in hybrid sp^2 orbitals above and below the molecular plane, as illustrated in Figure 1.2.[26] The delocalized orbital with the highest energy electrons in the ground state is known as the highest occupied molecular orbital (HOMO), while the closest unoccupied molecular orbital is known as the LUMO. Electronic transitions between the HOMO and LUMO often require less energy with increasing conjugation,[27,28] so materials with a smaller HOMO-LUMO gap are more likely to have accessible energy states and thus be usable as organic semiconductors (OSCs). Figure 1.2 shows the molecular structure of pentacene, a good example of an OSC used for OTFTs. Pentacene contains five fused conjugated rings and in one report has a HOMO level 4.8 eV below vacuum energy (-4.8 eV) and a LUMO level of 2.7 below vacuum energy (-2.7 eV).[29]

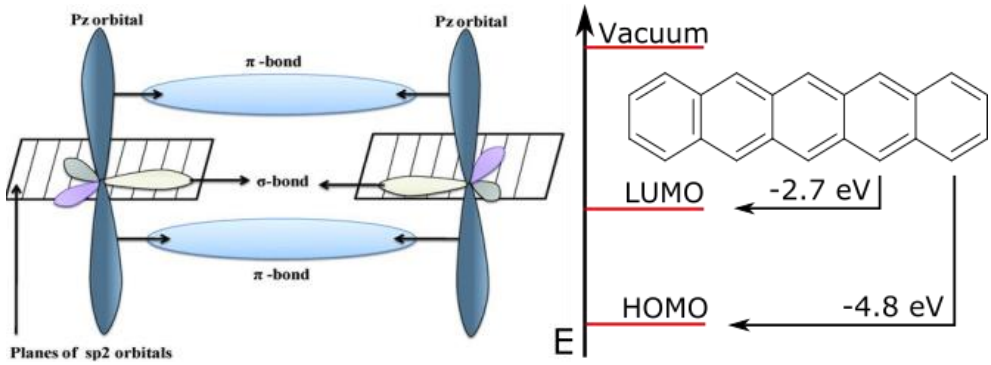

Figure 1.2: Illustration of the formation of delocalized orbitals in sp^2 bonded atoms (left) with the molecular structure of a conjugated organic semiconductor, pentacene, with its HOMO/LUMO levels (right). Left part adapted with permission from Polymer Reviews: (2014). 54(1), 33-111. Copyright Taylor & Francis.

Charge transport in solid-state small-molecule OSCs requires more than intrinsic semiconducting energetics. In a solid, molecules can pack together in many configurations, and motion of charge requires a low resistance path between molecules. Proposed mechanisms for this charge transport vary, but for small molecules a charge hopping model is often utilized.[26] In these models, an electron in the LUMO of an OSC might be able to move to the LUMO of an adjacent molecule, given enough incentive to overcome an energetic or hopping barrier. If an electron is removed from the HOMO of a molecule, it can leave behind a delocalized positive charge, referred to as a hole, which itself can hop between the HOMO levels of adjacent molecules. Although innately intrinsic semiconductors, OSCs that transport holes are contextually referred to as p-type, those that transport electrons are referred to as n-type and those that transport both are referred to as ambipolar. For reasons explained in Section 1.3.6, OSCs are more likely to be p-type, and much more research exists on p-type OTFTs.

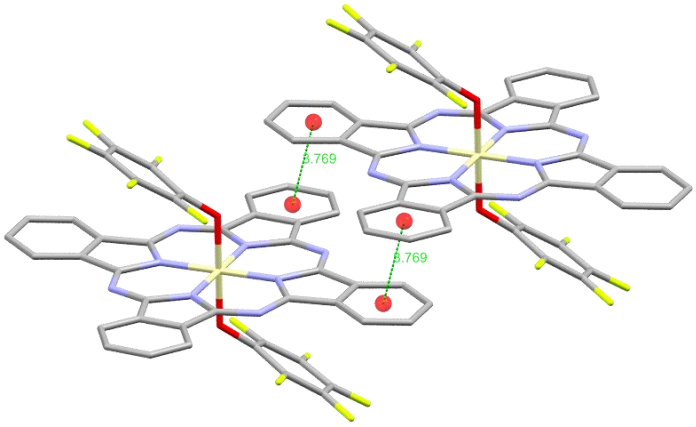

Figure 1.3: Illustration of π-π stacking between two silicon bis(pentafluorophenoxy) phthalocyanine (F_{10}-SiPc) molecules, highlighting the distance between fused benzene ring centroids d = 3.769 Å. Hydrogen atoms have been omitted for clarity.

The process of charge hopping between molecules can be described using Marcus Theory.[30] When a charge (electron or hole) moves from one molecule to another, the first molecule often requires energy to change geometry, an amount referred to as the molecular reorganization energy. The degree of orbital overlap, based on distance and relative orientation of adjacent molecules, is described as the transfer integral. The combination of a low reorganization energy and high transfer integral promotes charge transport between molecules, and both are related to

molecular structure and packing, including the distance between conjugated planes or π-π stacking distance,[27] illustrated in Figure 1.3 for two SiPc molecules. Given the single crystal structure of an OSC, density functional theory (DFT) calculations can use this model to predict charge transport mobility. The long-range organization of these crystals is often described with packing motifs illustrated into Figure 1.4, and relationships can be drawn between single crystal packing and charge transport as discussed in Section 1.3.3.[31] Despite these interesting analytical capabilities for organic single crystals, real thin films of OSCs produced by the methods described in Section 1.2.2 do not typically form with single crystal structures. Thin organic films may be amorphous, polycrystalline, a distinct thin-film phase, or a combination of phases. Consideration of this polymorphism is important to understanding charge transport in OSCs, and will be discussed in further sections.

Another important complication to charge transport in OSCs is the formation of trap states. Trap states are defined as localized energy states between the HOMO and LUMO levels.[32] For n-type materials, trap states are empty states that can accept an electron from the LUMO. Trap states that are close to the LUMO are called shallow traps, and those further away are called deep traps. For p-type materials trap states are filled states, able to accept a hole from the HOMO. Since these states are localized, they do not contribute to charge transport and high densities of trap states reduce charge transport capabilities. The filling of trap states may be reversible or irreversible, and they can exist on the OSC, in adsorbed gases, or other components of an organic electronic device such as an OTFT.

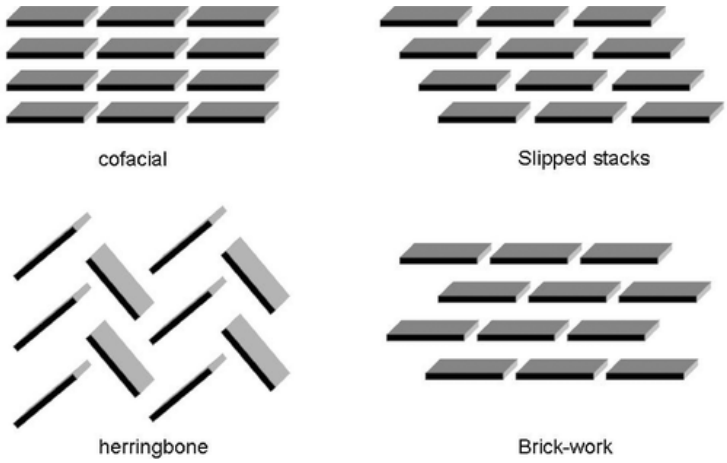

Figure 1.4: Illustration of possible crystal packing motifs of conjugated organic molecules. Adapted with permission from Chemical Reviews, 2011, 111 (8), 4833-4856. Copyright 2011 American Chemical Society.

1.2.2 OSC Deposition by Physical Vapor Deposition (PVD)

The formation of OSC films is critical to the construction of electronic devices including OLEDs, OTFTs, and OPVs. For OTFTs, there are two major categories of formation techniques: vacuum-based and solution-based. Solution-based methods including drop-casting, spin-coating, doctor blading and inkjet printing can be efficient, low-cost methods for electronic fabrication. Vacuum-based methods such as physical vapor deposition (PVD) are more expensive to set up and less efficient than solution-based methods. Despite these drawbacks, vacuum deposition reliably produces high uniformity films and is commercially utilized for OLED production.[33] For the scientific study of new OSCs, vacuum deposition is excellent because it does not require synthesizing molecules with solubilizing groups such as alkyl chains. Given the low solubility of the molecules characterized in Chapters 2 – 5, this section will focus on PVD.

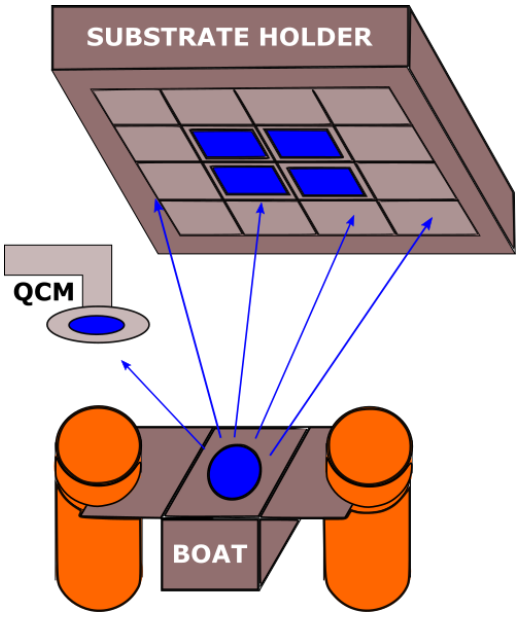

Figure 1.5: Illustration of physical vapor deposition (PVD) process in the Angstrom EvoVac system

The resistive PVD process is illustrated in Figure 1.5. A source (boat, crucible, etc.) made of a refractory material such as tungsten or tantalum is filled with material and heated by applying an electrical current through it in high vacuum, typically below 10^{-5} Torr.[34] Above a certain temperature, the material may sublime into vapor and travel through the vacuum until it reaches the target substrate and also a quartz crystal monitor (QCM). Because the vibration of the QCM is a function of mass, an accumulation in material causes a measurable change in frequency. Given a tooling factor that must be determined with a prior deposition, the QCM can be used to monitor the accumulation of material on the substrate in terms of thickness. Thus, the deposition rate on the substrate can be regulated with a PID controller.

When a molecule lands on a substrate, it can remain where it is or diffuse across the surface. The nucleation density (N) of sites in the growing semiconductor film can be related to the diffusion rate (D) and deposition rate (F).[35]

$$N \approx \frac{F}{D} \tag{1.1}$$

Over time, the nucleated material will form a thin film, which might on a microscopic scale look like those in Figure 1.6. The exact morphology of the film will depend on the deposition conditions such as rate and substrate temperature, the nature of the dielectric as discussed in Section 1.3.4, and the nature of the OSC.[31] Characterization techniques for these films will be discussed in the next section.

1.2.3 Characterization of OSC Films

Researchers fabricating thin-films for applications such as OTFTs often look to elucidate their physical, electrostatic, energetic and optical properties. An excellent review of the topic was written by Hu et al,[36] covering a variety of characterization techniques that have been used in investigations of organic transistors. This section will focus on briefly describing the techniques used in Chapters 2 – 5 and their relevance to OTFT characterization.

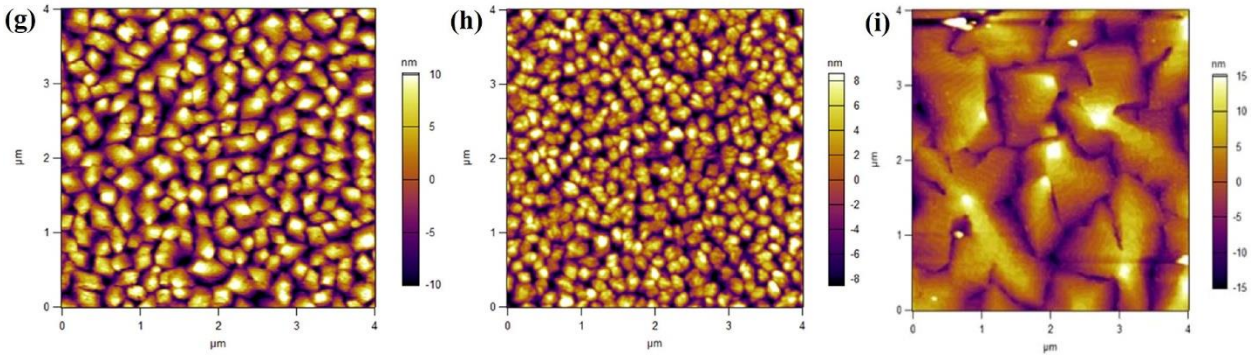

Figure 1.6: AFM surface morphologies of pentacene films grown on (g) bare-ZrO_2 surface; (h) HMDS (**34**, Figure 1.16A) modified surface; (i) PαMS (**37**, Figure 1.16C) modified surface. Adapted with permission from J. Phys. Chem. C, 2016, 120(18), 9949-9957. Copyright (2016) American Chemical Society.

1.2.3.1 Atomic Force Microscopy (AFM)

Due to the variable, disordered nature of many OSC thin films, imaging their surface can provide useful morphological information to help explain their electronic properties. AFM is a kind of scanning probe microscopy technique that is used to look at surface topology. As OSCs are often soft and fragile, tapping mode AFM is most frequently used because it minimizes the interaction of the tip with the surface.[36] In tapping mode AFM, an oscillating tip scans over a

surface, and its height is adjusted as interaction with the surface changes the oscillation amplitude in order to keep it constant. Figure 1.6 shows three example AFM images of a pentacene film deposited on three different surfaces.[37] The 3D motion of the tip on the surface of the films indicates granular features with different size, interconnectivity and roughness depending on the underlying layer. Additional information about nucleation and growth in the OSC film can be obtained by imaging at several different thicknesses. Both surface features and growth mechanisms are often used in conjunction with other characterization data to help explain the electrical performance of OTFTs.

1.2.3.2 X-Ray Diffraction (XRD)

A number of x-ray scattering techniques can be used to characterize OSC thin films, including powder x-ray diffraction (XRD) and grazing incidence x-ray diffraction (GIXD). XRD provides information about film order, packing, grain size, and orientation.[36] Figure 1.7 shows two different XRD patterns for pentacene deposited on two different modified polymer surfaces, along with corresponding AFM images.[38] The authors note the presence of two distinct phases on the ODTS-modified polymer dielectric, but only one phase with greater diffraction intensity on the HMDS-modified dielectric. Visual changes in the AFM images help the authors contextualize the difference. This kind of comparison between different conditions while pairing with AFM images is a common approach to interpreting XRD data in the context of OTFT development.

1.2.3.3 Ultraviolet Photoelectron Spectroscopy (UPS)

In ultraviolet photoelectron spectroscopy (UPS), fixed wavelength UV radiation is irradiated on an OSC thin film, and the kinetic energy of released photoelectrons is measured and converted into a spectrum of binding energy in the film.[36] Combined with inverse photoemission spectroscopy (IPES), which measures radiative transitions from excited states,[39] these two techniques can probe the density of occupied and unoccupied states in an OSC film and identify the HOMO and LUMO levels.[40] UPS can also be used to characterize the energetic environment of an OSC-metal interface, including the interfacial dipole.[41] This information is important to understand charge injection at electrode-semiconductor interfaces, which in OTFTs can be a source of great resistance as discussed in Section 1.3.5.

1.2.3.4 Ultraviolet-Visible Absorption Spectroscopy (UV-Vis)

UV-Vis absorption spectroscopy is a common technique to characterize OSCs in solution or in films. By measuring light transmitted through a sample in a cuvette or on a transparent substrate, energetic and structural information about the OSCs can be determined.[36] For example, the low-energy onset of absorption, often referred to as the band gap (*Eg*), can be related to the difference between the HOMO and LUMO energy levels.[42] Comparing the spectra in the thin-film and in solution relays information about the solid-state packing of the molecules.[43] As discussed in subsequent sections, the energy levels and packing of an OSC both strongly impact charge transport in OTFTs.

.

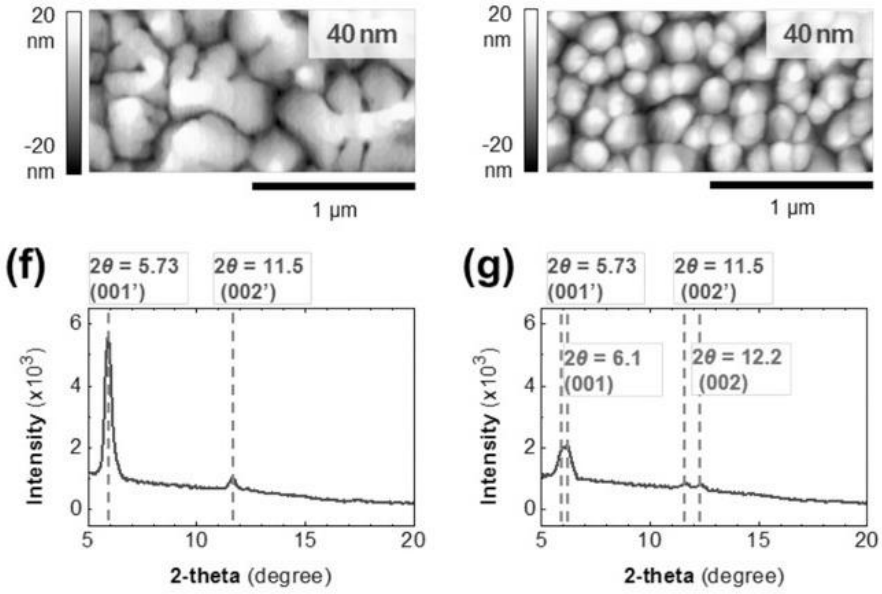

Figure 1.7: AFM images (top) and XRD spectra (bottom) of 40 nm thermally evaporated pentacene on f) HMDS-treated and g) ODTS-treated (**30**, Figure 1.16A) polymer dielectrics. Adapted with permission from Adv. Func. Mater. 2015, 25(28), 4462-4469. Copyright (2015) WILEY-VCH Verlag GmbH & Co. KGaA, Weinheim.

1.3 Device Engineering for Organic Thin-Film Transistors

This section contains four detailed subsections 1.3.3 – 1.3.6 that describe existing research that is relevant to understanding the significance of the research presented in Chapters 2 - 5. Prior to these subsections, the established mechanism of action and electronic characterization of OTFTs will be presented in 1.3.1 – 1.3.2 in order to provide context and definitions for understanding the subsequently summarized research.

1.3.1 OTFT Structure & Operation

The structure of an organic thin-film transistor (OTFT) shown in Figure 1.8A is designed to facilitate the electronic switching of a semiconducting thin-film between a resistive (off) state and conductive (on) state. Each of the four main components in the OTFT play a specific role, and the mechanism of action is illustrated in Figure 1.8B. As discussed in Section 1.2.1, the organic semiconductor (OSC) provides accessible energy states (HOMO or LUMO) for the injection of holes or electrons where ideally they exist as mobile charge carriers. To inject these carriers into the OSC, a bias is applied across the dielectric, usually referenced between the source and gate electrodes and denoted V_{GS}. According to the model, when V_{GS} exceeds a particular value, denoted the threshold voltage (V_T), charges injected from the source and drain (SD) electrodes begin to accumulate in a mobile sheet at the OSC-dielectric interface, blocked from reaching the gate by the insulating and capacitive dielectric. The presence of this conductive sheet can be measured by applying a bias to drive the charges between the SD electrodes, generating a current denoted I_{DS}. Thus, the gate electrode acts to control the conductivity of the OSC using V_{GS} as an input signal, while the source and drain electrodes facilitate the measurement of this change in conductivity as an output signal, I_{DS}. The characterization of this process will be detailed more in Section 1.3.2.

The relative position of the components can vary, with the four most common OTFT device architectures shown in Figure 1.8C. BGBC and TGTC devices are often referred to as coplanar structures, whereas BGTC and BCTG are often referred to as staggered. The conceptual difference between the two categories is that charge must move through the entire thickness of OSC from the SD electrodes to reach the OSC-dielectric interface in staggered devices, whereas in coplanar devices the electrode-OSC interface is close/coplanar to the OSC-dielectric interface. Practically, making each of these four architectures requires different equipment and considerations, but this

report is limited in scope to BG devices only. BG devices are often fabricated on conductive doped Si substrates with a thermally grown SiO_2 dielectric, requiring only the OSC and SD electrodes to be added. Since the OSC-dielectric interface is critical to charge transport and the OSC is formed directly on the dielectric in BG devices, researchers have made considerable effort engineering this interface. Section 1.3.4 summarizes some of these efforts. Since charge injection between the SD electrodes and OSC is also important to device performance, Section 1.3.5 describes efforts to improve the electrode-OSC interface.

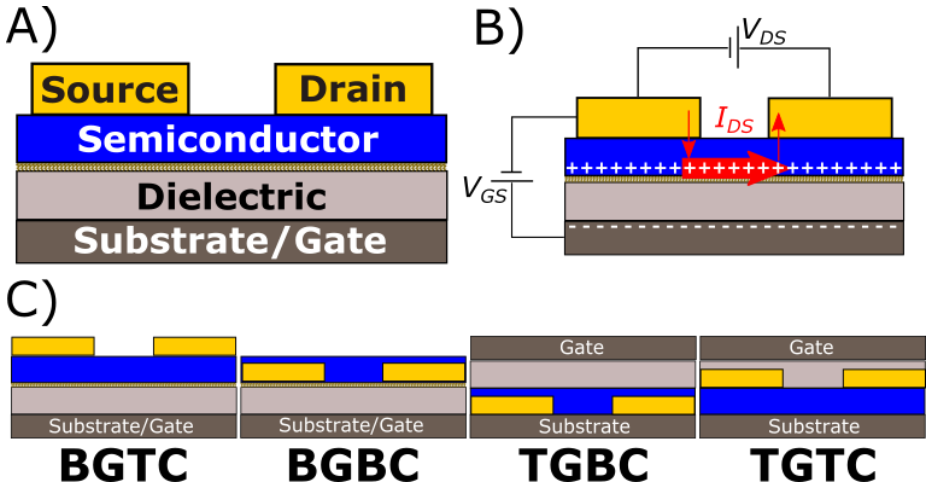

Figure 1.8: A) Schematic diagram of an organic thin film-transistor (OTFT), noting its components; B) Illustration of operation in an OTFT, where a gate bias V_{GS} polarizes the dielectric creating a sheet of mobile charges in the OSC – these charges can be moved across the semiconducting channel by applying a bias between the source and drain electrodes (V_{DS}); C) schematics for the relative layouts of four different OTFT architectures; Legend: BG – bottom gate; TG – top gate; BC – bottom [source-drain] contact; TC – top [source-drain] contact.

1.3.2 OTFT Characterization

The operation mechanism for an OTFT with geometry like in Figure 1.9 is often modelled like a metal-oxide semiconductor field-effect transistor (MOSFET), despite the fact that OTFTs operate with a different mechanism.[26] The output of an ideal OTFT in accumulation mode is shown in Figure 1.10, and looks similar to the output of a MOSFET device. Each curve shows the evolution of the source-drain current (I_{DS}) as a function of source-drain bias (V_{DS}) at different gate bias levels (V_{GS}). At low V_{GS} levels, only a small concentration of mobile charges exist in the OSC and thus I_{DS} remains low for all V_{DS}. This value of I_{DS} is defined as the off current (I_{OFF}), often reported as an order of magnitude, and can be limited in accuracy at low levels by the noise of the measurement equipment. At higher levels of V_{GS}, a mobile sheet of charges forms at the OSC-dielectric interface with a concentration proportional to the capacitance density of the dielectric (C_i). As conductivity (σ) is proportional to mobile charge density (n or p, Equation 1.2, for electrons and holes respectively), the slope of the I_{DS} (V_{DS}) curve increases in what is called the linear region of the output curve. An increasing V_{DS} reduces V_{GD}, gradually reducing the potential across a channel with length L as illustrated in Figure 1.9 (right). Thus at a certain level of V_{DS}, the channel becomes "pinched-off" in terms of charge density, and opposite sign (minority) charges are not easily injected. This slows and eventually stunts the additional flow of charge with V_{DS}, and I_{DS} levels off. This is called the saturation region of the output curve.

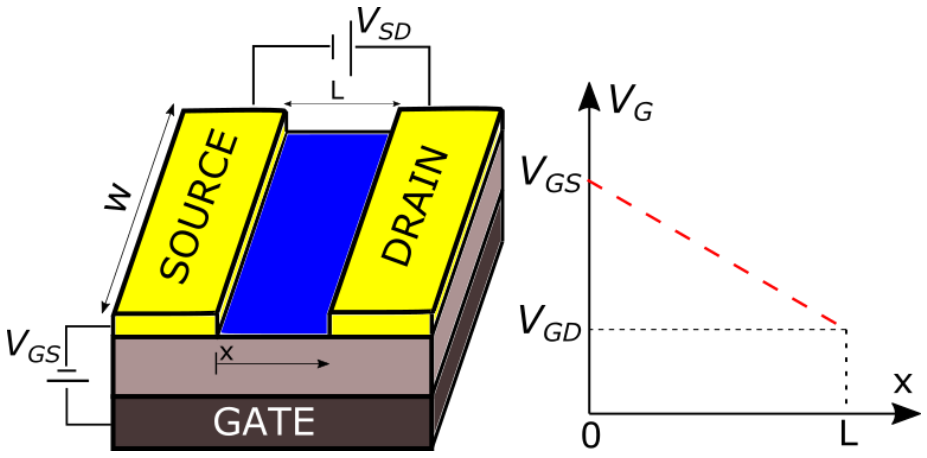

Figure 1.9: Left) OTFT schematic, showing channel length L and width W; Right) Potential profile for an ideal OTFT operating in the linear region where $V_{DS} << V_{GS}$.

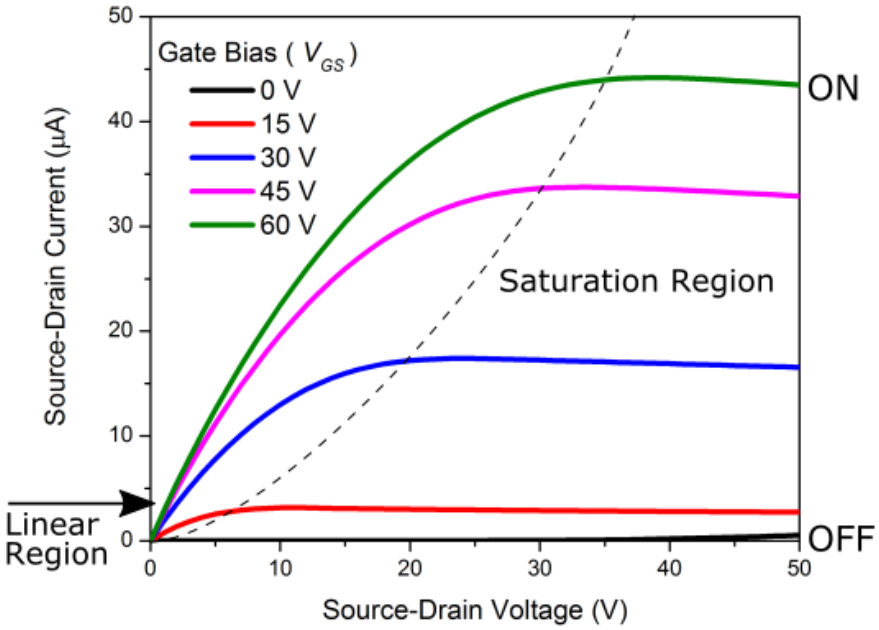

Figure 1.10: Example set of output curves for BGTC OTFTs with F_{10}-SiPc as the OSC (real data, unpublished). The dotted line illustrates the start of the saturation region, which varies with V_{GS}. The linear region where I_{DS} increases linearly with V_{DS} is noted as well. The most on and off states are labelled for the range of V_{GS} characterized for this device.

According to the MOSFET model, Equations 1.3 and 1.4 model I_{DS} as a function of V_{GS} in the saturation and linear region, respectively. The mobility these equations can be calculated for hole (μ_h) or electron (μ_e) accumulation, and is referred to as the field-effect mobility when determined this way with its measurement region typically specified. The formulae for μ in the saturation region and linear region are presented in Equation 1.5 and 1.6, respectively. To evaluate μ, $\sqrt{I_{DS}}$ or I_{DS} are obtained as a function of V_{GS} for a fixed value of V_{DS} in either the saturation or linear region. Figure 1.11 shows example plots of this data, often referred to as transfer curves. L and W are the physical length and width of the transistor channel, defined by the geometry of the source-drain electrodes (Figure 1.9).

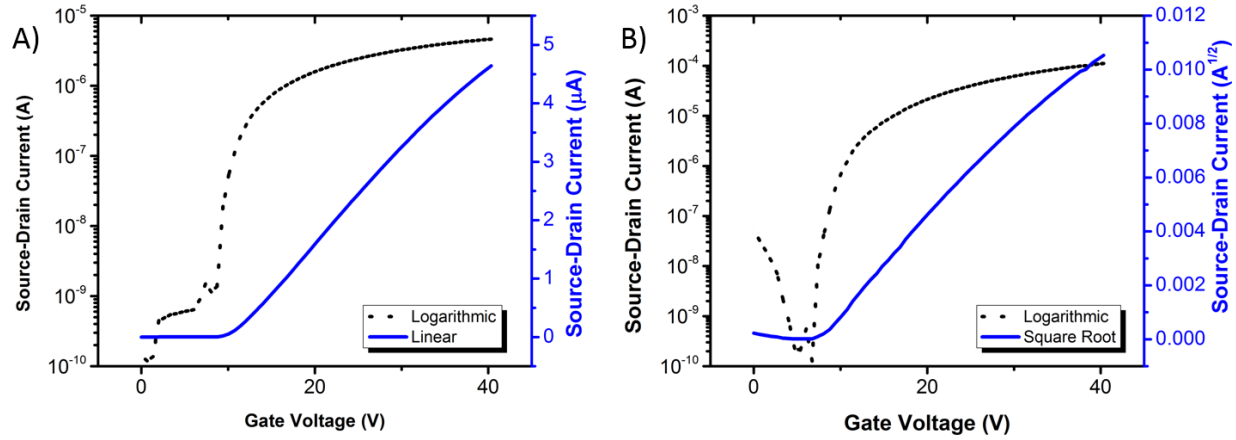

Figure 1.11: Transfer curves for the A) linear (V_{DS} = 2 V) and B) saturation (V_{DS} = 50 V) regions, shown as log plots of I_{DS} with respect to gate bias V_{GS}. Depending on the region, the data is linearized to find V_T and μ in accordance with Equation 1.3 (saturation) or 1.4 (linear). Unpublished data using F_{10}-SiPc OTFTs.

A few pieces of information can be determined from the transfer curves. V_T is typically equal to or slightly offset to the x-intercept of the linearized plots, depending on the calculation region. The maximum current in a transfer curve in the direction of accumulation is called the on current (I_{ON}), and is often used to calculate an order-of-magnitude (10^X) ratio with I_{OFF} ($I_{ON/OFF}$). Often, current begins to rise above I_{OFF} at a lower V_{GS} than V_T, and this value is labelled the onset voltage (V_{ON}). Between V_{ON} and V_T is the subthreshold region, from which the sub-threshold swing (SS) can be calculated. The derivatives required for Equations 1.5 and 1.6 are often not constant above V_T, and thus calculating μ values may require calculating within a specific V_{GS} region. This deviation from the ideal MOSFET model indicates there are other factors affecting OTFT measurements that are not accounted for and therefore that the intrinsic mobility may not equal the calculated field-effect μ.[23] The effect of contact resistance (R_C) is explained in Section 1.3.5 while trap-induced measurement variations dependent on characterization environment and time are explained in Section 1.3.6. Indeed, OTFTs are so sensitive to operation that the transfer curve with increasing V_{GS} may not be the same as the transfer curve with decreasing V_{GS}. This hysteretic effect is often documented as well.

$$\sigma = ne\mu_e + pe\mu_h \tag{1.2}$$

$$I_{DS} = \frac{\mu C_i W}{2L}(V_{GS} - V_T)^2 \tag{1.3}$$

$$I_{DS} = \frac{\mu C_i W}{L}((V_{GS} - V_T)V_{DS} - \frac{1}{2}V_{DS}^2)) \tag{1.4}$$

$$\mu = \frac{2L}{WC_i}\frac{d\sqrt{I_{DS}}}{dV_{GS}}\Big|_{V_{GS}>V_T} \tag{1.5}$$

$$\mu = \frac{L}{V_{DS}WC_i}\frac{dI_{DS}}{dV_{GS}}\Big|_{V_{GS}>V_T} \tag{1.6}$$

1.3.3 Molecular Structure Engineering for OTFTs

Modifying the chemical structure of existing organic semiconductors (OSCs) in order to tune their solid state properties and interaction with other components is an important research area in OTFT development. These alterations can provide information about the relationship between molecular structure and electronic performance in devices. Such structure-function relationships are contextual and can be difficult to ascertain and apply when so many confounding factors exist in a complex device such as an OTFT. Nonetheless, many studies have attempted to determine these relationships, usually by comparing devices made with systematically varied OSC molecular structures. This section will summarize some investigations into the effect of various modifications on the performance of small-molecule OSCs in OTFTs, with a separate section focusing on metal phthalocyanines (MPcs).

1.3.3.1 Small Molecules

Although a diverse array of small molecule OSCs can be incorporated into OTFTs, they share certain structural features and modifications to these features can often be categorized. Each molecule has a π-conjugated core, which can be modified by the incorporation of heteroatoms such as N, S, O, Se and Te, or by π-extension through fusion with or linear addition of other conjugated components.[27] The periphery of the core can also be modified with side-chains and functional groups. The exact impact of these changes depends, in general, on the nature of the core or base molecule and the nature of the modification.

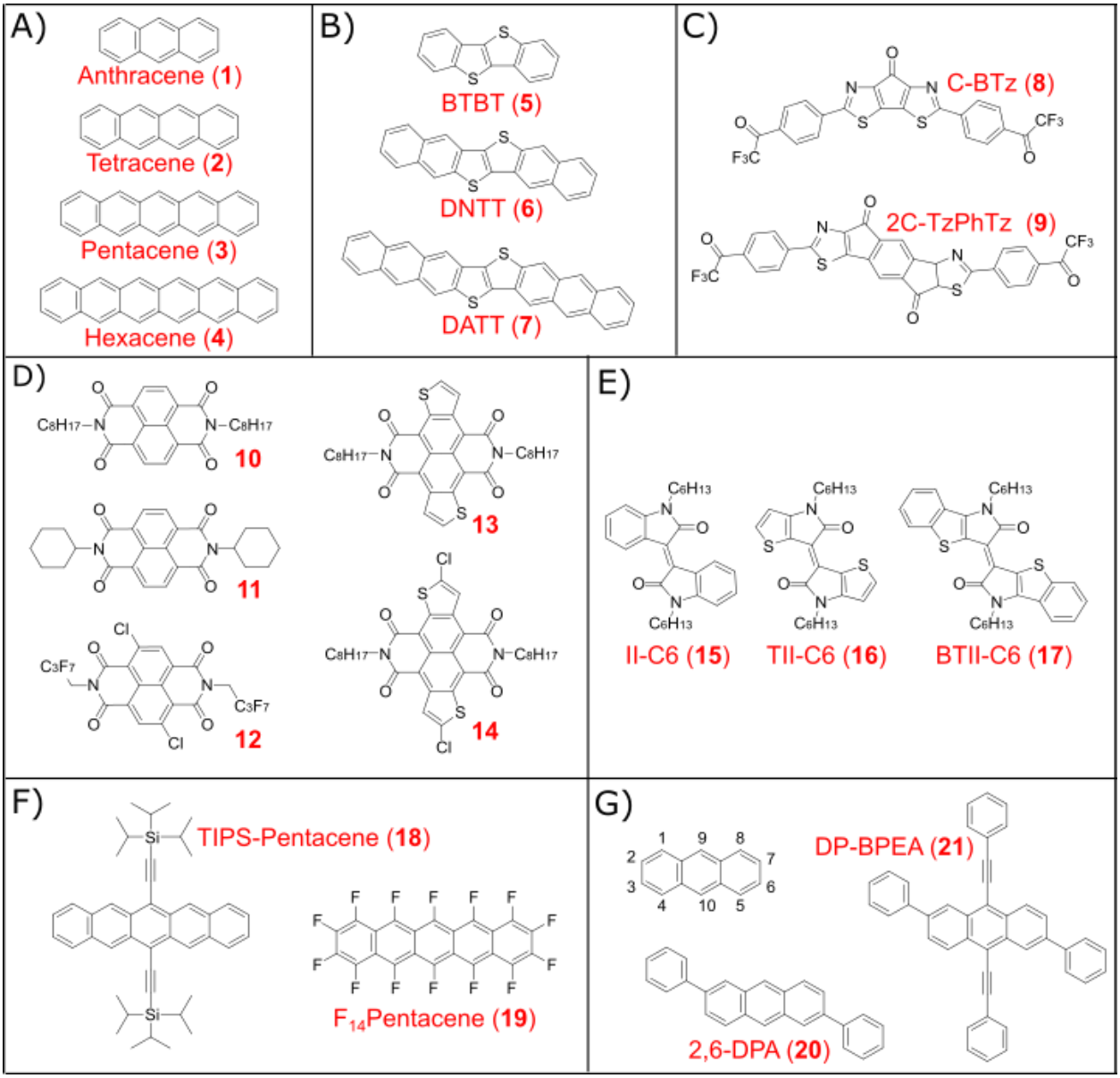

Figure 1.12: Chemical structures of various small molecules used for determining structure-function relationships, labelled when concise and divided by category: A) Acenes of various sizes; B) benzothieno[3,2-b][1]benzothiophene (BTBT) and its π-extended analogues C) carbonyl-bridged bithiazole (CBB) functionalized with two trifluoroacetylphenyl groups (**8**) and its core-modified analogue (**9**); D) derivatives based off of the naphthalene diimide (NDI) core; E) derivatives based off of the isoindigo (II) core; F) pentacene derivatives; G) Substitution positions for anthracene and two derivatives with rigid substituents

Figure 1.12A shows the most frequently studied small molecule OSC, pentacene (**3**), and several other acenes that differ only in their number of fused rings. Density functional theory (DFT) calculations on single crystals of this molecular series concluded that as conjugation increases, the HOMO of the molecule moves towards vacuum, charge transfer integrals increase, and molecular reorganization energies decrease.[44] The decreased HOMO level means that larger acenes are less stable to oxidation, while the other two changes suggest charge hopping between molecules is enhanced, which leads to an increase in theoretical mobility. Thus, increasing conjugation with fused benzene rings can present a trade-off between stability and performance. Incorporating fused thiophene units can deepen the HOMO and increase stability, with DNTT (**6**, Figure 1.12B) showing a HOMO level of -5.4 eV, much deeper than -4.4 eV for hexacene, despite the same number of rings.[45] DNTT OTFTs[46] demonstrated μ_h of 2.4-3.1 $cm^2V^{-1}s^{-1}$ while its π-extended analogue DATT (**7**, Figure 1.12B) demonstrated μ_h of 2.3 to 3.0 $cm^2V^{-1}s^{-1}$ with a reasonably deep HOMO of -5.1 eV.[47] The role of thiophene units and π-extension was studied for soluble isoindigo derivatives **15**-**17** in Figure 1.12E.[48] Of the three molecules, the benzothienoisoindigo derivative BTII-C6 had the highest μ_h of 0.18 $cm^2V^{-1}s^{-1}$ due to increased planarity and molecular overlap, with the shallowest HOMO of -5.2 eV due to the increased conjugation. Fused thiophene units can stabilize the LUMO level in n-type OSCs as well. Compared to C8-NDI (**10**, Figure 1.12D), C8-NDTI (**13**, Figure 1.12D) has a deeper LUMO level by 0.2 eV.[49] Because the additional thiophene units are easier to functionalize than the interior rings, many NDTI derivatives can be synthesized with LUMO levels as deep as -4.2 eV. The best performing derivatives are functionalized at the alpha position on the thiophene units, with dichloro-substituted NDTI derivative **14** (Figure 1.12D) demonstrating an air-stable μ_e of 0.3 $cm^2V^{-1}s^{-1}$.[50] In another example, the central unit in C-BTz (**8**, Figure 1.12C) was extended to include an additional electron withdrawing carbonyl group in 2C-TzPhTz (**9**, Figure 1.12C).[51] This reduced the LUMO level from -3.64 eV to -3.8 eV and reduced the π-π stacking distance, resulting in improved air stability and electron mobility.

Improved solid-state packing and OTFT performance can also be achieved by the addition of unfused conjugated substituents. Anthracene (**1**, Figure 1.12A) has been modified in the 2, 6, 9 and 10 positions as illustrated in Figure 1.12G with good results in OTFTs.[52] Single crystal organic field-effect transistors (SCOFETs) of anthracene demonstrated μ_h of only 0.02 $cm^2V^{-1}s^{-1}$,[53] while 2,6-DPA (**20**, Figure 1.12G) demonstrated μ_h up to 34 $cm^2V^{-1}s^{-1}$ in SCOFETs[54] and μ_h of 8 - 16

$cm^2V^{-1}s^{-1}$ in OTFTs.[55] The herringbone packing motif of 2,6-DPA creates an ultra-close π-π stacking distance of 2.85 Å, greatly facilitating charge transport. For comparison, the closest stacking distance for anthracene in ambient conditions is 3.6 Å.[56] The HOMO level of 2,6-DPA, -5.6 eV,[52] is deep enough to produce problems with contact resistance, as discussed in Section 1.3.5. Replacing the phenyl groups with napthyl groups reduces the HOMO to -5.3 eV, much closer to the work function of gold, and produced SCOFETs with μ_h up to 12.3 $cm^2V^{-1}s^{-1}$. Another method to increase conjugation without fused rings is to attach ethynylphenyl groups, such as in DP-BPEA (**21**, Figure 1.12G), raising the HOMO level to -5.4 eV (from -5.6 eV for 2,6-DPA) and producing OTFTs with μ_h of 1.37 $cm^2V^{-1}s^{-1}$.[57]

Solubilizing groups such as alkyl chains are often added to the core of small molecule OSCs to facilitate solution processing. These groups impact self-assembly and molecular stacking in thin-films with the potential to enhance mobility or other electronic properties.[58] However, because side-chains are insulating, they may disrupt charge transport, especially with branched chains.[27] A famous positive example is the 6,13-bis(triisopropyl-silylethynyl) (TIPS) group which has been attached to pentacene to form the soluble TIPS-pentacene (**18**, Figure 1.12F), which demonstrated μ_h up to 3.8 $cm^2V^{-1}s^{-1}$ in SCOFETs.[59] N-type materials can be modified with solubilizing groups as well. Fluoroalkyl chains were used to increase solubility and air stability for naphthalene diimide (NDI) derivatives, perhaps by decreasing the permeability of the films to ambient gases that might degrade performance.[60] In another study on NDI-based molecules, cyclohexyl side groups (**11**, Figure 1.12D) were compared to hexyl side groups (**10**, Figure 1.12D) with the goal of increasing conformational rigidity while maintaining solubility.[61] The cyclohexyl-substituted NDI molecule formed more ordered films with higher order diffraction than the hexyl control, and performed better in OTFTs, but devices were not air stable.

Electron withdrawing groups are often attached to the conjugated core to stabilize it against oxidation.[27] This can improve the stability of n-type OSCs, or convert p-type OSCs to n-type. This tactic was applied to p-type CuPc to make F_{16}CuPc (**23**, M = Cu, Figure 1.13), an n-type OSC that will be discussed in the next section. Perfluoropentacene (**19**, Figure 1.12F) was reported in 2004, demonstrating unipolar n-type transport with μ_e of 0.04 to 0.11 $cm^2V^{-1}s^{-1}$ in OTFTs.[62] For both tetracene (**4**, Figure 1.12A) and pentacene (**3**, Figure 1.12A), perfluorination decreases electron affinity and ionization energy by 1 eV while significantly altering solid-state packing.[63] Although fluorine is often used because it is small and highly electronegative, other withdrawing groups can

be incorporated into the periphery of OSCs as well. To improve performance in soluble n-type NDI derivatives, the four core hydrogens were systematically substituted with chlorine atoms.[64] The best performance was consistently obtained when only two hydrogens were replaced (**12**, Figure 1.12D). OTFTs using **12** had a deeper LUMO level (-4.01 eV) than the hydrogenated control (-3.72 eV), which contributed to stable electron conduction. However, the tetra-substituted derivative did not demonstrate good π-π stacking, potentially due to the steric hindrance of the large chlorine substituents.

1.3.3.2 Metal Phthalocyanines

The basic structure of an MPc molecule (**22**) is shown in Figure 1.13, where a central atom, often a metal or metalloid, is chelated by a π-conjugated ring. There are several structural elements in this class of molecule with potential to affect charge transport in OTFTs including the choice of central atom, the π-conjugated ring itself, peripheral substitutions to the outer H atoms of the ring, and axial attachments to certain central atoms such as Si or Sn. Changes to these elements have been studied both computationally and experimentally in OTFTs and single crystal field-effect transistors (SCOFETs), with similar techniques as with the organic small molecules described in the previous section.

The central atom of the MPc plays an important role in its geometry and electronic properties. Many Pcs including Zn, Cu, Co, Mn, Ni, Fe and metal-free (H_2Pc) have a planar structure, but several other configurations are possible. VOPc and TiOPc (**25**, M = V or Ti, Figure 1.13) have cone-shaped geometries, larger atoms may form complexes with multiple atoms or rings such as $LuPc_2$[65] or Eu_2Pc_3[66] and group XIV atoms (**24**, M = Si, Ge and Sn, Figure 1.13) can form distorted planar structures with axial attachments that rise out of the phthalocyanine plane. Cone-shaped molecules have demonstrated the best hole mobility in OTFTs, with average μ_h = 3.31 $cm^2V^{-1}s^{-1}$ for TiOPc[67] and $\mu_{h,avg}$ = 1.99 $cm^2V^{-1}s^{-1}$ for VOPc,[68] but planar MPcs have been studied much more intensely. Kloc et. al. studied the effect of systematically changing the central atom in planar MPcs on SCOFET performance.[69] Most characterized MPcs (Zn, Mn, Fe, Co, Cu but not Ni) outperformed H_2Pc, which the authors attributed to increased intermolecular interactions. H_2Pc has only Van der Waals interactions, while MPcs undergo charge transfer to enhance molecular attraction. The authors suggest this attraction is enhanced by an increased number of singly occupied dz^2 orbitals on the central atom, with Zn and Mn demonstrating the

best performance in SCOFETs. This enhanced attraction resulted in a lower π-π stacking distance, which DFT calculations associated with higher charge transfer integrals between molecules. The same authors studied n-type peripherally fluorinated MPcs and found the same trend for SCOFET performance based on a smaller group of central atoms, with F_{16}ZnPc outperforming F_{16}CoPc and F_{16}CuPc, respectively.[70] The relative performance of each molecule was again explained by the DFT-calculated transfer integral, which was inversely proportional to the π-π stacking distance in the single crystal.

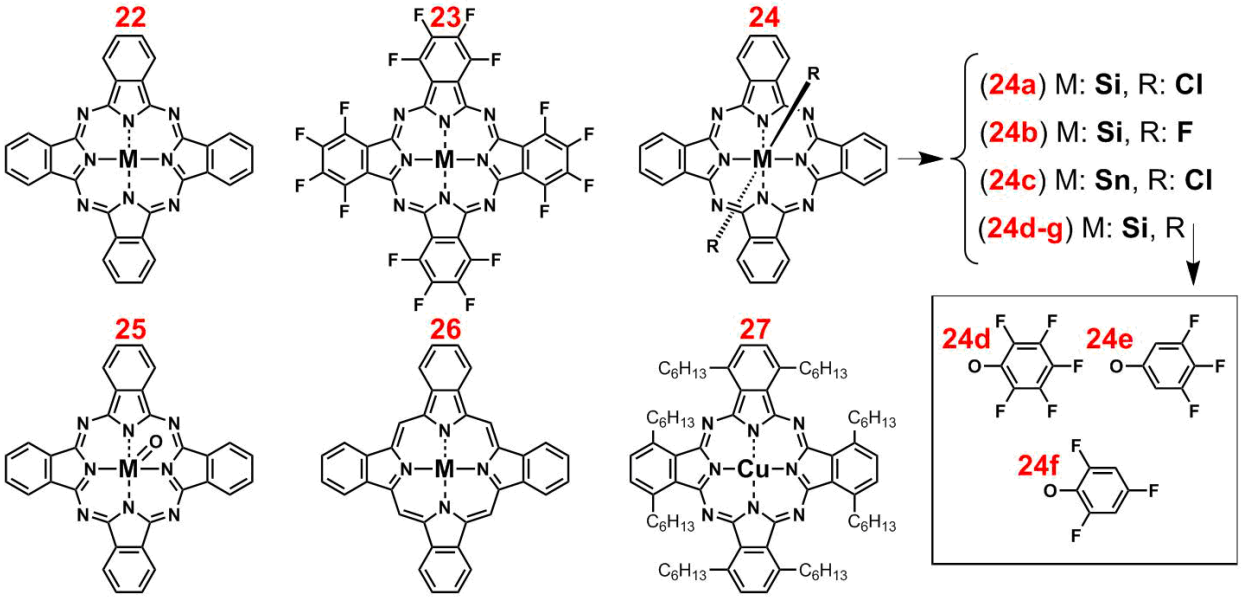

Figure 1.13: Chemical structures for various classes of metal phthalocyanine (MPc) and related structures: (**22**) base MPc; (**23**) peripherally fluorinated MPc; (**24**) group XIV MPcs with symmetric axial substituents in the R positions; (**25**) metal oxide phthalocyanines; (**26**) metal tetrabenzoporphyrins (MTBPs); (**27**) soluble CuPc with symmetric hexyl groups on the outer ring

Altering the π-conjugated core of an MPc molecule is another technique that can be used to alter its electronic properties. Hamuryudan et. al. incorporated ethynylphenyl groups, which are often used for π-extension, into a soluble CoPc derivative, obtaining functional OTFTs with reasonable mobility.[71] Metal tetrabenzoporphyrin (**26**, MTBP, Figure 1.13) is structurally similar to an MPc, with the four non-coordinating nitrogens in the ring replaced with CH. OTFTs with NiTBP[72] and CuTBP[73] OSCs demonstrated saturation μ_h of 0.22 and > 1 $cm^2V^{-1}s^{-1}$ in air, respectively, but $I_{ON/OFF}$ was only 10^3 and 10^2, indicating an undesirably high off-state

conductivity. P-type MPcs in general show greater air stability and lower off currents, potentially due to stabilizing effects of the additional nitrogen atoms in the π-conjugated core.

Peripheral modification is a common way to alter MPcs in order to increase solubility, change solid-state packing, or change energy levels to convert from P to N type. The electron-withdrawing peripheral fluorine atoms in **23** reduce the LUMO level from the hydrogenated **22**, with UPS measurements indicating a difference of 1.6 eV for ZnPc in 1996.[74] By 1998, F_{16}CuPc was demonstrated as an air-stable, n-type OSC for OTFTs,[75] and it is one of the most studied air-stable n-type materials. The symmetric alkyl-substituted CuPc derivative **27** in Figure 1.13 forms a liquid crystalline phase with μ_h up to 0.7 $cm^2V^{-1}s^{-1}$,[76] higher than that obtained in CuPc SCOFETs.[69] Here, peripheral modification bestows both solubility and beneficial morphological changes at the cost of synthetic simplicity. Another synthetic complication during MPc peripheral modification is the formation of isomers, with the mobility of a mixture potentially higher or lower than that of pure films of each isomer.[77]

Axial modification of dichlorinated group XIV MPcs such as $SiCl_2$Pc or $SnCl_2$Pc (**24a** and **24c**, Figure 1.13) is a simple process that can change the energetics and packing of the base molecules. As shown in Figure 1.14, SiPcs can stack in different ways, depending on the axial substituent.[22] Although it is much bulkier, replacing –Cl in **24a** with pentafluorophenoxy (–OC_6F_5) to make F_{10}SiPc (**24d**, Figure 1.13) improved the solid-state packing, creating noticeable π-π stacking in the single crystal.[21] This enhanced stacking was observed for the other fluorinated phenoxy derivatives **24e**,**f** with the stacking mode and distance changing depending on the position and frequency of F atoms on the phenoxy axial attachments.[19] The LUMO level of the materials, based off of UPS measurements of ionization energy and UV-Vis measurements of optical band gap, was estimated to range between -3.5 eV and -4.0 eV, with the deeper levels close to the threshold required for air-stable n-type conduction. DFT modelling on single crystals of **24b-f** indicated that they were most likely anisotropic hole conductors, except for F_{10}SiPc which might show 2D hole transport.[78] F_{10}SiPc and **24b** were also predicted to demonstrate 2D electron transport, albeit with a lower mobility than for holes. Clearly, axial substitution in SiPcs provides a simple synthetic handle to alter their solid-state arrangement and energetics, two major factors affecting charge transport in OTFTs.

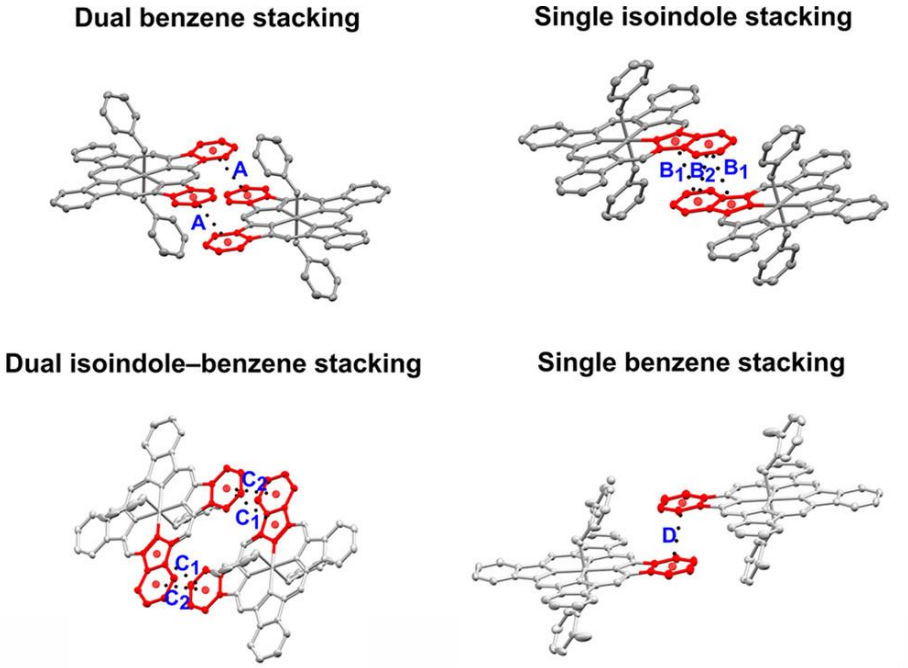

Figure 1.14: π–π interaction modes of SiPcs. Adapted with permission from Cryst. Growth Des., 2018, 18 (5), 3193-3201. Copyright 2018 American Chemical Society.

1.3.3.3 Outlook / Conclusion

There are many ways in which small molecule semiconductors have been modified in order to change their electronic properties in OTFTs or SCOFETs. The options for and effect of these molecular alterations change depending on the base molecule, with many negative examples of substitution presented in literature along with the positive. When researching new classes of OSCs for OTFTs, systematic modification is a viable option to explore structure-function relationships with the goal of designing better-performing molecules. Although synthetic complexity is not always considered, simple and high-yield modifications to base molecules are economically prudent methods to obtain series of analogous molecules. Existing studies can act as guides for the strategic selection of modifications based on the desired outcome and class of molecule.

1.3.4 The Semiconductor-Dielectric Interface

The interface between the semiconductor and dielectric is critical to OTFT operation, as it lies directly adjacent to the sheet of charge that forms upon polarization of the gate electrode then travels through the first few monolayers of the OSC from the source to the drain. For the bottom-gate (BG) configurations shown in Figure 1.8C, the OSC is deposited upon the dielectric, creating a complex set of physical and electronic interactions between the materials that ultimately affects the charge transport properties of the resulting device. To control these interactions, the dielectric of BG devices is typically modified with a self-assembled monolayer (SAM) or by the insertion of a discrete interlayer. The following section describes common and novel methods of dielectric modification and their observed effects on the electronic and morphological properties of the OSC in field-effect transistors. It will focus in scope on devices fabricated using physical vapor deposition (PVD, Section 1.2.2), although relevant research with solution methods will be covered as well.

1.3.4.1 Dielectric Modification Methods

The most common method of modifying the dielectric is by the formation of a self-assembled monolayer (SAM). The type of molecule used for such a surface treatment depends on the dielectric material, and several methods of performing it have been explored. The most commonly reported inorganic dielectrics for BG devices are either SiO_2 or metal oxides such as HfO_x or Al_2O_x. Although polymer dielectrics are required for all-organic devices, they suffer from several downsides for materials development research and applications such as pinholes, low capacitance density (C_i) due to low dielectric constant and high required thickness,[79] and miscibility in organic solvents required for solution processing of the OSC.[80] Inorganic dielectrics are reliable insulators, with SiO_2 formed through the convenient and controlled thermal oxidation of silicon wafers while other metal oxides demonstrate the high C_i required for low-voltage operation. Thus, most SAM treatments are designed for these oxides. Figure 1.16A gives examples of trichlorosilanes (**28-30**, **35**) and trimethoxysilanes (**31**), which are often used to form SAMs on SiO_2, and phosphonates (**32**, **33**, **36**), which are often used for metal oxides.

There are several methods for forming an SAM using an organosilane on SiO_2 dielectrics, including solution phase reaction, vapor phase reaction, and spin-coating. The solution phase reaction involves immersing a SiO_2 substrate into a solvent-organosilane mixture while the vapor-phase reaction involves exposing the substrate to organosilane vapor. In both cases, multiple

reactions are possible at the substrate surface, as illustrated in Figure 1.15. Individual molecules hydrolyze, producing HCl or methanol, with reactive hydoxyl (–OH) groups that further condense with –OH groups on the surface or on other molecules. Thus, single molecules may react directly with the surface ("covalent attachment"), or oligomers may grow away from the surface ("vertical polymerization") or along the surface ("horizontal polymerization").[81] Both solution and vapor methods can produce multiple layers and aggregates due to these multiple possibilities. To produce a reliable monolayer, Bao et. al. reported spin-coating long-chain organosilanes dissolved in an intermediate polarity solvent such as trichloroethylene (TCE).[82] The compromise between solvent and substrate affinity led to the formation of high quality monolayers that demonstrated a high level of crystallinity compared to more typically amorphous silane SAMs. This process was derived from a similar procedure designed for phosphonates on various oxide surfaces.[83]

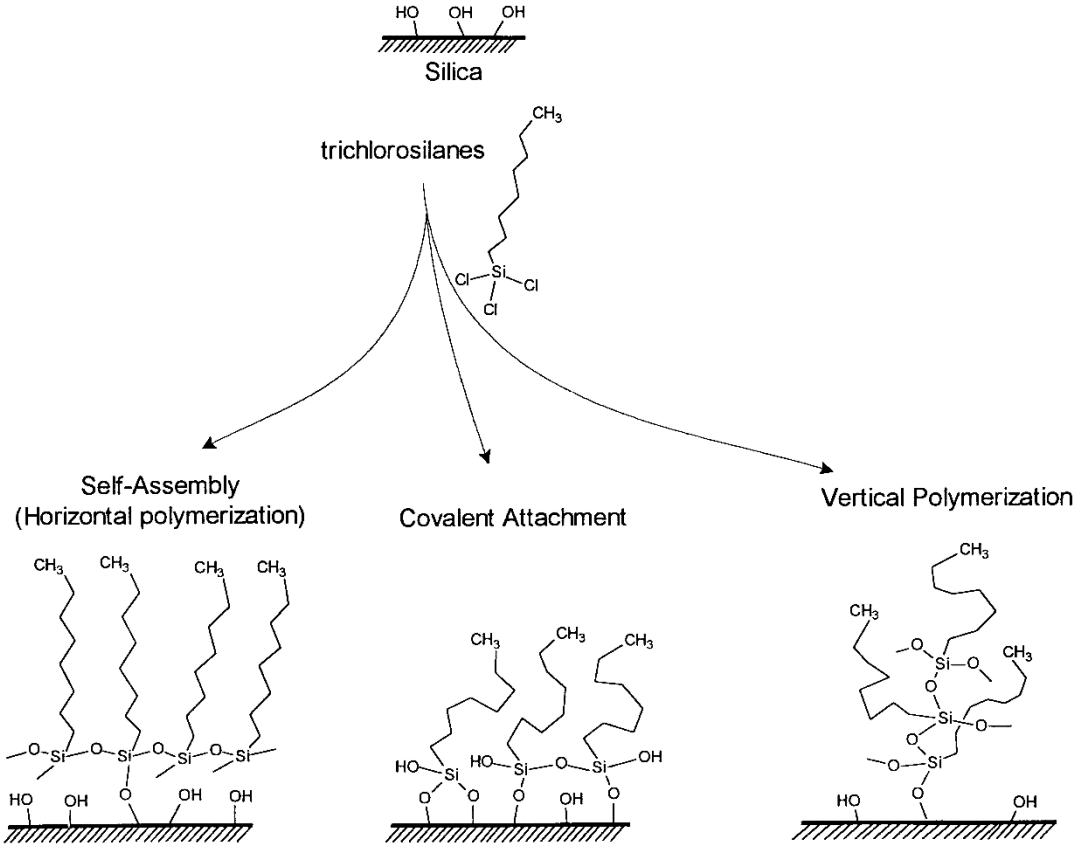

Figure 1.15: Possible products of the reaction of alkylchlorosilanes with silicon dioxide surfaces. Adapted with permission from Langmuir, 2000, 16(18), 7268-7274. Copyright 2000 American Chemical Society.

An alternative method to alter the dielectric surface properties is to insert a discrete layer or interlayer composed of a thin film of polymer or small organic molecules. Ideally, the capacitive properties of the dielectric are not significantly diminished, while the critical surface properties become more optimal. Polymer interlayers can be spin-cast onto the substrate while small molecules can be deposited by solution or vacuum methods. In a few cases, polymer interlayers that can be grafted onto the substrate, using chemistry similar to SAMs.[80,84] The effect of all these interlayers on OTFT operation will be described in the following section.

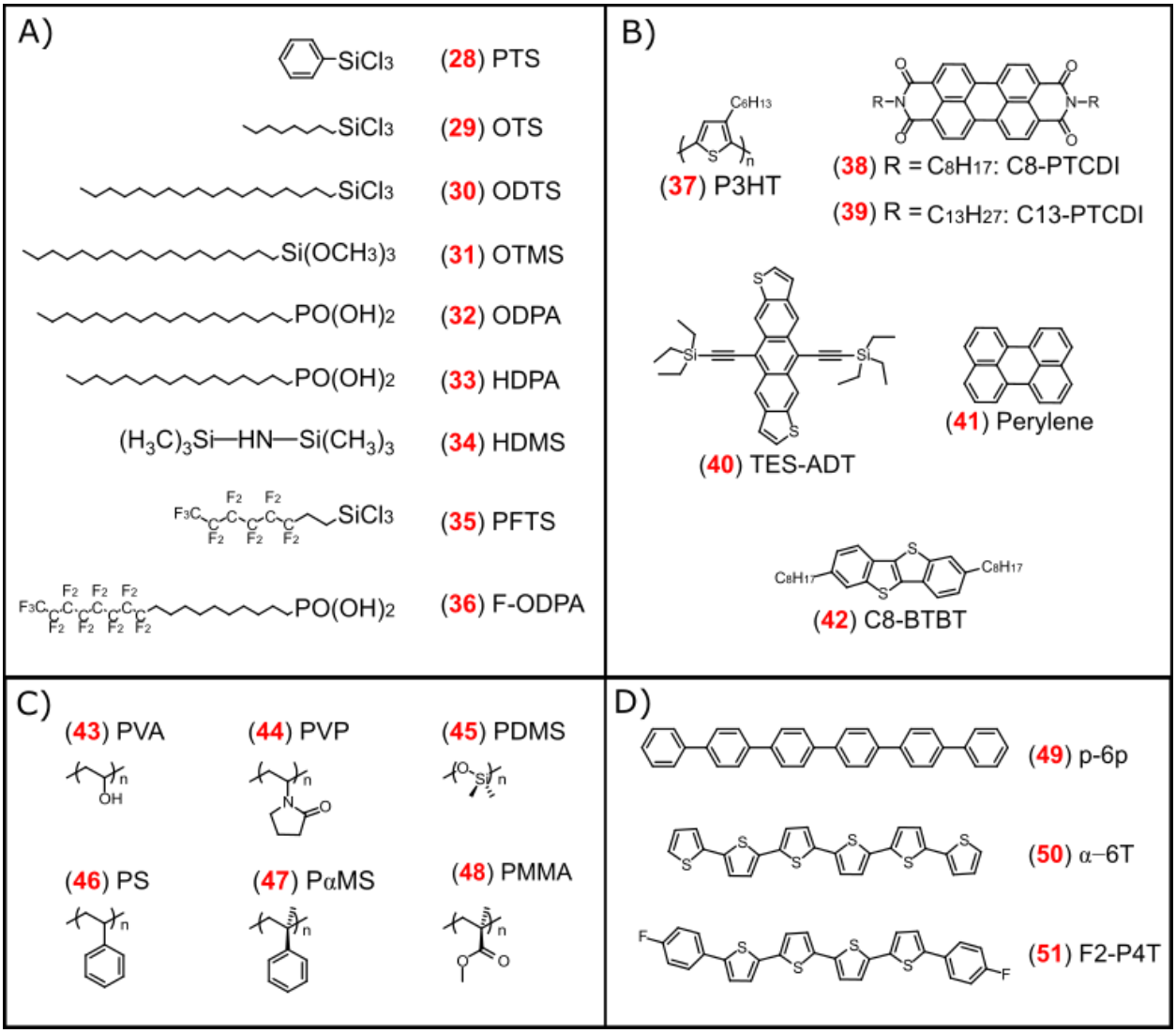

Figure 1.16: List of chemicals referred to in this section: A) molecules used in self-assembled monolayers (SAMs); B) organic semiconductors (OSCs); C) polymer interlayer (PIL) materials; D) small molecule interlayer (SMIL) materials

1.3.4.2 Effects of Dielectric Modification

Modification of the dielectric in BG OTFTs with an interlayer or SAM attempts to control its physical and energetic interactions with the OSC. The surface properties of the dielectric including its roughness and surface energy impact the morphology of the developing semiconductor film as it forms, resulting in different growth modes and degrees of organization.[79] Several energetic interactions can occur independent of morphology. Electronic coupling between the dielectric and the OSC may increase the breadth of the trap state distribution in the OSC band gap, increasing the energetic barrier to charge transport. A surface dipole at the edge of the dielectric may induce charge density in the OSC, altering V_T. Hydroxyl groups at the surface of a dielectric may act as charge traps and attract water molecules in air that further increase charge trapping, especially for n-type semiconductors. These effects have been studied for a number of semiconductors and interlayers/SAMs.

The SAM method is perhaps the most common technique for dielectric modification, as it requires only an anchor group reactive to the substrate, a linking chain (typically alkyl), and a terminal group that controls surface properties.[85] Alkylsilanes such as octadecyltrichlorosilane (ODTS, **30**, Figure 1.16A) and octyltrichlorosilane (OTS, **29**, Figure 1.16A) and their phosphonate analogues produce hydrophobic surfaces with high water contact angles. These low surface energy surfaces reject water, shield the OSC from electronic coupling with the high-k dielectric and hydroxyl-associated trap states, and can induce favorable morphological growth.[79] In 1997, pentacene (**3**, Figure 1.12A) OTFTs using ODTS SAMs demonstrated superior hole mobility over control devices using bare SiO_2, with AFM images suggesting the molecules formed ordered dendritic grains.[86] For alumina dielectrics, 1-phosphonohexadecane (HDPA, **33**, Figure 1.16A) SAMs demonstrated superior mobility over alumina controls and higher surface energy, polar, fluorinated, or shorter-chain SAMs.[87] AFM imaging in this study documented the growth of the pentacene film at several thicknesses, indicating a favorable layer-by-layer growth and obtaining μ_h averaging 2.0 $cm^2V^{-1}s^{-1}$. Using a crystalline SAM formed from spin-coating octadecyltrimethoxysilane (OTMS, **31**, Figure 1.16A) increased μ_h to 2.8 $cm^2V^{-1}s^{-1}$ for pentacene OTFTs, while demonstrating electron mobility for n-type C_{60} of 4.7 $cm^2V^{-1}s^{-1}$.[82] With these successful results for pentacene, organosilane surface treatments were often applied to other semiconductors including phthalocyanines, with titanyl phthalocyanine (TiOPc, **25**(M=Ti), Figure

1.13) devices on Si/SiO_2/ODTS substrates demonstrating μ_h of 3.3 $cm^2V^{-1}s^{-1}$.[67] This excellent performance was attributed to the highly ordered edge-on morphology that formed on the ODTS-modified SiO_2, which contrasted the amorphous morphology and poor μ_h in unmodified devices.

The insertion of ultra-low surface energy SAMs with fluorinated alkyl chains into p-type OTFTs has been demonstrated to shift V_T positively.[85] In order to determine the source of this shift in V_T (ΔV_T), Klauk et. al. varied the thickness of Al_2O_3 dielectric layers with octadecylphosphonic acid (ODPA, **32**, Figure 1.16A) and an analogous PA with seven fluorinated terminal carbons (F-ODPA, **36,** Figure 1.16A).[88] They found that the ΔV_T in F-OPDA corresponded inversely to the capacitance of the dielectric, implying that a space-charge region of injected positive carriers was responsible for the shift. This effect was not observed for ODPA, where ΔV_T was constant and not a function of the dielectric C_i, indicating the ΔV_T was due to an opposition to the small SAM electrostatic potential. The authors also considered the effect of morphology on the ΔV_T, and found that it was too similar for both SAMs to be responsible for the observed changes. In at least one case, use of fluorinated SAMs has led to decreased mobility compared to the bare dielectric or non-fluorinated SAMs, indicating they may induce unfavorable morphology.[87]

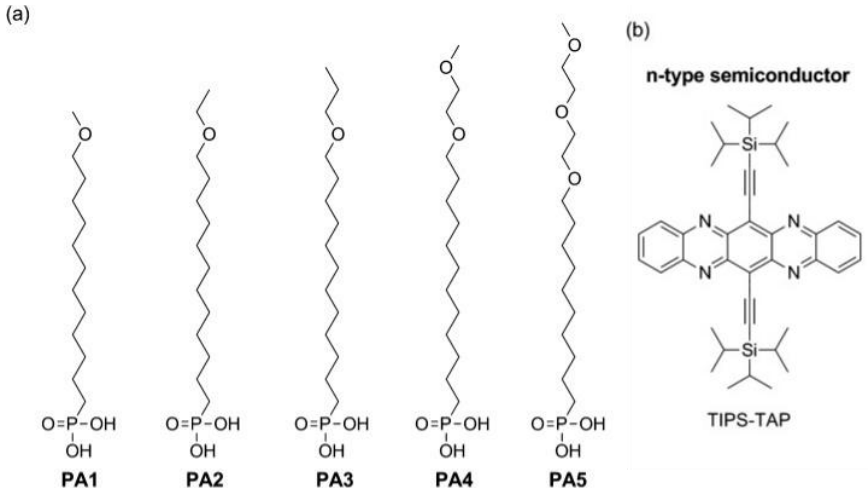

Figure 1.17: Structural formula of phosphonic acids with oxygen atoms inserted into the alkyl chain; b) n-type semiconductor TIPS-TAP. Adapted with permission from Angewandte Chemie International Edition 52(24). 2013. 6222-6227. Copyright 2013 WILEY-VCH Verlag GmbH & Co. KGaA, Weinheim

Although hydrophobic SAMs with alkyl terminal groups and chain links are commonly used, they may present physical and morphological issues during active layer fabrication. For solution-processed materials, lack of adhesion to the low surface energy substrate may prevent film formation, instead producing 3D-ordered OSCs that do not cover the dielectric and thus cannot efficiently transport charge.[89] For vacuum deposited films, the lack of adhesion may also lead to undesirable 3D island growth with many grain boundaries.[85] Thus, more hydrophilic SAMs such as hexamethyldisilazane (HMDS, **34**, Figure 1.16A) or phenyltrichlorosilane (PTS, **28**, Figure 1.16A) are utilized to increase adhesion and improve film morphology. In one case, an organosilicon polymer with similar surface chemistry to SiO_2 was modified with HMDS, OTS, and trichloro(1H,1H,2H,2H-perfluorooctyl) silane (PFTS, **35**, Figure 1.16A) SAMs.[38] They found the highest mobility for pentacene OTFTs (0.59 $cm^2V^{-1}s^{-1}$) was using HMDS SAMs, due to a layer-by-layer growth facilitated by substrate-OSC adhesion. XRD characterization of the films showed sharper, more intense peaks on the HMDS-modified substrates compared to OTS, indicating a greater degree of structural order, and only the OTS-modified substrates showed presence of the bulk phase, which is considered to transport charge less efficiently than the thin-film phase. In another case, anthracene-terminated phosphonic acids (ATPAs) used as SAMs were compared to ODPA on high-capacitance HfO_x dielectrics in pentacene OTFTs.[35] Devices using these ATPAs had marginally higher μ_h, less reduction to the unmodified C_i, and lower leakage currents compared to ODPA, indicating the somewhat higher surface energy of the anthracene-terminated SAMs was favorable for device operation. For rougher AlO_x dielectrics, phenoxy-terminated PAs had higher μ_h and lower V_T compared to the ATPAs, which the authors attribute to the smoothing properties of the SAM. To further investigate the effects of modifying terminal groups, oxygen (-O-) linking groups were incorporated at different positions and frequencies near the end of alkylphosphonic acid molecules and tested in OTFTs using an n-type solution-processable molecule (TIPS-TAPS) as the OSC (Figure 1.17).[89] They found that increasing the number of oxy chain links and moving them closer to the end of the chain increased the surface energy of the SAM, which facilitated adhesion during drop-casting. Only the lowest surface energy SAM was not suitable for film formation, and μ_h averaged between 0.88 and 1.2 $cm^2V^{-1}s^{-1}$ for the resulting OTFTs, at least two orders of magnitude larger than for PTS and HMDS modified dielectrics. A downside of these more hydrophilic modifications is their tendency to attract water, which acts as an electron trap and degrades mobility substantially when characterized in air instead

of N_2, down to 0.02 $cm^2V^{-1}s^{-1}$ for one SAM. Overall, it is unclear that a general rule can be applied about the relationship between SAM surface energy and the morphology of a given semiconductor. The consensus seems to be that both high and low surface energy SAMs can produce desirable morphology for high μ, but unmodified surfaces are almost universally poorly performing.

Polymer and small molecule interlayers (PILs/SMILs) work in similar principle to SAMs, but are typically formed as discrete layers rather than by reaction with the dielectric. Like for SAMs, variation in optimal surface energy is reported along with different engineering strategies. In some cases, the performance of OTFTs using PILs exceeds that of SAMs. In one study, ZnO_2 dielectrics were prepared and modified with nothing, an HMDS SAM, or a poly(α-methylstyrene) (PαMS, **47**, Figure 1.16C) interlayer.[37] AFM images of pentacene grown on the low surface energy PαMS interlayer showed large, interconnected grains, while those grown on HMDS and the bare substrate were much smaller. Thus, the mobility with the PIL was up to 0.51 $cm^2V^{-1}s^{-1}$, considerably higher than the maximum 0.11 $cm^2V^{-1}s^{-1}$ for HMDS. The authors found an increase in OSC mobility as the ZnO_2 dielectric was annealed at a higher temperature, despite no obvious change to the PαMS interlayer. They suggested that the high density of charges due to the higher dielectric constant (k) of the hotter-annealed dielectric might fill trap states in the OSC more effectively, leaving behind more mobile charges. Without an interlayer, ionic polarization with high-k dielectrics typically decreases mobility. In one study with perylene (**41**, Figure 1.16B) OSCs and a mixture of SAMs and PILs, low surface-energy OTS and PDMS (**45**, Figure 1.16C) demonstrated superior mobility and structural order compared to SiO_2 modified with PS (**46**, Figure 1.16C), PMMA (**48**, Figure 1.16C), and napthyl and phenyl terminated silanes.[90] Another study with pentacene found superior mobility for PS and PMMA interlayers compared to HMDS and bare SiO_2 dielectric.[91] In contrast with other studies, AFM images of the pentacene grown on the higher surface energy HMDS and SiO_2 showed larger grains despite weaker charge transport. Devices with these dielectric surfaces had lower operational and long-term stability, which the authors attributed to a higher trap density and increased adsorption of water. This may be an even larger issue with n-type OSCs such as C8-PTDCI (**38**, Figure 1.16B), with high surface energy polymers with hydroxyl groups such as poly(vinyalcohol) (PVA, **43**, Figure 1.16C) and poly (4-vinylphenol) (PVP, **44**, Figure 1.16C) PILs demonstrating considerably lower μ_e and over-time

stability in air compared OTFTs using PMMA and PαMS interlayers.[92] In this example, no significant difference in morphology was found to explain the performance variations in N_2 or air.

Like with an SAM, polymers chains can be designed to react with the dielectric surface as well, creating a grafted polymer brush. The advantage of such a brush is that is modifies the surface properties like a discrete PIL but is less fragile and more compatible with solution processing which might dissolve a typical PIL. In one study with pentacene OSCs, a grafted 19.5 kDa polystyrene (PS) polymer brush demonstrated μ_h up to 0.82 $cm^2V^{-1}s^{-1}$, higher than a lower molecular weight PS brush, and HMDS and ODTS modified SiO_2.[84] XRD synchrotron analysis indicated a higher proportion of thin-film phase on the polymer brushes, with a higher proportion of bulk phase on the SAMs, suggesting morphological reasons for the variation in charge transport. PS brushes were also used to modify SiO_2 dielectrics in TC OTFTs with several OSCs including pentacene, TES-ADT(**40**, Figure 1.16B), PTCDI-13 (**39**, Figure 1.16B) and P3HT(**37**, Figure 1.16B).[80] The performance of the polymer brush devices exceeded that of HMDS in every case, and greatly exceeded the performance of a non-brush PS PIL for solution processed devices. The benefits of such brushes, including those formed by surface-initiated polymerization, have yet to be fully explored for OTFTs.

A small molecule interlayer (SMIL) can be formed by the deposition of a thin organic film, typically between 0 and 10 nm, between the dielectric and the OSC. Although this is less often reported than SAMs or PILS, it has demonstrated promise for OTFTs. For metal phthalocyanines (MPcs), small semiconducting oligomers such as para-sexiphenyl (p-6p, **59**, Figure 1.16D) and α-sexithiophene (α-6T, **50**, Figure 1.16D) have been deposited on the dielectric, separating it from the OSC and allowing the weak epitaxial growth of MPc films with favorable morphology for charge transport.[93] A 2 nm SMIL of p-6p produced μ_h up to 0.32 $cm^2V^{-1}s^{-1}$ for p-type ZnPc (**22**, M=Zn, Figure 1.13) and 0.11 $cm^2V^{-1}s^{-1}$ for n-type F_{16}CuPc (**23**, M=Cu, Figure 1.13).[94] Using a fluorobenzene capped thiophene oligomer (F2-P4T, **51**, Figure 1.16D) as opposed to p-6p in vanadyl phthalocyanine (VOPc, **25**, M=V, Figure 1.13) OTFTs increased μ_h from 1.5 to 2.6 $cm^2V^{-1}s^{-1}$ while decreasing V_T by about 10 V.[68] The authors attribute the V_T decrease observed to the dipole-inducing effect of the F atoms discussed earlier for fluoroalkyl SAMs. Another way to use a SMIL for favorable morphological growth is to spin-coat a thin film of the same material prior to PVD, providing a template for the growth of the film. In one study, spin-coating a molecular

monolayer of C8-BTBT (**42**, Figure 1.16B) on PTS-treated SiO_2 increased the film organization as measured with XRD, increased the OTFT μ_h and decreased its V_T.[95] A unique SMIL has been reported using low-k metal-organic frameworks (MOFs).[96]

1.3.4.3 Conclusion/Outlook

The OSC-dielectric interface is critical to OTFT performance and is important to consider for any research program in OTFT development. Disagreement in the field about the ideal nature of the surface dielectric in bottom-gate devices prior to semiconductor formation and limited expertise in the wide variety of modification techniques make these considerations challenging. Thus, a careful, data-driven approach is essential, rather than the assumption of a best method for dielectric modification. Understanding the intricate combination of morphological and electronic interactions at the interface and how to characterize them will assist in such a measured approach.

1.3.5 The Semiconductor-Electrode Interface

The current (I_{DS}) and therefore state of an OTFT is measured between the source and drain (SD) electrodes, often composed of a thin film (40-80 nm) of a highly conductive metal such as gold (Au). These electrodes play a significant, sometimes overlooked role in OTFT operation, since carrier injection between them and the OSC can be hindered by a number of factors, reducing measured I_{DS}.[24] This current decrease affects the measurement of device performance and invalidates the assumptions required for to use the MOSFET equations to extract field-effect mobility and threshold voltage.[23] The following section describes the source and effect of this contact resistance (R_C), how it is calculated, and what research exists on decreasing it in OTFTs.

1.3.5.1 Sources of Contact Resistance (R_C)

The most common materials used for OTFT SD electrodes are inorganic metals such as Au, often chosen for their deep work function and high conductivity. Regardless of design architecture, the electrodes form an interface with the OSC which requires the injection of charge from the electrodes to the OSC. In addition, the charges must sometimes move through the OSC to the channel from the contacts. These processes may be semi-Ohmic, essentially free of resistance, or non-Ohmic, where they are impeded by R_C. This resistance is affected by a number of properties of the OSC, the metal, and the interface that they form. At a most basic level, the difference in energy between the relevant frontier molecular orbital (HOMO, for holes; LUMO, for electrons) and the work function of the metal contact creates an injection barrier that contributes to R_C.[97] As the materials form an interface, they may interact in a number of ways including charge transfer, chemical reaction, surface dipole interactions, image force and metal-induced gap states in the OSC.[98] These interactions produce an interfacial dipole which can create or enlarge an injection barrier even when the energy difference of the separate materials is small. This injection barrier is a universal issue with OTFTs using OSC-metal interfaces, and a number of strategies have been developed to decrease it which will be discussed in Section 1.3.5.3.

Some sources of R_C depend on the device architecture. For BC devices (Figure 1.8C), deposition of the OSC on the contacts may create physical gaps and a small injection area, especially if the OSC is thin.[99] For devices with staggered contacts like BGTC and TGBC, charges moving from the source to drain must move from the contact to the conductive channel, a thin layer adjacent to the dielectric. Since most OSCs have low conductivity, this creates a contribution

to R_C called the bulk resistance which is increased with channel thickness and decreased by V_G due to current crowding.[100] The low conductivity of the OSC can impede the injection process as well, with charge traps and low mobility in the vicinity of the metal contacts increasing R_C further.

1.3.5.2 R_C Calculations and Effect on OTFT Characterization

The MOSFET equations from which OTFT μ and V_T are calculated assume $R_C = 0$. Since R_C is generally quite low for inorganic transistors such as Si MOSFETs (< 0.1 Ωcm),[100] this assumption is good for the context in which the equations were developed. For OTFTs, where R_C is much higher and can be comparable to the channel resistance, the equations are often invalid.[101] To account for this apparent issue, several methods of calculating R_C during OTFT characterization exist and are described in the following section.

Equation (1.7) shows the basic relationship between channel and contact resistance, from which the transmission line method (TLM) for calculating contact resistance can easily be derived. Here is the equation used in the TLM to calculate R_C:

$$R_{TOT} = \frac{L}{W\mu C_i(V_{GS}-V_T)} + R_C \quad (1.7)$$

Where R_{TOT} is calculated from the inverse slope of output curves at various V_{GS}, and is a function of V_{GS}. R_C is calculated from the y-intercept of a plot of R_{TOT} against L for a given value of V_{GS}, and can also be calculated from the slope if the equation is multiplied by $\frac{W}{L}$ in what is called the modified transmission line method (mTLM).[102] What is assumed for this calculation is that other parameters such as W, μ, C_i, and V_T do not vary across different devices with distinct L, that R_C is not a function of L, and that R_C is a function of V_{GS}. In practice, this is a good method to calculate R_C if devices with different channel lengths are available, assuming a relatively high device-to-device uniformity. This assumption may be poor for non-homogenous films such as percolating networks of carbon nanotubes, where inter-tube connections may increase R_C as L increases.[103] Despites its downsides, TLM can be used to estimate a more intrinsic value of linear mobility (μ_o) for a set of devices, using the following equation:[104]

$$\mu_o = \frac{1}{C_i}\frac{dm}{dV_G} \; where \; m = \frac{dL}{d(R_{tot}W)} \quad (1.8)$$

Unfortunately, it is not as simple to correct saturation field-effect mobility, although a scaling method can be used assuming apparent (measured) mobility (μ_{app}) is known for devices with different channel lengths:[24]

$$\mu_{app} = \mu_o(1 - \frac{\mu_o C_i \alpha}{L}) \quad (1.9)$$

Another method for calculating R_C in transistors and accounting for its effects is the Y-function method (YFM).[99] This method calculates corrected values of μ and V_T for individual OTFTs in addition to R_C and a mobility attenuation parameter θ. Since it uses individual devices, the variation of device parameters assumed constant in the TLM method is not an issue. R_C and other parameters can be extracted directly from an individual transfer curve, allowing device-to-device and over-time analysis. A major assumption used by the YFM is that R_C is not a function of V_{GS}, as it yields only a single value for a given device. Although in general the TLM finds that R_C does vary with V_{GS}, the assumption seems to hold true at higher values of V_{GS} where R_C is relatively constant. Another limitation of the YFM is that is only applies to data in the linear region, so OTFTs with large Schottky barriers and poor linear region definition that require use of the saturation region for analysis cannot use this method.

A third method for calculating R_C is the four point gated probe techniques (gFPP).[97] This method uses two individual measurements of potential within the channel to determine potential drops at the source and drain separately assuming potential drop along the channel is linear. While a major advantage of this technique is its ability to distinguish between the two different contact resistances, which the TLM and YFM techniques cannot, it is also more difficult to implement due to the incorporation of the channel probes.

1.3.5.3 Reducing Contact Resistance in OTFTs

At least one recent review exists describing methods to decrease *Rc* in OTFTs.[100] The most common methods include selecting alternative metals to use as contacts, using an interlayer between the metal contact and the OSC (Figure 1.18A), modifying the contact with a self-assembled monolayer (SAM, Figure 1.18B), and doping the OSC. This section will describe the theory behind these methods and examples of how they have been used to reduce R_C in OTFTs.

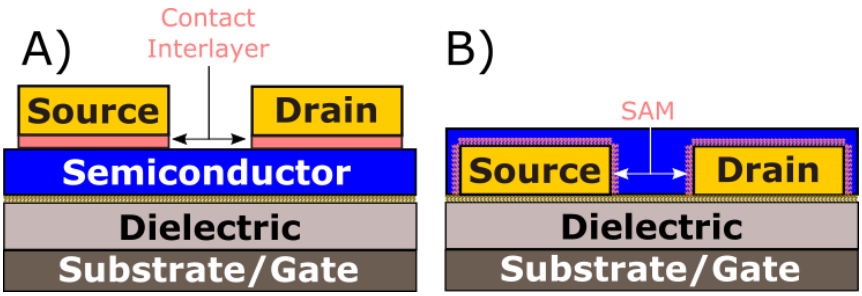

Figure 1.18: Diagrams illustrating A) use of contact interlayer in BGTC OTFTs; B) use of contact SAMs in BGBC OTFTs

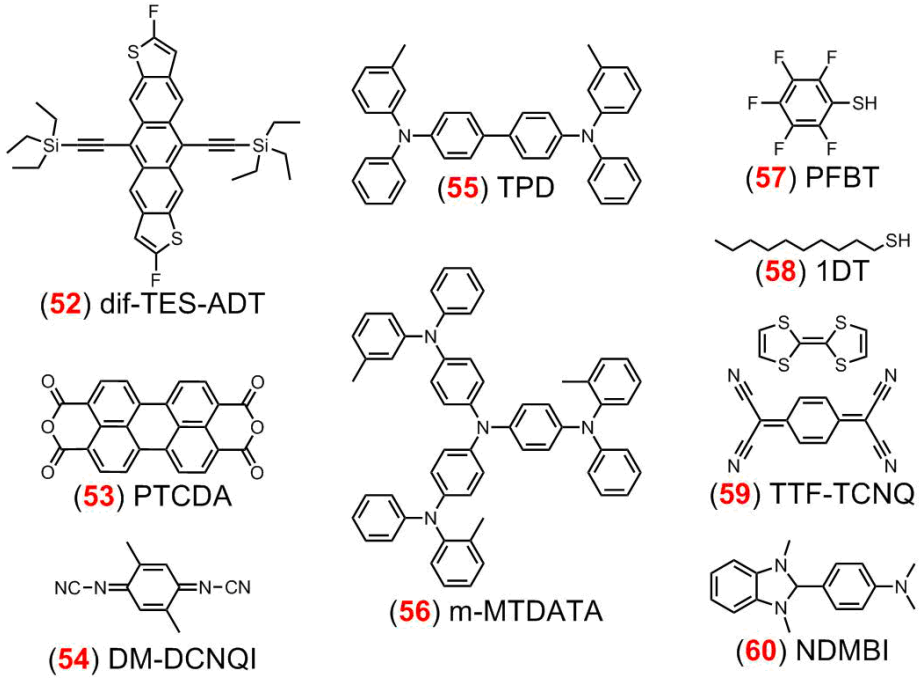

Figure 1.19: Various molecules referenced in this section that have not been previously shown. **52-54**: OSCs; **55-56**: hole transport interlayers; **57-58**: electrode SAM materials; **59**: organic metal; **60**: electron dopant material

Selecting a different metal for use as contact material is a relatively simple method to reduce R_C. For carbon-nanotube TFTs, Pd provided a more Ohmic contact with higher μ_h than Au, Ti and Al, respectively, suggesting deep work-function metals are superior for hole conduction.[103] Another report, however, found that Cu has lower R_C than Au for pentacene OTFTs, which the authors attribute to the latter having a wider trap distribution at the OSC-metal interface, not because of an injection barrier caused by the metal work functions.[105] Electrode substitution can

improve n-channel performance too, with boron subphthalocyanine (BSubPc) OTFTs with low work-function Ca electrodes demonstrating improved μ_e and decreased V_T compared to those with Au electrodes, likely due to reduced R_C.[106] An alternative option to traditional electrodes is selecting an organic metal for the SD contacts, which can form a more homogenous interface with the OSC and which can have tunable work-function based on composition.[107] These organic metals are typically insoluble charge transfer salts such as tetrathiafulvene-tetracyanoquinodimethane (TTF-TCNQ, **59**, Figure 1.19), which can be co-evaporated from the same source at a relatively low temperature. Other organic metals can be solution processed or deposited separately. Using an organic metal has drastically increased μ_h compared to Au or Ag in P-type OTFTs.[108,109] However, in one report TTF-TCNQ performed more poorly than Au in terms of both mobility and R_C for n-type OTFTs using dimethyldicyanoquinone diamine (DM-DCNQI, **54**, Figure 1.19).[110] Thus, organic metals may not be appropriate for all OSCs.

Introducing an interlayer between the metal contact and the OSC may reduce R_C in a number of ways, depending on the material used. In one example, a thin (2-4 nm) insulating layer of Si_3N_4 was used to reduce R_C for pentacene (**3**, Figure 1.12A) and PTCDA (**53**, Figure 1.19) OTFTs.[98] The role of the insulating layer is to decrease the interaction between the OSC and metal and remove the Fermi level (E_F) pinning responsible for an interfacial dipole that increases R_C. It must be thick enough to sufficiently decrease the interaction and de-pin E_F without becoming so thick that it blocks charge. Inorganic semiconductors, especially metal oxides, are more frequently used. MoO_3, which is also used in organic photovoltaics as a hole transport layer, can be incorporated between a metal contact and OSC in a p-type OTFT to reduce R_C. Such an interlayer can undergo charge transfer with the metal or OSC, creating a reduced film of MoOx.[111,112] This charge injection reduces the interfacial dipole and creates a more conductive region around the contact-OSC interface, both of which decrease R_C. Using this strategy in OTFTs allows the inexpensive metal Al to replace Au without compromising performance due to its low work function,[113,114] and can be used with Au to decrease V_T and improve subthreshold characteristics.[115] It is now commonplace for MoO_3 to be incorporated into p-type OTFTs without explicitly characterizing its effect. Other materials that have been used as contact interlayers to improve hole injection include charge transfer salts and organic small molecules. N,N′-Bis(3-methylphenyl)-N,N′-diphenylbenzidine (TPD, **55**, Figure 1.19) was used as an interlayer between pentacene and Ag, with lower R_C, lower V_T and higher μ_h than for devices using Ag, Au, and Ag with an MoO_3

interlayer.[116] Copper phthalocyanine (CuPc)[117] and 4,4′,4″-Tris[phenyl(m-tolyl)amino]triphenylamine (m-MTDATA, **56**, Figure 1.19)[118] have also been reported as interlayers to reduce R_C for pentacene OTFTs. Fewer studies have been conducted using interlayers to reduce R_C for n-type OTFTs. Charge transfer salts[119] and low work-function metal oxides such as TiO_x[120] have been demonstrated, but R_C values are typically higher than for their p-type counterparts, with a recent review reporting about 32-300 kΩcm with contact modification, compared to as low as 8.8 kΩcm for p-type OTFTs.[100]

Although the interlayer method can be used in both top and bottom contact devices, using an SAM to modify the contact works only for the latter, since modification is typically done before OSC deposition.[100] The role of the SAM in decreasing R_C is to push the interface dipole in a particular direction, with the chemical nature of the SAM determining the direction of the push. Electron-withdrawing molecules such as perfluoroalkylthiols (PFATs) or pentafluorobenzenethiol (PFBT, **57**, Figure 1.19) assemble on metal surfaces such as Au due to sulfur-metal interactions, and deepen the effective work function of the contact. Electron-donating molecules such as 1-decanethiol (1DT, **58**, Figure 1.19) can have the opposite effect, reducing the effective work function of the contact. In one study, 1DT hindered hole injection, increasing R_C, while PFATs had the opposite effect, reducing R_C and improving μ_h.[121] In another study, similar SAMs were introduced into OTFTs with an ambipolar semiconducting polymer and the effect on both charge transport types was analyzed.[122] The authors found that 1DT reduced R_C for both electrons and holes, with the latter an unexpected result, while its fluorinated analogue had the expected result of reducing R_C for holes while increasing it for electrons. Recently, PFBT has been used to reduce R_C for OTFTs using pentacene[123] and 2,8-difluoro-5,11-bis(triethylsilylethynyl)anthradithiophene (dif-TES ADT, **52**, Figure 1.19),[101] with the latter demonstrating μ_h up to 20 $cm^2V^{-1}s^{-1}$.

Doping the OSC is another method to reduce R_C in OTFTs by improving the charge mobility of the intrinsic OSC in the vicinity of the contacts and by screening charge-hindering trap states.[100] There are a number of methods to achieve this doping, including using a doping interlayer as discussed earlier, blending a dopant material into the OSC, or exposing the device to dopants after fabrication. Blends of [6,6]-phenyl C_{61} butyric acid methyl ester (PCBM), an n-type OSC, and (4-(1,3- dimethyl-2,3-dihydro-1H-benzoimidazol-2-yl)phenyl)dimethylamine (NDMBI, **60**, Figure 1.19), an n-type dopant, were used to make air stable OTFTs.[124] More recently, aminosilane

vapor was exposed to n-type OTFTs in a controlled atmosphere, reducing V_T and increasing μ_e.[125] This post-fabrication doping reduces charge traps in the OSC without introducing μ_e-lowering defect sites by blending the dopant into the film during fabrication. Unfortunately, both studies did not report the change in R_C upon doping, highlighting the need for more widespread adaptation of such analysis during OTFT characterization.

1.3.5.4 Conclusion/Outlook

Overall, it is clear that reducing contact resistance is an important goal in order to improve OTFT performance, with flexible and varied options available for addressing that goal. With intrinsic parameters like field-effect mobility distorted by R_C, reliable device characteristics cannot be reported while it remains unaccounted for. Exploring different methods for reducing, calculating and accounting for R_C should be prioritized for any research group studying OTFTs.

1.3.6 Operational and Environmental Stability

The electronic output and characterization parameters (μ, V_T, etc.) of organic transistors often vary significantly with time and characterization environment. This change in OTFT performance can make both accurate parameter reporting and practical applications requiring reliable electronics difficult. To understand the source of the variation and increase device stability, researchers have conducted many theoretical and practical studies. This section will focus on describing the origin of electronic instability in OTFTs and methods to reduce it with a focus on N-type OSCs, which have particular sensitivity to ambient degradation, and metal phthalocyanines (MPcs).

1.3.6.1 Sources of Operational Instability

When gathering transfer characteristics over time from an OTFT, the gate bias (V_{GS}) required to inject charges into the OSC typically changes in the direction of the bias, resulting in a shifted threshold voltage (ΔV_T).[126] This so-called gate bias stress can occur in conjunction with changes to field-effect mobility (μ), sub-threshold slope (SS), and off current (I_{OFF}). Complicating and compounding these changes is the characterization environment, which directly affects charge transport and can interact with the gate bias stress. Air is a mixture of gases including water vapor (H_2O), oxygen (O_2) and trace oxidants such as NO_x that can electrochemically, chemically, and physically interact with the dielectric and OSC with or without the presence of mobile charges. The result of these interactions is altered charge transport and polarization properties, especially in N-type materials.

The potential of electrochemical reactions between neutral and charged organic semiconducting polymers was reported in 1997 by Einerhand et al., with particular consideration for the stability of n-type polymers.[127] The oxidation of the conductive polymer anion in the presence of water alone is presented (Reaction 1.1), along with a more general oxidation in the presence of water and oxygen (Reaction 1.2a and 1.2b, rearranged to show different reactants):

$$2Pol^- + 2H_2O \leftrightarrow 2OH^- + H_2 + 2Pol^0 \qquad (1.1)$$

$$O_2 + 4H^+ + 4e^- \leftrightarrow 2H_2O \qquad (1.2a) \qquad O_2 + 2H_2O + 4e^- \leftrightarrow 4OH^- \qquad (1.2b)$$

The oxidation processes in Reactions 1.2a-b happen more readily than those in Reaction 1.1, meaning the electrochemical stability of polymer anions is lower towards the combination of water and oxygen than that of water alone. The same actions can withdraw electrons from p-type materials, potentially increasing the density of mobile holes or doping the OSC, but since HOMO energies are typically much deeper than LUMO energies, the mechanism in Reaction 1.1 is less likely to occur. As these interactions can either decrease or increase the concentration of mobile charges or trap states in OTFTs over time, subsequent studies into operational stability and bias stress in ambient conditions often introduce H_2O and O_2 separately during characterization to ascertain their individual and combined effects.

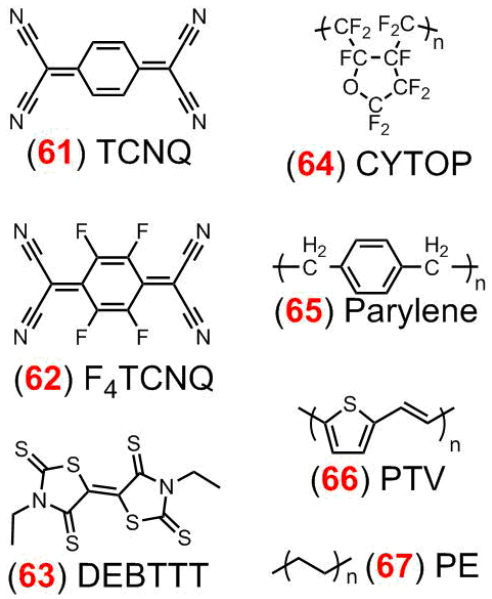

Figure 1.20: Various molecules referenced in this section that have not been previously shown.

Bias stress in p-type polythenylene vinylene (PTV, **66**, Figure 1.20) OTFTs was examined in 1999 by measuring the decay in I_{DS} over time in devices with fixed input V_{GS} and V_{DS} and in different environments (vacuum, O_2, H_2O).[128] Although I_{DS} decreased over time for all characterization environments, it decreased more rapidly in water vapor, indicating bias stress was enhanced. Since using an HMDS (**34**, Figure 1.16A) passivating layer on the SiO_2 dielectric decreased the bias stress in another study,[129] the authors concluded the dielectric surface must likely played an important role in the trap formation. Devices characterized in O_2 showed slightly increased I_{DS}, indicating a possible doping effect without change to bias stress.

The role of the dielectric was further explored in 2005 by Friend et al., who used attenuated-total-reflection FTIR (ATR-FTIR) to measure the concentration of Si-OH groups in an n-type OTFT.[130] They found that with the positive gate bias which accompanies n-type accumulation, the intensity of the Si-OH band decreased. The authors proposed that the Si-OH underwent reversible electrochemical reduction to form $Si\text{-}O^-$ in the presence of positive gate bias. To counteract this process in n-type OTFTs, they found that a passivating surface treatment with ODTS (**30**, Figure 1.16A) or HMDS was inferior to that of a polyethylene interlayer, and incorporated their own novel crosslinked hydroxyl-free PIL into devices.

In 2009, single carbon nanotube (CNT) field-effect transistors with either SiO_2 or parylene (**65**, Figure 1.20) dielectrics were exposed to different gas combinations (O_2, H_2O, N2, O_2+H_2O) to determine their effect on electrical performance.[131] In air, OFETs with parylene dielectrics were ambipolar, while SiO_2 devices were unipolar p-type, while after annealing in vacuum 24h for 120 ºC both became ambipolar. From this baseline ambipolar state, exposure to the various non-inert gas combinations decreased electron transport, especially with the combination of O_2 and H_2O. They argued that an electrochemical interaction between H_2O-solvated oxygen and electrons from the CNTs was responsible for the decline in performance, as in Reactions 1.2a-b. This casts O_2 as the electron acceptor and trap site for mobile electrons, as opposed to the dielectric surface. Reversing the gate bias, the authors claim, would drive the reaction backwards and restore performance, as is typically observed with bias stress effects.

A report by de Leeuw et al. in 2012 described a comprehensive mechanism for bias stress in the form of ΔV_T in P and N-type OFETs involving electrochemical interactions between ambient gases (H_2O, O_2), the organic semiconductor, and –OH groups on the surface of the dielectric.[126] The characteristics of typical ΔV_T are described as nearly universal, slowly reversible over time, increased by the presence of H_2O, impacted in magnitude but not dynamics by V_{GS} and unaffected by V_{DS}. Using scanning Kelvin probe microscopy (SKPM), they examine the potential profile of channels on bare SiO_2 dielectric and full OTFTs under gate bias. They observed slowly decaying potential profiles without the presence of the OSC, which decreases when the SiO_2 is passivated by HMDS. They conclude that the –OH groups on the SiO_2 surface are responsible for this slow decay, and exist in equilibrium with $–O^-$. This equilibrium can be altered by the adsorption of water on the surface, which facilitates the exchange of charge from the OSC. Protons in the SiO_2

dielectric have slight mobility, and diffuse through it, counteracting the gate bias and inducing an opposing electric field. This proton migration is slow but reversible, explaining the rate and reversibility of most observed ΔV_T shifts in OTFTs. Thus, trapped charges in this model are within the dielectric layer, not the OSC.

Another study in 2018 used SKPM to examine potential profiles on many dielectric materials during bias stress, with and without the presence of ambient gases and with polymer and small molecule semiconductor OTFTs.[132] They noticed a similar jump then gradual decay upon application and removal of gate bias in the absence of semiconductor in all dielectrics with protonated functional groups such as –OH, -NH_2 and –COOH, but not in polystyrene (PS) or CYTOP (**64**, Figure 1.20), which lack these functional groups. This process could be mitigated but not eliminated by using a hydrophobic SAM, and a high density SAM was more effective than a low density one for this purpose. Thus, they conclude the dielectric surface is the source of electrochemical trapping of positive or negative charges that oppose the gate bias and that can be slowly recovered. By exposing the substrates to water vapor, they determined that both trapping and recovery are facilitated by adsorbed water at the dielectric surface. In BGBC devices with several OSCs, they determine that trapping occurs mainly near the source electrode where the gate bias is highest and that a drop in observed mobility with gate bias can be explained through the surface trapping mechanism. This drop is most obvious in devices with SiO_2 dielectrics, and can be substantially decreased by passivation of the dielectric or by eliminating water from the devices.

Sirringhaus et. al. carefully investigated the non-electrochemical effects of H_2O and O_2 on n-type polymer OSCs in 2012.[133] Noting that polymers with LUMO deeper than -3.7 eV should be stable towards the oxidation in Reaction 1.1, they selected an OSC with a LUMO of -4.0 eV, and avoided Reactions 1.2a-b by introducing the gases separately. Upon limited O_2 exposure, the linear mobility of the OTFTs decreased without change in the saturation mobility, indicating an increase in contact resistance (R_C). An increase onset voltage (V_{ON}) and hysteresis was observed as well, indicating the presence of trapped negative charges. Using charge accumulation spectroscopy (CAS), the authors determined that these trapped charges were not on the polymer chain, and first principles DFT calculations suggested that a trap state forms upon interaction of the polymer chain with molecular O_2. This trap state was located about 0.5 eV below the LUMO level and localized on the O_2 molecule, explaining why CAS did not detect the trapped charges on

the polymer chain. The observed increase in R_C could be due to the depletion of charges near the contacts. Upon exposure to water vapor, OTFTs demonstrated a decrease in mobility that worsened over time. Although some reversible electrochemical trap formation was detected, the authors found that much of the mobility loss was irreversible, with CAS and Raman spectroscopy suggesting that the lost mobile charges localized on degraded polymer chains, perhaps in the naphthalene diimide (NDI) unit. As this unit is commonly used in n-type OSCs, chemical degradation due to H_2O exposure is an issue that can lead to irreversible operational instability, and could occur with other functional units as well.

1.3.6.2 Improving Stability for N-type OTFTs

Air stable n-type OSCs have not been frequently reported compared to p-type OSCs, potentially due to their increased sensitivity to the various electrochemical and chemical degradation mechanisms described in the preceding section. The most common methods to increase stability in n-type OTFTs are to use an electrochemically inactive dielectric or dielectric-OSC interlayer, to encapsulate the device, or to modify the semiconductor itself to make it more stable. This section will briefly discuss dielectric and semiconductor engineering to decrease bias stress and improve operating stability.

An overview of dielectric modification was discussed in Section 1.3.4, with the previous Section 1.3.6.1 discussing specific effects on operating stability. Two major conclusions with regards to dielectrics are a) polymer interlayers (PILs) are generally superior compared to self-assembled monolayers (SAMs) when used on SiO_2 to reduce bias stress and b) hydroxyl groups either on PILs or the dielectric itself reduce operational stability.[91,92,130,132] Examples of polymer interlayers that have demonstrated good dielectric stability are PαMS,[92] PMMA,[91,92] PS,[91,132] PE (**67**, Figure 1.20),[130] and CYTOP.[132]

Two strategies for increasing n-type stability in OTFTs and OFETs in ambient conditions involve designing OSCs with deep LUMO levels to prevent oxidation or tight solid-state packing in order to reduce infiltration of the active film with water. Incorporating electron-withdrawing groups into OSCs is one way to reduce the LUMO level. For example, Brown et al. reported the use of copper hexadecafluorophthalocyanine (F_{16}CuPc) in OTFTs, demonstrating μ_e up to 0.03 $cm^2V^{-1}s^{-1}$ when characterized in air,[75] attributing the stability to the deep LUMO level of F_{16}CuPc,

reported elsewhere as -4.8 eV.[134] Tetracyanoquinodimethane (TCNQ, **61**, Figure 1.20) was reported as a stable n-type OSC against electrochemical oxidation with water and oxygen by Einerhand in 1997, due to its high electron affinity.[127] Fluorinated TCNQ derivatives were combined with a [1]benzothieno[3,2-b][1]-benthiophene (BTBT, **5**, Figure 1.12B) derivative to form charge transfer salts that were incorporated into OTFTs and single crystal organic field-effect transistors (SCOFETs). The tetrafluorinated-TCNQ charge transfer salt (F_4-TCNQ, **62**, Figure 1.20) initially performed somewhat worse when characterized in air compared to vacuum in OTFTs but slowly improved over one year with μ_e reaching 2.6×10^{-3} $cm^2V^{-1}s^{-1}$ and V_T reaching 7 V.[135] SCOFETs were much more stable both initially and after a year in air, which the authors attribute to the single crystal being impermeable to water and oxygen. The same research group reported a sulfur-rich electron acceptor, DEBTTT (**63**, Figure 1.20), with a deep LUMO energy of -4.4 eV.[136] Despite the low LUMO energy, the V_T of thin-film devices shifted positively over time, reaching 66-69 V after storage in air for 4 weeks. SCOFETs were again much more resistant to property changes, reinforcing the idea that a high level of molecular order can increase device stability. Another group was more successful in producing air-stable thin-film n-type small molecule devices with μ_e up to 0.14 $cm^2V^{-1}s^{-1}$ with V_T of 24 V.[51] The authors took an existing molecule and increased its conjugation while incorporating an electron withdrawing carbonyl group (**9**, Figure 1.12C) resulting in a LUMO drop from -3.64 to -3.79 eV. Other reported air-stable semiconductors include organic radicals based on dithienothiophene,[137] and sulfur-rich nickel complexes.[138]

1.3.6.3 Operational Stability of Metal Phthalocyanines

Studies into environmental and operating stability have been conducted for both N-type and P-type MPcs, although they have received less attention than semiconducting polymers. In 1974, Takeya et al. noticed that PbPc devices had higher conductivity and a lower charge hopping barrier after annealing in O_2.[139] They proposed that O_2 forms a charge transfer state with PbPc, with the "hole-like" positive charge slightly dissociated from the negative charge localized on the O_2 molecule. In 2001, Schottky devices with ZnPc sandwiched between electrodes were exposed to water and oxygen.[140] The authors found that O_2 acts as an electron acceptor, releasing holes and increasing bulk conductivity, while the H_2O vapor affected only surface conductivity. Other studies considered the role of ambient gases in CuPc. In 2006, Yan et al. found that storing P-type

CuPc OTFTs in air for 150 days caused ΔV_T of +20 V and +4.7 V for Ta_2O_5 and SiO_2 dielectrics, respectively, along with an increase in off current.[141] These changes, which were not seen when devices were stored in vacuum, could be reversed by annealing in vacuum. Storage for 24h in a combination of O_2 and H_2O produced similar ΔV_T as seen in air after 150 days, whereas storage in isolated gases did not produce the same bias stress. Thus, the authors conclude that Reaction 1.2b is occurring, with the combination of O_2 and H_2O doping the CuPc OSC. They found encapsulating the OTFTs with crosslinked PVA improved the stability of the devices. Other studies have suggested alternative explanations for the degradation of CuPc OTFTs in ambient conditions. In 2009, Kummel et al. looked at the effect of ambient atmosphere components (N_2, H_2O, O_2, NO_x) on reversible bias stress in CuPc OTFTs.[142] They found that exposure to air increased I_{OFF}, shifted V_T positively, deteriorated sub-threshold characteristics and reduced saturation, especially in devices with thicker CuPc films. This deterioration was attributed to the oxidizing effects of atmospheric NO_x, enhanced by adsorption through additional grain boundaries in the thick films. Recovery was attributed to the displacement of NO_x by H_2O, especially in the presence of O_2. Since bias stress effects in CuPc and other OSCs are often reversible and time-dependent, a pulsed gate is a clever way to reduce ΔV_T. Kummel et al. studied the effects of duty cycle and frequency of gate bias application on CuPc OTFTs in the context of chemical sensing where baseline drift caused by changes in electrical properties is particularly undesirable.[143] They found that with OTFTs where the gate was applied only 10% of the time at 1 Hz pulse frequency or less, baseline drift could be kept below 1%. This technique facilitated the reliable sensing of methanol with three different phthalocyanine semiconductors.

Fewer studies have been conducted on the stability of N-type Pcs, probably because they are relatively uncommon. F_{16}CuPc, which is relatively air-stable and has a deep-lying LUMO level, demonstrated 92-97% mobility loss in BC OTFTs and 99% in TC OTFTs after storage in air for 100 days.[144] CuPc, on the other hand, lost between 28-31% in BC and 83-88% in TC, suggesting it is more stable over time. Top contact tin (IV) phthalocyanine oxide (SnOPc, **25**, M=Sn, Figure 1.13) devices demonstrated a decrease in mobility from about 0.09 to 0.06-0.07 $cm^2V^{-1}s^{-1}$ with a shift in V_T from 40 to 46 V after storage in air for 32 days.[145]

1.3.6.4 Conclusion/Outlook

The electrical stability of OTFTs is affected by the application of gate bias, interaction with ambient gases, dielectric surface, and choice of organic semiconductor. While the effects of these factors cannot always be isolated from one another, characterization of instability under different environments is important to careful reporting of electrical properties and interpreting the performance of new materials. Bias stress should be minimized where possible, and the development of new, air-stable n-type materials is still imperative.

1.4 References

(1) Wang, Y.; Ke, X.; Xiao, Z.; Ding, L.; Xia, R.; Yip, H. Organic and Solution-Processed Tandem Solar Cells with 17.3% Efficiency. *Science.* **2018**, *361* (6407), 1094–1098.

(2) Lin, Y.; Adilbekova, B.; Firdaus, Y.; Yengel, E.; Faber, H.; Sajjad, M.; Zheng, X.; Yarali, E.; Seitkhan, A.; Bakr, O. M.; El-Labban, A.; Schwingenschlögl, U.; Tung, V.; McCulloch, I.; Laquai, F.; Anthopoulos, T. D. 17% Efficient Organic Solar Cells Based on Liquid Exfoliated WS2 as a Replacement for PEDOT:PSS. *Adv. Mater.* **2019**, 1902965.

(3) Fiore, V.; Battiato, P.; Abdinia, S.; Jacobs, S.; Chartier, I.; Coppard, R.; Klink, G.; Cantatore, E.; Ragonese, E.; Palmisano, G. An Integrated 13.56-MHz RFID Tag in a Printed Organic Complementary TFT Technology on Flexible Substrate. *IEEE Trans. Circuits Syst. I Regul. Pap.* **2015**, *62* (6), 1668–1677.

(4) Kim, Y.-H.; Yoo, B.; Anthony, J. E.; Park, S. K. Controlled Deposition of a High-Performance Small-Molecule Organic Single-Crystal Transistor Array by Direct Ink-Jet Printing. *Adv. Mater.* **2012**, *24* (4), 497–502.

(5) Gelinck, G.; Heremans, P.; Nomoto, K.; Anthopoulos, T. D. Organic Transistors in Optical Displays and Microelectronic Applications. *Adv. Mater.* **2010**, *22* (34), 3778–3798.

(6) Kim, S.-J.; Lee, J.-S. Flexible Organic Transistor Memory Devices. *Nano Lett.* **2010**, *10* (8), 2884–2890.

(7) Leong, W. L.; Mathews, N.; Tan, B.; Vaidyanathan, S.; Dötz, F.; Mhaisalkar, S. Towards Printable Organic Thin Film Transistor Based Flash Memory Devices. *J. Mater. Chem.* **2011**, *21* (14), 5203–5214.

(8) Peng, B.; Ren, X.; Wang, Z.; Wang, X.; Roberts, R. C.; Chan, P. K. L. High Performance Organic Transistor Active-Matrix Driver Developed on Paper Substrate. *Sci. Rep.* **2014**, *4*, 6430.

(9) Grau, G.; Kitsomboonloha, R.; Swisher, S. L.; Kang, H.; Subramanian, V. Printed Transistors on Paper: Towards Smart Consumer Product Packaging. *Adv. Funct. Mater.* **2014**, *24* (32), 5067–5074.

(10) Zang, Y.; Huang, D.; Di, C.; Zhu, D. Device Engineered Organic Transistors for Flexible Sensing Applications. *Adv. Mater.* **2016**, *28* (22), 4549–4555.

(11) Ren, X.; Pei, K.; Peng, B.; Zhang, Z.; Wang, Z.; Wang, X.; Chan, P. K. L. A Low-Operating-Power and Flexible Active-Matrix Organic-Transistor Temperature-Sensor Array. *Adv. Mater.* **2016**, *28* (24), 4832–4838.

(12) Sokolov, A. N.; Tee, B. C.-K.; Bettinger, C. J.; Tok, J. B.-H.; Bao, Z. Chemical and Engineering Approaches To Enable Organic Field-Effect Transistors for Electronic Skin Applications. *Acc. Chem. Res.* **2012**, *45* (3), 361–371.

(13) Wu, X.; Ma, Y.; Zhang, G.; Chu, Y.; Du, J.; Zhang, Y.; Li, Z.; Duan, Y.; Fan, Z.; Huang, J. Thermally Stable, Biocompatible, and Flexible Organic Field-Effect Transistors and Their Application in Temperature Sensing Arrays for Artificial Skin. *Adv. Funct. Mater.* **2015**, *25* (14), 2138–2146.

(14) Tiwari, S.; Singh, A. K.; Joshi, L.; Chakrabarti, P.; Takashima, W.; Kaneto, K.; Prakash, R. Poly-3-Hexylthiophene Based Organic Field-Effect Transistor: Detection of Low Concentration of Ammonia. *Sensors Actuators B Chem.* **2012**, *171–172*, 962–968.

(15) Khan, H. U.; Roberts, M. E.; Johnson, O.; Förch, R.; Knoll, W.; Bao, Z. In Situ, Label-Free DNA Detection Using Organic Transistor Sensors. *Adv. Mater.* **2010**, *22* (40), 4452–4456.

(16) Lin, P.; Yan, F. Organic Thin-Film Transistors for Chemical and Biological Sensing. *Adv. Mater.* **2012**, *24* (1), 34–51.

(17) Strakosas, X.; Bongo, M.; Owens, R. M. The Organic Electrochemical Transistor for Biological Applications. *J. Appl. Polym. Sci.* **2015**, *132* (15), 41735.

(18) Campana, A.; Cramer, T.; Simon, D. T.; Berggren, M.; Biscarini, F. Electrocardiographic Recording with Conformable Organic Electrochemical Transistor Fabricated on Resorbable Bioscaffold. *Adv. Mater.* **2014**, *26* (23), 3874–3878.

(19) Lessard, B. H.; Grant, T. M.; White, R.; Thibau, E.; Lu, Z.; Bender, T. P. The Position and Frequency of Fluorine Atoms Changes the Electron Donor/Acceptor Properties of Fluorophenoxy Silicon Phthalocyanines within Organic Photovoltaic Devices. *J. Mater. Chem. A.* **2015**, *3* (48), 24512–24524.

(20) Lessard, B. H.; Lough, J.; Bender, T. P. Crystal Structures of Bis (Phenoxy) Silicon Phthalocyanines: Increasing π-π Interactions, Solubility and Disorder and No Halogen Bonding Observed. *Acta Cryst.* **2016**, *E72* (7), 988–994.

(21) Lessard, B. H.; White, R. T.; Al-amar, M.; Plint, T.; Castrucci, S.; Josey, D. S.; Lu, Z.;

Bender, T. P. Assessing the Potential Roles of Silicon and Germanium Phthalocyanines in Planar Heterojunction Organic Photovoltaic Devices and How Pentafluoro Phenoxylation Can Enhance π − π Interactions and Device Performance. *ACS Appl. Mater. Interfaces.* **2015**, *7* (9), 5076–5068.

(22) Raboui, H.; Lough, A. J.; Plint, T.; Bender, T. P. Position of Methyl and Nitrogen on Axial Aryloxy Substituents Determines the Crystal Structure of Silicon Phthalocyanines. *Cryst. Growth Des.* **2018**, *18* (5), 3193–3201.

(23) Bittle, E. G.; Basham, J. I.; Jackson, T. N.; Jurchescu, O. D.; Gundlach, D. J. Mobility Overestimation Due to Gated Contacts in Organic Field-Effect Transistors. *Nat. Commun.* **2016**, *7*, 1–7.

(24) Phys, J. A.; Natali, D.; Fumagalli, L.; Sampietro, M.; Natali, D.; Fumagalli, L.; Sampietro, M. Modeling of Organic Thin Film Transistors : Effect of Contact Resistances Modeling of Organic Thin Film Transistors : Effect of Contact Resistances. *J. Appl. Phys.* **2007**, *101* (1), 014501.

(25) Shirakawa, H.; Louis, E. J.; MacDiarmid, A. G.; Chiang, C. K.; Heeger, A. J. Synthesis of Electrically Conducting Organic Polymers: Halogen Derivatives of Polyacetylene, (CH)X. *J. Chem. Soc. Chem. Commun.* **1977**, *16*, 578–580.

(26) Kumar, B.; Kaushik, B. K.; Negi, Y. S. Organic Thin Film Transistors: Structures, Models, Materials, Fabrication, and Applications: A Review. *Polymer Reviews*. 2014, pp 33–111.

(27) Mei, J.; Diao, Y.; Appleton, A. L.; Fang, L.; Bao, Z. Integrated Materials Design of Organic Semiconductors for Field-Effect Transistors. *J. Am. Chem. Soc.* **2013**, *135* (18), 6724–6746.

(28) Zade, S. S.; Bendikov, M. From Oligomers to Polymer: Convergence in the HOMO−LUMO Gaps of Conjugated Oligomers. *Org. Lett.* **2006**, *8* (23), 5243–5246.

(29) Wang, Y.-Z.; Cao, L.; Qi, D.-C.; Chen, W.; Wee, A. T. S.; Gao, X.-Y. Tuning the Interfacial Hole Injection Barrier between P-Type Organic Materials and Co Using a MoO3 Buffer Layer. *J. Appl. Phys.* **2012**, *112* (3), 33704.

(30) Coropceanu, V.; Demetrio, A.; Filho, S.; Olivier, Y.; Silbey, R.; Bre, J. Charge Transport in Organic Semiconductors. *Chem. Rev.* **2007**, *107* (4), 926–952.

(31) Mas-torrent, M.; Rovira, C. Role of Molecular Order and Solid-State Structure in Organic

Field-Effect Transistors. *Chem. Rev.* **2011**, *111* (8), 4833–4856.

(32) Kaake, L. G.; Barbara, P. F. Intrinsic Charge Trapping in Organic and Polymeric Semiconductors: A Physical Chemistry Perspective. *J. Phys. Chem. Lett.* **2010**, *1* (3), 628–635.

(33) Ling, M. M.; Bao, Z. Thin Film Deposition , Patterning , and Printing In. *Chem. Mater.* **2004**, *16* (23), 4824–4840.

(34) Rossnagel, S. M. Thin Film Deposition with Physical Vapor Deposition and Related Technologies. *J. Vac. Sci. Technol. A Vacuum, Surfaces, Film.* **2003**, *21* (5), S74–S87.

(35) Hong, M.; Acton, O.; Hutchins, D. O.; Cernetic, N.; Jen, A. K. Multifunctional Phosphonic Acid Self-Assembled Monolayers on Metal Oxides as Dielectrics , Interface Modification Layers and Semiconductors for Low-Voltage High-Performance Organic Field-Effect Transistors. *Phys. Chem. Chem. Phys.* **2012**, *14* (41), 14110–14126.

(36) Wen, Y.; Liu, Y.; Guo, Y.; Yu, G.; Hu, W. Experimental Techniques for the Fabrication and Characterization of Organic Thin Films for Field-Effect Transistors. *Chem. Rev.* **2011**, *111* (5), 3358–3406.

(37) He, W.; Xu, W.; Peng, Q.; Liu, C.; Zhou, G.; Wu, S.; Zeng, M.; Zhang, Z.; Gao, J.; Gao, X.; Lu, X.; Liu, J. Surface Modification on Solution Processable ZrO2 High‐k Dielectrics for Low Voltage Operations of Organic Thin Film Transistors. *J. Phys. Chem. C* **2016**, *120* (18), 9949–9957.

(38) Seong, H.; Baek, J.; Pak, K.; Im, S. G. A Surface Tailoring Method of Ultrathin Polymer Gate Dielectrics for Organic Transistors : Improved Device Performance and the Thermal Stability Thereof. *Adv. Funct. Mater.* **2015**, *25* (28), 4462–4469.

(39) Johnson, P. D.; Hulbert, S. L. Inverse Photoemission. *Rev. Sci. Instrum.* **1990**, *61* (9), 2277–2288.

(40) Hill, I. G.; Kahn, A.; Cornil, J.; Dos Santos, D. A.; Brédas, J. L. Occupied and Unoccupied Electronic Levels in Organic π-Conjugated Molecules: Comparison between Experiment and Theory. *Chem. Phys. Lett.* **2000**.

(41) Hill, I. G.; Milliron, D.; Schwartz, J.; Kahn, A. Organic Semiconductor Interfaces: Electronic Structure and Transport Properties. *Appl. Surf. Sci.* **2000**.

(42) Costa, J. C. S.; Taveira, R. J. S.; Lima, C. F. R. A. C.; Mendes, A.; Santos, L. M. N. B. F. Optical Band Gaps of Organic Semiconductor Materials. *Opt. Mater. (Amst).* **2016**.

(43) Yassar, A.; Horowitz, G.; Valat, P.; Wintgens, V.; Hmyene, M.; Deloffre, F.; Srivastava, P.; Lang, P.; Garnier, F. Exciton Coupling Effects in the Absorption and Photoluminescence of Sexithiophene Derivatives. *J. Phys. Chem.* **1995**, *99* (22), 9155–9159.

(44) Watanabe, M.; Chang, Y. J.; Liu, S. W.; Chao, T. H.; Goto, K.; Islam, M. M.; Yuan, C. H.; Tao, Y. T.; Shinmyozu, T.; Chow, T. J. The Synthesis, Crystal Structure and Charge-Transport Properties of Hexacene. *Nat. Chem.* **2012**, *4* (7), 574–578.

(45) Zschieschang, U.; Ante, F.; Kälblein, D.; Yamamoto, T.; Takimiya, K.; Kuwabara, H.; Ikeda, M.; Sekitani, T.; Someya, T.; Nimoth, J. B.; Klauk, H. Dinaphtho[2,3-b:2′,3′-f]Thieno[3,2-b]Thiophene (DNTT) Thin-Film Transistors with Improved Performance and Stability. *Org. Electron. physics, Mater. Appl.* **2011**, *12* (8), 1370–1375.

(46) Yamamoto, T.; Takimiya, K. FET Characteristics of Dinaphthothienothiophene (DNTT) on Si/SiO 2 Substrates with Various Surface-Modifications. *Journal of Photopolymer Science and Technology*. 2007, pp 57–59.

(47) Niimi, K.; Shinamura, S.; Osaka, I.; Miyazaki, E.; Takimiya, K. Dianthra[2,3- b:2′,3′- f]Thieno[3,2- b]Thiophene (DATT): Synthesis, Characterization, and FET Characteristics of New π-Extended Heteroarene with Eight Fused Aromatic Rings. *J. Am. Chem. Soc.* **2011**, *133* (22), 8732–8739.

(48) Hasegawa, T.; Ashizawa, M.; Matsumoto, H. Design and Structure-Property Relationship of Benzothienoisoindigo in Organic Field Effect Transistors. *RSC Adv.* **2015**, *5* (75), 61035–61043.

(49) Takimiya, K.; Nakano, M. Thiophene-Fused Naphthalene Diimides: New Building Blocks for Electron Deficient p-Functional Materials. *Bull. Chem. Soc. Jpn.* **2018**, *91* (1), 121–140.

(50) Nakano, M.; Osaka, I.; Hashizume, D.; Takimiya, K. α-Modified Naphthodithiophene Diimides-Molecular Design Strategy for Air-Stable n-Channel Organic Semiconductors. *Chem. Mater.* **2015**, *27* (18), 6418–6425.

(51) Ie, Y.; Ueta, M.; Nitani, M.; Tohnai, N.; Miyata, M.; Tada, H.; Aso, Y. Air-Stable n-Type Organic Field-Effect Transistors Based on 4,9-Dihydro-s-Indaceno[1,2-b:5,6-b']Dithiazole-4,9-Dione Unit. *Chem. Mater.* **2012**, *24* (16), 3285–3293.

(52) Chen, M.; Yan, L.; Zhao, Y.; Murtaza, I.; Meng, H.; Huang, W. Anthracene-Based

Semiconductors for Organic Field-Effect Transistors. *J. Mater. Chem. C.* **2018**, *6* (28), 7416–7444.

(53) Aleshin, A. N.; Lee, J. Y.; Chu, S. W.; Kim, J. S.; Park, Y. W. Mobility Studies of Field-Effect Transistor Structures Based on Anthracene Single Crystals. *Appl. Phys. Lett.* **2004**, *84* (26), 5383–5385.

(54) Liu, J.; Zhang, H.; Dong, H.; Meng, L.; Jiang, L.; Jiang, L.; Wang, Y.; Yu, J.; Sun, Y.; Hu, W.; Heeger, A. J. High Mobility Emissive Organic Semiconductor. *Nat. Commun.* **2015**, *6* (May), 0–7.

(55) Liu, J.; Dong, H.; Wang, Z.; Ji, D.; Cheng, C.; Geng, H.; Zhang, H.; Zhen, Y.; Jiang, L.; Fu, H.; Bo, Z.; Chen, W.; Shuai, Z.; Hu, W. Thin Film Field-Effect Transistors of 2,6-Diphenyl Anthracene (DPA). *Chem. Commun.* **2015**, *51* (59), 11777–11779.

(56) Oehzelt, M.; Resel, R.; Nakayama, A. High-Pressure Structural Properties of Anthracene up to 10 GPa. *Phys. Rev. B - Condens. Matter Mater. Phys.* **2002**, *66* (17), 1–5.

(57) Liu, J.; Liu, J.; Zhang, Z.; Xu, C.; Li, Q.; Zhou, K.; Dong, H.; Zhang, X.; Hu, W. Enhancing Field-Effect Mobility and Maintaining Solid-State Emission by Incorporating 2,6-Diphenyl Substitution to 9,10-Bis(Phenylethynyl)Anthracene. *J. Mater. Chem. C.* **2017**, *5* (10), 2519–2523.

(58) Beaujuge, P. M.; Frechet, J. M. J. Molecular Design and Ordering Effects in π -Functional Materials for Transistor and Solar Cell Applications. *J. Am. Chem. Soc.* **2011**, *133* (50), 20009–20029.

(59) Li, H.; Tee, B. C. K.; Giri, G.; Chung, J. W.; Lee, S. Y.; Bao, Z. High-Performance Transistors and Complementary Inverters Based on Solution-Grown Aligned Organic Single-Crystals. *Adv. Mater.* **2012**, *24* (9), 2588–2591.

(60) Katz, H. E.; Lovinger, A. J.; Johnson, J.; Kloc, C.; Siegrist, T.; Li, W.; Lin, Y. Y.; Dodabalapur, A. A Soluble and Air-Stable Organic Semiconductor with High Electron Mobility. *Nature* **2000**, *404* (6777), 478.

(61) Shukla, D.; Nelson, S. F.; Freeman, D. C.; Rajeswaran, M.; Ahearn, W. G.; Meyer, D. M.; Carey, J. T. Thin-Film Morphology Control in Naphthalene-Diimide-Based Semiconductors: High Mobility n-Type Semiconductor for Organic Thin-Film Transistors. *Chem. Mater.* **2008**, *20* (24), 7486–7491.

(62) Sakamoto, Y.; Suzuki, T.; Kobayashi, M.; Gao, Y.; Fukai, Y.; Inoue, Y.; Sato, F.; Tokito,

S. Perfluoropentacene: High-Performance p-n Junctions and Complementary Circuits with Pentacene. *J. Am. Chem. Soc.* **2004**, *126* (26), 8138–8140.

(63) Delgado, M. C. R.; Pigg, K. R.; Da Silva Filho, D. A.; Gruhn, N. E.; Sakamoto, Y.; Suzuki, T.; Osuna, R. M.; Casado, J.; Hernández, V.; Navarrete, J. T. L.; Martinelli, N. G.; Cornil, J.; Sanchez-Carrara, R. S.; Coropceanu, V.; Rrédas, J. I. U. Impact of Perfluorination on the Charge-Transport Parameters of Oligoacene Crystals. *J. Am. Chem. Soc.* **2009**, *131* (4), 1502–1512.

(64) Lee, W.; Oh, J. H.; Suraru, S.; Chen, W.; Würthner, F. High-Mobility Air-Stable Solution-Shear-Processed n-Channel Organic Transistors Based on Core-Chlorinated Naphthalene Diimides. *Adv. Funct. Mater.* **2011**, *21* (21), 4173–4181.

(65) Chaure, N. B.; Sosa-Sanchez, J. L.; Cammidge, A. N.; Cook, M. J.; Ray, A. K. Solution Processable Lutetium Phthalocyanine Organic Field-Effect Transistors. *Org. Electron.* **2010**, *11* (3), 434–438.

(66) Kong, X.; Zhang, X.; Gao, D.; Qi, D.; Chen, Y.; Jiang, J. Air-Stable Ambipolar Field-Effect Transistor Based on a Solution-Processed Octanaphthoxy-Substituted Tris(Phthalocyaninato) Europium Semiconductor with High and Balanced Carrier Mobilities. *Chem. Sci.* **2015**, *6*, 1967–1972.

(67) Li, L.; Tang, Q.; Li, H.; Yang, X.; Hu, W.; Song, Y.; Shuai, Z.; Xu, W.; Liu, Y.; Zhu, D. An Ultra Closely Π-Stacked Organic Semiconductor for High Performance Field-Effect Transistors. *Adv. Mater.* **2007**, *19* (18), 2613–2617.

(68) Pan, F.; Tian, H.; Qian, X.; Huang, L.; Geng, Y.; Yan, D. High Performance Vanadyl Phthalocyanine Thin-Film Transistors Based on Fluorobenzene End-Capped Quaterthiophene as the Inducing Layer. *Org. Electron.* **2011**, *12* (8), 1358–1363.

(69) Jiang, H.; Hu, P.; Ye, J.; Ganguly, R.; Li, Y.; Long, Y.; Fichou, D.; Hu, W.; Kloc, C. Hole Mobility Modulation in Single-Crystal Metal Phthalocyanines by Changing the Metal–π/π–π Interactions. *Angew. Chemie* **2018**, *130* (32), 10269–10274.

(70) Jiang, H.; Ye, J.; Hu, P.; Wei, F.; Du, K.; Wang, N.; Ba, T.; Feng, S.; Kloc, C. Fluorination of Metal Phthalocyanines: Single-Crystal Growth, Efficient N-Channel Organic Field-Effect Transistors, and Structure-Property Relationships. *Sci. Rep.* **2014**, *4*, 1–6.

(71) Hamuryudan, E.; Nar, I.; Atsay, A.; Karaoglu, H. P.; Altindal, A. π-Extended Hexadeca-

Substituted Cobalt Phthalocyanine as an Active Layer for Organic Field-Effect Transistors. *Dalt. Trans.* **2018**, *47* (42), 15017–15023.

(72) Shea, P. B.; Kanicki, J.; Pattison, L. R.; Petroff, P.; Kawano, M.; Yamada, H.; Ono, N. Solution-Processed Nickel Tetrabenzoporphyrin Thin-Film Transistors. *J. Appl. Phys.* **2006**, *100* (3), 034502.

(73) Shea, P. B.; Pattison, L. R.; Kawano, M.; Chen, C.; Chen, J.; Petroff, P.; Martin, D. C.; Yamada, H.; Ono, N.; Kanicki, J. Solution-Processed Polycrystalline Copper Tetrabenzoporphyrin Thin-Film Transistors. *Synth. Met.* **2007**, *157* (4–5), 190–197.

(74) Karmann, E.; Meyer, J. P.; Schlettwein, D.; Jaeger, N. I.; Anderson, M.; Schmidt, A.; Armstrong, N. R. Photoelectrochemical Effects and (Photo)Conductivity of "n-Type" Phthalocyanines. *Mol. Cryst. Liq. Cryst. Sci. Technol. Sect. A Mol. Cryst. Liq. Cryst.* **1996**, *283* (1), 283–291.

(75) Bao, Z.; Lovinger, A. J.; Brown, J. New Air-Stable n-Channel Organic Thin Film Transistors. *J. Am. Chem. Soc.* **1998**, *120* (1), 207–208.

(76) Chaure, N. B.; Pal, C.; Barard, S.; Kreouzis, T.; Ray, A. K.; Cammidge, A. N.; Chambrier, I.; Cook, M. J.; Murphy, C. E.; Cain, M. G. A Liquid Crystalline Copper Phthalocyanine Derivative for High Performance Organic Thin Film Transistors. *J. Mater. Chem.* **2012**, *22* (36), 19179–19189.

(77) Dong, S.; Tian, H.; Huang, L.; Zhang, J.; Yan, D.; Geng, Y.; Wang, F. Non-Peripheral Tetrahexyl-Substituted Vanadyl Phthalocyanines with Intermolecular Cofacial π–π Stacking for Solution-Processed Organic Field-Effect Transistors. *Adv. Mater* **2011**, *23*, 2850–2854.

(78) Gali, S. M.; Matta, M.; Muccioli, L. Ambipolarity and Dimensionality of Charge Transport in Crystalline Group 14 Phthalocyanines: A Computational Study. *J. Phys. Chem. C* **2018**, *122* (5), 2554–2563.

(79) Sun, X.; Di, C.; Liu, Y. Engineering of the Dielectric – Semiconductor Interface in Organic Field-Effect Transistors. *J. Mater. Chem.* **2010**, *20* (13), 2599–2611.

(80) Kim, S. H.; Jang, M.; Yang, H.; Anthony, J. E.; Park, C. E. Physicochemically Stable Polymer-Coupled Oxide Dielectrics for Multipurpose Organic Electronic Applications. *Adv. Funct. Mater.* **2011**, *21* (12), 2198–2207.

(81) Fadeev, A. Y.; Mccarthy, T. J. Self-Assembly Is Not the Only Reaction Possible between

Alkyltrichlorosilanes and Surfaces : Monomolecular and Oligomeric Covalently Attached Layers of Dichloro- and Trichloroalkylsilanes on Silicon. *Langmuir* **2000**, *16* (4), 7268–7274.

(82) Ito, Y.; Virkar, A. A.; Mannsfeld, S.; Oh, J. H.; Toney, M.; Locklin, J.; Bao, Z. Crystalline Ultrasmooth Self-Assembled Monolayers of Alkylsilanes for Organic Field-Effect Transistors. *J. Am. Chem. Soc.* **2009**, *131* (13), 9396–9404.

(83) Nie, H.; Walzak, M. J.; Mcintyre, N. S. Delivering Octadecylphosphonic Acid Self-Assembled Monolayers on a Si Wafer and Other Oxide Surfaces. *J. Am. Chem. Soc.* **2006**, *110* (42), 21101–21108.

(84) Chem, J. M.; Park, S. H.; Lee, S.; Kim, J.; Breiby, D. W.; Kim, E.; Park, D. A Polymer Brush Organic Interlayer Improves the Overlying Pentacene Nanostructure and Organic Field-Effect Transistor Performance. *J. Mater. Chem.* **2011**, *21* (39), 15580–15586.

(85) Liu, D.; Miao, Q. Recent Progress in Interface Engineering of Organic Thin Film Transistors with Self-Assembled Monolayers. *Mater. Chem. Front.* **2018**, *2* (1), 11–21.

(86) Lin, Y.; Gundlach, D. J.; Nelson, S. F.; Jackson, T. N. Stacked Pentacene Layer Organic Thin-Film Transistors with Improved Characteristics. *IEEE Electron Device Lett.* **1997**, *18* (12), 606–608.

(87) Kelley, T. W.; Boardman, L. D.; Dunbar, T. D.; Muyres, D. V; Pellerite, M. J.; Smith, T. P. High-Performance OTFTs Using Surface-Modified Alumina Dielectrics. *J. Phys. Chem. B* **2003**, *107* (24), 5877–5881.

(88) Aghamohammadi, M.; Ro, R.; Zschieschang, U.; Ocal, C.; Boschker, H.; Weitz, R. T.; Barrena, E.; Klauk, H. Threshold-Voltage Shifts in Organic Transistors Due to Self-Assembled Monolayers at the Dielectric : Evidence for Electronic Coupling and Dipolar E Ff Ects. *ACS Appl. Mater. Interfaces* **2015**, *7* (41), 22775–22785.

(89) Liu, D.; Xu, X.; Su, Y.; He, Z.; Xu, J.; Miao, Q. Self-Assembled Monolayers of Phosphonic Acids with Enhanced Surface Energy for High-Performance Solution-Processed N-Channel Organic Thin-Film Transistors. *Angew. Chemie Int. Ed.* **2013**, *52* (24), 6222–6227.

(90) Effertz, C.; Lahme, S.; Schulz, P.; Segger, I.; Wuttig, M. Design of Novel Dielectric Surface Modifications for Perylene Thin-Film Transistors. *Adv. Energy Mater.* **2012**, *22* (2), 415–420.

(91) Sun, Q.; Zhuang, J.; Yan, Y.; Zhou, Y.; Han, S.; Zhou, L.; Roy, V. A. L.; Due, I. Investigation on the Mobility and Stability in Organic Thin Film Transistors Consisting of Bilayer Gate Dielectrics. *Phys. status solidi* **2016**, *213* (1), 79–84.

(92) Chen, F.-C.; Liao, C.-H. Improved Air Stability of -Channel Organic Thin-Film Transistors with Surface Modification on Gate Dielectrics. *Appl. Phys. Lett.* **2008**, *93* (10), 335.

(93) Melville, O. A.; Lessard, B. H.; Bender, T. P. Phthalocyanine-Based Organic Thin-Film Transistors: A Review of Recent Advances. *ACS Appl. Mater. Interfaces.* **2015**, *7* (24), 13105–13118.

(94) Wang, H.; Zhu, F.; Yang, J.; Geng, Y.; Yan, D. Weak Epitaxy Growth Affording High-Mobility Thin Films of Disk-Like Organic Semiconductors. *Adv. Mater.* **2007**, *19* (16), 2168–2171.

(95) Wang, Q.; Juarez-Perez, E. J.; Jiang, S.; Qiu, L.; Ono, L. K.; Sasaki, T.; Wang, X.; Shi, Y.; Zheng, Y.; Qi, Y.; Li, Y. Spin-Coated Crystalline Molecular Monolayers for Performance Enhancement in Organic Field-Effect Transistors. *J. Phys. Chem. Lett.* **2018**, *9* (6), 1318–1323.

(96) Gu, Z.; Chen, S.; Fu, W.; Zheng, Q.; Zhang, J. Epitaxial Growth of MOF Thin Film for Modifying the Dielectric Layer in Organic Field-Effect Transistors. *Appl. Mater. Interfaces* **2017**, *9* (8), 7259–7264.

(97) Natali, D.; Caironi, M. Charge Injection in Solution-Processed Organic Field-Effect Transistors : Physics , Models and Characterization Methods. *Adv. Mater.* **2012**, *24* (11), 1357–1387.

(98) Liu, Z.; Kobayashi, M.; Paul, B. C.; Bao, Z.; Nishi, Y. Contact Engineering for Organic Semiconductor Devices via Fermi Level Depinning at the Metal-Organic Interface. **2010**, 2–7.

(99) Xu, Y.; Minari, T.; Tsukagoshi, K.; Chroboczek, J. A.; Ghibaudo, G. Direct Evaluation of Low-Field Mobility and Access Resistance in Pentacene Field-Effect Transistors. *J. Appl. Phys.* **2010**, *107* (11).

(100) Liu, C.; Xu, Y.; Noh, Y. Y. Contact Engineering in Organic Field-Effect Transistors. *Mater. Today* **2015**, *18* (2), 79–96.

(101) Lamport, Z. A.; Barth, K. J.; Lee, H.; Gann, E.; Engmann, S.; Chen, H.; Guthold, M.;

McCulloch, I.; Anthony, J. E.; Richter, L. J.; DeLongchamp, D. M.; Jurchescu, O. D. A Simple and Robust Approach to Reducing Contact Resistance in Organic Transistors. *Nat. Commun.* **2018**, *9* (1).

(102) Xu, Y.; Gwoziecki, R.; Chartier, I.; Coppard, R.; Balestra, F.; Ghibaudo, G. Modified Transmission-Line Method for Contact Resistance Extraction in Organic Field-Effect Transistors. *Appl. Phys. Lett.* **2010**, *97* (6), 171.

(103) Xia, J.; Dong, G.; Tian, B.; Yan, Q.; Zhang, H.; Liang, X.; Peng, L. Metal Contact Effect on the Performance and Scaling Behavior of Carbon Nanotube Thin Film Transistors. *Nanoscale* **2016**, *8* (19), 9988–9996.

(104) Jo, G.; Maeng, J.; Kim, T. W.; Hong, W. K.; Choi, B. S.; Lee, T. Channel-Length and Gate-Bias Dependence of Contact Resistance and Mobility for In2O3 Nanowire Field Effect Transistors. *J. Appl. Phys.* **2010**, *102* (8), 084508.

(105) Wang, S. D.; Minari, T.; Miyadera, T.; Tsukagoshi, K.; Aoyagi, Y. Contact-Metal Dependent Current Injection in Pentacene Thin-Film Transistors. *Appl. Phys. Lett.* **2007**, *91* (20), 1–4.

(106) Yasuda, T.; Tsutsui, T. N-Channel Organic Field-Effect Transistors Based on Boron-Subphthalocyanine. *Mol. Cryst. Liq. Cryst.* **2006**, *462* (1), 3–9.

(107) Pfattner, R.; Rovira, C.; Mas-torrent, M. Organic Metal Engineering for Enhanced Field-Effect Transistor Performance. *Phys. Chem. Chem. Phys.* **2015**, *17*, 26545–26552.

(108) Haas, S.; Takahashi, Y.; Takimiya, K.; Hasegawa, T. High-Performance Dinaphtho-Thienothiophene Single Crystal Field-Effect Transistors. *Appl. Phys. Lett.* **2009**, *95* (2), 022111.

(109) Takahashi, Y.; Hasegawa, T.; Abe, Y.; Tokura, Y.; Nishimura, K.; Saito, G. High Mobility Organic Field-Effect Transistor Based on Hexamethylenetetrathiafulvalene with Organic Metal Electrodes. *Chem. Mater.* **2007**, *19* (26), 6382–6384.

(110) Wada, H.; Shibata, K.; Bando, Y.; Mori, T. Contact Resistance and Electrode Material Dependence of Air-Stable n-Channel Organic Field-Effect Transistors Using Dimethyldicyanoquinonediimine (DMDCNQI). *J. Mater. Chem.* **2008**, *18* (35), 4165–4171.

(111) Yi, Y.; Jeon, P. E.; Lee, H.; Han, K.; Kim, H. S.; Jeong, K.; Cho, S. W. The Interface State Assisted Charge Transport at the MoO3 /Metal Interface. *J. Chem. Phys.* **2009**, *130*

(9), 1–4.

(112) Gwinner, M. C.; Pietro, R. Di; Vaynzof, Y.; Greenberg, K. J.; Ho, P. K. H.; Friend, R. H.; Sirringhaus, H. Doping of Organic Semiconductors Using Molybdenum Trioxide: A Quantitative Time-Dependent Electrical and Spectroscopic Study. *Adv. Funct. Mater.* **2011**, *21* (8), 1432–1441.

(113) Bai, Y.; Liu, X.; Chen, L.; Zhu, W. Q.; Jiang, X. Y.; Zhang, Z. L. Organic Thin Film Field Effect Transistors with MoO3 /Al Electrode and OTS/SiO2 Bilayer Gate Insulator. *AD'07 - Proc. Asia Disp. 2007* **2007**, *1*, 613–616.

(114) Chu, C. W.; Li, S. H.; Chen, C. W.; Shrotriya, V.; Yang, Y. High-Performance Organic Thin-Film Transistors with Metal Oxide/Metal Bilayer Electrode. *Appl. Phys. Lett.* **2005**, *87* (19), 1–3.

(115) Kano, M.; Minari, T.; Tsukagoshi, K. Improvement of Subthreshold Current Transport by Contact Interface Modification in p -Type Organic Field-Effect Transistors. *Appl. Phys. Lett.* **2009**, *94* (14), 6–9.

(116) Panigrahi, D.; Kumar, S.; Dhar, A. Contact Engineering for Efficient Charge Injection in Organic Transistors with Low-Cost Metal Electrodes. *Appl. Phys. Lett.* **2017**, *111* (17).

(117) Chen, F. C.; Kung, L. J.; Chen, T. H.; Lin, Y. S. Copper Phthalocyanine Buffer Layer to Enhance the Charge Injection in Organic Thin-Film Transistors. *Appl. Phys. Lett.* **2007**, *90* (7).

(118) Young Park, S.; Noh, Y. H.; Lee, H. H. Introduction of an Interlayer between Metal and Semiconductor for Organic Thin-Film Transistors. *Appl. Phys. Lett.* **2006**, *88* (11).

(119) Baeg, K. J.; Kim, J.; Khim, D.; Caironi, M.; Kim, D. Y.; You, I. K.; Quinn, J. R.; Facchetti, A.; Noh, Y. Y. Charge Injection Engineering of Ambipolar Field-Effect Transistors for High-Performance Organic Complementary Circuits. *ACS Appl. Mater. Interfaces.* **2011**, *3* (8), 3205–3214.

(120) Cho, B. S.; Seo, J. H.; Lee, K.; Heeger, A. J. Enhanced Performance of Fullerene N-Channel Field-Effect Transistors with Titanium Sub-Oxide Injection Layer. *Adv. Funct. Mater.* **2009**, *19* (9), 1459–1464.

(121) Marmont, P.; Battaglini, N.; Lang, P.; Horowitz, G.; Hwang, J.; Kahn, A.; Amato, C.; Calas, P. Improving Charge Injection in Organic Thin-Film Transistors with Thiol-Based Self-Assembled Monolayers. *Org. Electron. physics, Mater. Appl.* **2008**, *9* (4), 419–424.

(122) Cheng, X.; Noh, Y. Y.; Wang, J.; Tello, M.; Frisch, J.; Blum, R. P.; Vollmer, A.; Rabe, J. P.; Koch, N.; Sirringhaus, H. Controlling Electron and Hole Charge Injection in Ambipolar Organic Field-Effect Transistors by Self-Assembled Monolayers. *Adv. Funct. Mater.* **2009**, *19* (15), 2407–2415.

(123) Li, S.; Guérin, D.; Lmimouni, K. Improving Performance of OFET by Tuning Occurrence of Charge Transport Based on Pentacene Interaction with SAM Functionalized Contacts. *Microelectron. Eng.* **2018**, *195* (April), 62–67.

(124) Wei, P.; Oh, J. H.; Dong, G.; Bao, Z. Use of a 1 H -Benzoimidazole Derivative as an n -Type Dopant and To Enable Air-Stable Solution-Processed n -Channel Organic Thin-Film Transistors. **2010**, 8852–8853.

(125) Shin, N.; Zessin, J.; Lee, M. H.; Hambsch, M.; Mannsfeld, S. C. B. Enhancement of N-Type Organic Field-Effect Transistor Performances through Surface Doping with Aminosilanes. *Adv. Funct. Mater.* **2018**, *28* (34), 1–7.

(126) Bobbert, P. A.; Sharma, A.; Mathijssen, S. G. J.; Kemerink, M.; De Leeuw, D. M. Operational Stability of Organic Field-Effect Transistors. *Adv. Mater.* **2012**, *24* (9), 1146–1158.

(127) De Leeuw, D. M.; Simenon, M. M. J.; Brown, A. R.; Einerhand, R. E. F. Stability of N-Type Doped Conducting Polymers and Consequences for Polymeric Microelectronic Devices. *Synth. Met.* **1997**, *87* (1), 53–59.

(128) Matters, M.; de Leeuw, D. M.; Herwig, P. T.; Brown, A. R. Bias-Stress Induced Instability of Organic Thin Film Transistors. *Synth. Met.* **1999**, *102* (1–3), 998–999.

(129) Matters, M.; de Leeuw, D. M.; Vissenberg, M. J. C. M.; Hart, C. M.; Herwig, P. T.; Geuns, T.; Mutsaers, C. M. J.; Drury, C. J. Organic Field-Effect Transistors and All-Polymer Integrated Circuits. *Opt. Mater. (Amst).* **1999**, *12* (2–3), 189–197.

(130) Chua, L.; Zaumseil, J.; Chang, J.; Ou, E. C.; Ho, P. K. H.; Sirringhaus, H.; Friend, R. H. General Observation of N-Type Field-Effect Behaviour in Organic Semiconductors. *Nature* **2005**, *434* (7030), 194–199.

(131) Aguirre, B. C. M.; Levesque, P. L.; Paillet, M.; St-antoine, B. C.; Desjardins, P.; Martel, R. The Role of the Oxygen / Water Redox Couple in Suppressing Electron Conduction in Field-Effect Transistors. *Adv. Mater.* **2009**, *2* (21), 3087–3091.

(132) Un, H. I.; Cheng, P.; Lei, T.; Yang, C. Y.; Wang, J. Y.; Pei, J. Charge-Trapping-Induced

Non-Ideal Behaviors in Organic Field-Effect Transistors. *Adv. Mater.* **2018**, *30* (18), 1–8.

(133) Pietro, R. Di; Fazzi, D.; Kehoe, T. B.; Sirringhaus, H. Spectroscopic Investigation of Oxygen- and Water-Induced Electron Trapping and Charge Transport Instabilities in n‐Type Polymer Semiconductors. *J. Am. Chem. Soc.* **2012**, *134* (36), 14877–14889.

(134) Shen, C.; Kahn, A. Electronic Structure, Diffusion, and p-Doping at the Au/F16CuPc Interface. *J. Appl. Phys.* **2001**, *90* (9), 4549–4554.

(135) Higashino, T.; Dogishi, M.; Kadoya, T.; Sato, R.; Kawamoto, T.; Mori, T. Air-Stable n-Channel Organic Field-Effect Transistors Based on Charge-Transfer Complexes Including Dimethoxybenzothienobenzothiophene and Tetracyanoquinodimethane Derivatives. *J. Mater. Chem. C.* **2016**, *4* (25), 5981–5987.

(136) Filatre-Furcate, A.; Higashino, T.; Lorcy, D.; Mori, T. Air-Stable n-Channel Organic Field-Effect Transistors Based on a Sulfur Rich π-Electron Acceptor. *J. Mater. Chem. C.* **2015**, *3* (15), 3569–3573.

(137) Zhang, H.; Dong, H.; Li, Y.; Jiang, W.; Zhen, Y.; Jiang, L.; Wang, Z.; Chen, W.; Wittmann, A.; Hu, W. Novel Air Stable Organic Radical Semiconductor of Dimers of Dithienothiophene, Single Crystals, and Field-Effect Transistors. *Adv. Mater.* **2016**, 7466–7471.

(138) Anthopoulos, T. D.; Anyfantis, G. C.; Papavassiliou, G. C.; De Leeuw, D. M. Air-Stable Ambipolar Organic Transistors. *Appl. Phys. Lett.* **2007**, *90* (12).

(139) Takeya, K.; Yohda, H.; Kojima, K.; Yasunaga, H. Effect of Oxygen on Electrical Properties of Lead Phthalocyanine. *J. Phys. Soc. Japan* **1974**, *37* (4), 1024–1030.

(140) Kerp, H. R.; Westerduin, K. T.; van Veen, A. T.; Faassen, E. E. Quantification and Effects of Molecular Oxygen and Water in Zinc Phthalocyanine Layers. *J. Mater. Res.* **2001**, *16* (2), 503–511.

(141) Yan, X.; Wang, H.; Yan, D. An Investigation on Air Stability of Copper Phthalocyanine-Based Organic Thin-Film Transistors and Device Encapsulation. *Thin Solid Films* **2006**, *515* (4), 2655–2658.

(142) Jin, S.; Royer, J.; Colesniuc, C.; Sharoni, A.; Bohrer, F.; Kummel, A.; Trogler, W.; Park, J.; Schuller, I. Ambient Induced Degradation and Chemically Activated Recovery in Copper Phthalocyanine Thin Film Transistors. *J. Appl. Phys.* **2009**, *106* (3), 34505–34508.

(143) Yang, R. D.; Park, J.; Colesniuc, C. N.; Schuller, I. K.; Trogler, W. C.; Kummel, A. C.

Ultralow Drift in Organic Thin-Film Transistor Chemical Sensors by Pulsed Gating. *J. Appl. Phys.* **2007**, *102* (3).

(144) Nénon, S.; Kanehira, D.; Yoshimoto, N.; Fages, F.; Videlot-Ackermann, C. Shelf-Life Time Test of p- and n-Channel Organic Thin Film Transistors Using Copper Phthalocyanines. *Thin Solid Films* **2010**, *518* (19), 5593–5598.

(145) Huang, L.; Yu, B.; Song, D.; Geng, Y.; Zhu, F.; Yan, D. Tin (IV) Phthalocyanine Oxide: An Air-Stable Semiconductor with High Electron Mobility. *Appl. Phys. Lett.* **2008**, *92* (14), 143303.

Chapter 2: Organic thin-film transistors incorporating a commercial pigment (Hostasol Red GG) as a low-cost semiconductor

2.1 Preamble

This section describes the context in which the research was performed, relating it to the development of the lab and my own research goals at the time. It describes the contributions of each author and the significance of the research.

2.1.1 Context

At this stage in my research, we had recently obtained both the probe station for testing OTFTs (March 2016) and thermal evaporator (October 2016). I started by troubleshooting these pieces of equipment, using well known OSCs such as P3HT and CuPc in BGBC transistors where the gate, dielectric and electrodes came on chips fabricated in Germany by Fraunhofer IPMS. As the characterization software and fabrication procedures became more established, I wanted to test new materials that had not been published before in OTFTs. I tried making a number of devices with small molecules based off of benzothioxanthene dicarboxylic anhydride (BDA) and the structurally similar 14H-anthra[2,1,9-mna]thioxanthen-14-one (Hostasol Red GG, Solvent Orange 63), with the latter consistently producing functional p-type devices. Given my understanding of the importance of dielectric modification for device design, I wanted to explore using different surface treatment methods to optimize the performance of Red GG OTFTs and to establish protocols for future device fabrication and characterization.

2.1.2 Contributions of Authors

I designed the experiments independently or in consultation with Dr. Lessard, developing several protocols for equipment used in the process including the electrical probe station and thermal evaporator. I performed all experiments and characterization, including contact angle measurements, XRD, AFM (with assistance from Alex Steeves), substrate treatments, OTFT fabrication and electrical characterization. I designed and wrote >95% of the LabView program used to characterize and

index OTFT data, working from a simple program written by Kreus Inc. to communicate with the Keithley. I wrote the entire manuscript and supporting information, creating all figures and graphs.

Ian Therrien primarily worked with synthesizing and characterizing BDA derivatives which did not work in OTFTs. He did purification and characterization of Red GG donated by Clariant. Dr. Nicole Rice conferred with the author on her results on surface treatment variations and assisted in editing the paper. Professor Lessard selected and procured the semiconducting materials, consulted for the project experiments, and assisted with editing the paper.

2.1.3 Significance of Research

I fabricated and characterized the first OTFTs/OFETs using the commercial pigment Red GG. In order to optimize these devices, I conducted controlled experiments using different surface treatments to modify the dielectric and different substrate temperatures during deposition. These parameter variations are well established in literature, but never conducted for thin films of this material. In order to explain the variation in OTFT performance observed when changing the surface treatment or deposition temperature, I used AFM and XRD to examine thin-film morphology and structural order. While these devices did not perform with high enough field-effect mobility for most applications, they demonstrated potential for a group of unexplored molecules based off of Red GG to be used as low-cost semiconductors in a field where complex and expensive molecules are common.

The rest of Chapter 2 has been adapted from Dyes and Pigments: Melville, O. A., Rice, N. A., Therrien, I., & Lessard, B. H., ***2018,*** *149, 449-455, DOI: 10.1016/j.dyepig.2017.10.034 © 2017 Elsevier Ltd.*

Abstract

Inexpensive carbon-based semiconducting materials are of interest for the manufacturing of organic thin-film transistors (OTFTs) for use in radio-frequency tags, gas sensors, printed logic circuits and flexible screens. The molecular organization of these materials at the interface with the dielectric layer in an OTFT is critical to device performance. We incorporated an inexpensive commercial pigment, 14*H*-anthra[2,1,9-*m,n,a*]thioxanthen-14-one (Hostasol Red GG, Solvent Orange 63), which has not been characterized before as a semiconductor in OTFTs. We found that of the four surface treatments used to modify the silicon dioxide (SiO_2) dielectric, octyltrichlorosilane (OTS) had the greatest effect on device operation. We also illustrate the importance of moisture in the surface chemistry and its direct implications to film forming and device performance. Furthermore, increasing substrate temperature during physical vapor deposition of Red GG generally decreased device performance, despite increasing molecular organization and apparent grain size as characterized with atomic force microscopy (AFM). Optimized OTFTs had a field-effect mobility of up to 5 x 10^{-5} cm^2/Vs, an on/off current ratio the order of 10^3 and a threshold voltage around 10 V. These results demonstrate the important role of processing conditions for Red GG-based OTFTs and could be applied to optimizing devices made with synthetic derivatives of Red GG for improved performance in this family of relatively inexpensive and unexplored semiconducting compounds.

2.2 Introduction

Organic thin film transistors (OTFTs) are emerging as viable or superior alternatives to their inorganic counterparts for applications including chemical sensors,[1] radio-frequency tags,[2] flexible logic circuits,[3] and electronic displays.[4] As we continue to hone the performance of existing high performance organic semiconductors, it remains important to continue exploring alternative materials. There is a wealth of existing but untested small molecules and polymers that could be incorporated into OTFTs. Low-cost materials and their simple synthetic derivatives are excellent options to bolster the potential economic advantage of organic electronics in a competitive market.

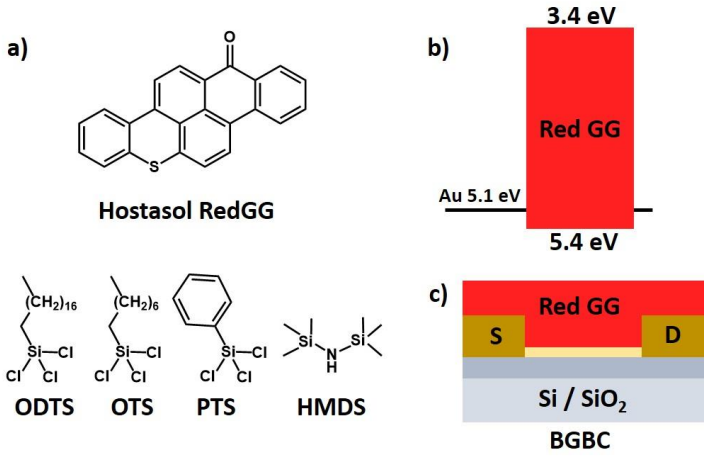

Figure 2.1: (a) Structure of Red GG and the four silanes used to treat the SiO_2 dielectric and schematics of **(b)** the energy levels of Red GG and the work-function of gold as well as **(c)** bottom-gate, bottom-contact organic thin film transistor (OTFT) device architecture.

Conventionally, the small organic molecules used in the active layers of OTFTs, like pentacene[5] or copper phthalocyanine,[6,7] have a conjugated carbon backbone that allows for charge transport through π-π interaction between molecules. Figure 2.1 (a) shows the molecular structure of a conjugated thioxanthene benzanthrone commercially known as Hostasol Red GG or Solvent Orange 63, a pigment primarily used for colouring plastics. To the best of our knowledge, OTFTs containing active layers composed of Red GG have not yet been reported.

The microstructure and chemical environment of the organic semiconducting active layer, especially around the interface with the dielectric, strongly affects the performance of the transistor. Grain size, interconnectivity, and molecular orientation, along with charge traps from dangling bonds at the dielectric-semiconductor and semiconductor-electrode interfaces, can collectively impact OTFT

performance measures like threshold voltage (V_T), field-effect mobility (μ) and on/off ratio ($I_{on/off}$).[8] Figure 2.1 (c) shows the structure of a bottom-gate, bottom contact (BGBC) OTFT. Modifying the dielectric with a thin interlayer that separates the bulk of the insulating material from the semiconducting active layer is commonly utilized to both improve film qualities and reduce charge traps. This interlayer is typically composed of a solution-cast polymer,[9,10] vacuum-deposited molecules like *para*-sexiphenyl (p-6p)[11] or tetratetracontane (TTC)[7], or a self-assembled monolayer[5,12-19]. In the latter case, silanes[13] and phosphonates[14,15] are often employed due to their reactivity to thermally grown silicon dioxide on silicon substrates.. Octadecyltrichlorosilane[5,12] (ODTS), octyltrichlorosilane[16,17] (OTS), phenyltrichlorosilane[18] (PTS), and hexamethyldisilazane[19] (HMDS), the structures of which can be found in Figure 2.1 (a), have all been used to improve transistor performance by modifying the surface of the SiO_2 dielectric. Most explanations point to the reduction in dangling hydroxy bonds and the decrease in surface energy as the source of these improvements; the reduction in these bonds decreases the presence of charge traps while the hydrophobic surface tends to template a superior film with either increased grain size, density or interconnectivity.[8]

Self-assembled monolayers of silanes are made by different methods in literature, including spin-casting,[20] and assembly in solution[17] or vapor phase.[21,22] The nature of the produced surface depends on the silane and reaction conditions. Trichlorosilanes like OTS and ODTS are not innately reactive towards the hydroxyl groups on a hydrolyzed SiO_2 surface, and require either a catalyst (which may not produce a monolayer) or a precursory reaction with water.[23] Once hydrolyzed, the silanes may condense with each other, forming oligomers which can bind to the surface or continue to react with each other to form unwanted aggregates. In an uncontrolled atmosphere, the amount of water is difficult to regulate, while in an inert atmosphere there may be insufficient water.

For small molecules that are deposited in vacuum using physical vapor deposition, the rate of deposition and temperature of the substrate have been identified as factors that affect film properties and hence OTFT performance.[22,24,25] Weak epitaxial growth of films on a smooth, weakly interacting surface can also result in improved OTFT performance.[26] However, increasing the temperature above 120 °C can degrade self-assembled monolayers of ODTS and decrease performance.[27]

In this report, we investigate different surface treatments (OTS, ODTS, PTS, and HMDS) in terms of their surface energy and effect on the performance of OTFTs using Red GG as the active component. The character of the Red GG films, as determined using X-ray diffraction (XRD) and

atomic force microscopy (AFM), is correlated to these results. Additionally, we investigate the effect of rinsing substrates with water prior to their reaction with silanes in solution (OTS, ODTS, PTS) or vapor phase (HMDS). We also report on the electrochemical characteristics, thermal stability and absorbance properties of Red GG films and solutions.

2.3 Results/Discussion

2.3.1 Surface Treatments

Clean and UV-ozone treated Si/SiO_2 wafers were reacted with the four different silanes shown in Figure 2.1 (a) as described in the experimental section. The water contact angle on these surfaces increased from hydrophilic (~10º) to the values shown in Table 2.1. The highest contact angle measured was for ODTS, which has the longest hydrocarbon chain, and the smallest increase in contact angle was found when using PTS, which has an aromatic substituent. When the Si/SiO_2 wafers were rinsed with water and isopropanol after the UV-ozone treatment but before the silane treatment, the contact angles increased slightly (Table 2.1). The substrates also visibly repulsed toluene more strongly during cleaning. This is logical given that water is required for the hydrolysis and subsequent reaction of the silanes with the surface,[23] so the adsorbed water molecules on the surface may speed the reaction and increase the surface coverage with silanes (and therefore surface hydrophobicity). Furthermore, when performing the silane reactions in a glove box (<1 ppm H_2O) with dry solvent there was a much smaller change in contact angle post reaction, indicating low silane surface coverage. Visible aggregates were often seen on the substrates with the ODTS and PTS surface treatments. Figure 2.10 shows atomic force microscopy (AFM) images of the OTS and ODTS treated surfaces. The rinsed and unrinsed OTS surfaces are smooth and featureless, while the ODTS surface appears extremely rough without rinsing, and shows small circular aggregates on a relatively flat surface with rinsing. These results illustrate the importance of the details of surface modification. ODTS is more prone to forming aggregates, while rinsing clearly affects at least the contact angle and sometimes the surface morphology.

Table 2.1: Contact angle measurements (presented as a range) for Si/SiO_2 substrates with different surface treatments, with and without rinsing the wafer with H_2O before surface treatment.

	Water Contact Angle (º)	
Surface Treatment	No Rinsing	Rinsing
OTS	98-99	99-101
ODTS	101-102	101-104
HMDS	80-83	85-89
PTS	81-84	85-88

2.3.2 X-Ray Diffraction

Once the substrates were functionalized, Red GG was deposited using physical vapour deposition (PVD), and the resulting films were characterized by X-ray diffraction (XRD). Figure 2.11 compares the resulting XRD measurements of the Red GG films on OTS-treated Si/SiO_2 substrate and on untreated glass. Three peaks, at $2\theta \approx 7.6°$, 15° and 22.5°, exist on both substrates and correspond to diffraction through the (002), (004) and (006) planes as predicted from the single crystal XRD spectrum shown in Figure 2.14. The single crystal structure of Red GG (CCDC# 1568015) is shown in Figure 2.12 and all the crystallographic data can be found in Tables S1-S7 of the supporting information. The shortest π-π stacking distance in the single crystal is 3.65 Å, which is greater than other high performing p-type organic materials such as dichloropentacene (3.48 Å)[28] or 6,13-bis(triisopropylsilylethynyl) pentacene (TIPS-pentacene, 3.08 to 3.35 Å depending on the processing conditions).[29] A structural disorder exists in the crystal, wherein the positions of the sulfur and oxygen atoms are interchangeable in the solid state, suggesting the molecule is thermodynamically comfortable in either orientation. Figure 2.2 compares the XRD results for Red GG films on the different surface treatments. The films on all surfaces except for the PTS-treated surface show diffraction through the (002) plane. The films on OTS and ODTS-treated surfaces show diffraction through the (004) plane but only the one on the OTS-treated surface shows diffraction through the (006) plane. As these diffractions are all in the same direction, this indicates more long-range structural order in the z-direction for the film on the OTS-treated surface compared to the others. As diffraction occurs through the z-direction but not in others, the ordered components of the film are potentially oriented as shown in Figure 2.12A, with π-π stacking perpendicular to the substrate and charge transport parallel to the substrate, which is favorable for OTFTs. It is important to note that the

intensity of the (002), (004), and (006) peaks are relatively low in comparison to the baseline noise, suggesting that this stacking of the molecules is likely not consistent throughout the film and that there are significant portions of the film where the molecules are disordered.

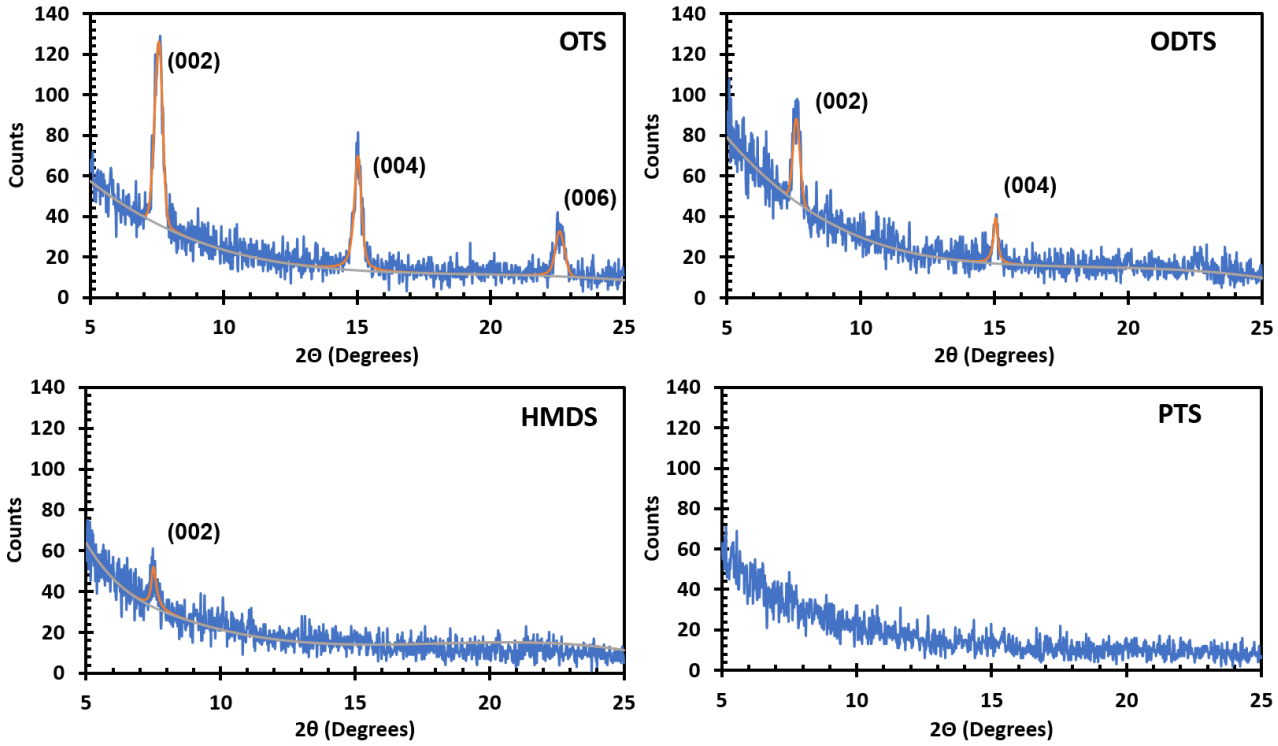

Figure 2.2: Comparison of X-ray diffraction measurements performed on Red GG deposited on Si/SiO_2 substrates with different surface treatments, including a rinsing step. The grey and orange lines represent background and peaks designations, respectively.

2.3.3 Organic Thin-Film Transistors

BGBC OTFTs were fabricated with several parameters varied, including identity of the surface treatment molecule (ODTS, OTS, HMDS, and PTS) and incorporation or omission of a water/isopropanol rinsing step. Table 2.2 summarizes the device performance for each set of variables, obtained from the transfer curves in the saturation region.

Table 2.2: Mobilities for Red GG OTFTs using different surface treatments, and without (No Rinsing) or with (Rinsing) water rinsing step. Both the untreated and PTS-modified devices with a rinsing step did not demonstrate a field effect. Reported errors are either standard deviations (mobility, V_T) or order of magnitude ranges ($I_{on/off}$).

Surface Treatment	No Rinsing			Rinsing		
	Mobility (cm^2/Vs)	V_T (V)	$I_{on/off}$	Mobility (cm^2/Vs)	V_T (V)	$I_{on/off}$
None	1.04±0.19E-6	11±6	10^1	-	-	-
OTS	2.41±0.49E-5	14±3	10^2-10^3	3.71±0.63E-5	9±1	10^2-10^3
ODTS	3.88±5.30E-6	24±19	10^1-10^2	1.52±0.28E-5	9±2	10^2
HMDS	5.71±1.32E-6	-5±5	10^1-10^2	4.74±1.25E-6	-8±2	10^1-10^2
PTS	3.19±1.15E-6	7±6	10^1-10^2	-	-	-

Figure 2.3 compares a typical output for an OTS device, demonstrating conventional linear-saturation behavior, to an example output of a UV-ozone treated control, which does not saturate and has much lower currents. The poor performance of the latter is expected, given the charge traps on the pendant hydroxyl bonds on the SiO_2 surface and the poor film forming characteristics on such a hydrophilic surface.[27,30] The OTS devices demonstrated the highest field-effect mobility and on-off ratios but have high hysteresis. Figure 2.4 compares the transfer characteristics of the OTS devices to the HMDS devices, which have a threshold voltage closer to zero and lower hysteresis. These results suggest that that the choice of silane significantly impacts OTFT field-effect mobility and hysteresis. One explanation for the higher mobility of OTFTs using an OTS treatment is the higher level of structural order with charge transport parallel to the substrate in films deposited on OTS, as demonstrated by the XRD data discussed above. However, the mobility is low compared to other p-type organic semiconductors such as pentacene derivatives.[28,29] This could be due to the larger π-π stacking distance of Red GG, or the relatively low structural order in these thin films, as the intensity of diffraction is significantly less than what is seen in the thin films used for high performance pentacene OTFTs of similar thickness.[31]

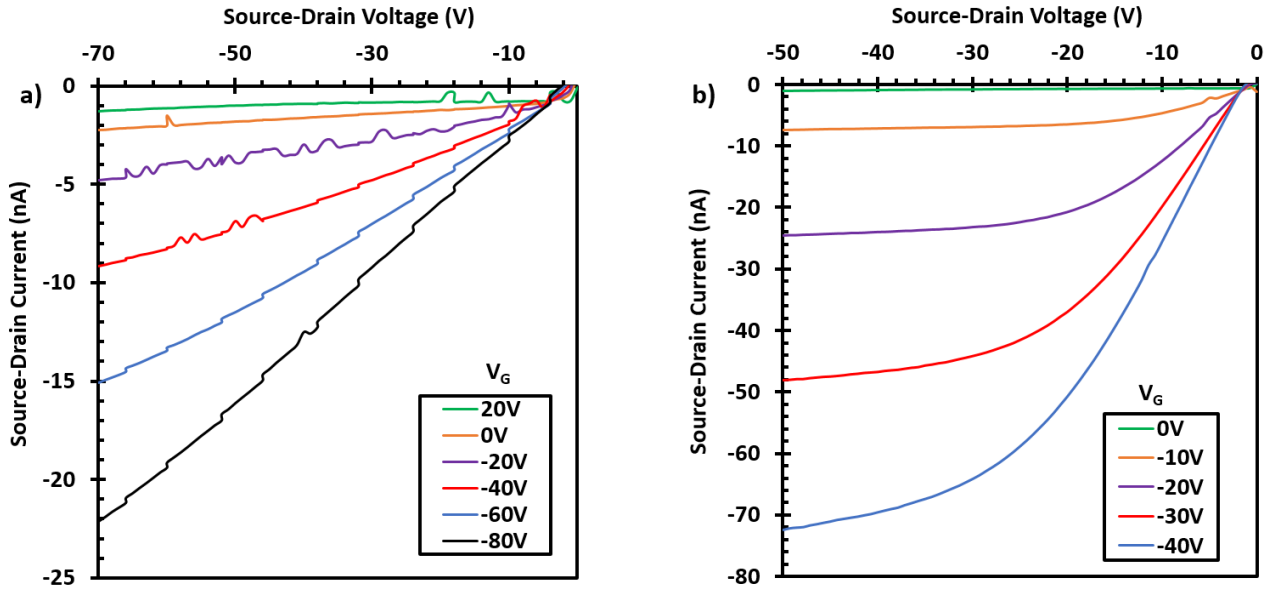

Figure 2.3: Typical output curves for Red GG OTFTs on a plasma treated (a) and OTS treated (b) surface. Channel length = 2.5 µm, width = 2000 µm. V_G stands for gate voltage.

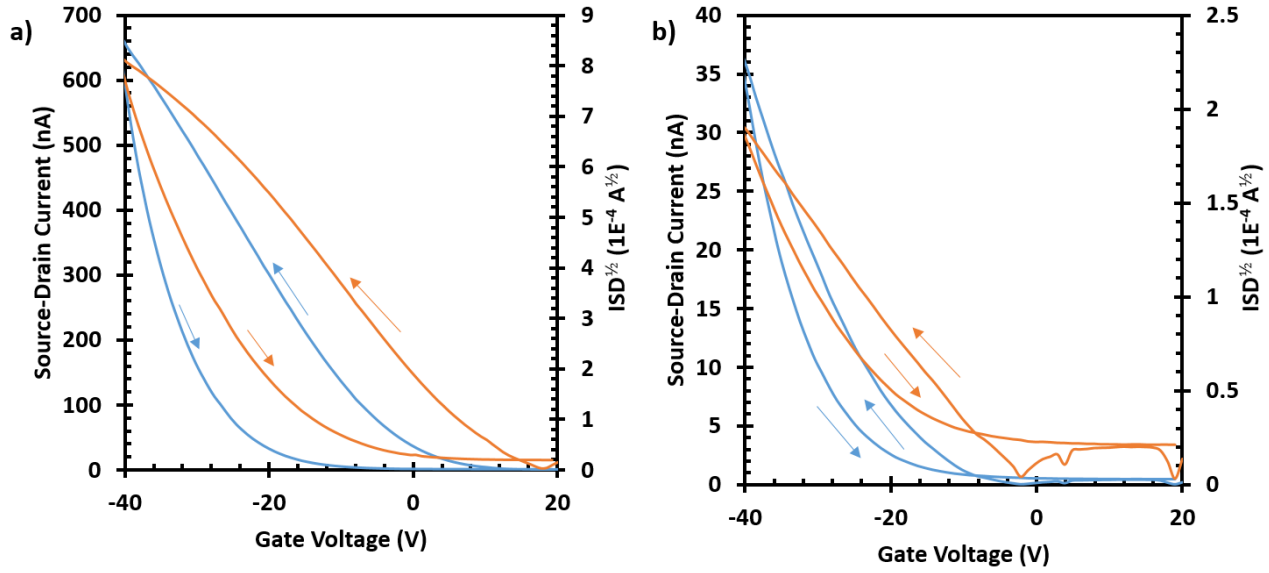

Figure 2.4: Typical transfer curves for Red GG OTFTs with an OTS surface treatment (a) and a HMDS surface treatment (b). The source-drain voltage was held at -50V for all scans.

AFM was used to investigate the structural differences between the best performing devices. The layers produced from OTS (with and without rinsing) and ODTS (with rinsing) (Figure 2.10**)** were relatively smooth compared to ODTS (without rinsing), the latter of which resulted in poorly performing devices compared to the other three. Figures 5 (b) and (e) show AFM images of Red GG films on ODTS and OTS treated substrates with a rinsing step (prior to silane functionalization). Both films show evidence of similarly-sized elongated structures, but on the ODTS film they appear less frequently clearly resolved. It is possible that the visible aggregates seen in Figure 2.10 (d) contributed to this difference. The order apparent on the OTS film could explain its more pronounced diffraction pattern and improved mobility, as the densely packed crystals may provide more continuous pathways for the movement of charge.

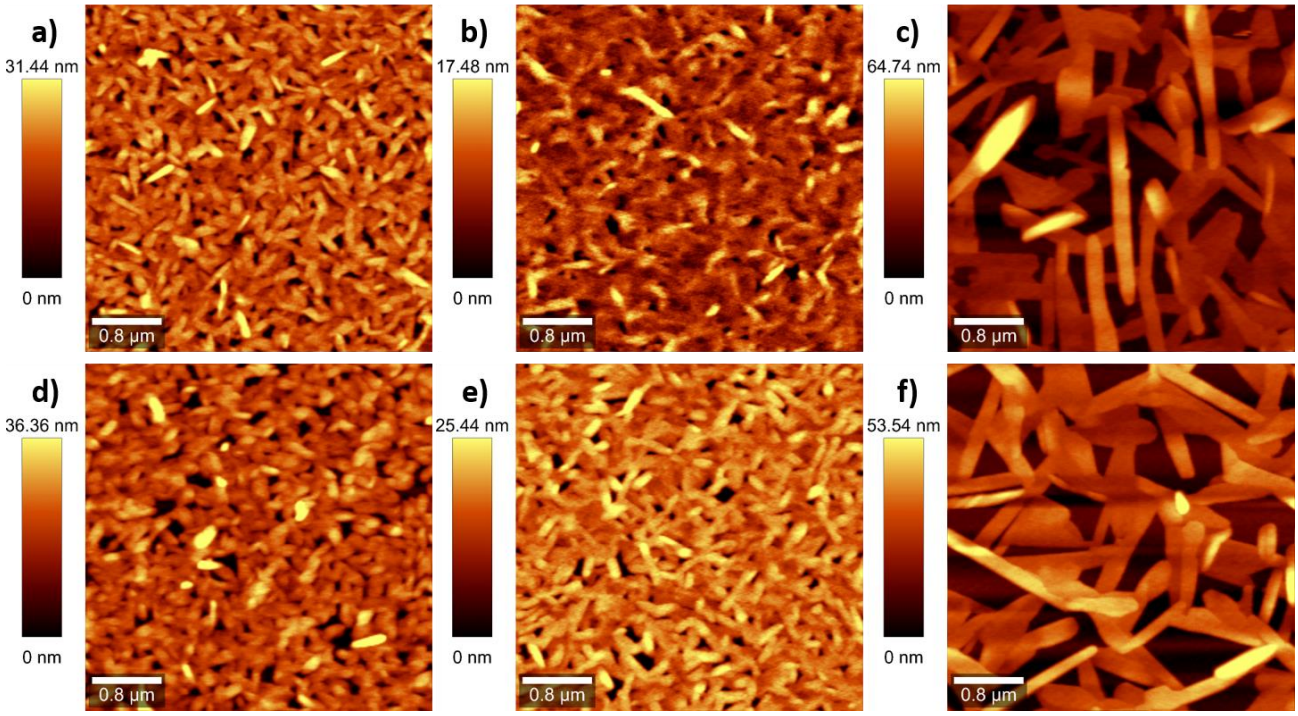

Figure 2.5: Typical atomic force microscopy (AFM) images of Red GG films deposited on ODTS (a,b,c) and OTS (d,e,f) at room temperature without rinsing (a,d), with rinsing (b,e), and with rinsing and a depositing temperature of 105 °C (c,f).

2.3.4 Effect of Aqueous Rinsing Prior to Silane Functionalization

As shown in Figure 2.6, the water rinsing step improved mobility for devices using substrates modified with OTS (+54%) and ODTS (+290%), while slightly decreasing the mobility for HMDS-modified substrates (-17%). No field effect was observed from devices prepared using a combination

of water rinsing and PTS. Rinsing prior to surface modification increased the area and height of the (002) diffraction peak for all surface treatments except PTS, indicating an increased crystallinity or structural order in the deposited films. Comparing the AFM images for Red GG deposited on ODTS and OTS with and without rinsing (Figures 5 (a,b) and (d,e), respectively), it appears the films on modified surfaces that used a rinsing step are more dense with less variation in height overall, despite the same amount of material being deposited. A more dense film, especially by the interface, should provide better pathways for charge transport. These improved film characteristics and OTFTs performances could result from the altered surface beneath. For ODTS, rinsing produced a smoother surface to deposit upon, potentially explaining the smoother Red GG film above it. For OTS, the silane-treated surface appears similar with the rinsing step, although on average it was slightly more hydrophobic afterwards. As water is required for the silanes to condense with each other and the surface,[23] it is possible the extra water just ensures a more consistent surface treatment. It is possible that longer reaction times with the other silanes would achieve a similar effect, but longer reaction times (>1 hour) were not possible as the gold electrodes, which use an indium tin oxide (ITO) adhesion layer, begin to delaminate, especially with rinsing.

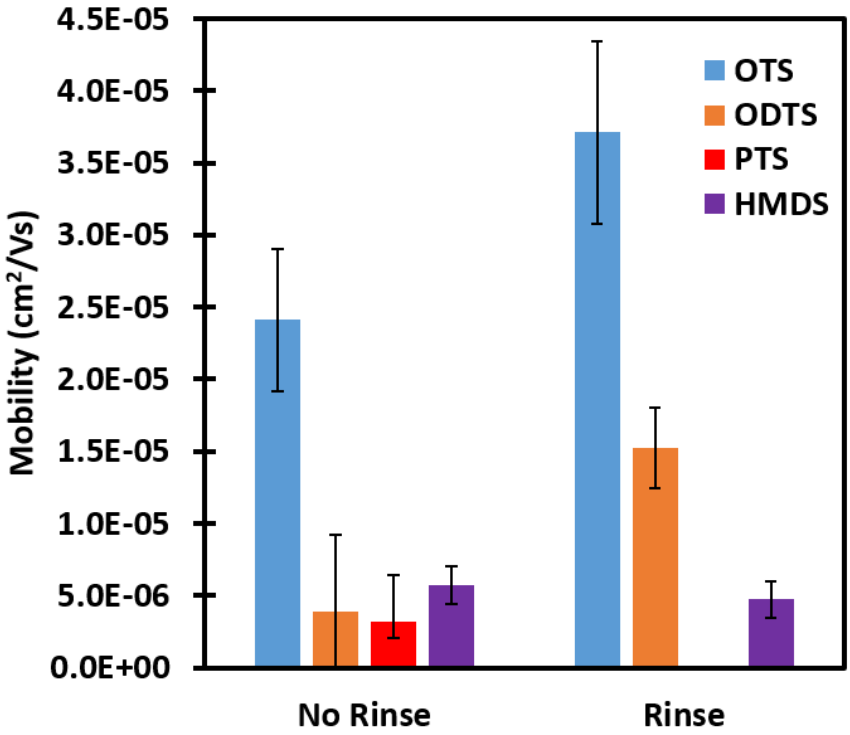

Figure 2.6: Average field effect mobility of Red GG OTFTs made with different surface treatments measured in the saturation region (V_{SD} = -50V) for L = 2.5 and 5 µm devices. Films were deposited at room temperature. Error bars represent the standard deviation of all measurements.

2.3.5 Effect of Deposition Temperature

Deposition with the substrate at high temperature can increase the diffusion of molecules on the substrate itself and increase grain size.[24] We examined increasing the temperature for ODTS and OTS-treated substrates while depositing Red GG at three substrate temperatures. Figure 2.7 shows how the mobility changes as temperature increases. For the ODTS devices, the mobility decreases when the semiconducting layer is deposited above room temperatures, while for the OTS devices, the mobility stays constant before rapidly dropping. The same trend for mobility was observed for the integrated intensity of the (002) diffraction peak of the Red GG films. Films deposited on substrates which were heated to 120 °C, and the film deposited on an ODTS treated substrate heated to 70 °C were visibly a different colour from the other films (Figure 2.13). AFM images for Red GG films deposited at 105 °C (Figure 2.5 (c) and (f) for ODTS and OTS, respectively), show what appears to be 3-dimensional growth. Compared to the lower temperature films, these larger crystals have wider gaps between them, producing a much rougher film. This likely contributes to the decreased performance by removing direct electrode-electrode charge pathways along the surface.

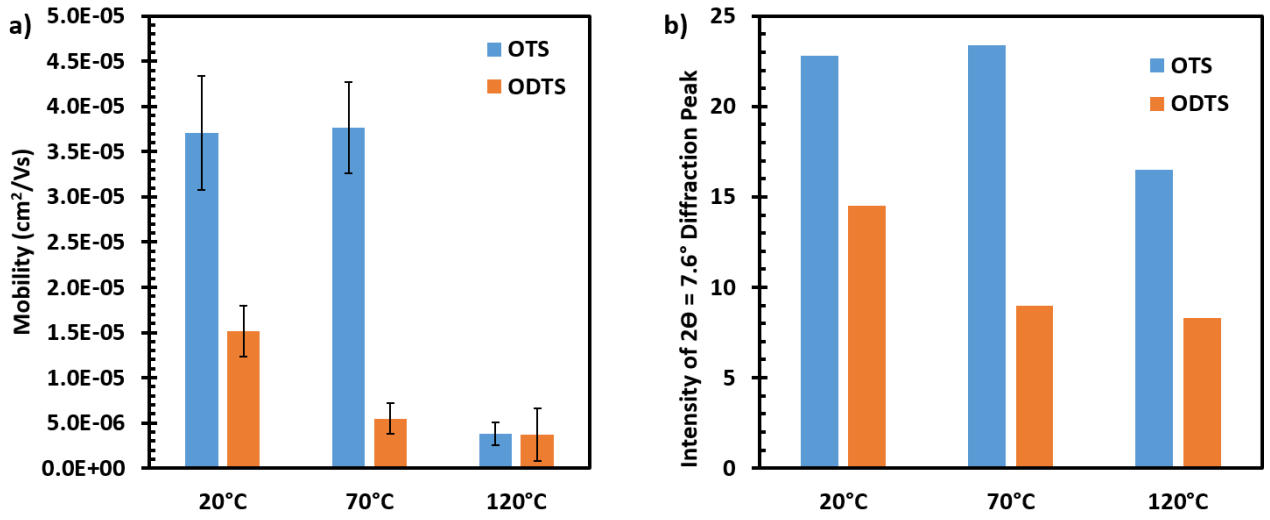

Figure 2.7: Average field effect mobility (a) and integrated intensity of the (002) diffraction peak (b) for OTFTs with Red GG active layers deposited at different temperatures with the same amount of material. Error bars are standard deviations of all measurements, and XRD measurements were performed only once.

2.4 Conclusion

We demonstrate the first example of OTFTs that use the thioxanthene benzanthrone Red GG as the semiconductive layer. This inexpensive pigment demonstrates varied performance depending on the processing conditions used to make the film, including the chemical modification of the surface it is deposited upon and the substrate temperature during deposition. We found the greatest OTFT performance was obtained when the SiO_2 surface was treated with UV-ozone and rinsed with water prior to OTS treatment. For devices with an OTS-modified dielectric, Red GG deposition on unheated (room temperature) and heated (70 °C) substrates had similar performances; a sharp drop in performance was observed when the deposition temperature was increased to 120 °C. This drop in performance was also accompanied by a colour change of the films. The highest mobility devices showed x-ray diffraction through the (002), (004) and (006) planes similar to the single crystal, indicating limited structural order with π-π orbital stacking perpendicular to the substrate. The relatively low performance of these OTFTs, with field-effect mobilities the order of 10^{-5} cm^2/Vs and on/off ratios of 10^3, could be improved by increasing this level of structural order or by decreasing the π-π orbital stacking distance. The results serve as an excellent baseline for the testing of chemical derivatives or analogs of Red GG that could have these more desirable film properties and act as a starting point for device engineering and optimization through improved fabrication techniques.

2.5 Experimental

2.5.1 Preparation of Field Effect Transistors

Pre-cut silicon wafers with 230 nm of thermally grown SiO_2 and pre-patterned gold electrodes (W = 2000 μm, L = 2.5 μm and 5 μm were used for testing) manufactured by Fraunhofer IPMS were used as substrates. The thermal resist was removed using acetone and the devices were dried using nitrogen before 15 minutes of treatment with oxygen plasma to clean and hydrolyze the surface. Prior to surface treatment with organosilanes, substrates were rinsed with water and isopropanol before drying with nitrogen to ensure a consistent amount of water. Surface treatments were performed in toluene (2 mL) in closed 20 mL scintillation vials at 70 °C for 1 hour, with 1% v/v of either octyltrichlorosilane (OTS), octadecyltrichlorosilane (ODTS) or phenyltrichlorosilane (PTS). Hexamethyldisilazane (HMDS) treatments were done in sealed vials at 80 °C for 2 hours, with 50 μL of HMDS (not directly in contact with the substrate). After surface treatment, substrates were rinsed

with toluene and isopropanol before drying in nitrogen and then left under vacuum at 70 °C for one hour to remove residual solvent. Dried substrates were transferred into a vacuum chamber manufactured by Angstrom Engineering, and Red GG (donated by Clariant, purified using train sublimation) films were deposited using physical vapor deposition from a resistive boat. The rate of deposition was measured using a quartz crystal monitor with thickness calibrated by measurement of the thickness of a previously deposited film. The target thickness of active layers was 300 Å, with a deposition rate of 0.3 ± 0.15 Å/s. The actual thickness varies with the surface, but the amount of material deposited was kept constant. In some cases, the substrates were heated with a lamp prior to deposition, using a calibrated thermocouple to measure and maintain the temperature during deposition.

2.5.2 Electrical Testing

Electrical measurements were made on a custom electrical probe station with environmental chamber with controlled atmosphere, oesProbe A10000-P290 (Element Instrumentation Inc. & Kreus Design Inc.) using a Keithley 2614B to set V_{DS} and V_{GS} and to measure I_{DS}. Voltages were increased in a step-wise manner, rather than pulsed, with a delay of 100 ms between measurements. Each device was tested three times. All hole mobilities were measured in the saturation region (V_{GS} = -40V) using the following equation:

$$I_{DS} = \frac{\mu C_i W}{2L}(V_{GS} - V_T)^2 \quad (2.1)$$

Where L and W represent the channel length and width. The capacitance density (C_i) of the gate dielectric is calculated using $C_i = \frac{\varepsilon_0 \varepsilon_r}{t}$ where t is the thickness of the dielectric (230nm) and ε_r is the relative dielectric constant of SiO_2. μ is the field-effect mobility and is calculated from the slope of best fit though the most linear region of $\sqrt{I_{DS}}$ plotted against V_{GS}. The threshold voltage V_T is calculated as the x-intercept of the same line fitting.

Powder X-ray Diffraction (PXRD) measurements were done using a Rigaku Ultima IV powder diffractometer. The X-ray source is Cu Kα (λ=1.5418 A). Contact angle measurements were made using a goniometer. Water droplets with a volume of 1 μL were deposited slowly onto the substrates. Cyclic voltammetry was performed in dichloromethane using a platinum working electrode and a Ag/AgCl reference electrode. UV-Visible absorbance spectroscopy was performed using a Cary 5000 spectrophotometer using a 10 mm quartz cuvette. A Cary Eclipse Fluoresecence Spectrophotometer was used for fluorescence experiments; slit widths were set to 2.5

nm for both the excitation and emission, and a 10 mm quartz cuvette was used. Thermogravimetric analysis (TGA) was performed under nitrogen using a TA Instruments Q5000 IR machine. A WITec Alpha 300 integrated microscope (WITec, Germany) was used to collect AFM images by Digital Pulsed Force (DPFM) mode. Images were obtained with a tetrahedral tip with a radius of 20 nm attached to a 0.05 N/m triangular cantilever (MLCT, Bruker, USA)

2.6 Acknowledgements

Special thanks to Dr. Bulat Gabudillin for his assistance with x-ray diffraction (PXRD and single crystal), Alexander Steeves and Dr. Fabio Variola for their assistance with atomic force microscopy, James Macdermid, Louis Tremblay, Franco Ziroldo and Gerard Nina for their technical assistance and Clariant for generously donating the Red GG sample.

2.7 Supplementary Information

2.7.1 Red GG Characterization

Figure 2.8 (a) shows the UV-Vis absorption of Red GG in toluene and in the solid state. In solution, the maximum absorption occurs around 500 nm and the onset of absorption at 558 nm, corresponding to a band gap of 2.2 eV. These results correlate well to values reported by Cao et al. who characterized the optical properties of Red GG in CH_2Cl_2.[1] The extinction coefficients (ε) constant was found to be 17 000 L · mol^{-1} · cm^{-1} using the Beer-Lambert law. In solid state, as expected, we observed a broadening of the absorption profile with an associated red-shift of the maximum absorption occurring at around 523 nm with the onset at about 613 nm, corresponding to a band gap of 2.0 eV. Figure 2.8 (b) shows a cyclic voltammogram for Red GG. The onset of oxidation for the ferrocene reference was 0.44 V and for Red GG it was 1.07 V. The energy of the highest occupied molecular orbital (HOMO) for Red GG was determined to be 5.4 eV using equation 2.2.

$$E_{HOMO} = \left[\left(E_{ox} - E_{ox,ferrocene}\right) + 4.8\right]eV \quad (2.2)$$

Assuming a HOMO-LUMO energy difference equal to the solid-state band gap (2.0 eV), the LUMO energy was calculated at approximately 3.4 eV. A graphical representation of the bad gap of Red GG can be found in Figure 2.1 (b).

Thermogravimetric analysis (TGA) of Red GG (Figure 2.9) was performed under nitrogen and revealed a decomposition temperature (T_d) of 326 ºC (the temperature when at 5 wt% loss) followed by a full material decomposition by 400 ºC. Prior to device integration, Red GG was easily purified using train sublimation under vacuum well below the T_d.

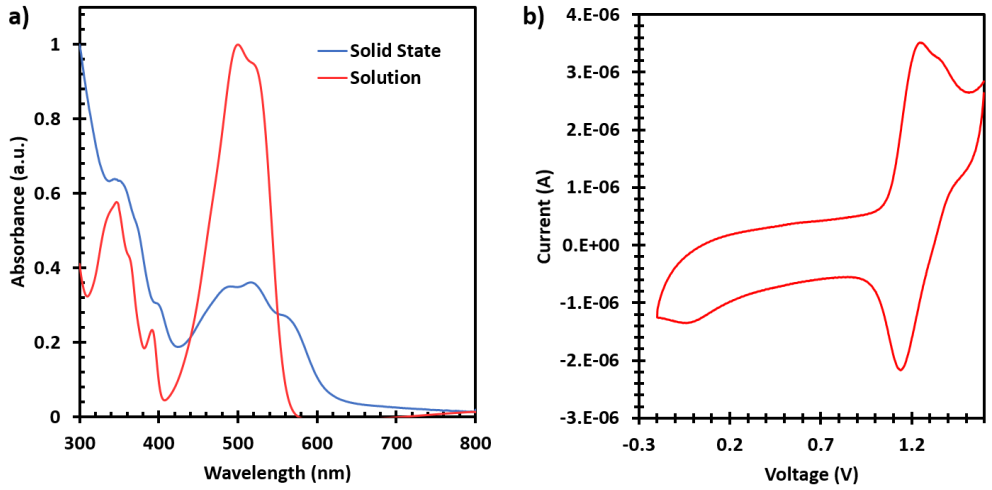

Figure 2.8 (a) UV-Vis absorption spectra for Hostasol Red GG in toluene (orange line) and solid state (blue dashed line). (b) Electrochemical spectra of Hostasol Red GG in DCM using a three electrode cell.

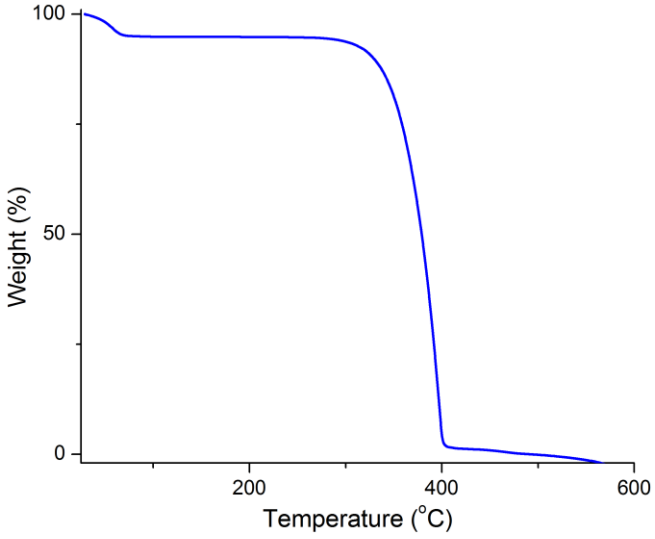

Figure 2.9 Thermogravimetric analysis (TGA) spectra for Red GG

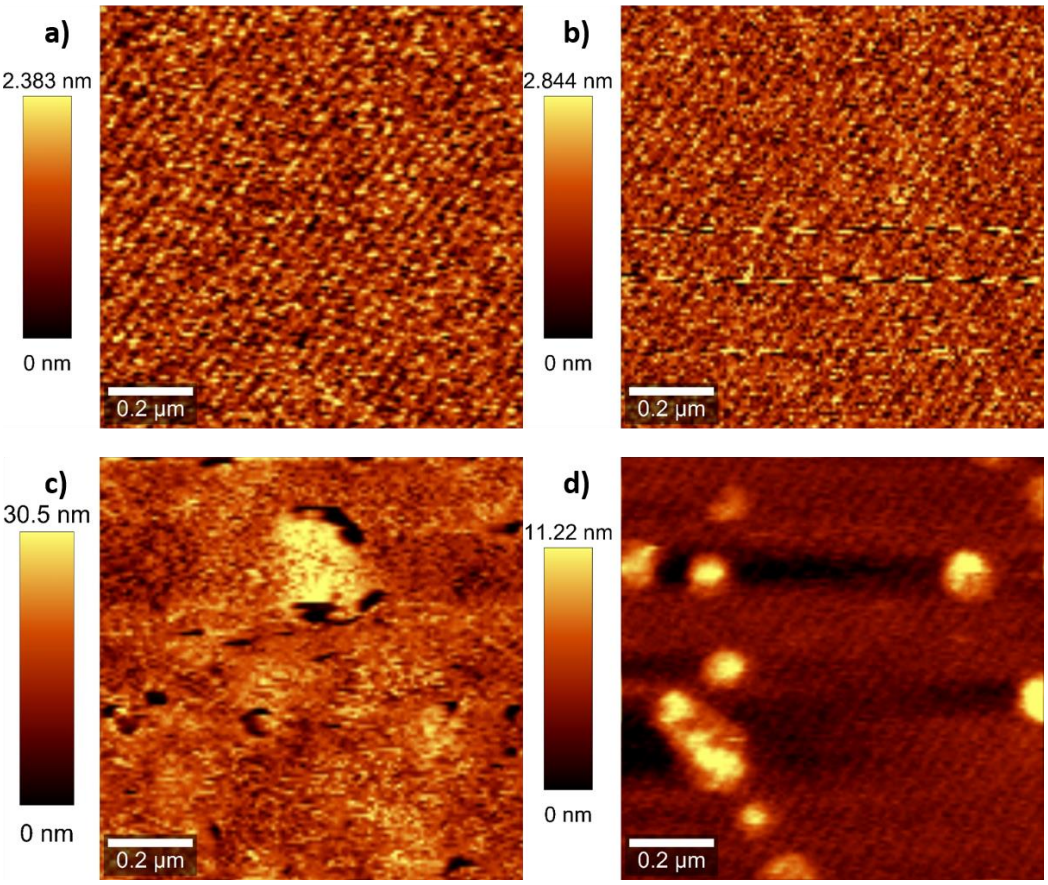

Figure 2.10: Atomic force microscopy (AFM) images of OTS-treated SiO_2 (a,b) and ODTS-treated SiO_2 (c,d). A water/isopropanol rinsing step was included in the preparation of b and d.

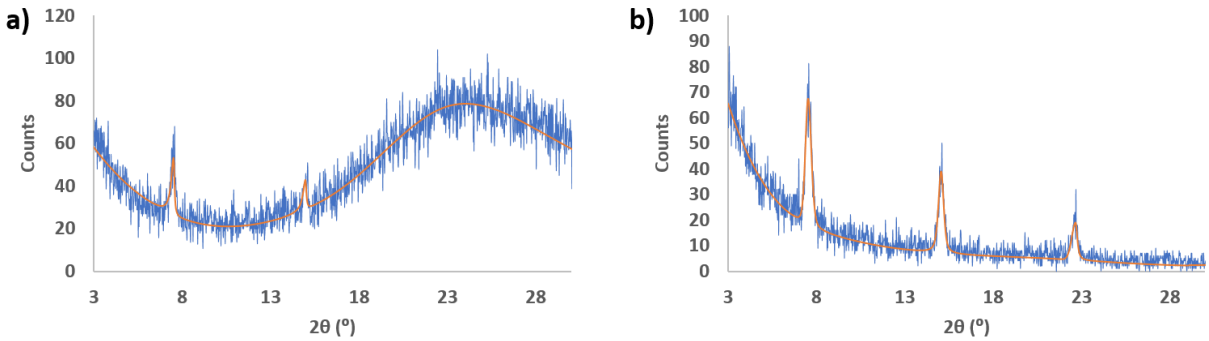

Figure 2.11: Comparison of X-ray diffraction of Red GG deposited on glass (a) and octyltrichlorosilane (OTS) treated Si/SiO_2 (b). The large curve in the left image is typical of amorphous SiO_2.

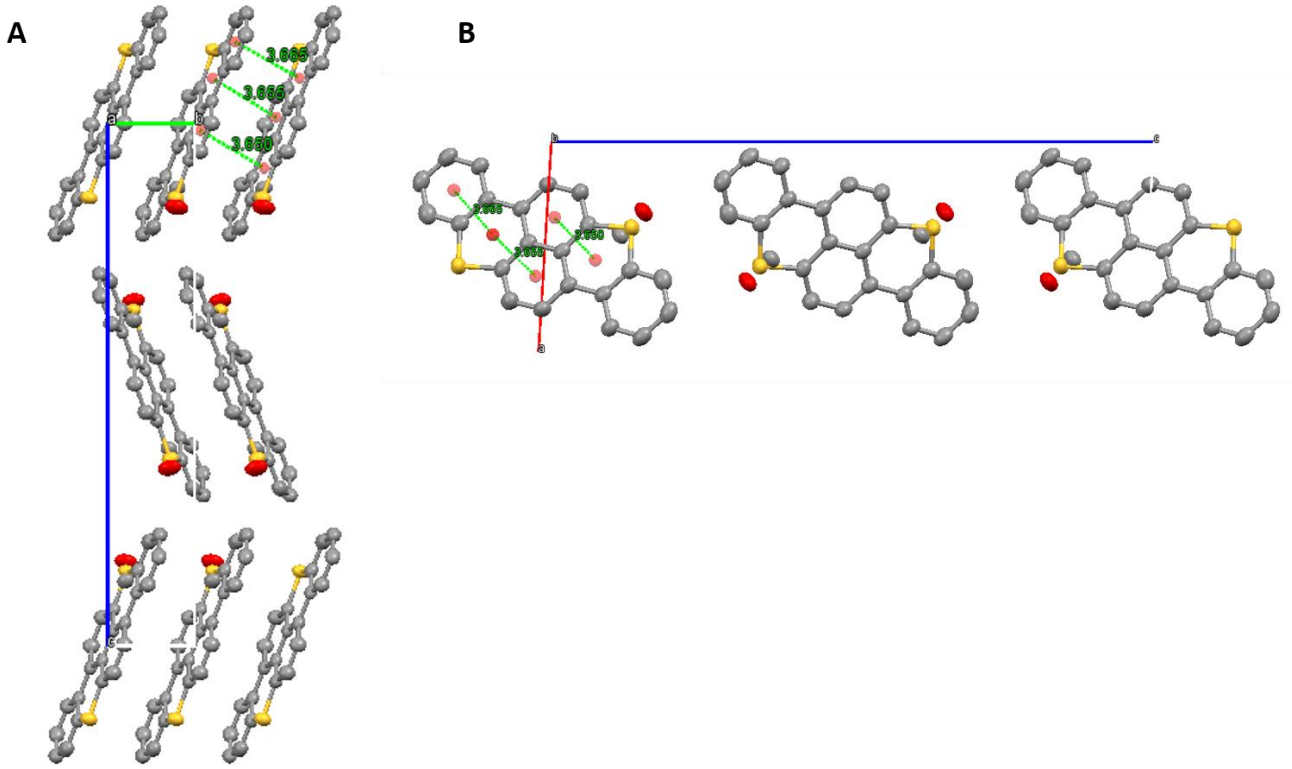

Figure 2.12: Single crystal x-ray diffraction structure of 14*H*-anthra[2,1,9-*m,n,a*]thioxanthen-14-one (Hostasol Red GG), where the ellipsoids represent the 50% electron probability clouds. Unit vectors a, b, and c are labelled from two different perspectives. (CCDC# 1568015)

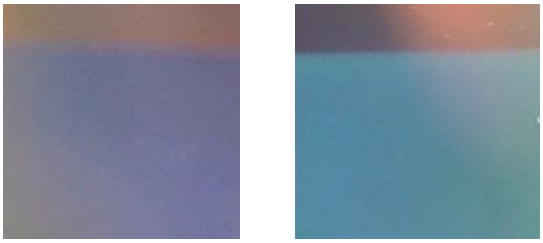

Figure 2.13: Photographic comparison of Red GG deposited on octadecyltrichlorosilane at room temperature (left) and 70 °C (right), demonstrating the colour change. Photos taken through an optical microscope.

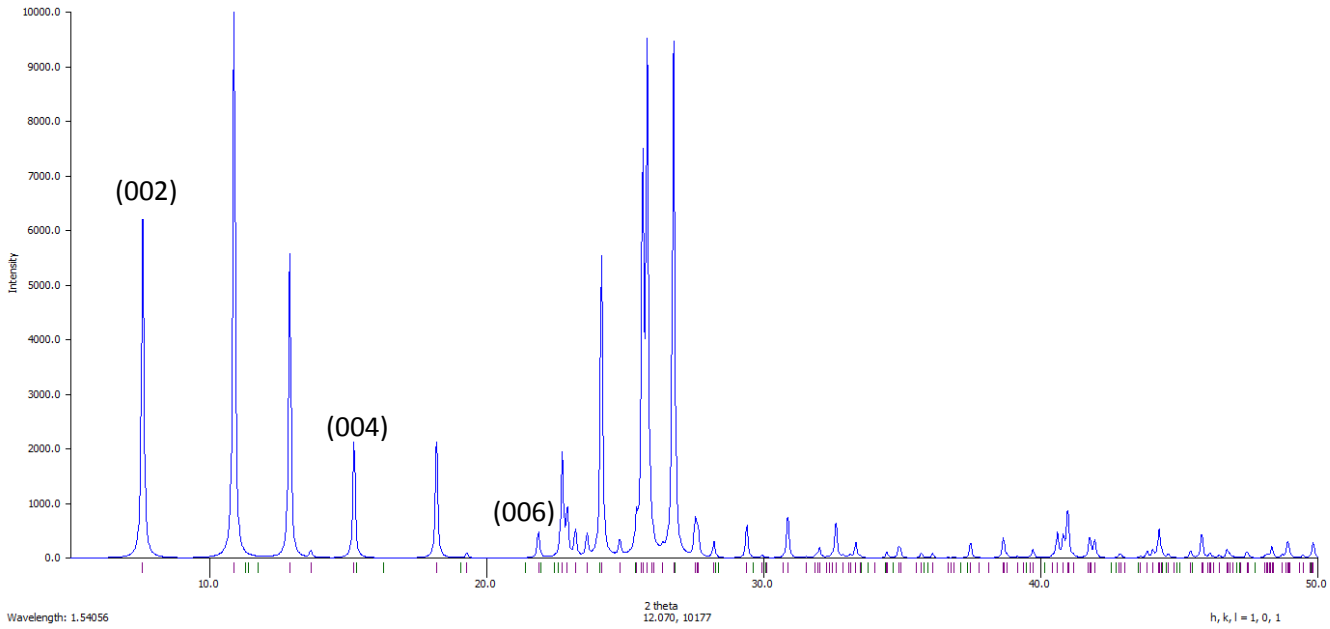

Figure 2.14: Predicted PXRD spectrum determined from single crystal XRD structure of Red GG.

2.7.2 Single Crystal Data

Single crystal data was omitted as it is not contribute significantly to the scope of discussion. The raw data can be obtained at the following address: http://doi.org/10.5517/ccdc.csd.cc1pmn43

2.8 Bibliography

(1) Lin, P.; Yan, F. Organic Thin-Film Transistors for Chemical and Biological Sensing. *Adv. Mater.* **2012**, *24* (1), 34–51.

(2) Subramanian, V.; Chang, P. C.; Member, S.; Lee, J. B.; Member, S.; Molesa, S. E.; Volkman, S. K. Printed Organic Transistors for Ultra-Low-Cost RFID Applications. *IEEE Trans. Components Packag. Technol.* **2005**, *28* (4), 742–747.

(3) Sekitani, T.; Zschieschang, U.; Klauk, H.; Someya, T. Flexible Organic Transistors and Circuits with Extreme Bending Stability. *Nat. Mater.* **2010**, *9* (12), 4–6.

(4) Gelinck, B. G.; Heremans, P.; Nomoto, K.; Anthopoulos, T. D. Organic Transistors in Optical Displays and Microelectronic Applications. *Adv. Mater.* **2010**, *22* (34), 3778–3798.

(5) Shtein, M.; Mapel, J.; Benziger, J. B.; Forrest, S. R. Effects of Film Morphology and Gate Dielectric Surface Preparation on the Electrical Characteristics of Organic-Vapor-Phase-Deposited Pentacene Thin-Film Transistors. *Appl. Phys. Lett.* **2002**, *81* (2), 268–270.

(6) Bao, Z.; Lovinger, A. J.; Dodabalapur, A. Organic Field-Effect Transistors with High Mobility Based on Copper Phthalocyanine. *Appl. Phys. Lett.* **1996**, *69* (20), 3066–3068.

(7) Kraus, M.; Richler, S.; Opitz, A.; Brutting, W.; Haas, S.; Hasegawa, T.; Hinderhofer, A.; Schreiber, F. High-Mobility Copper-Phthalocyanine Field-Effect Transistors with Tetratetracontane Passivation Layer and Organic Metal Contacts. *J. Appl. Phys.* **2010**, *107* (9), 94503.

(8) Melville, O. A.; Lessard, B. H.; Bender, T. P. Phthalocyanine-Based Organic Thin-Film Transistors: A Review of Recent Advances. *ACS Appl. Mater. Interfaces* **2015**, *7* (24), 13105–13118.

(9) Bertolazzi, S.; Wünsche, J.; Cicoira, F.; Santato, C.; Bertolazzi, S.; Wu, J.; Cicoira, F.; Santato, C. Tetracene Thin Film Transistors with Polymer Gate Dielectrics Tetracene Thin Film Transistors with Polymer Gate Dielectrics. *Appl. Phys. Lett.* **2011**, *013301*, 1–4.

(10) Tarabella, G.; Bertolazzi, S.; Bocoum, M.; Barba, L.; Arrighetti, G.; Lutterotti, L. The Correlation between Gate Dielectric, Film Growth, and Charge Transport in Organic Thin Film Transistors: The Case of Vacuum-Sublimed Tetracene Thin Films. *J. Mater. Chem. C* **2013**, *1* (5), 967–976.

(11) Wang, H.; Zhu, F.; Yang, J.; Geng, Y.; Yan, D. Weak Epitaxy Growth Affording High-Mobility Thin Films of Disk-Like Organic Semiconductors. *Adv. Mater.* **2007**, *19* (16), 2168–2171.

(12) Salleo, A.; Chabinyc, M. L.; Yang, M. S.; Street, R. A. Polymer Thin-Film Transistors with Chemically Modified Dielectric Interfaces. *Appl. Phys. Lett.* **2002**, *81* (23), 4383–4385.

(13) Oteyza, D. G. De; Barrena, E.; Ossó, J. O.; Dosch, H.; Meyer, S.; Pflaum, J. Controlled Enhancement of the Electron Field-Effect Mobility of Transistors by Use of Functionalized Substrates. *Appl. Phys. Lett.* **2005**, *87* (18), 183504.

(14) Yusuke, F.; Rongbin, Y.; Koji, O.; Kazume, N.; Mamoru, B. Improved Organic Thin Film Transistor Performance Utilizing a DH-[alpha]6T Submonolayer. *Mol. Cryst. Liq. Cryst.* **2013**, *580* (1), 110.

(15) Mcdermott, J. E.; Mcdowell, M.; Hill, I. G.; Hwang, J.; Kahn, A.; Bernasek, S. L.; Schwartz, J. Organophosphonate Self-Assembled Monolayers for Gate Dielectric Surface Modification of Pentacene-Based Organic Thin-Film Transistors : A Comparative Study. *J. Phys. Chem. A* **2007**, *111* (49), 12333–12338.

(16) Li, Y.; Singh, S. P.; Sonar, P. A High Mobility P-Type DPP-thieno[3,2-B]thiophene Copolymer for Organic Thin-Film Transistors. *Adv. Mater.* **2010**, *22* (43), 4862–4866.

(17) Wu, Y.; Liu, P.; Ong, S.; Zhao, T. S.; Botton, G.; Zhu, S. Controlled Orientation of Liquid-Crystalline Polythiophene Semiconductors for High- Performance Organic Thin-Film Transistors. *Appl. Phys. Lett.* **2005**, *86* (14), 142102.

(18) Kyungsun, S. K.; Seung, R.; Chang, W. Solution-Processed Organic Field-Effect Transistors Patterned by Self-Assembled Monolayers of Octadecyltrichlorosilane and Phenyltrichlorosilane. *J. Mater. Sci.* **2010**, *45* (2), 566–569.

(19) Chang, J.; Sun, B.; Breiby, D. W.; Nielsen, M. M.; Giles, M.; Mcculloch, I.; Sirringhaus, H. Enhanced Mobility of Poly (3-Hexylthiophene) Transistors by Spin-Coating from High-Boiling-Point Solvents. *Chem. Mater.* **2004**, *16* (23), 4772–4776.

(20) Ito, Y.; Virkar, A. A.; Mannsfeld, S.; Oh, J. H.; Toney, M.; Locklin, J.; Bao, Z. Crystalline Ultrasmooth Self-Assembled Monolayers of Alkylsilanes for Organic Field-Effect Transistors. *J. Am. Chem. Soc.* **2009**, *131* (26), 9396–9404.

(21) Takeya, J.; Yamagishi, M.; Tominari, Y.; Hirahara, R.; Nishikawa, Y. N.; Kawase, T.; Shimodas, T. Very High-Mobility Organic Single-Crystal Transistors with in-Crystal Conduction Channels. *Appl. Phys. Lett.* **2007**, *90* (10), 102120.

(22) Weitz, R. T.; Amsharov, K.; Zschieschang, U.; Villas, E. B.; Goswami, D. K.; Burghard, M.; Dosch, H.; Jansen, M.; Kern, K.; Klauk, H. Organic N-Channel Transistors Based on Core-

Cyanated Perylene Carboxylic Diimide Derivatives. *J. Am. Chem. Soc.* **2008**, *130* (14), 4637–4645.

(23) Fadeev, A. Y.; Mccarthy, T. J. Self-Assembly Is Not the Only Reaction Possible between Alkyltrichlorosilanes and Surfaces : Monomolecular and Oligomeric Covalently Attached Layers of Dichloro- and Trichloroalkylsilanes on Silicon. *Langmuir* **2000**, *16* (18), 7268–7274.

(24) Yadav, S.; Kumar, P.; Ghosh, S. Optimization of Surface Morphology to Reduce the Effect of Grain Boundaries and Contact Resistance in Small Molecule Based Thin Film Transistors. *Appl. Phys. Lett.* **2012**, *101* (19), 193304–193307.

(25) Krauss, T. N.; Barrena, E.; Oteyza, D. G. De; Zhang, X. N.; Dehm, V.; Wu, F.; Dosch, H. X-Ray / Atomic Force Microscopy Study of the Temperature-Dependent Multilayer Structure of PTCDI-C8 Films on SiO2. *J. Phys. Chem. C* **2009**, *113* (11), 4502–4506.

(26) Yang, J.; Yan, D. Weak Epitaxy Growth of Organic Semiconductor Thin Films. *Chem. Soc. Rev.* **2009**, *38* (9), 2634–2645.

(27) Kim, H. J.; Lee, H. H.; Kim, J. W.; Jang, J.; Kim, J.-J. Surface Dependent Thermal Evolution of the Nanostructures in Ultra-Thin Copper(ii) Phthalocyanine Films. *J. Mater. Chem.* **2012**, *22* (18), 8881–8886.

(28) Chem, J. M. High Performance Organic Thin Film Transistor Based on Pentacene Derivative. J. Mater. Chem. **2012**, *22* (21), 10496–10500.

(29) Verploegen, E.; Mannsfeld, S. C. B.; Kim, D. H.; Lee, S. Y.; Hector, A.; Aspuru-guzik, A.; Toney, M. F.; Bao, Z.; Link, C. Tuning Charge Tr ansport in Solution-Sheared Organic Semiconductors Using Lattice Strain. Nature. **2011**, *480* (7378): 504–508

(30) Korodi, I. G.; Lehmann, D.; Hietschold, M.; Zahn, D. R. T. Improving the Mobility of CuPc OFETs by Varying the Preparation Conditions. *Appl. Phys. A* **2013**, *111* (3), 767–773.

(31) Dimitrakopoulos, B. C. D.; Malenfant, P. R. L. Organic Thin Film Transistors for Large Area Electronics. *Adv. Mater*. **2002**, *14* (2), 99–117.

Chapter 3: Silicon phthalocyanines as N-type semiconductors in organic thin film transistors

3.1 Preamble

This section describes the context in which the research was performed, relating it to the development of the lab and my own research goals at the time. It describes the contributions of each author and the significance of the research.

3.1.1 Context

By summer 2017 I had fabricated and characterized a number of transistors, including poly((3-hexyl)tellurophene) and BGTC CuPc and poly((3-hexyl)thiophene) devices. Although some results were promising, I was unable to detect a reliable sensing response for CO_2 in any experiments, which was my goal at the time. I observed that devices showed shifts in performance over time and characterization atmosphere (as discussed in Section 1.3.6**)**, which I thought would make reliable sensing experiments difficult. Thus, when I observed reasonably high n-type behaviour in OTFTs using SiPc molecules originally incorporated into photovoltaics, I decided to investigate them further. By September 2017, I had already tested a number of SiPcs in OTFTs, and Professor Lessard wanted a practical lab component to his organic electronics course. Thus, we had students fabricate and characterize OTFTs using three SiPc OSCs as part of their lab component under strict supervision. The goal was to obtain clear structure-function relationship with regards to the size of the axial attachment and process optimization data as we varied the deposition rate, substrate temperature during deposition, and dielectric modification.

3.1.2 Contributions of Authors

I designed the OTFT fabrication and characterization experiments in consultation with Professor Lessard. I oversaw these experiments with Trevor Grant as they were performed by undergraduate students. I performed the PXRD experiments and analysis. I analyzed and formatted AFM images that were obtained by technicians at ARC. I analyzed and presented in table and

graphical format all of the OTFT data. I wrote the OTFT section of the Results/Discussion in the paper and contributed to the introduction.

Trevor Grant synthesized all three SiPc OSCs used in these experiments and characterized their UPS, UV-Vis and single crystal XRD data. He helped oversee device fabrication and characterization. He wrote the chemical synthesis and characterization section of the paper, contributed to the introduction, and helped edit the manuscript. Professor Lessard helped to edit the manuscript, develop the experiments and select the materials.

3.1.3 Significance

This work presented the first SiPcs for OTFTs, significant because of several desirable properties of SiPcs. Although phthalocyanine OSCs in general have excellent stability and a few such as CuPc have been studied extensively in OTFTs, there are limited examples of Pcs with good electron mobility. Synthesis of $SiCl_2Pc$ and its axially substituted derivatives was straightforward, and changing the size of the axial attachment could clearly be related to the mobility in OTFTs. All derivatives were n-type when characterized under vacuum and with some process optimization μ_e of above 0.01 $cm^2V^{-1}s^{-1}$ could be obtained, not state-of-the-art but approaching the 1 $cm^2V^{-1}s^{-1}$ mark that is considered exceptional for contemporary thin film devices. Thus, synthetically accessible n-type OSCs with a wide variety of functionalization potential through the axial connection were demonstrated for promising use in OTFTs. Most of the analytical results from molecular and process variation were clear and logical based on existing precedent, facilitating further study of the SiPc molecular class.

The rest of Chapter 3 has been adapted from Journal of Materials Chemistry C: Melville, O. A., Grant, T. M., & Lessard, B. H., ***2018,*** *6 (20), 5482-5488, DOI: 10.1039/C8TC01116H with permission from the Royal Society of Chemistry*

Abstract

Silicon phthalocyanines (SiPcs) represent a large class of molecules that have been studied as donors, acceptors and ternary additives in organic photovoltaics but not in organic thin-film transistors (OTFTs). We synthesized three novel SiPcs using axial substitution and examined their performance as the active layer in bottom-gate bottom-contact (BGBC) OTFTs. All three molecules exhibit N-type behaviour, with the dibenzoate substituted SiPc showing the greatest field-effect mobility of roughly 6 x 10^{-4} cm^2 V^{-1} s^{-1} in vacuum. This performance improved to >0.01 cm^2 V^{-1} s^{-1} when using a combination of dielectric modification with octadecyltrichlorosilane (ODTS) and a substrate temperature during deposition of 200 °C. These promising results point towards the possibility of high performance N-type SiPcs by exploring the wealth of available options in axial and peripheral substitution and careful process control during fabrication.

3.2 Introduction

Metal phthalocyanines (MPcs) have garnered interest for organic thin-film transistor (OTFT) applications due to their thermal and chemical stability, ease of synthesis, and ability to transport both holes and electrons effectively. The most commonly studied MPcs for OTFT applications utilize divalent metals such as copper (CuPc) or zinc (ZnPc). Phthalocyanine oxides of metals such as vanadium (VOPc)[1–6] or titanium (TiOPc)[7] have more recently seen interest, with the latter currently holding the highest P-type mobility for phthalocyanines of up to 10 $cm^2 V^{-1} s^{-1}$.

Like many other organic semiconductors, performance for N-type phthalocyanines lags behind that of their P-type counterparts. Tin phthalocyanine (SnPc) has shown promising N-type results in OTFTs, with SnPc dichloride (Cl_2-SnPc)[8] and SnPc oxide (SnOPc)[9] achieving electron mobilities up to 0.30 and 0.44 $cm^2V^{-1}s^{-1}$, respectively. While only a few examples are found in the literature, devices reported using these materials have high threshold voltages, ≥27V and ≥36V, respectively. The most commonly reported N-type phthalocyanine for OTFTs is copper hexadecafluorophthalocyanine (F_{16}CuPc), for which electron mobilities up to 0.27 $cm^2 V^{-1} s^{-1}$ combined with threshold voltages of ~16 V have been demonstrated for vapor deposited devices.[10]

Enhancement of device performance can be achieved by improving the solid state arrangement of the semiconductor through chemical functionalization.[11–13] Divalent MPcs such as CuPc can only possess peripheral substituents, for which F_{16}CuPc is already functionalized and cannot be further modified. Therefore, control of the solid-state packing of these MPc thin films made with physical vapour deposition in OTFTs is often limited to procedural modifications, such as using a heated substrate during deposition or modifying the dielectric interface.[14] This molecular packing, including the arrangement and orientation of molecules and the amount of π- π overlap between neighbouring molecules, has a strong impact on device performance including field-effect mobility. Recently, silicon phthalocyanine (SiPc) has seen increased interest in organic photovoltaic (OPV)[15–23] and organic light emitting diode (OLED)[24–26] applications due to its ability to form thermally stable derivatives through axial substitutions. These axial substituents provide a simple synthetic handle to incorporate a range of functional groups to increase solubility or control solid state arrangement.[14,16] Despite its wide range of chemical derivatives, SiPcs have not yet been reported in OTFTs.

In this study we investigate the use of axially substituted SiPcs as active N-type materials in OTFTs. We present the synthesis and single crystal structures of three novel SiPcs with

increasingly bulky aromatic axial substituents. We look at the effect of the axial substituent on the performance of bottom-gate bottom-contact (BGBC) OTFTs while establishing a baseline for optimizing deposition rate, substrate temperature during deposition and dielectric modification for SiPc-based OTFTs. By systematically increasing the size of the pendant group, we expect to change the crystal structure of the SiPc molecules. The arrangement of the phthalocyanine conjugated rings in the crystal, including the pi-pi stacking distance and degree of overlap should impact the performance in thin-film transistors and give an indication of what crystal structures will be favorable for OTFTs using other SiPcs.

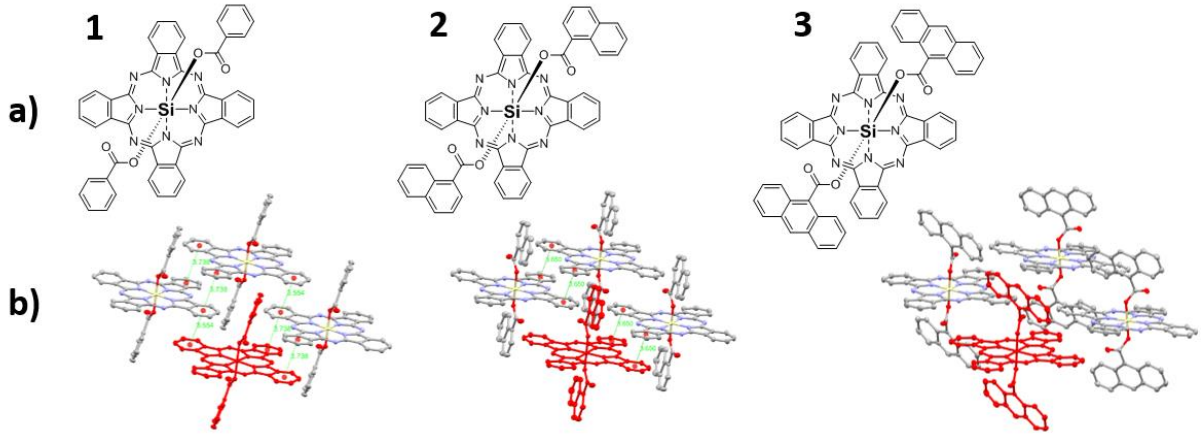

Figure 3.1: a) Chemical structures of three axially substituted silicon phthalocyanines b) Solid-state arrangement of **1** (CCDC#:1817435)) **2** (CCDC#:1817436), and **3** (CCDC#:1817437) obtained from single crystal X-ray diffraction. Molecular overlap with a centroid-centroid distance < 4Å are indicated with dotted green lines**.**

3.3 Results and Discussion

3.3.1 Chemical Synthesis and Characterization

We synthesized a series of silicon phthalocyanines (SiPcs) with three different aromatic carboxylic groups through a 1-step reaction from Cl_2-SiPc. Resulting molecules are shown in Figure 3.1a, isolated as fine blue powders sparingly soluble in common organic solvents. The materials were characterized by UV-Vis absorbance and fluorescence spectroscopy, the resulting

spectra for the three compounds can be seen in Figure 3.6 in the supporting information. In all cases the values obtained were similar to previous reports of SiPc derivatives.[18] Ultraviolet photoelectron spectroscopy (UPS) was also performed on thin films of **1, 2** and **3** and the spectra can be found in Figure 3.7**.** In all cases a work function of 4.4 eV was obtained and HOMO level (offset) = 1.6 eV and 2.1 eV; resulting in ionization energies (*IE*) of 6.0 eV (**1** and **2**) and 6.5 eV (**3**), These values are similar to those obtained previously for other SiPc derivatives.[18] It is interesting to note however that **3** has the deepest *IE* of all three derivatives.

Table 3.1. Summary of single crystal XRD data for centroid-centroid distances of <4 Å

Compound	Distance Between Aromatic Planes [Å]	Angle Between Aromatic Planes	Centroid-Centroid Distance [Å]	Slip Angle*
1	3.448 (Dual benzene) 3.365 (Isoindoline)	0°	3.738, 3.738 (Dual Benzene) 3.554 (Isoindoline)	22.7°, 21.4° (Dual benzene) 12.9° (Isoindoline)
2	3.460	0°	3.650, 3.650	17.4°, 17.7°
3	N/A	5.74°	N/A	N/A

.*Slip angle is slightly different depending on which centroid is used. The measurements were performed in accordance to previous studies.[18]

Crystals of each of the three compounds **1a** (CCDC#:1817435), **2** (CCDC#:1817436) and **3** (CCDC#:1817437) were grown from sublimation and characterized by single crystal X-ray diffraction. Figure 3.1b illustrates the packing motif for the three substituted Pcs. As expected, the size of the axial substituents has a significant effect on the packing of the Pc chromophores. The crystal structures were analysed using previously determined metrics for the degree of π-π overlap between neighbouring phthalocyanine molecules: the shortest centroid-centroid distance between Pc peripheral aromatic groups, the angle between the centroid-centroid line and the normal of the aromatic centroid (slip angle), as well as the distance and angle between the Pc aromatic planes.[18,27] Table 3.1 shows a summary of the packing metrics for each of the substituted Pcs. Tabulation of all crystallographic data can be found in the supporting information.

The substituted SiPcs stack in a lamellar motif with overlap of single isoindoline groups and/or overlap of two adjacent benzene rings in the phthalocyanine chromophore. **1** and **2** exhibit significant π-π interactions with parallel stacking of the aromatic Pc planes at distances of 3.365/3.448 Å and 3.460 Å, respectively. These distances are comparable to those of F_{16}CuPc

Table 3.2: Summarized of top performing bottom-gate, bottom-contact (BGBC) OTFTs fabricated using three different axially substituted silicon phthalocyanines

Material [a]	$\mu_{e,avg}$ $(cm^2V^{-1}s^{-1})$	$\mu_{e,max}$ $(cm^2V^{-1}s^{-1})$	Avg. $V_T(V)$	$I_{on/off}$	*Rate* [b] $(Å s^{-1})$	T_{sub} [b] (°C)
1	6.16±1.48 x 10^{-4}	9.25 x 10^{-4}	23.0±1.3	10^2-10^3	0.5	150
2	1.85±0.50 x 10^{-4}	3.28 x 10^{-4}	17.5±2.7	10^2-10^3	0.5	100
3	4.35±0.77 x 10^{-5}	5.56 x 10^{-5}	15.0±0.6	10^1-10^2	0.5	100

a) Materials: silicon phthalocyanines (SiPc) with chemical structure in Figure 3.1.

b) Rate: Deposition rate of organic semiconductor. T_{sub} = substrate temperature during deposition.

(3.25/3.26 Å)[28-30] and Cl_2-SnPc (3.4 Å)[8]. 1 shows the potential for 2D charge transport displaying both dual benzene stacking, with a centroid-centroid distance of 3.738 Å and slip angles of 22.7°/21.4°, and isoindoline stacking with a centroid-centroid distance of 3.554 Å and a slip angle of 12.9°. **2** shows a slightly shorter centroid-centroid distance of 3.650 Å for dual benzene stacking due to smaller slip angles of 17.4° and 17.7°, however it does not exhibit isoindoline stacking and therefore allows for only 1D charge transport. **3** shows no significant π-π interactions of the Pc as the bulky anthracene functional groups do not allow for overlap of the phthalocyanine chromophores.

3.3.2 Organic Thin Film Transistors

3.3.2.1 Comparison of OTFTs using different axially substituted SiPcs

We constructed bottom-gate, bottom-contact (BGBC) OTFTs using plasma treated substrates with prefabricated electrodes using the three different SiPcs as the active layer material. Table 3.2 compares the best electrical performances for the three molecules, and Figure 3.9 shows sample transfer characteristics. The best electron field-effect mobility (μ_e) devices under all deposition conditions were achieved with **1**, and as such they tended to have a higher on/off current ratio ($I_{on/off}$) due to an increased on-current. The devices using **3** showed the lowest μ_e and $I_{on/off}$. The same trend was seen for threshold voltage (V_T), with values closer to zero being more desirable for lower power consumption. Given the analytical method, this means that the materials with more substantial current increases due to the field-effect saw them at a higher gate voltage than for the materials with smaller increases. This is further demonstrated by the output curves for each material, samples of which are shown in Figure 3.2. Relatively large current increases are seen in

the range 20 V < V_{GS} < 40 V for 1, but below that increases are smaller compared to 2. All samples show some contact resistance, as demonstrated by an offset between the y-axis and the start of the linear region of the output curve. This is often seen in devices in the bottom-gate, bottom-contact (BGBC) configuration.[31]

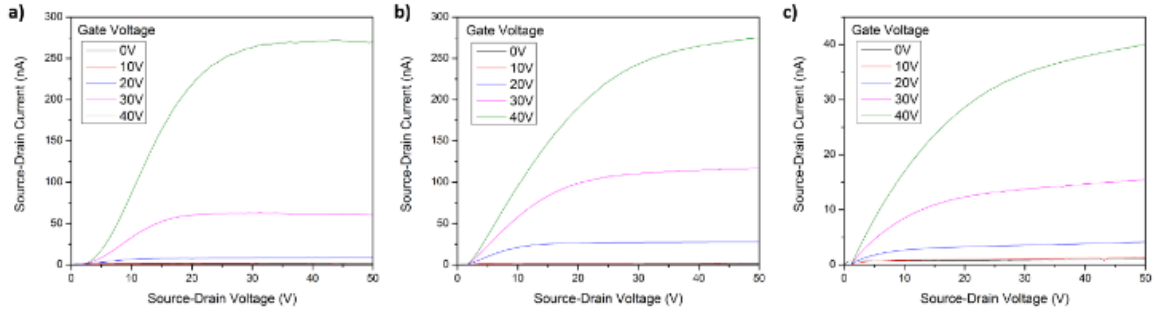

Figure 3.2: Sample output curves for three different axially substituted silicon phthalocyanines used as the active layer for OTFTs (**1** (a); **2** (b); **3** (c)). Deposition was made at room temperature at 0.5 Ås^{-1}.

The three synthesized SiPcs vary only in their axial attachments to the central silicon atom, so these electrical performance variations are likely attributed to the influence of these groups on the solid state packing of the materials in the thin films that compose the active layers of the OTFTs. Based on the UV-vis/fluorescence and UPS data (Figure 3.6 & 3.7), axial changes to SiPc have little effect on the HOMO/LUMO energy gap. It is however interesting to note that the lowest V_T was obtained for devices fabricated using **3** which could be due to favourable energetic match between the molecules LUMO level and the work function of gold. The structures of the molecules as determined using single crystal x-ray diffraction are shown in Figure 3.1b. Both the single crystals diffracted by XRD and the thin films used in devices were obtained by thermal evaporation and, while not identical, can provide insight on the chemical structure relationship to transistor performance. Notably **3** displays little π-π overlap, likely the reason for relatively low field-effect mobility. On the other hand, **2** has the closest π-π stacking distance between molecules but does not demonstrate the greatest field-effect mobility (Table 3.2). This could be due to the 2D arrangement of π-π stacking pathways of the **1** molecules which the **2** molecules lack (Figure 3.1). Figure 3.3 demonstrates how the $\mu_{e,avg}$ of the three materials varies with deposition rate and substrate temperature during the physical vapor deposition of the organic films. When forming the semiconducting film in a BGBC OTFT, the sublimed molecules interact with the surface of the

dielectric and themselves. The nature of the surface, the substrate temperature during deposition, and the rate of deposition can all affect phthalocyanine film formation, and ultimately final device performance.[14] The orientation of the molecules in the film, their structural regularity, and microstructure all can impact the ability of charge to move between source and drain, and hence the field-effect mobility. For all materials, a small increase in mobility was seen for devices where the deposition rate was lowest, which was expected due to the molecules having more time for arranging on the surface resulting in improved structural order. The relationship with substrate temperature during deposition was less clear, with most devices showing an optimal temperature above 25 °C after which mobility appears to decrease. Regardless, these results clearly show that **1** is the highest performing SiPc derivative in this series and therefore we decided to further optimize its OTFTs.

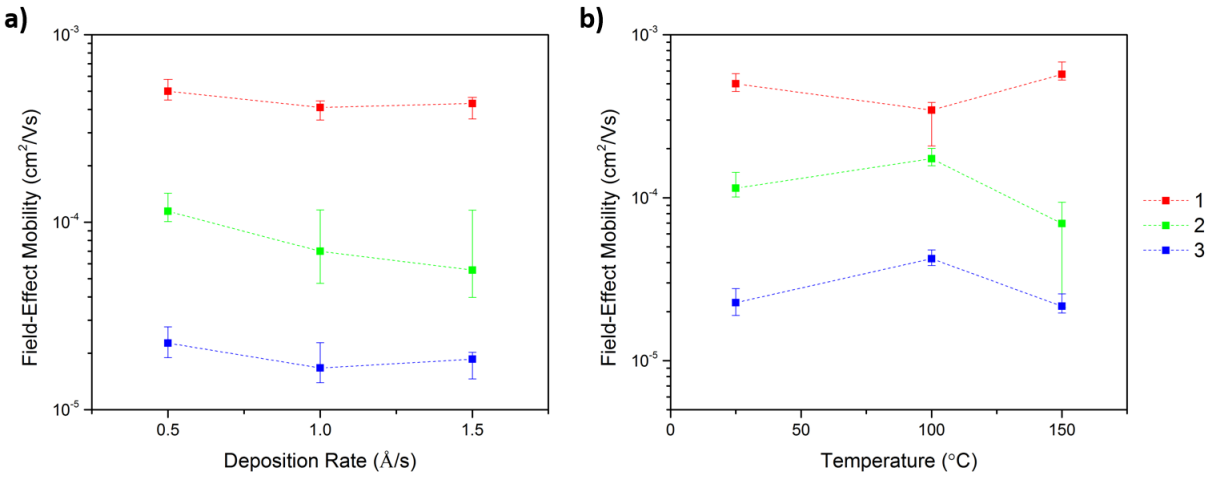

Figure 3.3: Electron field-effect mobility variations with **a)** deposition rate and **b)** substrate temperature during the physical vapor deposition of the active layer using three different axially substituted silicon phthalocyanines (**1**, **2**, and **3**). Data points shown are medians with error bars that show interquartile ranges.

3.3.2.2 Comparison of OTFTs using 1 and different dielectric surface treatments

Dielectric modification using silanes is a common technique to improve the performance of bottom gate OTFTs.[7,32] We investigated the effect of modifying the SiO_2 dielectric with three trichlorosilanes: trichloro(octyl)silane (OTS), trichloro(octadecyl)silane (ODTS), and trichloro(1H,1H,2H,2H-perfluorooctyl)silane (FOTS) on the performance of devices using **1** as

the active layer. **1** was chosen because it demonstrated the highest $\mu_{e,max}$ *and* $\mu_{e,avg}$ of the SiPc series. Figure 3.4a shows how the field-effect mobility for each surface treatment varies with substrate temperature during deposition and the best results for each are summarized in Table 3.3. Sample transfer curves are shown in Figure 3.4b for 200 °C. When the substrates were at room temperature during deposition, little difference in OTFT performance was observed between PT, OTS or ODTS functionalized substrates. However when heating to 200 °C, $\mu_{e,avg}$ of films on OTS and ODTS modified substrates demonstrated an increase of more than a factor of 15 from devices without surface treatment (PT). While a slight improvement in OTFT performance was also recorded for FOTS functionalize substrates with increased substrate temperature, the overall performance was always inferior to all other treatments. As the FOTS reacts rapidly with the surface without water or heat, it could be forming a disordered layer rather than an ordered monolayer, resulting in a poor surface to template the formation of an ordered SiPc thin film.[33] At 250 °C, the deposited films were visibly non-homogenous, showing what appeared to be thinner areas especially on the OTS treated substrate. The atomic force microscopy (AFM) images of the films in Figure 3.10 help elucidate the source of the performance changes. Isotropic granular structures appear upon OTS surface treatment which elongate and form a more interconnected structure by 200 ºC where the optimal mobility was measured. By 250 ºC, large, poorly connected features dominate the topology. This likely contributes to a lower field-effect mobility.

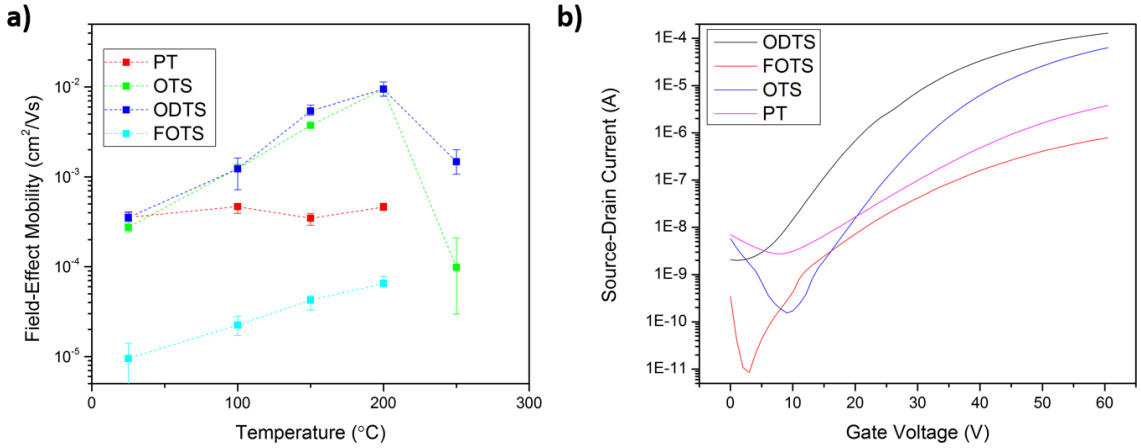

Figure 3.4: **a)** Electron field-effect mobility of OTFTs with active layers of **1** deposited using physical vapor deposition on different modified SiO_2 surfaces at different substrate temperatures. Data points shown are medians with error bars that show interquartile ranges **b)** Sample transfer curves for OTFTs using **1** deposited at 200°C with channel length L = 2.5 µm on different modified SiO_2 surfaces

Table 3.3: Summarized performance of bottom-gate, bottom-contact (BGBC) field-effect transistors made with **1** as the active layer deposited upon a silane-modified dielectric Legend: PT=Plasma Treated/Control. Errors are standard deviations.

Surface Treatment[a)]	$\mu_{e,avg}$ ($cm^2V^{-1}s^{-1}$)	$\mu_{e,max}$ ($cm^2V^{-1}s^{-1}$)	Avg. V_T (V)	$I_{on/off}$	$Rate$[b)] ($Å s^{-1}$)	T_{sub}[b)] (ºC)
PT	$4.66\pm0.47 \times 10^{-4}$	5.55×10^{-4}	26.3±3.2	10^2-10^3	0.3	200
OTS	$9.43\pm1.02 \times 10^{-3}$	1.07×10^{-2}	26.9±2.9	10^4-10^5	0.3	200
ODTS	$9.61\pm2.32 \times 10^{-3}$	1.35×10^{-2}	21.2±2.1	10^3-10^5	0.3	200
FOTS	$6.70\pm1.33 \times 10^{-5}$	8.56×10^{-5}	22.2±1.7	10^2-10^4	0.3	200

a) Surface Treatment on SiO_2 layer prior to deposition of **1**: trichloro(octyl)silane (OTS), trichloro(octadecyl)silane (ODTS), trichloro(1H,1H,2H,2H-perfluorooctyl)silane (FOTS) and plasma treated (PT) as the control

b) Rate: Deposition rate of organic semiconductor. T_{sub} = substrate temperature during deposition.

We have previously found a correlation between measured OTFT $\mu_{e,avg}$ and the intensity of diffraction measured from the organic film.[34] A sample diffraction pattern for a film of **1** is shown in Figure 3.8 in the supporting information. All samples showed small diffraction above the baseline around $2\theta = 14.3°$, which does not correspond to diffraction through a plane as predicted from the single crystal data. However, the four devices with the highest field-effect mobility showed diffraction above the baseline around $2\theta = 9.6°$, indicating structural order in the (001) direction of the single crystal in the film. Figure 3.5 sums the intensity of both areas of diffraction above the baseline to include all samples, and correlates this value to the $\mu_{e,avg}$. This summation corresponds to the relative crystallinity of the thin film, and because the amount of deposited material was kept constant, we can compare devices made under different processing conditions. A clear increase in relative crystallinity with $\mu_{e,avg}$ was observed. This correlation suggests that increased structural order within the film caused by the dielectric surface modification and increased substrate temperature during deposition (Figure 3.5b) results in the increased performance. However, the extent of diffraction is still limited compared to that of SnOPc deposited on para-sexiphenyl,[9] suggesting there is room for improvement in the structural ordering of SiPc materials.

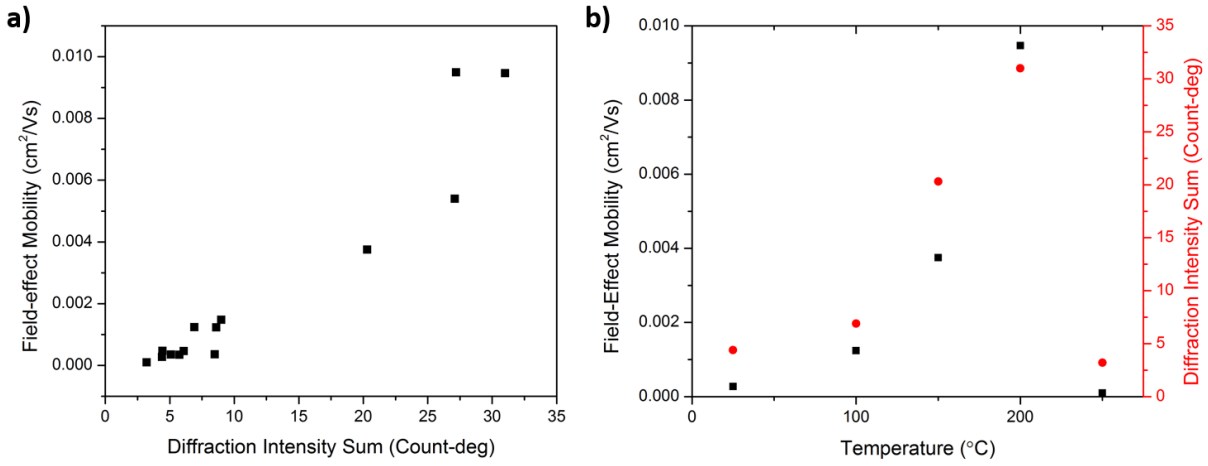

Figure 3.5: **a)** Electron field-effect mobility of BGBC OTFTs made using **1** compared with the total observed diffraction above baseline measured using x-ray diffraction **b)** A visual comparison of the effect of substrate temperature during deposition on the field-effect mobility and diffraction above baseline in two areas on OTS treated substrates

3.4 Experimental

3.4.1 Materials

Benzoic acid, 1-napthoic acid, 9-anthracene carboxylic acid were purchased from Oakwood Chemicals and used as received. Dichlorosilicon phthalocyanine (Cl_2-SiPc) was synthesized as described in the literature.[35] Trichloro(octyl)silane (OTS, 97%), trichloro(octadecyl)silane (ODTS, ≥ 90%), and trichloro(1H,1H,2H,2H-perfluorooctyl)silane (FOTS, 97%) were all obtained from Sigma-Aldrich, used as received and stored in a glovebox.

3.4.2 Synthesis of Functionalized Phthalocyanines

3.4.2.1 Synthesis of Bis(benzoate) silicon phthalocyanine (1)

In a three-neck round bottom flask with a reflux condenser, Cl_2-SiPc (0.5 g, 0.82 mmol), benzoic acid (1.0 g, 8.2 mmol) and toluene (30 mL) were heated to 120 °C for 20 h. The product was methanol and filtered by gravity. The product was purified by train sublimation prior to device integration. Yield: 0.511 g (79.8 %). UV-Vis (Toluene) λ_{max} = 691 nm. HRMS (EI) calcd for 782.1844, found 782.1846. EA: expected wt%: C (70.58 %), H (3.35 %) and N (14.31 %) – analysis wt%: C (71.05 %), H (3.50 %) and N (14.51 %).

3.4.2.2 Synthesis of Bis(1-napthoate) silicon phthalocyanine (2)

2 was synthesized in a similar procedure to **1** using 1-napthoic acid (1.4 g, 8.2 mmol) as a reagent. Yield: 0.603 g (83.5 %). UV-Vis (Toluene) λ_{max} = 685 nm. HRMS (EI) calcd for 882.2161, found 882.2159. EA: expected wt%: C (73.46 %), H (3.42 %) and N (12.69 %) – analysis wt%: C (74.00 %), H (3.75 %) and N (12.79 %).

3.4.2.3 Synthesis of Bis(9-anthronate) silicon phthalocyanine (3)

3 was synthesized in a similar procedure to **1**, using 9-anthranoic acid (1.8 g, 8.2 mmol) as a reagent. Yield: 0.639 g (79.5 %). UV-Vis (Toluene) λ_{max} = 691 nm. EA: expected wt%: C (75.75 %), H (3.49 %) and N (11.40 %) – analysis wt%: C (76.29 %), H (3.81 %) and N (11.49 %). MS data could not be obtained as the molecular weight of **3** is beyond the calibrated range of the mass spectrometer.

3.4.3 Material Characterization

UV-Vis absorption and fluorescence spectra were measured from an Ocean Optics Flame spectrophotometer and DH-2000 light source, with a 10 mm path-length quartz cuvette. Elemental analysis was performed with an Isotope Cube elemental analyzer (Elementar). Powder X-ray Diffraction (PXRD) measurements were done using a Rigaku Ultima IV powder diffractometer, with an x-ray source of Cu Kα (λ = 1.5418 A). The scan range was $5° < 2\theta < 22.5°$ and the scan rate was 1°/minute. Measurements were done directly on the substrates after electrical testing was finished. Peak integrals were determined by manually defining the peak and baseline. Ultraviolet photoelectron spectroscopy (UPS) was performed on a VG ESCALAB 3 MKII with a He I (21.2 eV) source and the sample was characterized under UHV (5.0 x 10-9 Torr). Electron takeoff angle of 0° and energy step size 0.05 eV with an Analysed depth < 10 nm.

3.4.4 Preparation of Field-Effect Transistors

Silicon substrates with a thermally grown, 230 nm thick SiO_2 dielectric and pre-patterned gold source-drain electrodes (W = 2000 μm, L = 2.5, 5, 10 and 20 μm) were purchased from Fraunhofer IPMS and used to make bottom gate, bottom-contact (BGBC) transistors. Each substrate was rinsed in acetone to clean off the protective resist, and then treated with oxygen

plasma for 15 minutes. Three surface treatments with organosilanes were performed in solution on the substrates. 0.1% v/v solutions of: (OTS), (ODTS), and (FOTS) were prepared in dry toluene in a glove box. Each substrate that was to be treated with OTS and ODTS was first rinsed with water and isopropanol before being dried with nitrogen to ensure a consistent amount of water. Substrates to be treated in FOTS solution were not rinsed. After 1 hour of treatment at 70 °C in sealed scintillation vials, substrates were removed and rinsed with toluene before being dried with nitrogen and further dried in a vacuum oven for one hour at 70°C. Dried substrates were transferred into a thermal evaporator manufactured by Angstrom Engineering. SiPcs (**1**, **2** and **3**) were heated in a tungsten boat to just below their sublimation point in a vacuum chamber with pressure below 2 x 10^{-6} torr, and their rate of deposition was then controlled using a quartz crystal monitor and a PID controller. The rate of deposition varied depending on the experiment (0.3 $Å s^{-1}$, 0.5 $Å s^{-1}$, 1.0 $Å s^{-1}$, and 1.5 $Å s^{-1}$) and the total thickness was set to 250 Å, although the exact value may have varied. The substrate was sometimes held at an elevated temperature (100 °C, 150 °C, 200 °C, 250 °C) during the deposition using a calibrated thermocouple to measure and control the temperature.

3.4.5 Electrical Testing

Transfer and output curves were obtained using a custom electrical probe station, oesProbe A10000-P290 (Element Instrumentation Inc. & Kreus Design Inc.) using a Keithley 2614B to set V_{DS} and V_{GS} and to measure I_{DS}. OTFTs were transferred into the chamber from the evaporator using an evacuated tube to avoid exposure to air and water in the atmosphere. The chamber was pumped down to ~10 Pa then refilled with nitrogen twice before finally being pumped down to < 0.1 Pa for testing.

Each device had its transfer characteristics taken four times, with the field-effect mobility, threshold voltage, and on/off ratio determined from the final run. V_{GS} was varied from 0 V to 60 V and V_{DS} was fixed at 50 V, in the saturation region of the output curve for lower gate voltages. Electron field-effect mobilities were calculated using the following equation:

$$I_{DS} = \frac{\mu C_i W}{2L}(V_{GS} - V_T)^2 \quad (3.1)$$

L and W represent the channel length and width. The capacitance density (C_i) of the gate dielectric is calculated using $C_i = \frac{\varepsilon_0 \varepsilon_r}{t}$ where t is the thickness of the dielectric (230nm) and ε_r is the relative dielectric constant of SiO_2. μ is the field-effect mobility and is calculated from the slope of best fit

around the steepest region of $\sqrt{I_{DS}}$ plotted against V_{GS}. The threshold voltage V_T is calculated from the x-intercept of that line. Our experimental data, assuming a constant capacitance density, does not demonstrate a perfectly linear relationship between $I_{SD}^{1/2}$ and the gate bias V_{GS} above V_T. Figure 3.11 shows the V_T and μ_e of a typical device plotted as a function of V_{GS} by fitting Equation 1 between every two adjacent data points. Both variables increase to a maximum and then begin to decrease again at higher gate voltages. In order to measure characteristic values, we assessed both metrics in a 10 V region around these maxima. The results suggest that the devices turn on at a higher gate voltage and have a higher field-effect mobility than is demonstrated for all gate voltages. This representation of the mobility is averaged over a range and excludes higher gate voltages where the device may still be operating in the linear region.

3.5 Conclusions

A series of axially substituted silicon phthalocyanines with benzoate (**1**), 1-napthoate (**2**) and 9-anthronate (**3**) groups were synthesized, characterized by single crystal X-ray diffraction, and incorporated into BGBC OTFTs as active materials, a first for SiPcs in literature to our knowledge. Electron field-effect mobilities of 9.3 x 10^{-4}, 3.3 x 10^{-4}, and 5.6 x 10^{-5} $cm^2V^{-1}s^{-1}$ were achieved on oxygen plasma treated substrates for **1**, **2**, and **3**, respectively. The difference in mobility between the three compounds was attributed, in part, to the degree of π-π overlap in their respective crystal structures and the possibility of **1** creating 2D charge-transfer pathways. The OTFT performance of **1** was further optimized with dielectric surface treatments using organosilanes. A maximum electron mobility of 1.2 x 10^{-2} $cm^2V^{-1}s^{-1}$ was achieved using an octadecyltrichlorosilane (ODTS) surface treatment and a deposition temperature of 200 °C, with an average threshold voltage ~21 V. These results show promise for SiPcs as N-type active materials in OTFTs and demonstrate how axial substituents can change the molecular packing and subsequently the field-effect mobility. Future work will look at using alternative SiPcs with different axial and peripheral substituents in order to maximize molecular overlap and charge transfer to improve OTFT performance.

3.6 Acknowledgements

The authors are grateful for financial support from the NSERC Discovery Grant to B.H.L. Infrastructure used to complete this work was acquired using CFI-JELF and NSERC RTI. We thank Dr. Lough (University of Toronto) for his help with x-ray diffraction of the single crystals and Dr. Gabudillin for his assistance with x-ray diffraction (PXRD). We want to thank Dr. Lefebvre from the LASM facility (École Polytechnique Montréal) for UPS characterization. We would also like to thank Prof. Timothy Bender (University of Toronto) for fruitful discussions about SiPcs and all the undergraduate students who helped gather data for this study as part of their course laboratory (CHG4359A University of Ottawa).

3.7 Supplementary Information

3.7.1 Additional Figures

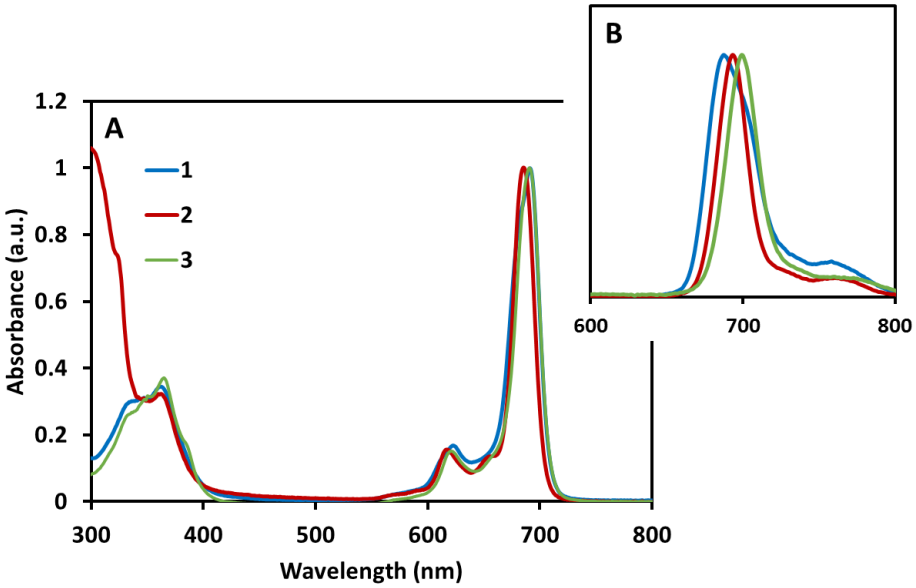

Figure 3.6: (A) Normalized UV-Vis absorption and (B) normalized fluorescence in toluene solution for **1 (**blue) **2** (red) and **3** (green).

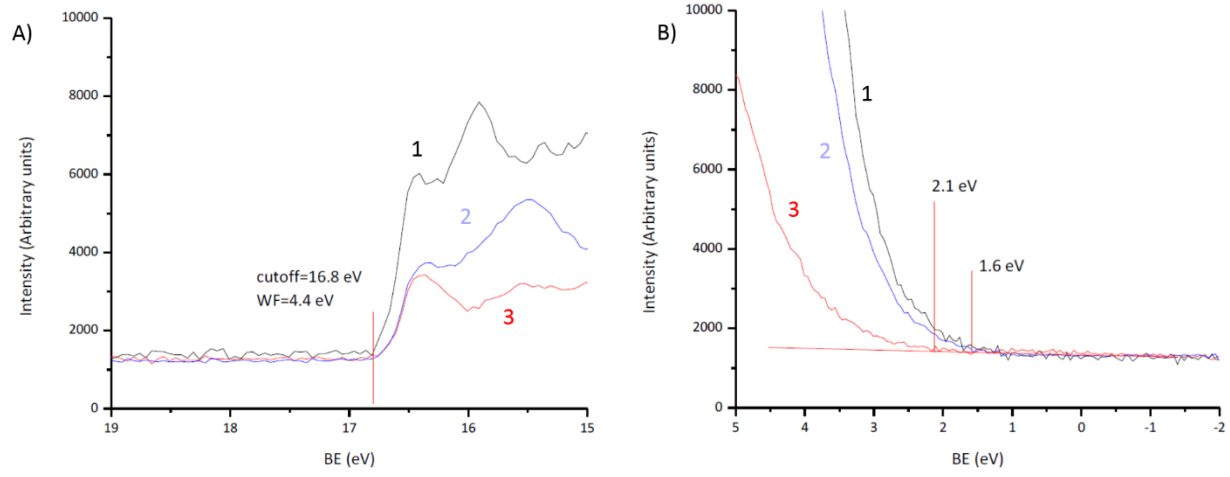

Figure 3.7: Ultraviolet photoelectron spectroscopy (UPS) for 1 (black), 2 (blue) and 3 (red) where A) is a close of the high binding energy peak used to determine the work function and B) are the low binding energy peaks used to determine the HOMO offset.

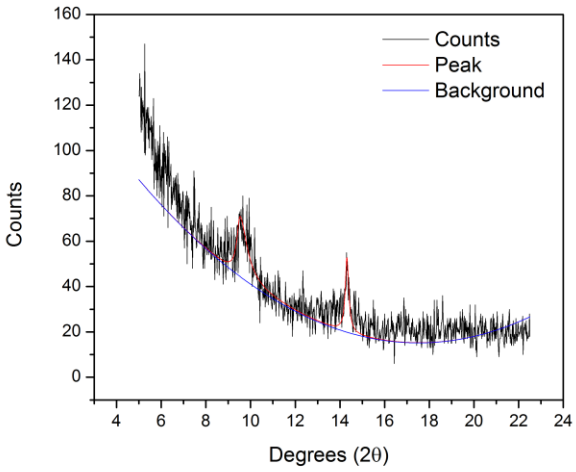

Figure 3.8: X-ray diffraction pattern for 25 nm thick film of **1** deposited on ODTS treated SiO_2 at 200 °C. Peaks and background were manually assigned to term peak intensity above background.

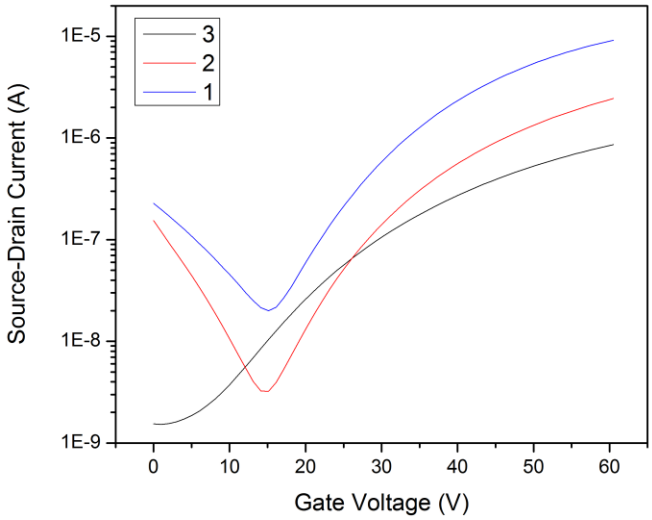

Figure 3.9: Sample transfer curves for OTFTs using three different active SiPcs with channel length L = 2.5 μm

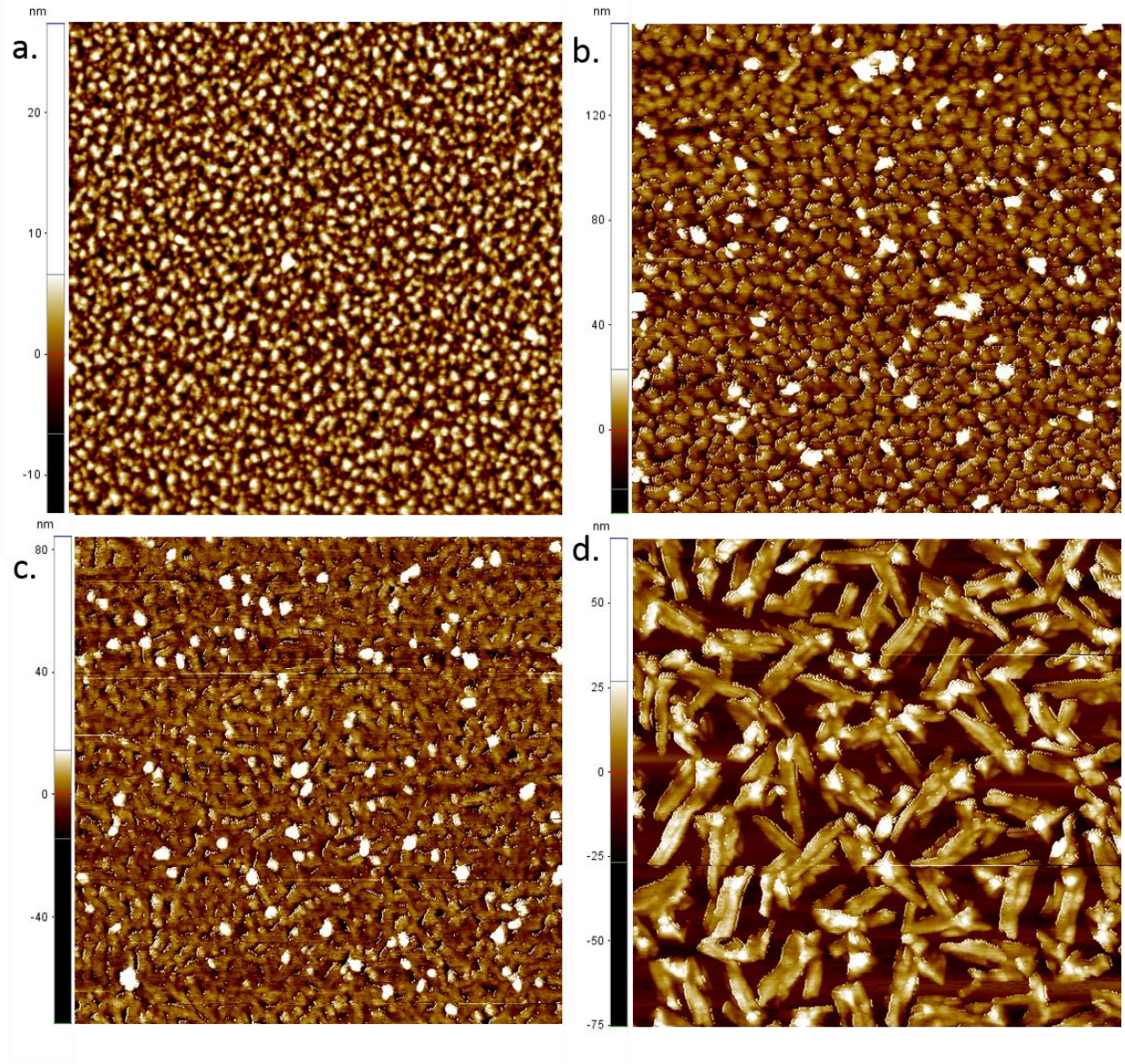

Figure 3.10: Atomic force microscopy (AFM) images of **1** deposited on different surfaces: a. Plasma treated, room temperature substrate; b. OTS-treated, room temperature substrate; c. OTS-treated, 200 ºC substrate; d. OTS-treated, 250 ºC substrate. All images are 4x4 μm.

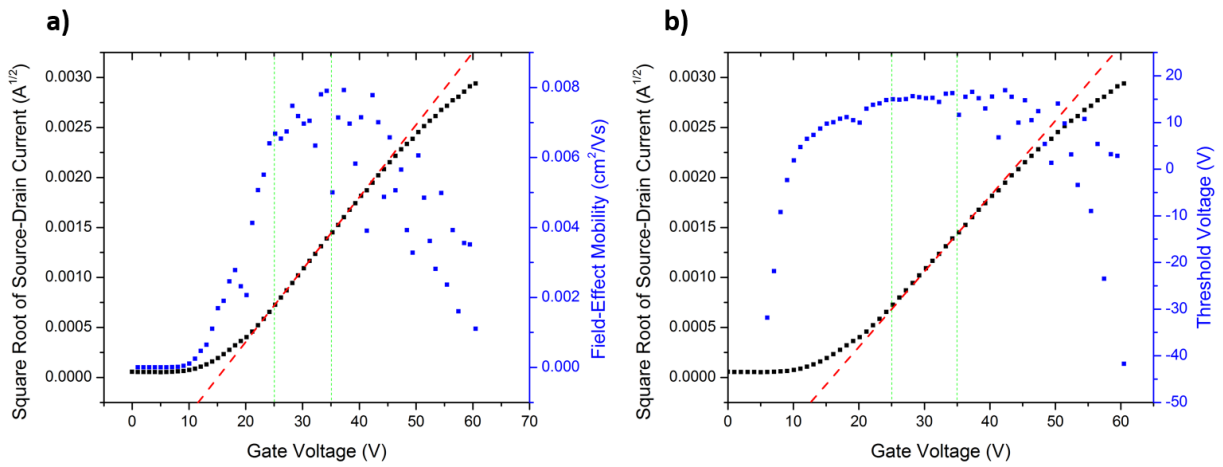

Figure 3.11: **a)** Saturation region electron field-effect mobility (μ_e) and **b)** threshold voltage (V_T) compared with the square root of source-drain current as a function of gate bias (V_{GS}) for an OTFT using **1** as the active semiconducting layer deposited at 200 ºC on an ODTS surface treated dielectric (L = 20 µm). The green lines represent the bounds used to fit this data linearly to Equation 3.1, resulting in a line of best fit (red, dashes) with slope proportional to the calculated μ_e and x-intercept equal to the reported V_T.

3.7.2 Single Crystal Data

Single crystal data was omitted as it is over 50 pages long and does not contribute significantly to the scope of discussion. The raw data can be obtained at the following address:
http://www.rsc.org/suppdata/c8/tc/c8tc01116h/c8tc01116h2.cif

3.8 References

(1) Wang, L.; Liu, G.; Wang, H.; Song, D.; Yu, B.; Yan, D.; Wang, L.; Liu, G. Switch-on Transient Behavior of Vanadium Phthalocyanine Based Organic Transistors. *Appll. Phys. Lett.* **2007**, *91*, 063511.

(2) Wang, L.; Li, Y.; Song, X.; Liu, X.; Zhang, L.; Yan, D. Improved Interfacial and Electrical Properties of Vanadyl-Phthalocyanine Metal-Insulator-Semiconductor Devices with Silicon Nitride as Gate Insulator. *Appl. Phys. Lett.* **2013**, *103*, 243302.

(3) Wang, L.; Qin, H.; Zhang, W.; Zhang, L.; Yan, D. High Reliability of Vanadyl-Phthalocyanine Thin- Film Transistors Using Silicon Nitride Gate Insulator. *Thin Solid Films* **2013**, *545*, 514–516.

(4) Dong, S.; Tian, H.; Huang, L.; Zhang, J.; Yan, D.; Geng, Y.; Wang, F. Non-Peripheral Tetrahexyl-Substituted Vanadyl Phthalocyanines with Intermolecular Cofacial π–π Stacking for Solution-Processed Organic Field-Effect Transistors. *Adv. Mater* **2011**, *23*, 2850–2854.

(5) Pan, F.; Tian, H.; Qian, X.; Huang, L.; Geng, Y.; Yan, D. High Performance Vanadyl Phthalocyanine Thin-Film Transistors Based on Fluorobenzene End-Capped Quaterthiophene as the Inducing Layer. *Org. Electron.* **2011**, *12* (8), 1358–1363.

(6) Wang, H.; Zhou, Y.; Roy, V. A. L.; Yan, D.; Zhang, J.; Lee, C. Polymorphism and Electronic Properties of Vanadyl-Phthalocyanine Films. *Org. Biomol. Chem.* **2014**, *15*, 1586–1591.

(7) Li, L.; Tang, Q.; Li, H.; Yang, X.; Hu, W.; Song, Y.; Shuai, Z.; Xu, W.; Liu, Y.; Zhu, D. An Ultra Closely Π- Stacked Organic Semiconductor for High Performance Field- Effect Transistors. *Adv. Mater.* **2007**, *19* (18), 2613–2617.

(8) Song, D.; Wang, H.; Zhu, F.; Yang, J.; Tian, H.; Geng, Y.; Yan, D. Phthalocyanato Tin(IV) Dichloride: An Air-Stable, High-Performance, n-Type Organic Semiconductor with a High Field-Effect Electron Mobility. *Adv. Mater.* **2008**, *20* (11), 2142–2144.

(9) Song, D.; Zhu, F.; Yu, B.; Huang, L.; Geng, Y.; Yan, D.; Song, D.; Zhu, F.; Yu, B.; Huang, L.; Geng, Y.; Yan, D. Tin (IV) Phthalocyanine Oxide : An Air-Stable Semiconductor with High Electron Mobility. *Appl. Phys. Lett.* **2008**, *92*, 143303.

(10) Shao, X.; Wang, S.; Li, X.; Su, Z.; Chen, Y.; Xiao, Y. Single Component P- , Ambipolar and n-Type OTFTs Based on Fluorinated Copper Phthalocyanines. *Dyes Pigm.* **2016**, *132*,

378–386.

(11) Chem, J. M. High Performance Organic Thin Film Transistor Based on Pentacene Derivative : **2012**, 10496–10500.

(12) Sheraw, B. C. D.; Jackson, T. N.; Eaton, D. L.; Anthony, J. E. Functionalized Pentacene Active Layer Organic Thin-Film Transistors. **2009**, No. 23, 2009–2011.

(13) Anthony, J. E. Functionalized Acenes and Heteroacenes for Organic Electronics. **2006**, 5028–5048.

(14) Melville, O. A.; Lessard, B. H.; Bender, T. P. Phthalocyanine-Based Organic Thin-Film Transistors: A Review of Recent Advances. *ACS Appl. Mater. Interfaces.* **2015**, *7* (24), 13105–13118.

(15) Honda, S.; Nogami, T.; Ohkita, H.; Benten, H.; Ito, S. Improvement of the Light-Harvesting Efficiency in Polymer/Fullerene Bulk Heterojunction Solar Cells by Interfacial Dye Modification. *ACS Appl. Mater. Interfaces.* **2009**, *1* (4), 804–810.

(16) Honda, S.; Ohkita, H.; Benten, H.; Ito, S. Multi-Colored Dye Sensitization of Polymer/Fullerene Bulk Heterojunction Solar Cells. *Chem. Commun. (Camb).* **2010**, *46* (35), 6596–6598.

(17) Honda, S.; Ohkita, H.; Benten, H.; Ito, S. Selective Dye Loading at the Heterojunction in Polymer/Fullerene Solar Cells. *Adv. Energy Mater.* **2011**, *1* (4), 588–598.

(18) Lessard, B. H.; Grant, T. M.; White, R.; Thibau, E.; Lu, Z.; Bender, T. P. The Position and Frequency of Fluorine Atoms Changes the Electron Donor/Acceptor Properties of Fluorophenoxy Silicon Phthalocyanines within Organic Photovoltaic Devices. *J. Mater. Chem. A.* **2015**, *3* (48), 24512–24524.

(19) Grant, T. M.; Gorisse, T.; Dautel, O.; Wantz, G.; Lessard, B. H. Multifunctional Ternary Additive in Bulk Heterojunction OPV : Increased Device Performance and Stability. *J. Mater. Chem. A.* **2017**, 1581–1587.

(20) Online, V. A.; Dang, M.; Grant, T. M.; Yan, H.; Seferos, D. S.; Bender, T. P. Organic Photovoltaic Devices †. **2017**, 12168–12182.

(21) Lessard, B. H.; Dang, J. D.; Grant, T. M.; Gao, D.; Seferos, D. S.; Bender, T. P. Bis(Tri-n-Hexylsilyl Oxide) Silicon Phthalocyanine: A Unique Additive in Ternary Bulk Heterojunction Organic Photovoltaic Devices. *ACS Appl. Mater. Interfaces.* **2014**.

(22) Ke, L.; Min, J.; Adam, M.; Gasparini, N.; Hou, Y.; Perea, J. D.; Chen, W.; Zhang, H.;

Fladischer, S.; Sale, A.; Spiecker, E.; Tykwinski, R. R.; Brabec, C. J.; Ameri, T. A Series of Pyrene-Substituted Silicon Phthalocyanines as Near-IR Sensitizers in Organic Ternary Solar Cells. *Adv. Energy Mater.* **2016**, *6*, 1502355.

(23) Ke, L.; Gasparini, N.; Min, J.; Zhang, H.; Adam, M.; Rechberger, S.; Forberich, K.; Zhang, C.; Spiecker, E.; Tykwinski, R. R.; Brabec, C. J.; Ameri, T. Panchromatic Ternary/Quaternary Polymer/Fullerene BHJ Solar Cells Based on Novel Silicon Naphthalocyanine and Silicon Phthalocyanine Dye Sensitizers. *J. Mater. Chem. A Mater. energy Sustain.* **2017**, *5* (6), 2550–2562.

(24) Zysman-colman, E.; Ghosh, S. S.; Xie, G.; Varghese, S.; Chowdhury, M.; Sharma, N.; Cordes, D. B.; Slawin, A. M. Z.; Samuel, I. D. W. Solution-Processable Silicon Phthalocyanines in Electroluminescent and Photovoltaic Devices. **2016**.

(25) Lessard, B. H.; White, R. T.; Al-amar, M.; Plint, T.; Castrucci, S.; Josey, D. S.; Lu, Z.; Bender, T. P. Assessing the Potential Roles of Silicon and Germanium Phthalocyanines in Planar Heterojunction Organic Photovoltaic Devices and How Pentafluoro Phenoxylation Can Enhance $\pi - \pi$ Interactions and Device Performance. *ACS Appl. Mater. Interfaces.* **2015**, *7* (9), 5076–5068.

(26) Bender, T. P.; Greenham, N. C.; Pearson, A. J.; Credgington, D. Silicon Phthalocyanines as Dopant Red Emitters for Efficient Solution Processed OLEDs. *J. Mater. Chem. C.* **2017**, *5* (48), 12688–12698.

(27) Lessard, B. H.; Lough, J.; Bender, T. P. Crystal Structures of Bis (Phenoxy) Silicon Phthalocyanines: Increasing π-π Interactions, Solubility and Disorder and No Halogen Bonding Observed. *Acta Cryst.* **2016**, *E72* (7), 988–994.

(28) Ke, L.; Min, J.; Adam, M.; Gasparini, N.; Hou, Y.; Perea, J. D.; Chen, W.; Zhang, H.; Fladischer, S.; Sale, A.; Spiecker, E.; Tykwinski, R. R.; Brabec, C. J.; Ameri, T. A Series of Pyrene-Substituted Silicon Phthalocyanines as Near-IR Sensitizers in Organic Ternary Solar Cells. *Adva* **2016**, *6*, 1502355.

Chapter 4: Ambipolarity and Air Stability of Silicon Phthalocyanine Organic Thin-Film Transistors

4.1 Preamble

This section describes the context in which the research was performed, relating it to the development of the lab and my own research goals at the time. It describes the contributions of each author and the significance of the research.

4.1.1 Context

As early as summer 2017 I had obtained promising results with several SiPcs, including two fluorinated phenoxy derivatives (F_{10}-SiPc and 345F-SiPc). After finishing work on the previous SiPc project, I continued to attempt to optimize these devices, focusing on F_{10}-SiPc. A number of changes to the setup of the thermal evaporator including attempts to reduce material usage coincided with inconsistent device performance. Eventually, I was able to address these inconsistencies by addressing contamination issues with the new setup and obtaining new supplies. I was curious about the fluctuation in n-type and p-type performance for the ambipolar SiPcs depending on characterization environment, and performed some experiments to illustrate it. I became increasingly aware of issues related to operational instability and contact resistance in OTFTs and attempted to highlight those issues in the research. This was a slow process and the final paper was only published in 2019.

4.1.2 Contributions of Authors

I designed all experiments independently and fabricated all SiPc OTFTs used in the study. I characterized most of the OTFTs used in the study, and performed all OTFT-related analysis. I performed PXRD experiments and analyzed AFM and PXRD data. I researched contact resistance (R_C) models, discussed them with Professor Park, and implemented several analytical programs in LabView to calculate R_C and intrinsic mobility, not all of which were used in the final version. I created all figures with some help from Professor Lessard and wrote the entire manuscript.

Trevor Grant patiently synthesized and purified multiple batches of the SiPc materials used in these experiments. Brendan Mirka assisted with characterization of a few OTFTs and obtained the AFM images presented in the report. Nicholas Boileau fabricated and characterized F_{16}CuPc devices as procedurally comparative controls. I consulted with Professor Park on contact resistance modelling and other analysis related to questions asked by reviewers. Professor Lessard helped with figures and suggested testing the materials. All co-authors contributed to editing.

4.1.3 Significance

Although we had already demonstrated that SiPcs were promising n-type materials for OTFTs and established some simple structure-function and procedure-function relationships, the electron mobility was still lower than state-of-the-art devices, even within the phthalocyanine family. This research demonstrated that silicon bispentafluorophenoxy phthalocyanine (F_{10}-SiPc) can demonstrate consistent electron mobility of around 0.2 cm^2/Vs (maximum 0.54 cm^2/Vs) with threshold voltage as low as 12 V, arguably superior to all n-type phthalocyanines in OTFTs. Other reported PVD-based devices using F_{16}CuPc or Sn(IV)Pcs have comparable μ_e, but both required a small molecular dielectric modification process we could not reproduce, and the latter devices tended to have relatively high V_T. Our process-comparable F_{16}CuPc devices performed much worse than the F_{10}-SiPc, with a mobility over an order of magnitude lower. I also examined some of the ambient stability of SiPcs, establishing a tentative relationship between LUMO/HOMO levels and electron/hole transport in air/vacuum. I examined the bias stress in SiPc OTFTs by comparing a pulsed gate to a constant gate bias and by measuring ΔV_T.

The rest of Chapter 4 has been adapted with permission from Advanced Electronic Materials: Melville, O. A., Grant, T. M., Mirka, B., Boileau, N. T., Park, J., & Lessard, B. H., ***2019****, 5 (8), 1900087, DOI: doi.org/10.1002/aelm.201900087 © 2019 WILEY-VCH Verlag GmbH & Co. KGaA, Weinheim*

Abstract

Silicon phthalocyanines (SiPcs) are a class of conjugated, planar molecule that have recently been investigated for use in organic photovoltaics (OPVs), organic light-emitting diodes (OLEDs) and organic thin-film transistors (OTFTs) due to their variable structure and ease of synthesis. Bottom-gate, bottom-contact OTFTs with four SiPc derivatives used as the semiconducting layers were prepared using physical vapor deposition. Devices using bis(pentafluorophenoxy) silicon phthalocyanine (F_{10}-SiPc) deposited on 140 °C substrates demonstrated electron field-effect mobilities (μ) of up to 0.54 $cm^2V^{-1}s^{-1}$, among the best currently reported for n-type phthalocyanine-based transistors. All materials showed dramatic changes in charge transport when characterized under vacuum ($P < 0.1$ Pa) compared to in air at atmospheric pressure, typically switching from electron majority charge carriers to holes, with the change dependent on material structure and energetics. F_{10}-SiPc is close to balanced ambipolar in air, with μ around 5×10^{-3} $cm^2V^{-1}s^{-1}$ for both holes and electrons. These results demonstrate SiPcs' potential as n-type semiconductors in OTFTs as well as their adjustable charge transport as affected by operation environment.

4.2 Introduction

The performance and availability of electron-conducting organic semiconductors lags behind those that conduct holes in electronic applications such as organic thin film transistors (OTFTs).[1–3] As inverters and other more complex logic circuit components require both types of materials, it is imperative to continue exploring n-type carbon-based molecules in OTFTs and other applications. In addition to electronic performance metrics like field-effect mobility (μ), straightforward material synthesis and ease of integration into devices are also important in order to properly evaluate their potential.

Metal phthalocyanines (MPcs) are conjugated macrocycles that chelate a central metal atom and have found application in the dyes and pigments industry for decades.[4] Recently, MPcs have also been extensively studied in imaging/therapy,[5] catalysis,[6] organic photovoltaics (OPVs)[7,8] and OTFTs[9] due to their excellent thermal stability and ease of synthesis. Soluble and insoluble derivatives have shown excellent charge transport characteristics in OTFTs, with hole field-effect mobilities (p-type) of up to 10 $cm^2V^{-1}s^{-1}$ for titanyl phthalocyanine (TiOPc) deposited in vacuum[10] and 1.7 $cm^2V^{-1}s^{-1}$ for one spin-cast and solution annealed Eu_2Pc_3 derivative.[11] The best reported vacuum deposited n-type phthalocyanines are copper hexadecylfluoro phthalocyanine ($F_{16}CuPc$)[12], with several reports of electron field-effect mobilities (μ_e) up to 0.27 $cm^2V^{-1}s^{-1}$ and tin (IV) oxide phthalocyanine (SnOPc)[13], with one report of μ_e up to 0.44 $cm^2V^{-1}s^{-1}$. Both materials required a high temperature deposition on a small molecule interlayer for optimal performance.

Silicon phthalocyanines (SiPcs) are a class of MPc with a synthetic handle lacked by divalent metal centered MPcs such as CuPc and ZnPc. The axial chloro groups on dichloro silicon phthalocyanine (**1**, Figure 4.1) react with organic acids and phenols, producing a variety of derivatives including bis(pentafluorophenoxy) silicon phthalocyanine (**2**, Figure 4.1). These derivatives have different packing motifs in the solid state with the bulkier axial groups sometimes improving the π-π stacking required for the efficient lateral charge transport that causes a high μ.[14–16] Density functional theory (DFT) calculations predict μ_e between 0.01 and 0.09 $cm^2V^{-1}s^{-1}$ depending on the axis of transport for **2**, with 2-dimensional charge transport pathways for both holes and electrons.[17] In practice, changes in this axial group affect performance in OPVs with both improved open circuit voltage and short circuit current when using **2** compared to **1** as the acceptor or donor material.[14,15] Recently we published the first use of SiPc derivatives in OTFTs,

with dibenzoate functionalized SiPc demonstrating the highest electron μ of 0.01 $cm^2V^{-1}s^{-1}$ using an octyltrichlorosilane (OTS) dielectric treatment and a substrate temperature held at 200 °C during deposition.[18]

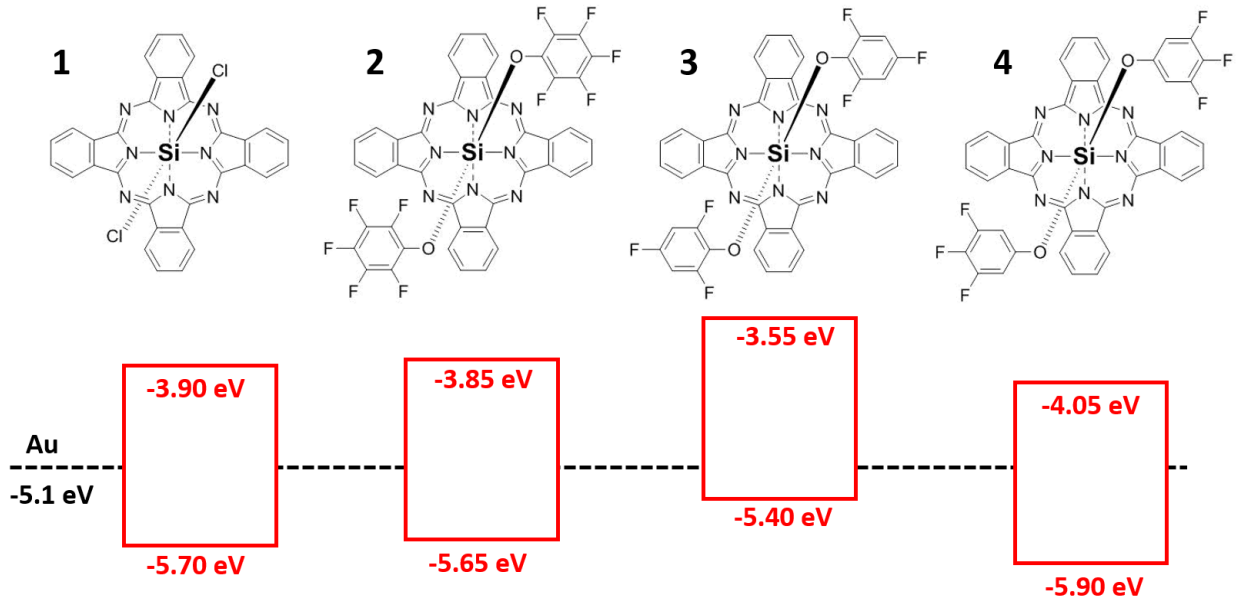

Figure 4.1: Molecular diagrams of dichloro silicon phthalocyanine (**1,** Cl_2-SiPc) bis(pentafluorophenoxy) silicon phthalocyanine (**2,** F_{10}-SiPc), bis(2,4,6-trifluorophenoxy) silicon phthalocyanine (**3**, 246F-SiPc) and bis(3,4,5-trifluorophenoxy) silicon phthalocyanine (**4**, 345F-SiPc). The red insets below each diagram represent the HOMO and LUMO of each material, obtained previously by Bender et al.[14]

Many n-type materials such as C_{60} show reduced or negligible field-effect in air, requiring inert or low pressure conditions to operate effectively.[19] Oxygen in air has been shown to act as an electron trap for OTFTs using an n-type semiconducting polymer,[20] with an energetically favorable transition of electrons from the lowest unoccupied molecular orbital (LUMO) of the n-type organic semiconductor to absorbed oxygen molecules. For OTFTs using an n-type perylene diimide (PDI) derivative, both water and oxygen in air can degrade the performance.[21] For other PDI derivatives, the thickness and morphology of the semiconducting film along with the LUMO level of the molecule have been shown to affect air stability in OTFTs.[22] For carbon nanotube (CNT) based OTFTs, the synergistic presence of oxygen and air have been shown to suppress electron conduction,[23] while air has enhanced the p-type field-effect mobility compared to low vacuum.[24]

These changes in field-effect properties have not been well-studied in many molecular classes for OTFTs, including phthalocyanines, but are vital to understanding their operating limitations and potential for sensing applications.

In this study, we report the electrical characteristics of bottom-gate, bottom contact (BGBC) OTFTs made with the physical vapor deposition of four SiPc derivatives (**1**-**4**, Figure 4.1) as the semiconducting films. These films are characterized using atomic force microscopy (AFM) and x-ray diffraction (XRD) to correlate film structure to electrical performance parameters such as μ and threshold voltage (V_T). Finally, the effect of testing environment and gate bias stress on μ, V_T, and charge polarity for each material is examined.

4.3 Results & Discussion

4.3.1 OTFT Fabrication and Optimization of 1 and 2

Bottom-gate, bottom-contact OTFTs were fabricated by depositing **1** and **2** as the active semiconducting layers on plasma treated substrates (PT) and octyltrichlorosilane (OTS) modified substrates held at various temperatures during deposition. These devices were characterized for electrical performance in order to find optimal fabrication conditions. Previously we found optimal OTFT performance in terms of μ was for SiPcs deposited on OTS-modified substrates heated to 200 ºC.[18] OTFTs produced using **1** and **2** showed similar trends in performance, with optimal results when deposited on OTS-modified substrates heated to 140 ºC instead of 200 ºC (Figure 4.10). Average electron field-effect mobilities under these optimized conditions were 0.02 $cm^2V^{-1}s^{-1}$ and 0.12 $cm^2V^{-1}s^{-1}$, respectively (Table 4.1). To investigate the source of the electrical performance variations between the molecules deposited under different conditions, we performed x-ray diffraction (XRD) and atomic force microscopy (AFM) on the resulting thin films. Figures 2 and 3 depicts XRD spectra and AFM images, respectively, for 30 nm films of **2** deposited on an a) oxygen PT substrate; b) OTS treated substrate; c) OTS treated substrate heated at 140 °C during deposition; and d) OTS treated substrate heated at 200 °C during deposition. Figure 4.11 shows the height distributions of the raw data for scans unadjusted for contrast enhancement. On the PT surfaces, films of **2** are consistent but contain either very small or no distinct structural features by AFM with only a small amount of XRD diffraction intensity. When treating the substrate with OTS prior to deposition, small but distinct features appear in the AFM images of the resulting SiPc

film and the diffraction intensity increases substantially in the (010) and (020) directions as determined from the single crystal diffraction pattern. When the temperature of the substrate increases to 140 °C during the deposition of **2**, the feature size on the AFM images increases considerably along with surface roughness, with domains up to about 500 nm in length and increased height appearing regularly (Figure 4.3c, Figure 4.11). This change in feature size is accompanied by a large increase in the (001) diffraction peak and a minor decrease in the (010), (020) and (110) peaks (Figure 4.2). This suggests a morphological change occurs during higher temperature depositions that may be responsible for the increased μ. At 200 °C, the film is even rougher with features that appear less distinct, laterally smaller and vertically greater than at 140 °C, and the diffraction for all the peaks except (001) has decreased. These results suggest that the combination of OTS dielectric modification and modest substrate heating during deposition afford optimal OTFT results. A common explanation is that the deposited molecules mildly interact with the hydrophobic OTS-modified surface and diffuse on the surface into ordered structures that are better able to transport charge.[19] Increasing the temperature of the substrate during deposition encourages this diffusion by increasing the kinetic energy of the molecules on the surface, while excessive temperatures can cause low grain density on the surface or other non-ideal growth patterns.[26]

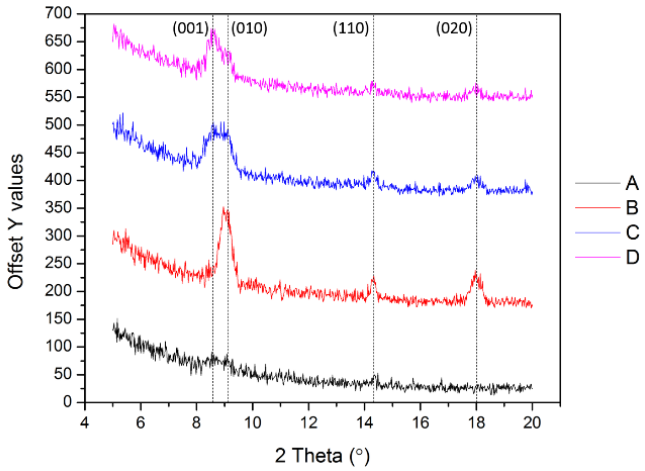

Figure 4.2: Diffraction pattern for thin films of **2** made with physical vapor deposition under different conditions: A) plasma treated (PT) substrate, room temperature deposition; B) OTS-treated substrate, room temperature deposition; C) OTS-treated substrate, 140 °C deposition; D) OTS-treated substrate, 200 °C deposition

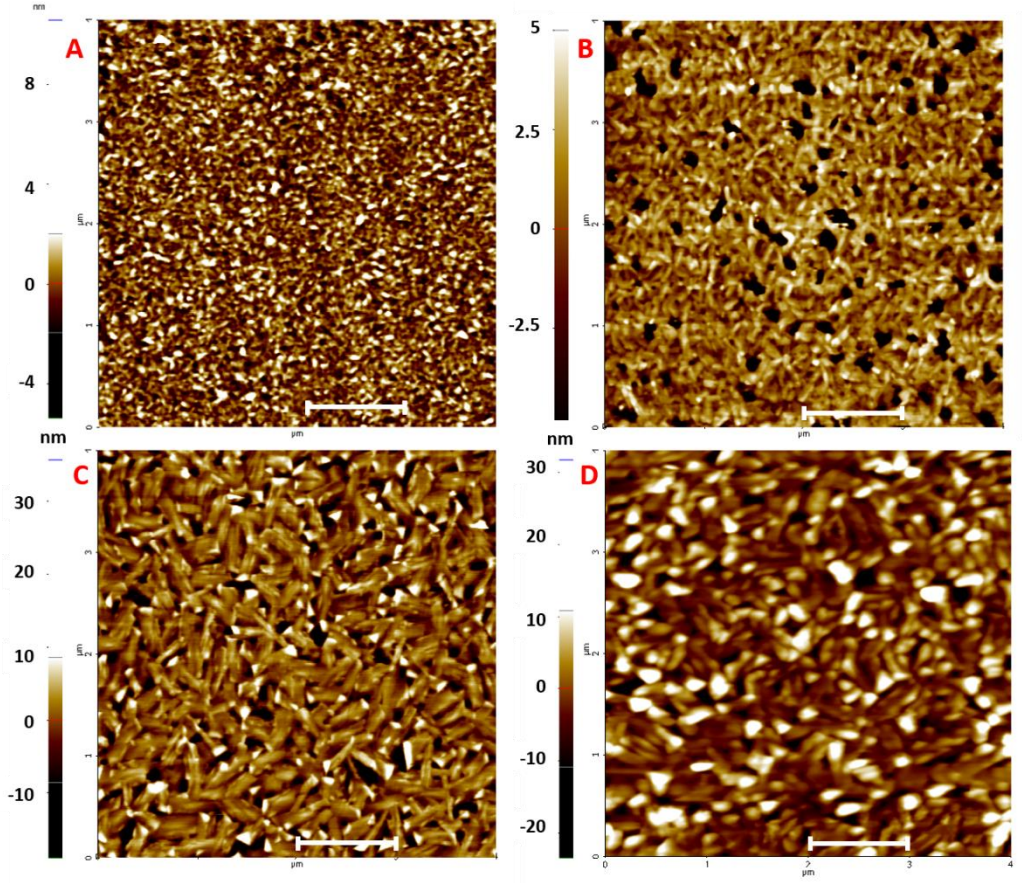

Figure 4.3: Topographic atomic force microscopy (AFM) images of **2** deposited upon: A) plasma treated (PT) substrate; B) octyltrichlorosilane (OTS) treated substrate; C) OTS treated substrate held at 140 °C; D) OTS treated substrate held at 200 °C. White bar represents 1 µm.

Table 4.1: Summary of the saturation-region electron field-effect mobility (μ_e, mean and maximum values), mean threshold voltage (V_T) and on/off current ratio ($I_{on/off}$) for bottom-gate, bottom-contact transistors (Count is the number tested) with various SiPcs as the active semiconductor deposited on substrates heated to 140 °C. OTFTs were tested in vacuum (P < 0.1 Pa) without being exposed to air. Values are uncorrected for contact resistance.

Material	$\mu_{e,avg}$ ($cm^2V^{-1}s^{-1}$)	$\mu_{e,max}$ ($cm^2V^{-1}s^{-1}$)	V_T (V)	$I_{on/off}$	*Count*
1	2.23×10^{-2}	9.73×10^{-2}	37.2 ± 14.1	10^5	109
2	1.19×10^{-1}	5.37×10^{-1}	12.0 ± 4.8	10^{4-5}	57
3	2.27×10^{-2}	4.31×10^{-2}	35.2 ± 3.4	10^{4-5}	8
4	1.98×10^{-2}	3.14×10^{-2}	17.1 ± 7.5	10^{4-5}	36
F_{16}CuPc	2.43×10^{-2}	5.62×10^{-2}	-7.9 ± 5.1	10^{3-4}	36

4.3.2 Material Comparison

OTFTs using **1-4** were fabricated with OTS-modified substrates that were held at 140 ^{0} C during deposition, as the optimal condition determined for **1-2**. Additionally, OTFTs with F_{16}CuPc, a common n-type MPc, were fabricated under the same conditions for comparison. Table 4.1 summarizes the resulting devices' saturation-region electron field-effect mobility (μ_e), threshold voltage (V_T) and on/off current ratios ($I_{on/off}$). Leakage current between the gate and source, estimated as I_{DS} when V_{DS} = 0 V in the output curve at different V_{GS}, ranged between 0.1% and 1.4% of the maximum current for optimized devices. Figure 4.4 shows a characteristic output and transfer curve for an OTFT using **2**. These devices had the highest μ_e of all five materials, with some demonstrating μ_e above 0.5 $cm^2V^{-1}s^{-1}$, comparable to the best results reported for n-type phthalocyanine OTFTs in literature. Devices using **2** also had the lowest V_T of the SiPcs, averaging 12.0 V, with materials **1** and **3** showing much greater average V_T of 37.2 V and 35.2 V, respectively. OTFTs fabricated with an F_{16}CuPc active layer had μ_e averaging 0.024 $cm^2V^{-1}s^{-1}$, significantly lower than for **2**. Other researchers have reported improved n-type performance for F_{16}CuPc up to 0.27 $cm^2V^{-1}s^{-1}$ through dielectric modification with para-sexiphenyl (p-6p) or by significantly reducing the deposition rate[12,13,25,27]. Given the significantly lower performance measured here, it is conceivable that by using these approaches, the performance of **2** could be improved even further. However, for this study we kept the processing conditions constant for ease of comparing the different materials.

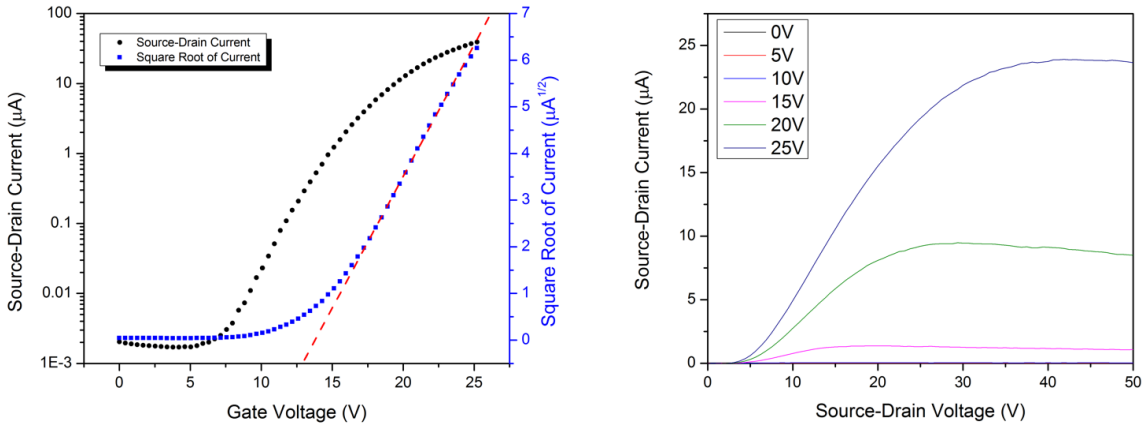

Figure 4.4: Transfer (V_{DS} = 50 V) and output curves for BGBC OTFTs using **2** as the active layer and tested under vacuum (P < 0.1 Pa). Active material was deposited on an OTS treated substrate held at 140 °C.

The difference between **1-4** and all previously reported SiPcs for OTFTs is the axial substituent attached to the central silicon atom. This substituent affects how the molecules pack in the solid state, with single crystals of **1-4** previously published and related to organic photovoltaic (OPV) performance.[14] The addition of the fluorinated phenoxy pendant groups in **2-4** induces significant π-π overlap between aromatic rings that is absent in **1**, potentially explaining their generally superior performance in OTFTs and OPVs. However, axial substitution does not always increase performance. In our previous work, we reported three different modified SiPcs which had a maximum μ_e of 0.01 $cm^2V^{-1}s^{-1}$, inferior to that reported for unfunctionalized **1**.[18] Single crystals of **2-4** pack differently than these previously reported derivatives, with the sp^3-hybridized carbon atom in the Si-O-C bond allowing the fluorinated phenoxy groups to bend closer to the phthalocyanine core than the benzoic, 1-naphthoic and 9-anthronate pendant groups linked by a sp^2-hybridized carbon atom, which end up relatively perpendicular to the Pc core. These bulky groups may interfere with packing during film formation, impeding charge transport compared to **1-4**. Density functional theory (DFT) calculations for single crystals of **2-4** have previously been reported, potentially providing insight into the difference in performance between the three materials.[17] Although single crystals of **2** were calculated to have a maximum μ_e of 0.09 $cm^2V^{-1}s^{-1}$, lower than the 0.20 and 0.19 $cm^2V^{-1}s^{-1}$ calculated for **3** and **4**, respectively, it is the only material

to theoretically possess 2-dimensional charge transport pathways through its single crystal. These extra transport pathways could increase the likelihood of uninterrupted electron flow between the source and drain electrodes for **2**, resulting in its superior performance. The diffraction intensity for thin films of **2** (Figure 4.2) was also significantly higher than for **1** (Figure 4.9), **3**, **4** and F_{16}CuPc films of similar thickness produced under similar conditions. Thus, another explanation for its superior performance is that molecules of **2** have a higher propensity to assemble into well-ordered structures during thin-film formation on OTS.

4.3.3 Characterization Conditions and Air Stability

The employed characterization conditions and device geometry significantly affected OTFT measurements, increasing device-to-device performance variability. Figure 4.7 (ESI) shows how μ_e changed with channel length (2.5, 5, 10, 20 μm) for a constant channel width (W = 2000 μm) with **1** and **2** as the active materials. The calculated μ_e increased with channel length for **2**, and remained relatively constant for **1**. Decreasing performance at lower channel lengths is associated with parasitic resistances between the contacts and semiconductor, consistent with the trend for **2**.[28] The presence of significant contact resistance (R_C) in devices using **2** is also suggested by its output (Figure 4.4**)** which has a relatively high amount of curvature near the origin compared to **1** (Figure 4.6). To examine the effects of contact resistance, we used the modified transmission line method[29] to obtain R_C as a function of V_{GS} (Figure 4.12) and to estimate theoretical saturation mobility without contact resistance (μ_0) using two methods described in the SI. Figure 4.12 shows the contact resistance as a function of gate bias, typically $10^{6\text{-}7}$ Ω for material **2**. Figure 4.7 shows μ_0 for two sets of 16 devices of **1** and **2**, approximately 0.025 and 0.42 cm^2/Vs, respectively. The relatively lower mobility for **1** increases channel resistance compared to **2**, decreasing the relative effect of R_C and thus resulting in a mobility that is relatively stable with channel length. The increasing μ of **2** with L, consistent across many tested conditions and replicates, suggests R_C is more significant when channel length is smaller. Thus, μ_0 more closely matches the mobility of L = 20 μm devices, averaging 0.21 cm^2/Vs compared to 0.12 cm^2/Vs when considering all tested OTFTs using material **2** in Table 4.1. It is possible that the devices are acting as Schottky barrier transistors, given the position of the work function of gold between that of the HOMO and LUMO of material **2**, the delayed linear region observed in Figure 4.4, and the high contact resistance.

Future work will focus on reducing R_C by modifying the source-drain contact material or device architecture to improve the consistency, analysis and performance of devices at all channel lengths.

Another factor that affected device performance was accumulated gate bias applied over time. The data presented in Table 4.1 are the values obtained after collecting transfer characteristics of each OTFT five times, with the gate bias constantly applied step-wise for about 30s for each run. Figure 4.8 (ESI) shows how the measured μ_e and V_T changed with the number of times transfer characteristics were collected. For both materials, μ_e increases, stabilizing after a few trials. V_T increases for material **2** over those trials, typically with ΔV_T around 2V, and with no consistent trend for material **1**. Positive V_T shifts in n-type materials during operation are typically associated with the filling of electron traps which then remain filled and oppose polarization.[30] These changes to V_T make it difficult to extract an accurate, singular value for μ_e, an important consideration when evaluating these OTFTs and others where such a shift exists or is not accounted for. To examine the impact of applying reduced gate bias on device operation using material **2**, transfer curves with a non-zero gate bias applied for only 20 ms between 80 ms intervals at 0 V (pulsed gate) were obtained and compared to those where non-zero bias was applied for 100 ms at each step without returning to 0 V. The unity current gain frequency (f_T) was estimated to be between 10^5 and 10^6 Hz at $V_{GS} = 25$ V for these devices, far exceeding the pulse frequency and allowing for measurable gain. The devices with a pulsed gate had a μ_e roughly 50% greater and a V_T of about 3 V lower than for those where the gate bias was constant, also showing much more consistent results over repeat trials. Thus, a non-constant gate bias is more desirable for operating SiPc-based OTFTs.

The largest impact on SiPc device performance was the characterization atmosphere, for which we initially evaluated in an evacuated chamber ($P < 0.1$ Pa) and then in air at atmospheric pressure after the devices had been removed from vacuum for 5 minutes. While our previous studies had looked at this comparison for carbon nanotubes wrapped in semiconducting polymers,[24] p-type small molecules,[31] and conjugated polymers,[32] we have not yet examined this effect on n-type small molecules, which are particularly sensitive to oxygen. Table 4.2 summarizes the changes observed for a single set (one substrate) of devices for each material, with Figure 4.5 showing sample transfer curves under each condition for material **2**. For **1**-**4**, n-type behavior changes similarly in transition from vacuum to air. All materials lose a significant portion of electron conduction, with OTFTs of **3** showing an average decrease in μ_e by a factor of 1000 and with an average ΔV_T of +8 V, indicating a large increase in trap density consistent with studies for

n-type semiconducting polymers.[20] This relatively large change compared to **1, 2,** and **4** might be due to the relatively shallow LUMO level of -3.55 eV for **3** (Figure 4.1), making it particularly susceptible to oxidation. However, the LUMO level of **1**-**4** does not strictly correspond to n-type conductivity in vacuum or air. Devices fabricated using **2** showed the highest performance under both conditions, despite **4** having the deeper LUMO level (Figure 4.1). For devices fabricated using **2**, μ_e decreased on average by a factor of 7.6 with an average ΔV_T of +13 V, indicating more resistance to oxidation than **1**, **3** and **4**. Film morphology, suggested to impact air stability for n-type small molecules in OTFTs,[22] may explain some of this difference. Another interesting phenomena observed for these devices was the change in p-type conduction as the devices transitioned from vacuum to air. Of the four SiPcs characterized, only **1** was entirely unipolar, showing no significant p-type conduction in vacuum or air. **2**-**4** all exhibited slight ambipolar behavior in vacuum, albeit with high V_T and low hole field-effect mobilities (μ_h). In air, **2**-**4** showed markedly increased p-type conduction, with μ_h increasing by a factor ranging between 10 and 100 and with V_T increasing [towards 0 V] by between 8 and 13 V. The best p-type performance was for **3** in air, which had a μ_h of 1.93 x 10^{-2} $cm^2V^{-1}s^{-1}$ and a threshold voltage of -26.0 V. It has been reported that p-type phthalocyanines such as ZnPc[33] and PbPc[34] have improved conductivity in air. This change may due to oxygen acting as an electron acceptor from the central metal atom, creating holes in some molecules. Increases in hole mobility in p-type materials as charge carrier density increases may be due to an increased density of states at the highest occupied energy level.[35] Thus, **3** may have superior performance in air due to increased interaction with oxygen at the more shallow HOMO level (Figure 4.1). However, HOMO level alone cannot explain p-type performance either, with **2** demonstrating superior hole conduction to **1** in air, despite similar energetics. This could be due to film morphology, or perhaps differences in the ability of a hole to form in the phthalocyanine ring when the silicon atom is attached to a –Cl instead of an –OR group. In any case, the HOMO and LUMO level of the materials appear to play some role in this N and p-type conduction as well, with material **3** showing the best p-type behavior in air and vacuum and the worst n-type conduction in air. This type of sensitivity could be exploited for sensors and inverters (where balanced carrier mobility is crucial), for instance, and certainly is important for device operation.

Table 4.2: Mean field-effect mobility (μ) and threshold voltage (V_T) of a single sample of OTFTs using materials **1**-**4** as semiconductors deposited at 140 ºC characterized in both vacuum (P < 0.1 Pa) and in air. Results were obtained both in hole accumulation (V_{GS}, V_{DS} < 0 V) and electron accumulation (V_{GS}, V_{DS} > 0 V) regions under both environmental conditions. Material **1** did not show a significant field-effect for holes under any condition and so relevant cells have been blacked out.

Material		N-Type (V_{GS}, V_{DS} > 0 V)		p-type (V_{GS}, V_{DS} < 0 V)	
		Vacuum	Air	Vacuum	Air
1	μ (cm^2/Vs)	1.55 x 10^{-2}	5.18 x 10^{-5}	n/a	n/a
	V_T (V)	35.3	39.9	n/a	n/a
2	μ (cm^2/Vs)	4.87 x 10^{-2}	6.40 x 10^{-3}	4.92 x 10^{-5}	4.16 x 10^{-3}
	V_T (V)	15.1	29.3	-60.5	-30.7
3	μ (cm^2/Vs)	2.90 x 10^{-2}	2.47 x 10^{-5}	1.51 x 10^{-3}	1.93 x 10^{-2}
	V_T (V)	32.6	45.4	-45.6	-26.0
4	μ (cm^2/Vs)	1.72 x 10^{-2}	2.95 x 10^{-4}	2.17 x 10^{-5}	2.37 x 10^{-3}
	V_T (V)	23.3	35.1	-58.4	-30.3

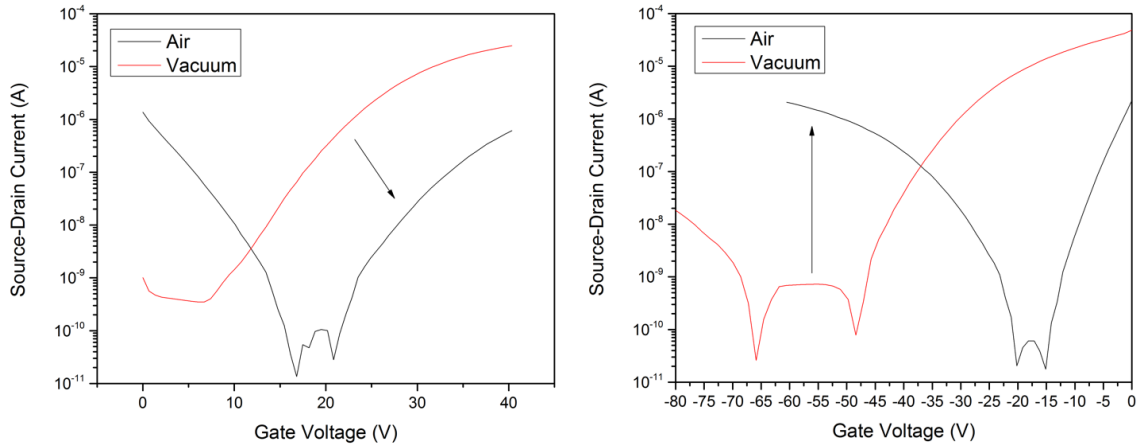

Figure 4.5 Sample transfer curves for OTFTs using **2** as the active layer when operated in the electron accumulation region (V_{GS} > 0 V, V_{DS} = 50 V, left) and hole accumulation region (V_{GS} < 0 V, V_{DS} = -50 V, right) and characterized either under vacuum or in air.

4.4 Conclusion

Silicon phthalocyanine (SiPc) derivatives **1-4** were incorporated into bottom-gate, bottom-contact organic thin-film transistors (OTFTs) as the active semiconducting layers using physical vapor deposition. Devices fabricated using **2-4** had comparable or higher electron field-effect mobilities (μ_e) and lower threshold voltages (V_T) than **1**, demonstrating that axial substitution of SiPcs can improve OTFT performance. Devices with **2** deposited on an octyltrichlorosilane-modified substrate held at 140 °C have μ_e up to 0.54 $cm^2V^{-1}s^{-1}$ in vacuum and V_T that stabilizes around 13 V. Using an SiPc material with simple synthesis and straight-forward device processing, we achieved a result that is among the best reported for n-type phthalocyanine-based transistors, and approaches the $\geq$1 $cm^2V^{-1}s^{-1}$ range of state of the art n-type materials. Additionally, axially substituted SiPcs **2-4** all showed some ambipolarity of charge transport, which depended both on material energetics and the characterization atmosphere. These adjustable electrical properties could be utilized for sensors, with further work developing and characterizing other axially substituted SiPcs for improved performance and sensing capability.

4.5 Experimental

4.5.1 OTFT Preparation

1[36], **2**[15] and **3**-**4**[14] were prepared according to previously described procedures and purified by train sublimation prior to device integration. Bottom-gate, bottom-contact devices were prepared from doped silicon wafers with 230 nm of thermally grown oxide and pre-patterned gold/indium tin oxide source-drain electrodes (L = 2.5, 5, 10, 20 μm; W = 2000 μm) purchased from Fraunhofer IPMS. The substrates were rinsed with acetone to remove their protective resist, dried with nitrogen, then treated with an oxygen plasma for 15 minutes to clean and hydrolyze their surfaces. They were rinsed with distilled water and isopropanol, dried with nitrogen, then surface treated with 1% v/v octyltrichlorosilane (OTS, 97%, Sigma) in dry toluene for 1 hour at 70 °C. OTS treated substrates were then rinsed with toluene and isopropanol, dried with nitrogen and transferred into a vacuum oven to dry for 1 hour at 70 °C. Silicon phthalocyanines **1-4** and F_{16}CuPc (TCI Chemicals, sublimed) were deposited using physical vapor deposition in an Angstrom EvoVac thermal evaporator with a target thickness of 300 Å and rate of 0.3 Å/s at various substrate temperatures. Heated substrates were allowed to cool to room temperature before being removed from the vacuum chamber, usually overnight.

4.5.2 OTFT Characterization

The backside of the devices was scratched with a diamond tipped pencil to ensure contact with the gate. They were transferred in an evacuated capsule to the oesProbe A10000-P290 (Element Instrumentation Inc. & Kreus Design Inc.) testing station. The testing chamber was evacuated and refilled with nitrogen twice before testing under vacuum (P < 0.1 Pa). Contact with the source-drain electrodes was made with BeCu alloy probe tips. Output curves were obtained by fixing the gate voltage (V_{GS}) at discrete values and sweeping the source-drain voltage (V_{SD}). Transfer curves were obtained by fixing V_{SD} in the saturation region at ±50 V. The electron/hole field-effect mobility and threshold voltage were determined according to a previously described procedure.[18] The capacitance density C_i of the SiO_2 dielectric was estimated using the thickness (230 nm) and dielectric constant (3.9): $C_i = \frac{k\varepsilon_0}{t} = 1.5x10^{-4}\ \frac{F}{m^2}$.

4.5.3 Film Characterization

Atomic force microscopy (AFM) images were obtained using a Park Systems NX10 in contact mode using a CONTR cantilever tip. Powder X-ray Diffraction (PXRD) spectra were obtained using a Rigaku Ultima IV powder diffractometer, with a Cu Kα (λ = 1.5418 Å) x-ray source. The scan range was 5° < 2θ < 20° and the scan rate was 1°/minute. Measurements were done directly on the substrates after electrical testing and AFM were completed.

4.6 Acknowledgments

The authors are very grateful for financial support from the NSERC DG to B.H.L and the Ontario Graduate Scholarship (OGS) to O.A.M. and T.M.G. Infrastructure used to complete this work was acquired using CFI-JELF and NSERC RTI.

4.7 Supporting Information

4.7.1 Additional Figures

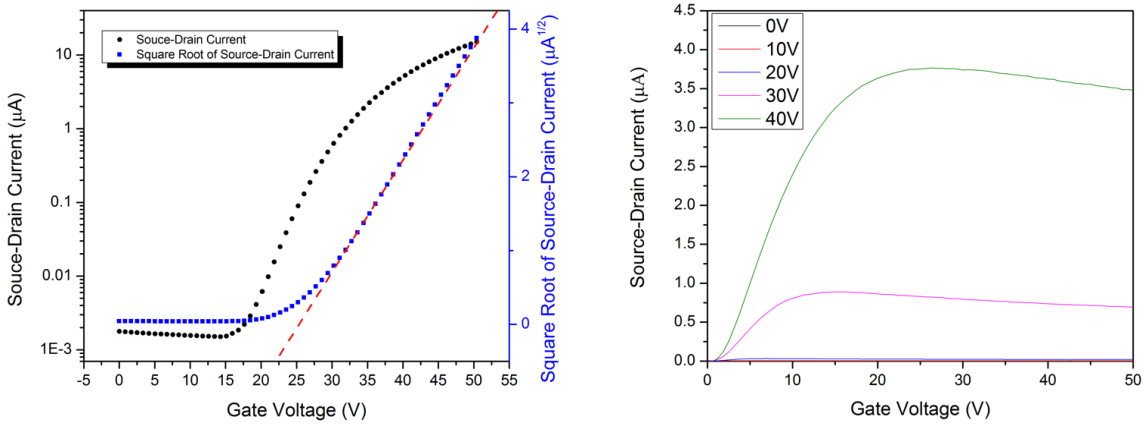

Figure 4.6: Transfer (V_{DS} = 50V) and output curves for BGBC OTFTs using **1** as the active layer and tested under vacuum (P < 0.1 Pa). Active material was deposited on an OTS treated substrate held at 120 °C.

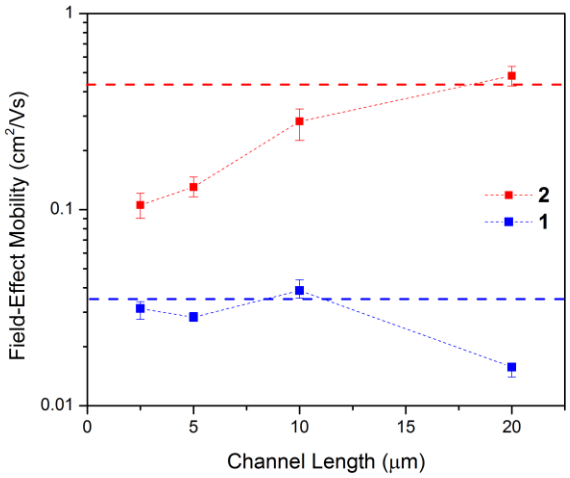

Figure 4.7: Effect of channel length on the saturation region electron field-effect mobility (μ_e) on 16 BGBC OTFTs of **1** and **2**. Data points are means and error bars represent the maximum and minimum values for each channel length. The dotted lines represent theoretical, contact-resistance free for each set of devices calculated using equation (3).

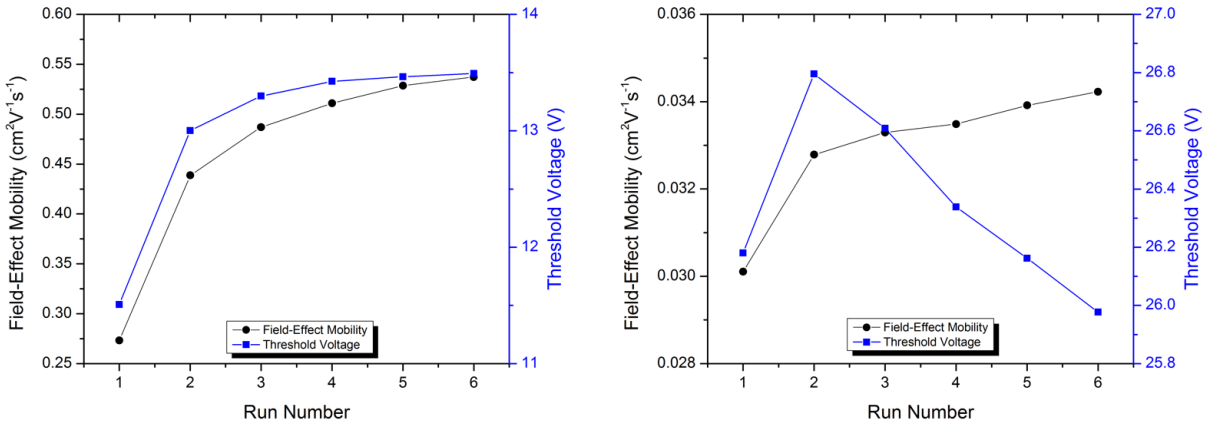

Figure 4.8: Illustration of changing mobility and threshold voltage after a number of runs wherein transfer characteristics were determined for bottom-gate, bottom-contact organic thin-film transistors of **1** (left) and **2** (right). Data points are for a sample device and results are typical.

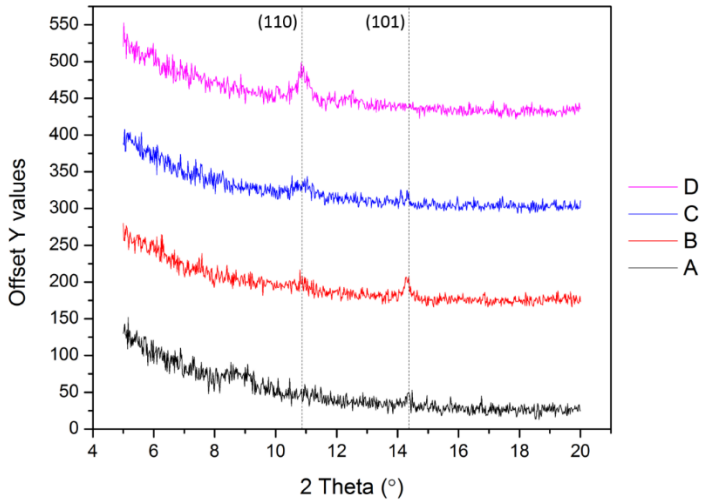

Figure 4.9: Diffraction pattern for thin films of **1** ($SiCl_2Pc$) made with physical vapor deposition under different conditions: A) Plasma treated substrate, room temperature deposition; B) OTS-treated substrate, room temperature deposition; C) OTS-treated substrate, 120 °C deposition; D) OTS-treated substrate, 200 °C deposition.

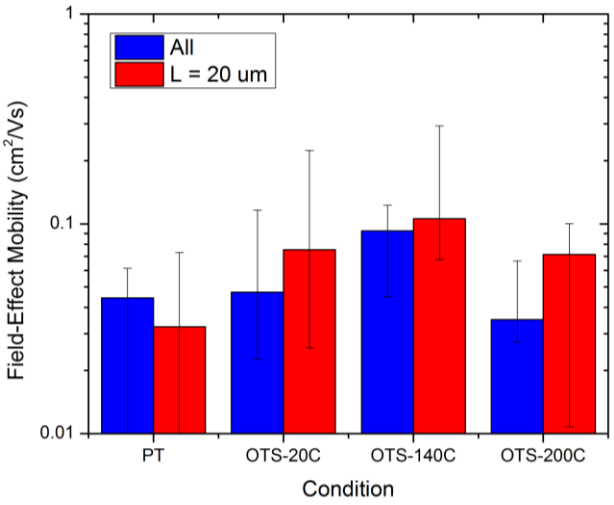

Figure 4.10: Field-effect mobility for OTFTs made using **2** as the active semiconductor with different substrate temperatures during deposition and surface treatments. Bar values represent the median and the errors bars represent interquartile ranges. Legend {PT: plasma treated control; OTS-20C: deposited on a room temperature substrate modified with OTS; OTS-140C: deposited on a 140 ºC substrate modified with OTS; OTS-200C: deposited on a 200 ºC substrate modified with OTS

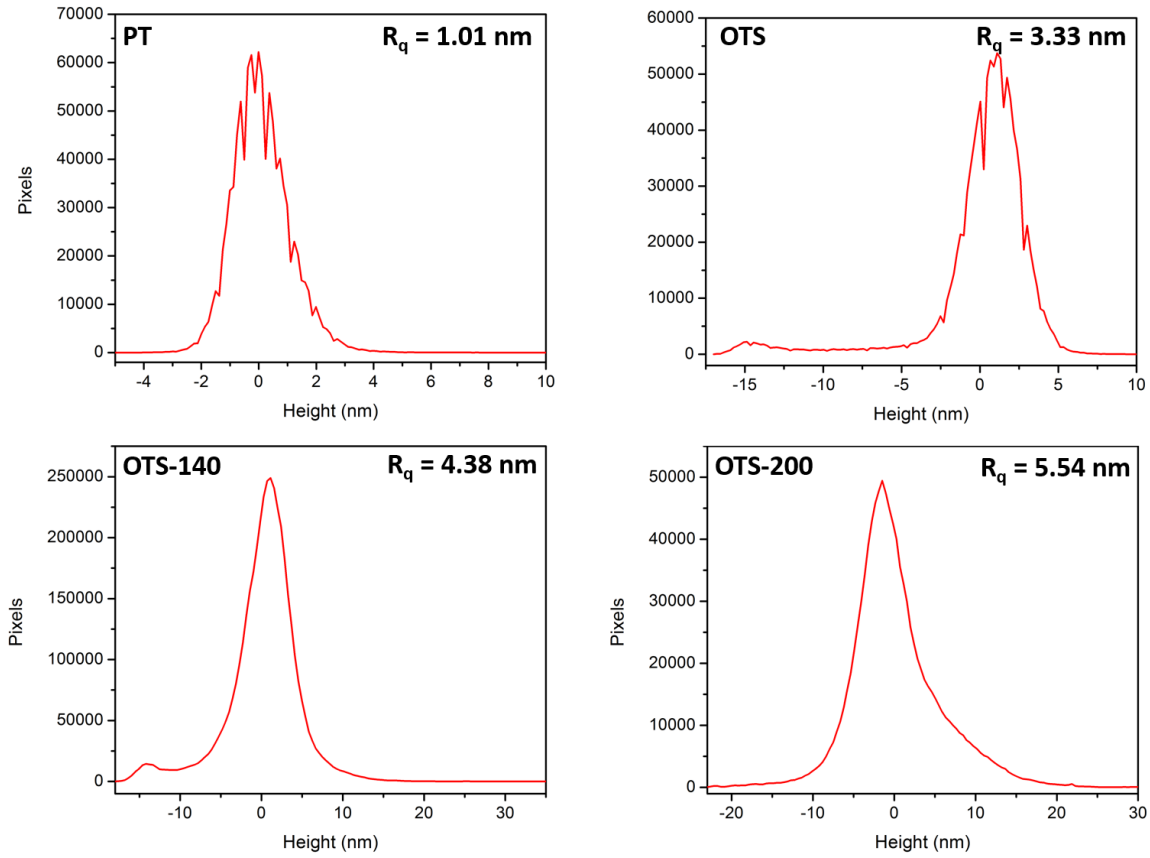

Figure 4.11: Height profiles for the AFM images in **Figure 4.3**. Rq is the rms surface roughness.

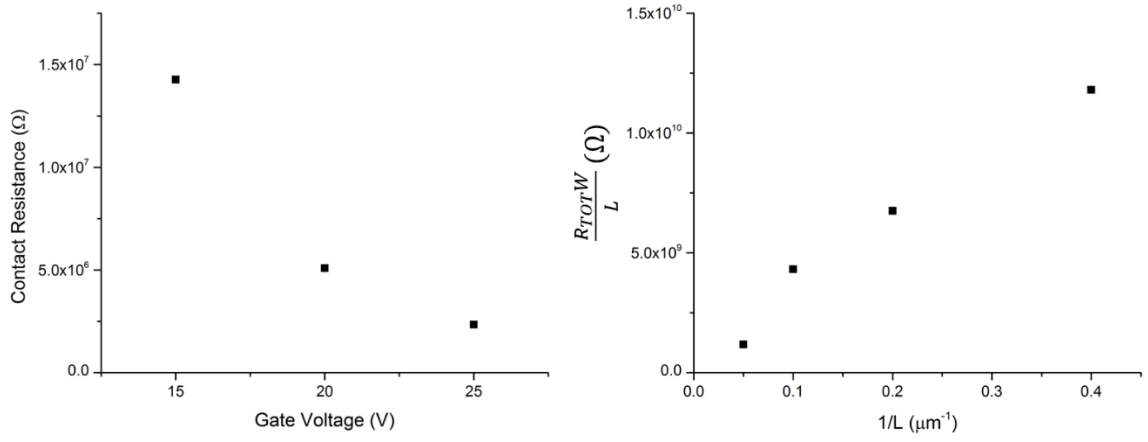

Figure 4.12: Example contact resistance profile as a function of gate voltage for material **2** (left) and example modified TLM method data at V_{GS} = 15 V for the same set of devices (right). The contact resistance at a given gate bias is proportional to the slope of this graph.

4.7.2 Contact Resistance Calculations

The modified transmission line method uses the output curves to estimate contact resistance (R_C) as a function of V_{GS}, using a slope instead of a y-intercept in the calculation.[29]

$$\frac{R_{TOT}W}{L} = \frac{1}{\mu C_i(V_{GS}-V_T)} + R_C W \frac{1}{L} \quad (4.1)$$

To calculate the total resistance (R_{TOT}) we used the inverse slope of the output curve in the linear region for each L and V_{GS}.

$$R_{TOT} = \frac{dV_{DS}}{dI_{DS}}\Big|_{linear\ region} \quad (4.2)$$

Figure 4.12 shows an example plot of $\frac{R_{TOT}W}{L}$vs $\frac{1}{L}$ at V_{GS} = 15 V, and the resulting graph of R_C vs V_{GS}, where the R^2 for the linear best fit of $\frac{R_{TOT}W}{L}$vs $\frac{1}{L}$ was at least 0.97 for all V_{GS}.

There are many models that account for contact resistance in the extraction of field-effect mobility. One model, demonstrated in Equation (4.3), assumes that μ is constant with V_{GS} for simplicity: [2]

$$\mu_{app} = \mu_0(1 - \frac{\mu_o C_i \alpha}{L}) \quad (4.3)$$

By plotting apparent mobility (μ_{app}) against $\frac{1}{L}$ the parameters μ_0 and α can be determined, with the former representing an estimate for contact resistance free mobility. This method obtains a single $\mu_0$for each set of devices.

Another method to estimate corrected mobility uses equation (4.4), where I_{DS} is adjusted at a given L for each V_{GS} within the range R_{TOT} and R_C are obtained (ie $V_{GS} > V_T$). This works as long as for R_{TOT} and R_C are positive values with $R_{TOT} > R_C$, and requires data to be interpolated between the discrete output curve V_{GS} values to apply to transfer curve data.

$$I'_{DS}(L,V_{GS}) = I_{DS}(L,V_{GS})\frac{R_{TOT}(L,V_{GS})}{R_{CH}(L,V_{GS})} = I_{DS}(L,V_{GS})\frac{R_{TOT}(L,V_{GS})}{R_{TOT}(L,V_{GS})-R_C(V_{GS})} \quad (4.4)$$

The slope of the square root of I'_{DS} is proportional to the corrected saturation mobility for each device, which could be measured as a function of V_{GS} if the analytical region is varied.

For the set of devices using material **2** shown in Figure 4.7, equation (4.3) estimated μ_0 = 0.42 $cm^2V^{-1}s^{-1}$ and equation (4.4) obtained values between 0.31 $cm^2V^{-1}s^{-1}$ and 0.78 $cm^2V^{-1}s^{-1}$ (averaging 0.53 $cm^2V^{-1}s^{-1}$) when analyzing the same V_{GS} region as used in the uncorrected mobility calculations. Equation (4.3) estimated μ_0 = 0.025 $cm^2V^{-1}s^{-1}$ for the set of devices using material **1** shown in **Figure 4.7**, while equation (4.4) had little impact due to $R_{TOT} >> R_C$ in most cases.

4.7.3 Unity Current Gain Frequency

The unity current gain frequency (f_T) was calculated as the ratio of the transconductance (g_m) to the gate capacitance (C_G). It is a function of V_{GS}, V_T, μ_e, and L.

$$f_T = \frac{g_m}{2\pi C_G} = \frac{\mu_e(V_{GS}-V_T)}{2\pi L^2} \quad (4.5)$$

4.8 References

(1) Lin, P.; Yan, F. Organic Thin-Film Transistors for Chemical and Biological Sensing. *Adv. Mater.* **2012**, *24* (1), 34–51.

(2) Gelinck, B. G.; Heremans, P.; Nomoto, K.; Anthopoulos, T. D. Organic Transistors in Optical Displays and Microelectronic Applications. *Adv. Mater.* **2010**, *22* (34), 3778–3798.

(3) Tixier-mita, A.; Ihida, S.; Ségard, B.; Cathcart, G. A.; Takahashi, T.; Fujita, H.; Toshiyoshi, H. Review on Thin-Film Transistor Technology , Its Applications , and Possible New Applications to Biological Cells. *Jpn. J. Appl. Phys.* **2016**, *55* (4S), 04EA08.

(4) Gsänger, M.; Bialas, D.; Huang, L.; Stolte, M.; Würthner, F. Organic Semiconductors Based on Dyes and Color Pigments. *Adv. Mater.* **2016**, *28* (19), 3615–3645.

(5) Zhang, Y.; Lovell, J. F. Recent Applications of Phthalocyanines and Naphthalocyanines for Imaging and Therapy. *WIREs Nanomed Nanobiotechnol.* **2017**, *9* (1), e1420.

(6) Sorokin, A. B. Phthalocyanine Metal Complexes in Catalysis. *Chem. Rev.* **2013**, *113* (10), 8152–8191.

(7) Rand, B. P.; Cheyns, D.; Vasseur, K.; Giebink, N. C.; Mothy, S.; Yi, Y.; Coropceanu, V.; Beljonne, D.; Cornil, J.; Brédas, J.; et al. The Impact of Molecular Orientation on the Photovoltaic Properties of a Phthalocyanine / Fullerene Heterojunction. *Adv. Funct. Mater.* **2012**, *22* (14), 2987–2995.

(8) Torre, G. De; Bottari, G.; Torres, T. Phthalocyanines and Subphthalocyanines : Perfect Partners for Fullerenes and Carbon Nanotubes in Molecular Photovoltaics. *Adv. Energy Mater.* **2017**, *7* (10), 1–21.

(9) Melville, O. A.; Lessard, B. H.; Bender, T. P. Phthalocyanine-Based Organic Thin-Film Transistors: A Review of Recent Advances. *ACS Appl. Mater. Interfaces.* **2015**, *7* (24), 13105–13118.

(10) Li, L.; Tang, Q.; Li, H.; Yang, X.; Hu, W.; Song, Y.; Shuai, Z.; Xu, W.; Liu, Y.; Zhu, D. An Ultra Closely Π-Stacked Organic Semiconductor for High Performance Field-Effect Transistors. *Adv. Mater.* **2007**, *19* (18), 2613–2617.

(11) Kong, X.; Zhang, X.; Gao, D.; Qi, D.; Chen, Y.; Jiang, J. Air-Stable Ambipolar Field-Effect Transistor Based on a Solution-Processed Octanaphthoxy-Substituted Tris(Phthalocyaninato) Europium Semiconductor with High and Balanced Carrier Mobilities. *Chem. Sci.* **2015**, *6*, 1967–1972.

(12) Shao, X.; Wang, S.; Li, X.; Su, Z.; Chen, Y.; Xiao, Y. Single Component P- , Ambipolar and n-Type OTFTs Based on Fluorinated Copper Phthalocyanines. *Dyes Pigm.* **2016**, *132*, 378–386.

(13) Huang, L.; Yu, B.; Song, D.; Geng, Y.; Zhu, F.; Yan, D. Tin (IV) Phthalocyanine Oxide: An Air-Stable Semiconductor with High Electron Mobility. *Appl. Phys. Lett.* **2008**, *92* (14), 143303.

(14) Lessard, B. H.; Grant, T. M.; White, R.; Thibau, E.; Lu, Z.; Bender, T. P. The Position and Frequency of Fluorine Atoms Changes the Electron Donor/Acceptor Properties of Fluorophenoxy Silicon Phthalocyanines within Organic Photovoltaic Devices. *J. Mater. Chem. A.* **2015**, *3* (48), 24512–24524.

(15) Lessard, B. H.; White, R. T.; Al-amar, M.; Plint, T.; Castrucci, S.; Josey, D. S.; Lu, Z.; Bender, T. P. Assessing the Potential Roles of Silicon and Germanium Phthalocyanines in Planar Heterojunction Organic Photovoltaic Devices and How Pentafluoro Phenoxylation Can Enhance $\pi - \pi$ Interactions and Device Performance. *ACS Appl. Mater. Interfaces.* **2015**, *7* (9), 5076–5068.

(16) Lessard, B. H.; Lough, J.; Bender, T. P. Crystal Structures of Bis (Phenoxy) Silicon Phthalocyanines: Increasing π-π Interactions, Solubility and Disorder and No Halogen Bonding Observed. *Acta Cryst.* **2016**, *E72* (7), 988–994.

(17) Gali, S. M.; Matta, M.; Muccioli, L. Ambipolarity and Dimensionality of Charge Transport in Crystalline Group 14 Phthalocyanines: A Computational Study. *J. Phys. Chem. C* **2018**, *122* (5), 2554–2563.

(18) Melville, O. A.; Grant, T. M.; Lessard, B. H. Silicon Phthalocyanines as N-Type Semiconductors in Organic Thin Film Transistors. *J. Mater. Chem. C.* **2018**, *6* (20), 5482–5488.

(19) Schmidt, R.; Oh, J. H.; Sun, Y.; Deppisch, M.; Krause, A.-M.; Radacki, K.; Braunschweig, H.; Konemann, M.; Erk, P.; Bao, Z.; et al. High-Performance Air-Stable n-Channel Organic Thin Film Transistors Based on Halogenated Perylene Bisimide Semiconductors. *J. Am. Chem. Soc.* **2009**, *131* (17), 6215–6228.

(20) Pietro, R. Di; Fazzi, D.; Kehoe, T. B.; Sirringhaus, H. Spectroscopic Investigation of Oxygen- and Water-Induced Electron Trapping and Charge Transport Instabilities in n‐Type Polymer Semiconductors. *J. Am. Chem. Soc.* **2012**, *134* (36), 14877–14889.

(21) Zschieschang, U.; Amsharov, K.; Jansen, M.; Kern, K.; Klauk, H.; Weitz, R. T. Separating the Impact of Oxygen and Water on the Long-Term Stability of n-Channel Perylene Diimide Thin-Film Transistors. *Org. Electron.* **2015**, *26*, 340–344.

(22) Toney, M. F.; Nordlund, D.; Oh, J. H.; Sun, Y.; Frank, W.; Schmidt, R.; Wurther, F.; Bao, Z. Interplay between Energetic and Kinetic Factors on the Ambient Stability of N-Channel Organic Transistors Based on Perylene Diimide Derivatives. *Chem. Mater.* **2009**, *21* (3), 5508–5518.

(23) Aguirre, B. C. M.; Levesque, P. L.; Paillet, M.; St-antoine, B. C.; Desjardins, P.; Martel, R. The Role of the Oxygen / Water Redox Couple in Suppressing Electron Conduction in Field-Effect Transistors. *Adv. Mater.* **2009**, *2* (21), 3087–3091.

(24) Rice, N. A.; Bodnaryk, W. J.; Mirka, B.; Melville, O. A.; Adronov, A.; Lessard, B. H. Polycarbazole-Sorted Semiconducting Single-Walled Carbon Nanotubes for Incorporation into Organic Thin Film Transistors. *Adv. Electron. Mater.* **2018**, 1800539.

(25) Wang, H.; Zhu, F.; Yang, J.; Geng, Y.; Yan, D. Weak Epitaxy Growth Affording High-Mobility Thin Films of Disk-Like Organic Semiconductors. *Adv. Mater.* **2007**, *19* (16), 2168–2171.

(26) Melville, O. A.; Rice, N. A.; Therrien, I.; Lessard, B. H. Dyes and Pigments Organic Thin-Fi Lm Transistors Incorporating a Commercial Pigment (Hostasol Red GG) as a Low-Cost Semiconductor. *Dyes Pigm.* **2018**, *149* (October 2017), 449–455.

(27) Gu, W.; Hu, Y.; Zhu, Z.; Liu, N.; Zhang, J.; Wang, J. Preparing Highly Ordered Copper Phthalocyanine Thin-Film by Controlling the Thickness of the Modified Layer and Its Application in Organic Transistors. *Solid-State Electron.* **2013**, *89*, 101–104.

(28) Zaumseil, J.; Baldwin, K. W.; Rogers, J. A.; Zaumseil, J.; Baldwin, K. W.; Rogers, J. A. Contact Resistance in Organic Transistors That Use Source and Drain Electrodes Formed by Soft Contact Lamination Contact Resistance in Organic Transistors That Use Source and Drain Electrodes Formed by Soft Contact Lamination. *J. Appl. Phys.* **2010**, *93* (10), 6117–6124.

(29) Xu, Y.; Gwoziecki, R.; Chartier, I.; Coppard, R.; Balestra, F.; Ghibaudo, G. Modified Transmission-Line Method for Contact Resistance Extraction in Organic Field-Effect Transistors. *Appl. Phys. Lett.* **2010**, *97* (6), 171.

(30) Sirringhaus, B. H. Reliability of Organic Field-Effect Transistors. *Adv. Mater.* **2009**, *21*

(38–39), 3859–3873.

(31) Rice, N.; Magnan, F.; Melville, O.; Brusso, J.; Lessard, B. Organic Thin Film Transistors Incorporating Solution Processable Thieno [3, 2-b] Thiophene Thienoacenes. *Materials (Basel).* **2018**, *11* (1), 8.

(32) Brixi, S.; Melville, O. A.; Boileau, N. T.; Lessard, B. H. The Influence of Air and Temperature on the Performance of PBDB-T and P3HT in Organic Thin Film Transistors. *J. Mater. Chem. C.* **2018**, *6*, 11972–11979.

(33) Kerp, H. R.; Westerduin, K. T.; van Veen, A. T.; Faassen, E. E. Quantification and Effects of Molecular Oxygen and Water in Zinc Phthalocyanine Layers. *J. Mater. Res.* **2001**, *16* (2), 503–511.

(34) Takeya, K.; Yohda, H.; Kojima, K.; Yasunaga, H. Effect of Oxygen on Electrical Properties of Lead Phthalocyanine. *J. Phys. Soc. Japan* **1974**, *37* (4), 1024–1030.

(35) Torricelli, F.; Kovács-vajna, Z. M.; Colalongo, L. The Role of the Density of States on the Hole Mobility of Disordered Organic Semiconductors. *Org. Electron.* **2009**, *10* (5), 1037–1040.

(36) Lowery, M. K.; Starshak, A. J.; Esposito, J. N.; Krueger, P. C.; Kenney, M. E. Dichloro(Phthalocyanino)Silicon. *Inorg. Chem.* **1965**, *4* (1), 128.

Chapter 5 - Contact Engineering Using Manganese, Chromium and Bathocuproine in Group XIV Phthalocyanine Organic Thin-Film Transistors

5.1 Preamble

This section describes the context in which the research was performed, relating it to the development of the lab and my own research goals at the time. It describes the contributions of each author and the significance of the research. This paper is still in preparation. We are currently waiting for UPS data to determine HOMO/LUMO levels and for potential explanations for the improved injection with the different interlayers. Also, molecular characterization is still ongoing, but EA and MS results strongly indicate the SnPcs have the expected formulae. The paper is mostly complete, but this additional data will help with details for the final publication.

5.1.1 Context

With a large Schottky barrier and contact resistance reducing the performance of BGBC devices from the previous study, I wanted to move to a TC architecture to reduce R_C and to control more of the device fabrication. Although this created new challenges, characterization was facilitated by hardware obtained from Ossila that makes contact with 20 devices on a single chip at once. I altered the LabView programs to work with the new hardware and we were able to fabricate and test more devices and conditions than before. I wanted to do structure-function comparison between analogous materials while working with interlayers between the metal electrode and organic semiconductor to reduce contact resistance and improve performance.

5.1.2 Contribution of Authors

I designed all OTFT experiments. I fabricated and characterized all devices with assistance from Benjamin King. I performed all electrical analysis, including writing a new program to measure contact resistance. I wrote all sections of the manuscript in its current form except the parts of the experimental section pertaining to synthesis.

Trevor Grant synthesized some of the materials and performed analytic studies on them including IR spectroscopy. With supervision from Trevor Grant, Kate Lochhead synthesized and characterized all four compounds used in the study, performed solution UV-Vis characterization, and wrote parts of the experimental section. Benjamin King assisted with device fabrication, characterization, and solid state UV-Vis characterization. Nicolas Boileau helped with setting up the "autotester" characterization equipment that facilitated testing so many OTFTs. Dr. Rice helped edit the paper and provided suggestions during writing. Mathieu Tousignant and Alexander Peltekoff helped with characterizing the substrates in terms of capacitive behaviour.

5.1.3 Significance

This paper demonstrated the first use of SiPcs in top contact OTFTs. The hypothesis that a metal interlayer (Cr or Mn) or a non-metal electron transport material (BCP) could improve charge injection between Au or Ag electrodes and n-type SiPc OSCs was tested and held true. The linear region characteristics, threshold voltage, and contact resistance all improved for SiPcs, especially F_{10}-SiPc. R_C was notably low in devices with Mn electrode interlayers, averaging about 12 kΩcm, which was lower than values obtained using other interlayers and n-type OSCs in a 2015 review (32-300 kΩcm).[1] Ambipolar 246F-SiPc was found to have both its electron and hole accumulation characteristics modulated in accordance with hypothesis. I also conducted these studies with analogous SnPcs that were synthesized by Kate Lochhead to see how their performance compared to that of the SiPcs. Although the SnPcs generally performed worse than their SiPc analogues in OTFTs, the F_{10}-SnPc devices had a strong increase in off current when BCP was used to cover the entire OSC, indicating doping. This interaction could be further explored to determine sensing capabilities of the SnPc derivatives. In general, the ideality of device output in this paper is much higher than in the previous two, demonstrating a step-up in terms of OTFT fabrication process using the more complex BGTC architecture.

The rest of the following chapter contains unpublished material.

Abstract

Silicon and tin (IV) phthalocyanines, which have been demonstrated as simple to synthesize n-type materials in organic thin-film transistors (OTFTs), have relatively shallow lowest unoccupied molecular orbital (LUMO) levels that create a Schottky barrier with the gold source-drain contacts typically used in device fabrication. To reduce the contact resistance (R_C) associated with this barrier and improve OTFT performance, we fabricated bottom gate, top contact (BGTC) devices using low work function metals (Mn/Cr) and an electron dopant material (bathocuproine, BCP) as contact interlayers. We characterized two novel tin phthalocyanines (SnPcs), tin bis(pentafluorophenoxy) phthalocyanine (F_{10}-SnPc) and tin bis(2,4,6-trifluorophenoxy) phthalocyanine (246F-SnPc), as organic semiconductors (OSCs) and compared them to their silicon analogues. We found that using Mn and Cr interlayers with SiPc OTFTs reduces R_C to as low as 11.8 kΩcm and reduces threshold voltage (V_T) to as low as 7.8 V while improving linear region mobility compared to devices using silver or gold electrodes only. BCP interlayers appear to reduce V_T in all SiPc and SnPc devices and increase the off-state conductivity of SnPc devices if covering the entire OSC. Overall, this work demonstrates the potential for metal interlayers and solid state organic interlayers for improving electron transport in low-cost, n-type OTFTs using group XIV phthalocyanines.

5.2 Introduction

Organic thin-film transistors (OTFTs) continue to demonstrate potential for use in chemical and biological sensing, high throughput circuit fabrication and printed electronics amongst other applications. Although considerable progress in OTFT development has been made in the past two decades, attention to reporting high field-effect mobility (μ) has sometimes eclipsed more practical aspects of device design such as low voltage operation and synthetic simplicity. For n-type organic semiconducting materials (OSCs), which are less frequently studied and which often demonstrate inferior performance compared to their p-type organic counterparts, high threshold voltages (V_T) and contact resistance (R_C) may limit their usefulness for practical applications.

Silicon and tin phthalocyanines (SiPcs and SnPcs) are two groups of n-type OSCs that have successfully been incorporated into OTFTs, demonstrating reasonable electron field-effect mobilities (μ_e) above 0.1 $cm^2V^{-1}s^{-1}$ for a few materials.[2–4] Figure 5.1 shows the basic structure of Si and Sn(IV) based Pcs, with two axial –R groups that provide a synthetic handle for changing the molecular structure and therefore its solid-state packing and energetics. This axial substituent affects OTFT performance using SiPc OSCs,[4,5] with **1** demonstrating the best performance to date, with an R_C-adjusted average μ_e of 0.19 $cm^2V^{-1}s^{-1}$ (up to 0.54 $cm^2V^{-1}s^{-1}$) and a V_T of 12 V when deposited on heated substrates in bottom gate, bottom contact (BGBC) architecture. Both the base molecule with dichloro axial groups and its substituted phenol derivatives are straightforward to synthesize and purify with sublimation, making large-scale production viable. Despite presenting these synthetic advantages and promising performance, both SiPcs and SnPcs suffer from a number of drawbacks in OTFTs typical for n-type OSCs. In particular, high V_T for SnPc devices (> 27 V)[3] and large R_C for SiPc devices (~10^4 kΩcm)[4] limit their present utility.

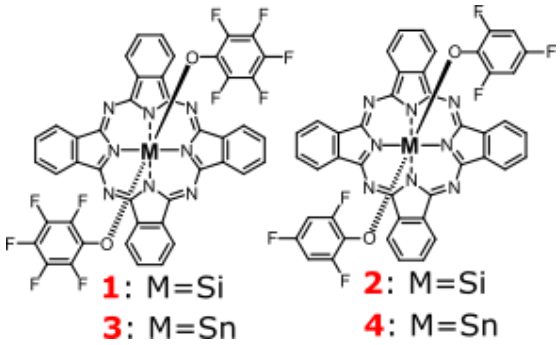

Figure 5.1: Schematic diagram of axially substituted silicon and tin(IV) phthalocyanines: **1**) F_{10}-SiPc; **2**) 246F-SiPc; **3**) F_{10}-SnPc; **4**) 246F-SnPc

Improving the interface between the source-drain electrodes and OSC has been identified as an important area for improving OTFT performance and reliability.[1] R_C, which is particularly significant at low channel lengths and with bottom contact architecture, can significantly affect the measurement of μ, either increasing or decreasing its apparent value.[6,7] Different approaches can be used to reduce R_C and obtain more intrinsic values of μ, addressing either the geometric or energetic causes of the resistance. Figure 5.2 shows bottom-gate, top-contact (BGTC) device architecture, which reduces R_C compared to bottom contact by increasing the charge injection area and eliminating the possibility of incomplete deposition in the channel during OSC deposition.[8] The energetic sources of R_C are the potential difference between the conductive frontier molecular orbital of the OSC (HOMO, for holes; LUMO, for electrons) and the work function of the source-drain electrodes, the interfacial dipole created from the adjacent materials, and charge traps near the metal-OSC interface.[9]

To reduce the injection barrier between the OSC and contacts, different strategies have been adopted depending on the majority charge carrier and device geometry.[1] For p-type materials, the goal is typically to deepen the work function of a cost-effective alternative to Au[10,11] or to counteract Fermi level pinning that can create an injection barrier with the OSC regardless of metal work function.[9] This can involve using a deep work function metal such as palladium,[12] incorporating a p-dopant, hole transport interlayer such as metal oxides like MoO_3[11,13,14] or organic materials like N,N′-Bis(3-methylphenyl)-N,N′-diphenylbenzidine (TPD)[10] or copper phthalocyanine (CuPc),[15] or modifying the contacts with a fluorinated SAM such as 1H,1H,2H,2H-perfluorodecanethiol (PFDT).[16–18] For the less-studied category of n-type materials, the injection barrier can be lowered by exposing the devices to electron dopants such as amines after fabrication,[19] by utilizing an electron injection/dopant interlayer such as a cesium salt,[20] or by modifying bottom-contact electrodes with an alkylthiol SAM.[16] It is also possible to replace the inorganic contact with an organic metal, forming a better interface with the OSC.[21] The work function of organic metals can be tuned through varying their chemical structure, making them suitable for n or p-type OSCs.

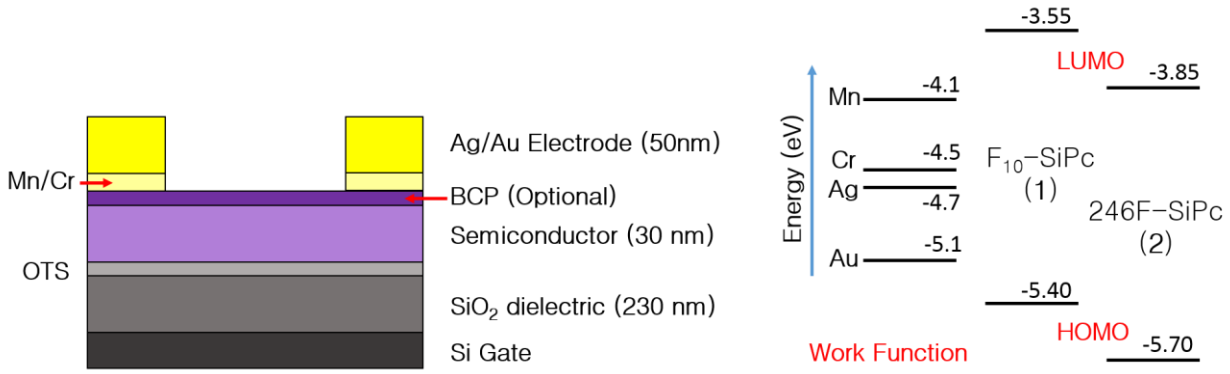

Figure 5.2: *Left*: Device schematic for bottom-gate, top-contact (BGTC) OTFTs with either an electron transport (BCP) or low work function metal (Mn/Cr) interlayer between the main electrode (Ag/Au) and organic semiconductor (OSC). *Right*: Energy level diagram for metal and organic components. LUMO/HOMO energies are taken from literature sources.[22]

For this study, the contact interlayer strategy was implemented with thin films of low work-function metal (Cr, Mn) or organic semiconductor (bathocuproine, BCP) deposited in between the n-type OSCs in Figure 5.1 and the high work-function contact (Au, Ag). As demonstrated in Figure 5.2, the reported LUMO levels of the OSCs range between -3.55 and -3.85 eV, significantly closer to the work function of Mn or Cr than Au. Mn has rarely been used as an electrode for OTFTs, perhaps due to its relatively low conductivity. Using Mn and Cr, chosen for its intermediate work function, as interlayers to the highly conductive Au and Ag might reduce the injection barrier and therefore contact resistance, improving OTFT performance. An alternative interlayer to reduce R_C is bathocuproine (BCP), a small organic molecule often used an electron transport layer in organic photovoltaics. This work presents the synthesis of two novel SnPcs and characterizes bottom-gate top-contact (BGTC) OTFTs made using these materials and their SiPc analogues as the active semiconducting layer. To improve device performance, the addition of Mn, Cr and BCP interlayers between the OSC and Au/Ag electrodes are investigated for each material.

5.3 Discussion

5.3.1 Synthesis of Tin Phthalocyanines

Synthesis for SnPcs **3**-**4** is described in the experimental section. The products were insoluble, blue-green powders that were purified using train sublimation. Due to lack of solubility, NMR could not be used to characterize the materials, and single crystals did not form from solution or sublimation to characterize them using single crystal x-ray diffraction. Mass spectrometry (MS) confirmed SnPc fragments with a single axial substituent but not both. As sometimes the full molecule is not detected in MS, elemental analysis (EA) was used on the purified powders to confirm the ratio of elements. C, N, and H percentages were all between 0.05 and 0.83% of the expected values for the di-substituted molecules, reinforcing that molecular structures **3** and **4** were obtained.

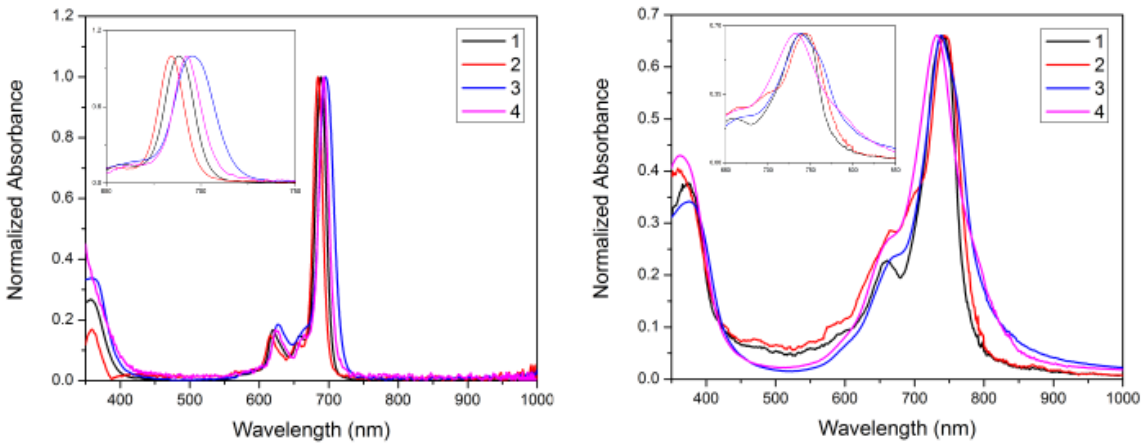

Figure 5.3: Normalized UV-Vis data for solution (left) and solid-state deposited on glass (right) for compounds **1**-**4** with insets on peak absorbance regions

All materials **1**-**4** were characterized by UV-Vis in solution and in thin films deposited on glass. Figure 5.3 summarizes the resulting spectra. The peak absorbance of the SnPcs is redshifted compared to the SiPcs in solution, and the optical band gap is slightly lower. For both central metals, the pentafluorophenoxy-substituted molecule (**1**, **3**) had slightly red-shifted peak absorbance compared to the partially-fluorinated molecule (**2**, **4**). In solid-state, all molecules show a broadened absorption indicative of solid-state interactions. Optical gap (E_g) for **1**-**4** are summarized in Table 5.1.

Material	Eg (eV)
F_{10}-SiPc	1.8
246F-SiPc	1.8
F_{10}-SnPc	1.7
246F-SnPc	1.7

Table 5.1: Optical gap data for OSCS **1-4**.

5.3.2 Organic Field-Effect Transistors

Bottom-gate, top-contact (BGTC) OTFTs were fabricated using materials **1-4** as OSCs, using both silver and gold source-drain (SD) electrodes and either Cr, Mn and BCP interlayers between the OSC and the electrodes (Au, Ag). The top contact configuration and the interlayers were both selected to improve the interface between the OSC and metal contact, potentially improving the electrical properties of the resulting devices. For simplicity, all physical vapor deposition (PVD) of OSCs was done at room temperature and devices were not annealed. The electrical performance differences between devices will be discussed on a material-by-material bias in the following sections.

5.3.2.1 OTFTs using F_{10}-SiPc:

F_{10}-SiPc (**1**) has previously been reported in bottom-gate, bottom-contact (BGBC) OTFTs, typically demonstrating ambipolar performance with weak hole transport and μ_e up to 0.54 $cm^2V^{-1}s^{-1}$ and V_T of 12 V when the active layer was deposited at 140 °C. Device performance varied significantly with channel length due to the substantial contact resistance (R_C ~10^4 kΩcm) often associated with BC devices and large injection barriers. Table 5.5 (SI) summarizes the performance of OTFTs using **1** as the OSC with the TC architecture and either Cr, Mn or BCP interlayers with Ag or Au electrodes. As shown in Figure 4 (left), resulting average saturation μ_e ranged between 0.09 and 0.27 $cm^2V^{-1}s^{-1}$ for all electrode combinations without requiring the high substrate temperature during deposition. As shown in Figure 4 (right), average V_T varied between 7.8 and 28.7 V for an operating V_{GS} range of 0 V to 60 V.

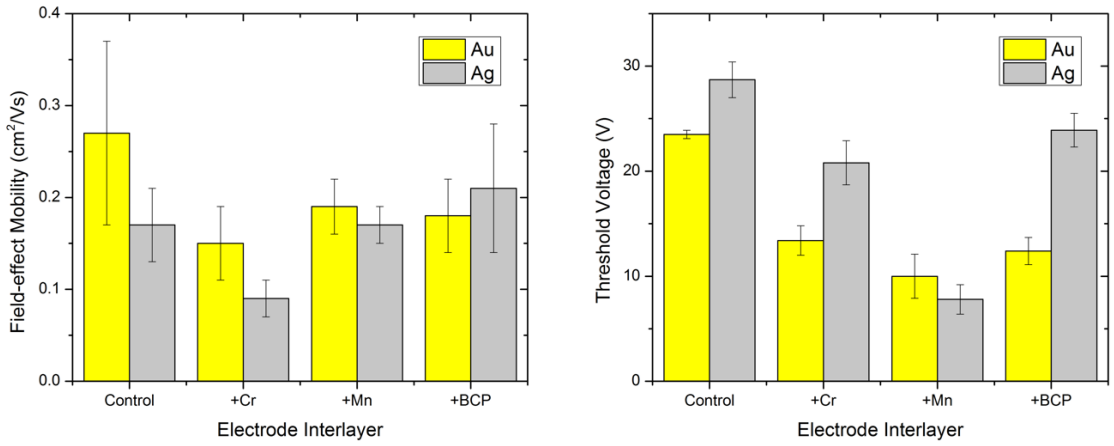

Figure 5.4: Saturation region properties for OTFTs using F_{10}-SiPc (**1**) as the OSC and with Au and Ag electrodes and Cr, Mn or BCP interlayers: Left) field-effect mobility; Right) threshold voltage. Error bars are standard deviations where $18 \leq n \leq 20$ devices.

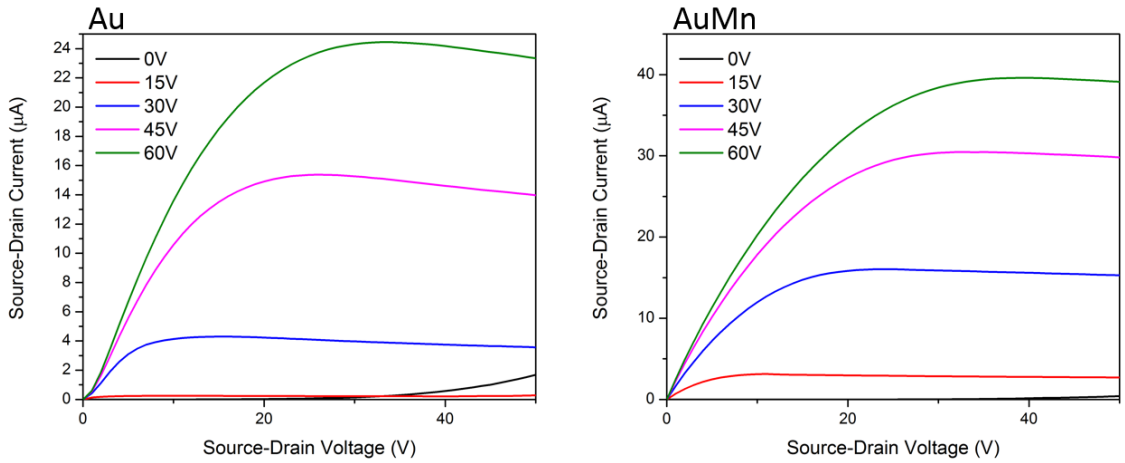

Figure 5.5: Output curves for OTFTs using F_{10}-SiPc (**1**) as the OSC and with Au contacts with and without a 10 nm Mn interlayer.

Figure 5.5 shows two typical output curves for OTFTs using **1**, one with 50 nm Au SD electrodes and one with Au SD electrodes with a 10 nm Mn interlayer (AuMn). Several qualitative differences can be observed when comparing the curves. First, the linear region of AuMn OTFTs extends straight from the origin without the change in concavity seen in the Au devices, indicating a more Ohmic contact. Second, the saturation characteristics of the AuMn devices are improved and there is less of an increase of I_{DS} with V_{DS} at $V_{GS} = 0$ V, indicating a suppression of minority

hole transport. Third, the V_T of the AuMn device appears to be reduced, with noticeable current at V_{GS} = 15 V. These qualitative differences were also observed for devices using Cr and BCP and with Ag main electrodes.

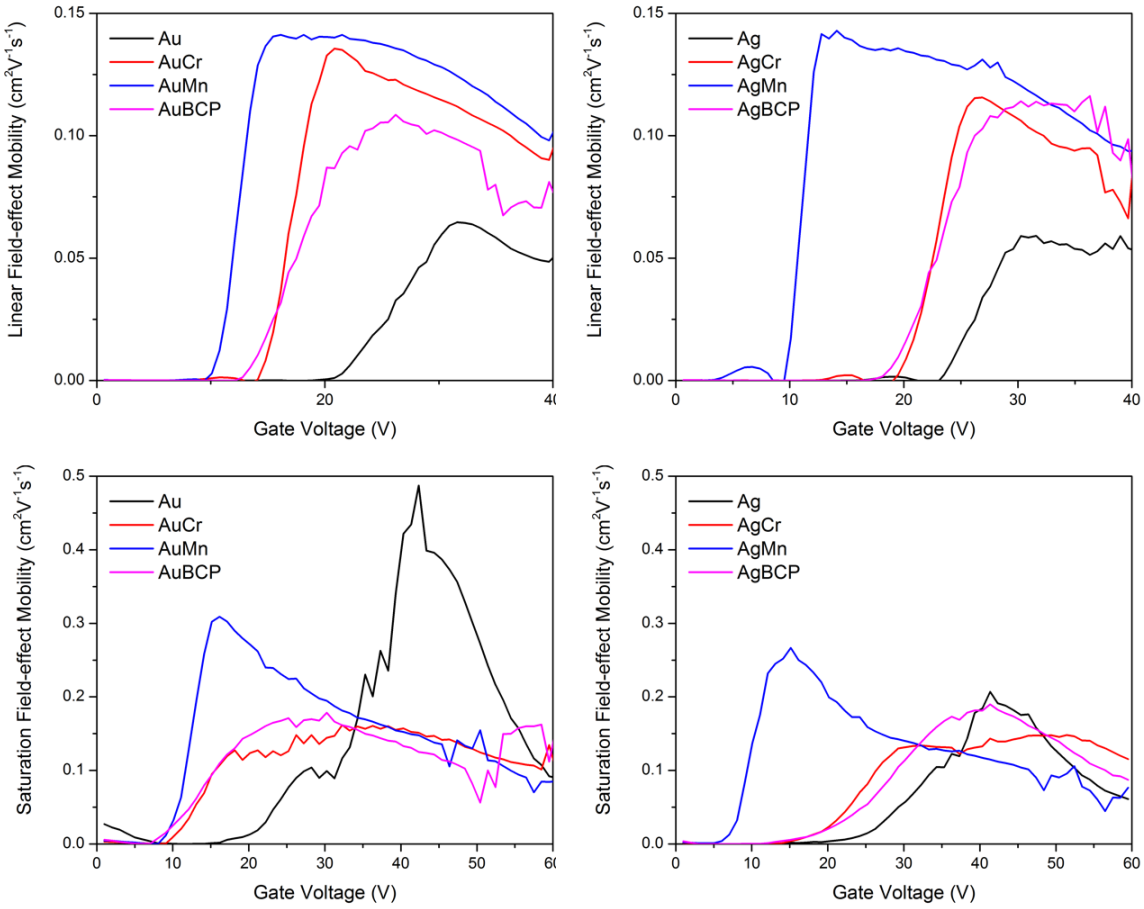

Figure 5.6: Field-effect mobility in the linear and saturation region as a function of gate voltage for devices using **1** as the OSC with average characteristics. Obtained from the derivative of the transfer curves.

This reduction in V_T using the three interlayers can be observed in Figure 5.4 (right) and also Figure 5.6, where mobility as a function of V_{GS} [$\mu(V_{GS})$] shifts towards zero. This more comprehensive view of the change in polarization can be seen in both the linear and saturation characteristics. Current increases at lower V_{GS} for Mn devices compared to Cr and BCP, which are similar, and occur at highest V_{GS} for Ag and Au controls. The mechanisms for this improved polarization using interlayers could benefit from further investigation, but it is likely different for non-metallic BCP compared to the other interlayers. The improved performance of Mn-containing

devices over the controls and those with Cr could be due to its lower work function which better matches the LUMO of **1** (Figure 5.2). This hypothesis does not hold true for Ag devices, which showed higher V_T than for Au, despite its lower work function. Wang et. al. demonstrated that for pentacene transistors, the injection barrier with the metal was not as important as the trap density at the interface between the electrode and OSC,[23] providing a possible explanation for the general inferior performance of Ag electrodes despite their more matching work function. Although in general worse than Au, Ag devices with Mn interlayers had the lowest average V_T of 7.8 V, indicating that low cost electrodes could be implemented in devices without compromising device performance.

Electrode	μ_e (lin) ($cm^2V^{-1}s^{-1}$)	V_T (V)	μ_0 ($cm^2V^{-1}s^{-1}$)	θ	R_CW (kΩcm)
Au	0.06±0.01	24.4±1.1	0.09±0.02	0.028±0.009	61.3±25.9
AuCr	0.13±0.03	15.5±1.6	0.15±0.04	0.013±0.005	18.1±7.8
AuMn	0.14±0.02	11.4±1.9	0.18±0.02	0.010±0.002	11.8±3.4
AuBCP	0.10±0.02	16.9±1.0	0.13±0.04	0.012±0.007	16.6±7.5
Ag	0.06±0.01	25.2±0.8	0.07±0.02	0.021±0.005	57.9±14.4
AgCr	0.11±0.03	22.9±1.0	0.14±0.05	0.018±0.009	26.3±8.4
AgMn	0.14±0.01	10.4±1.4	0.16±0.01	0.010±0.001	12.2±1.9
AgBCP	0.10±0.03	23.3±1.7	0.09±0.02	0.010±0.004	25.8±14.7

Table 5.2: Average contact resistance normalized to width (R_CW, W = 1000 μm) with fitting parameters θ and μ_0 for OTFTs using F_{10}-SiPc (**1**) as the OSC with different electrodes. ± Standard deviation for all values

The improvement in the linear region observed in Figure 5.4 is significant because it requires less power to operate devices in the linear region. Despite this, OTFT performance is often reported in the saturation region, where power consumption and required bias is much higher. The linear region characteristics for **1** devices are reported in Table 5.2. In general, they are similar to the saturation characteristics to within error, except for the Ag and Au control devices that seem to have considerably lower μ_e, indicating high contact resistance (R_C). Contact resistance creates difficulties extracting parameters such as V_T and μ, causing deviation from Equations 1.3-1.4 used

to calculate them.[6] If R_C decreases substantially with V_{GS}, this can cause an apparent increase in μ which stems from the R_C reduction rather than injection of charges from polarization. This change, which was observed in BC devices for **1**, can also be seen in the graph of μ_{sat} with V_{GS} for Au devices in Figure 5.6, which increases and then decreases sharply between 30 V < V_{GS} < 60 V. Devices with interlayers have a much more step-edge like shape, especially in the linear region, indicating good adherence to the MOSFET equations.

To confirm that differences in R_C are responsible for these changes in performance, two methods were utilized. The transmission line method (TLM) required large channel lengths (30-80 μm) for the TC devices used in this study due to the limitations of using shadow masks, much higher than for the BC devices in the previous study that were prefabricated using photolithography (2.5 – 20 μm). This led to poor adherence to the TLM and mTLM equations and difficulty obtaining consistent and realistic values. The Y-function method (YFM) estimates R_C for individual OTFTs assuming that it does not vary with V_{GS}.[8] OTFTs using **1** fit the described model well as shown in Section 5.7.2 in the SI, with the results listed in Table 5.2. Width-normalized R_C was highest for the Ag and Au controls, around 60 kΩcm. This decreased significantly for all interlayers, with the lowest R_C in devices using Mn interlayers around 10 kΩcm. This is much lower than the 1x10^4 kΩcm for BGBC devices using **1** and considerably lower than the 32-300 kΩcm reported for interlayer modified n-type OTFTs in a 2015 review.[1] Thus, the combination of BGTC architecture and the use of a low work-function metallic interlayer (Mn, Cr) or organic electron transport interlayer (BCP) combined with stable, high conductivity contact (Ag, Au) improves electron injection from **1**, decreasing V_T and R_C improving linear region mobility.

5.3.2.2 OTFTs using 246F-SiPc

The more shallow HOMO level of 246-SiPc (**2**) compared to **1** increases its tendency to conduct holes, thus increasing its ambipolarity. Figure 5.4 in the SI summarizes OTFT characteristics for electron accumulation in all devices using **2**, while Figure 5.7 shows typical output curves for both hole and electron accumulation in devices with Au contacts. Hole injection is hindered compared to electron injection based on the quality of the linear region, and strong tailing at high V_{DS} and low V_{GS} can be seen for both outputs. Although the devices have lower

mobility than **1**, their hole transport characteristics are significant enough to measure with variation in the contact material and interlayer.

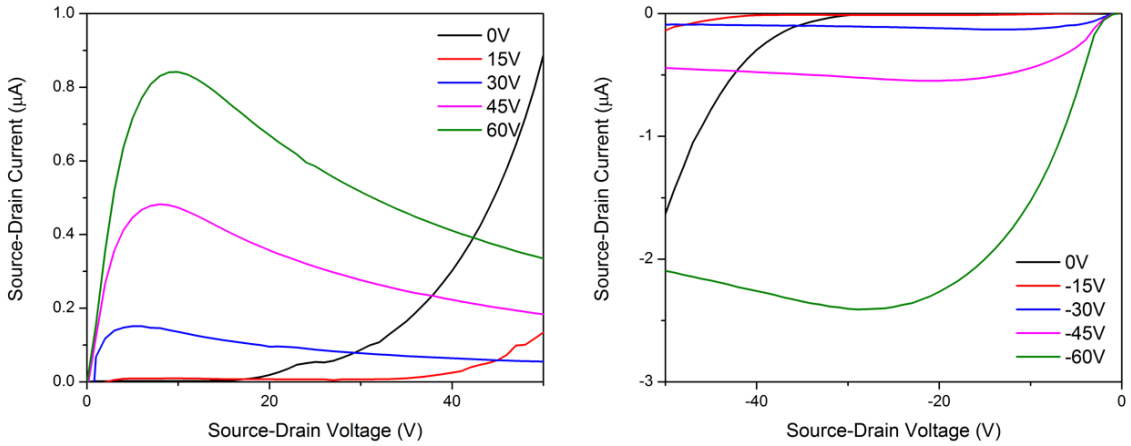

Figure 5.7: Output curves for 246F-SiPc (**2**) with Au contacts in electron (left) and hole (right) accumulation modes

In general, using BCP or a low work function metal as interlayers have the same effect on electron transport for **2** as **1**, although baseline device performance is lower in terms of both V_T and μ_e. Figure 5.8 shows the systematic decrease in V_T for electron accumulation when Mn, Cr or BCP are used as interlayers with Au contacts. On the other hand, hole injection is hindered by the addition of these interlayer components, with V_T systematically increasing. The energetic mismatch between the HOMO of the OSC and the work function of the adjacent metal in this case is increasing, while BCP may block hole injection. These results demonstrate that contact interlayers can be used to adjust the relative polarity of ambipolar SiPc OTFTs, suppressing or encouraging one type of transport over the other.

5.3.2.3 OTFTs using F_{10}-SnPc and 246F-SnPc OTFTs

SnPc devices were fabricated with each electrode configuration and characterized in nitrogen. Resulting devices had generally higher V_T, lower μ_e, and higher variance than the SiPc devices made under comparable conditions. OTFTs using **3** (Table 5.5, SI) had average μ_e ranging between 0.001 and 0.016 $cm^2v^{-1}s^{-1}$ and V_T ranging between 24.0 and 31.1 V. For OTFTs using **4** (Table 5.6, SI), μ_e ranged between 6.7 x 10^{-4} and 2.7 x 10^{-2} $cm^2v^{-1}s^{-1}$ and V_T ranged between 34.4

and 40.8 V. This relatively poor performance of the SnPcs compared to the analogous SiPcs could be due to a number of factors. The Sn-O bond is weaker than the Si-O bond, so it is possible the compounds degrade during thermal evaporation, creating impurities in the film. Since single crystals could not be obtained for **3**-**4**, their crystal structures cannot be compared to **1**-**2**.

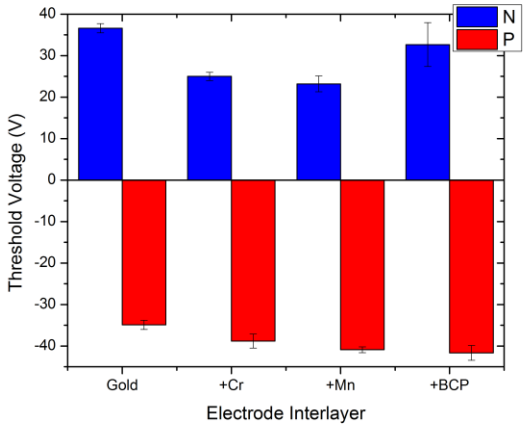

Figure 5.8: Threshold voltage for OTFTs using **2** as the OSC with Au contacts and Cr, Mn and BCP interlayers in e^- (blue) and h^+ (red) accumulation modes

Transfer curves for **3** are shown in Figure 5.8, and those for **4** are shown in Figure 5.12 (SI). For OTFTs using **3**, the addition of BCP increased the off current substantially. This zero-gate conductivity suggests that the presence of BCP dopes the OSC, and was seen for devices of **4** using Ag electrodes and a BCP interlayer as well. These devices had BCP, which is insulating, covering the entire film to simplify the fabrication process. To examine the apparent doping effect further, additional devices were fabricated where BCP was placed only between the contacts and the OSC in the cases where the off current increased. In each of these cases, μ_e was higher when BCP was only in the contact area, I_{OFF} was reduced to around 10^{-9} or 10^{-10} A, and V_T was 1.9 – 3.6 V lower than for control devices without BCP. The lower I_{OFF} compared to devices with BCP on the whole film indicates the doping effect is local, and the reduction in V_T compared to controls might be due to doping in the vicinity of the contacts that does not extend to the entire film. Output curves for AgBCP OTFTs using **3**-**4** are shown in Figure 5.13 in the SI. This increase in off current when BCP was deposited on the entire OSC film was not observed for SiPc devices, so it is possible that the larger Sn atom has a higher propensity for interaction with BCP than SiPc. Further

investigation is warranted to determine if this doping could be exploited to use SnPc-based devices as turn-on sensors for specific analytes that interact in the same way BCP does.

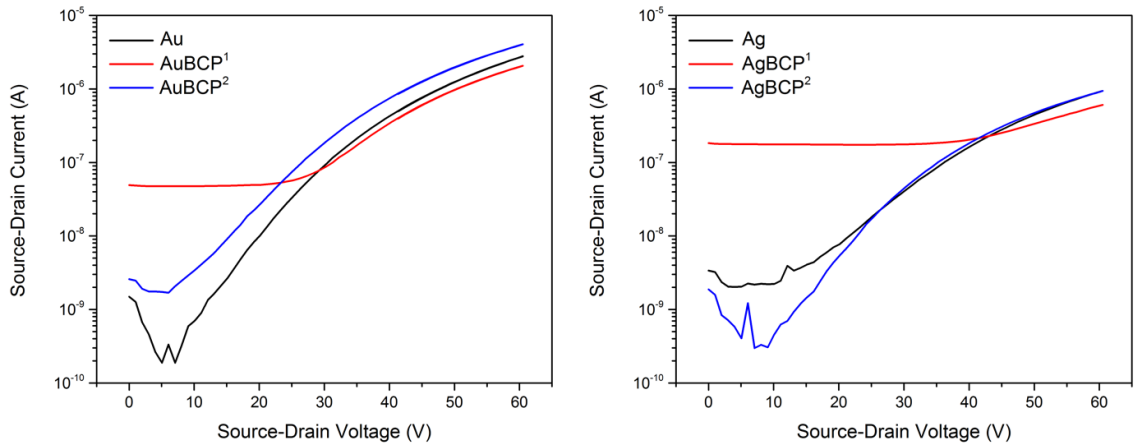

Figure 5.9: Transfer curves for OTFTs using F_{10}-SnPc (**3**) with average characteristics and different electrode combinations. *Notes: [1]BCP covered the entire OSC; [2]BCP covered only the electrode area of the OSC*

5.4 Conclusion

Top contact OTFTs using manganese, chromium, and bathocuproine as interlayers between high conductivity silver or gold electrodes and SiPc or SnPc semiconductors were fabricated and characterized. For F_{10}-SiPc (**1**), the best-performing of the OSCs, all three interlayers reduced threshold voltage, improved linear region mobility and reduced contact resistance. These results demonstrate the importance of contact engineering for n-type OSCs such as SiPcs, and suggest Ag electrodes with Mn interlayers can be used as a cost-effective and high-performance alternative to Au electrodes. Although the two novel SnPcs reported do not perform as well as their SiPc analogues, F_{10}-SnPc (**3**) in particular shows a strong tendency to increase off state conductivity in the presence of a bathocuproine (BCP) interlayer.

5.5 Experimental

5.5.1 Materials

All chemicals were used as purchased, without further purification. Chlorobenzene (99.5%) was purchased from Caledon Laboratories Ltd. Triethylamine (99.5%) and 2,4,6-trifluorophenol (99%) were obtained from Oakwood Chemicals. 2,3,4,5,6-pentafluorophenol (≥99.0%) was obtained from Sigma-Aldrich. Silicon phthalocyanine dichloride (SiPc-Cl_2),[24] and tin phthalocyanine dichloride (SnPc-Cl_2)[25] were synthesized according to the literature.

5.5.2 Methods

All syntheses were carried out under similar conditions. The reaction vessel, a 100 or 250 mL three-neck round-bottom flask, was sealed with rubber septa, and connected to a reflux condenser and a nitrogen inlet. The vessel was heated and stirred as its contents reacted. All glassware was dried with acetone. In purifications by train sublimation, CO_2 is used as the carrier gas.

5.5.2.1 Bis(pentafluoro phenoxy) silicon phthalocyanine

F_{10}-SiPc (**1**) was synthesized according to literature.[26] First, silicon phthalocyanine dichloride (0.40 g, 0.65 mmol) was added to a three-neck round-bottom flask, followed by 2,3,4,5,6-pentafluorophenol (0.72 g, 3.92 mmol) in a 6 molar excess. Finally, chlorobenzene (22 mL) was added as a solvent to the reactor. The flask was sealed with rubber septa and connected to a reflux condenser. It was heated to 120 ˚C. After reacting for approximately 20 hours, the desired product, F_{10}-SiPc (**1**), was precipitated out of the contents of the flask with the addition of isopropanol in a 15:1 volumetric ratio of isopropanol to chlorobenzene. The isopropanol mixture was filtered by gravity: the filtrate was a clear sky-blue colour, while the precipitate, F_{10}-SiPc (**1**), was a dark blue/purple powder (yield = 81 %). The product was purified by train sublimation at 280 ˚C (27 mTorr). UV-vis λ_{max} = 688 nm.

5.5.2.2 Bis(2,4,6-trifluoro phenoxy) silicon phthalocyanine

The synthesis of $(246F)_2$-SiPc followed the experimental procedure for the synthesis of F_{10}-SiPc (**1**), except 2,4,6-trifluorophenol (1.18 g, 8.00 mmol) was used in place of 2,3,4,5,6-pentafluorophenol. Filtration by gravity yielded a clear blue/green filtrate and a dark blue

precipitate, $(246F)_2$-SiPc (**2**, yield = 92 %). The product was purified by train sublimation at 320 ˚C (89 mTorr). UV-vis λ_{max} = 684 nm.

5.5.2.3 Bis(pentafluoro phenoxy) tin phthalocyanine

Tin phthalocyanine dichloride (0.30 g, 0.43 mmol), a 6 molar excess of 2,3,4,5,6-pentafluorophenol (0.50 g, 2.69 mmol), a 20 molar excess of triethylamine (0.84 g, 8.28 mmol), and chlorobenzene (20 mL) were mixed in a three-neck round-bottom flask connected to a reflux condenser. The contents were heated to 120 ˚C and reacted for approximately 20 hours. The contents of the flask were precipitated with isopropanol in a 15:1 volumetric ratio of isopropanol to chlorobenzene, then filtered by gravity. The filtrate was reported as a clear, light green liquid and the F_{10}-SnPc (**3**) product was a dark green/black powder (yield = 82 %). The product was purified by train sublimation at 305 ˚C (81 mTorr). UV-vis λ_{max} = 695 nm. Elemental analysis: expected wt%: C (52.99%), H (1.62%) and N (11.24%); analysis wt%: C (53.79%), H (1.38%) and N (12.06%).

5.5.2.4 Bis(2,4,6-trifluoro phenoxy) tin phthalocyanine

To synthesize $(246F)_2$-SnPc, the procedure for the synthesis of F_{10}-SnPc (**3**) was followed but 2,4,6-trifluorophenol (0.40 g, 3.35 mmol) was used in place of 2,3,4,5,6-pentafluorophenol. This produced a clear, tan-coloured filtrate, and the dark blue $(246F)_2$-SnPc powder (**4**, yield = 80 %). UV-vis λ_{max} = 692 nm. Elemental Analysis: expected wt%: C (57.11%), H (2.18%) and N (12.11%); analysis wt%: C (57.06%), H (1.66%) and N (12.35%).

5.5.3 Material Characterization

Ultraviolet-visible (UV-vis) absorption spectroscopy was performed using an Ocean Optics spectrometer with a 10 mm VWR quartz cuvette for solutions and glass slides for solid-state films. Elemental analysis for

5.5.4 OTFT Fabrication

Doped silicon substrates with 230 nm of thermally grown oxide supplied by University Wafer were rinsed with acetone to remove their protective resistance. Substrates were cleaned by sonication in acetone and methanol before drying with nitrogen and treatment with oxygen plasma

for 15 minutes. Cleaned substrates were rinsed with distilled water and isopropanol before drying in nitrogen and placing in 1% v/v solutions of octyltrichlorosilane (OTS, Sigma, 97%) in toluene. Substrates were kept in OTS solution for 60 hours at 70 °C to produce a self-assembled monolayer of OTS, then rinsed with toluene and isopropanol and dried with nitrogen. Surface-modified substrates were dried at 70 °C in vacuum to remove residual solvent before storage in the glove box overnight prior to semiconductor deposition. Semiconductor films were deposited on open substrates with a target rate of 0.2 $Å s^{-1}$ until 30 nm had deposited, although apparent thickness as determined using profilometry varied between 23 and 30 nm (margin of error about ±4 nm) despite adjusting tooling factor prior to deposition. For substrates with BCP, 2 nm of BCP (bathocuproine, Lumtec, >99.9%) was deposited afterwards on top of the semiconducting film. Prior to electrode deposition, the corners of each substrate were scratched to create contact between the deposited gate electrode and the doped silicon material beneath the oxide. Each substrate was placed on a shadow mask purchased from Ossila. For devices with Cr and Mn (source: Angstrom engineering) interlayers, 10±2 nm of material was deposited at approximately 0.5 $Å s^{-1}$ prior to deposition of 50 nm of either Ag or Au (source: Angstrom engineering). Prior to testing, the semiconducting film was scratched between devices to isolate them from themselves and the gate. Finished devices were left in a glove box with less than 2 ppm of O_2 and 0.5 ppm of water for up to 1 day before testing.

5.5.5 OTFT Characterization

Each chip was placed in a miniaturized testing setup developed by Ossila and characterized with in-house software in a nitrogen atmosphere (glove box). Current outputs (I_{DS} and I_{GS}) and voltage inputs (V_{GS} and V_{DS}) were measured and set, respectively, using a Keithley 2614B. For each OTFT on the substrate ($n \leq 20$), output and transfer curves were obtained automatically after ensuring functionality. For testing in the saturation region, V_{DS} = 50 V was used and for the linear region V_{DS} = 2 V was used. V_{GS} sweeps were typically from 0 V to 60 V for the saturation region and 0 V to 40 V for the linear region, which often exhibited significantly higher hysteresis when higher biases were used. In each case, the gate bias was pulsed with a duty cycle of 10% and a frequency of 10 Hz, rather than applied constantly, in order to decrease bias stress. In order for mobility and threshold voltage to stabilize, each device had its transfer characteristics collected three times and the third value was used for analysis. The mobility and threshold voltage were

calculated for the saturation and linear region using the following equations, with the assumption of negligible contact resistance and otherwise ideal behavior. Specific capacitance (C_i) values were estimated using impedance spectroscopy on the same substrates used for the experiments in the metal-insulator-metal configuration, and assumed to be constant. In each case, the mobility was plotted as a function of V_{GS} to determine the ideality of the data as it was being obtained. The uncorrected threshold voltage and mobility were obtained using Equations 1.3 - 1.6. Versions of μ corrected for contact resistance were obtained using the Y-function method (YFM).[8]

5.6 Supplementary Information

5.6.1 Extra Tables / Figures

Main Electrode	Electrode Interlayer	μ (cm^2/Vs)	V_T (V)
Au	None	$2.7\pm1.0\times10^{-1}$	23.5±0.4
Au	Cr	$2.7\pm0.4\times10^{-1}$	13.4±1.4
Au	Mn	$1.9\pm0.3\times10^{-1}$	10.0±2.1
Au	BCP	$1.8\pm0.4\times10^{-1}$	12.4±1.3
Ag	None	$1.7\pm0.4\times10^{-1}$	28.7±1.7
Ag	Cr	$0.9\pm0.2\times10^{-1}$	20.8±2.1
Ag	Mn	$1.7\pm0.2\times10^{-1}$	7.8±1.4
Ag	BCP	$2.1\pm0.7\times10^{-1}$	23.9±1.6

Table 5.3: Summarized electrical properties (μ: field-effect mobility, V_T: threshold voltage, ± standard deviation) for BGTC OTFTs fabricated with F_{10}-SiPc (**1**) as the OSC and either silver (Ag) or gold (Au) primary electrodes and either Cr, Mn or BCP interlayers between the OSC and main source-drain contacts

Main Electrode	Electrode Interlayer	μ (cm^2/Vs)	V_T (V)
Au	None	$8.9\pm4.0\times10^{-2}$	36.6±1.1
Au	Cr	$7.8\pm1.1\times10^{-2}$	25.0±1.0
Au	Mn	$6.1\pm0.9\times10^{-2}$	23.2±1.9
Au	BCP	$1.2\pm0.5\times10^{-2}$	32.7±5.3
Ag	None	$5.7\pm1.2\times10^{-2}$	35.3±1.7
Ag	Cr	$4.2\pm0.5\times10^{-2}$	31.2±1.6
Ag	Mn	$4.4\pm1.4\times10^{-2}$	27.4±1.7
Ag	BCP	$5.2\pm0.9\times10^{-2}$	28.2±3.5

Table 5.4: Summarized electrical properties (μ: field-effect mobility, V_T: threshold voltage, ± standard deviation) for BGTC OTFTs fabricated with 246F-SiPc (**2)** as the OSC and either silver (Ag) or gold (Au) primary electrodes and either Cr, Mn or BCP interlayers between the OSC and main source-drain contacts

Main Electrode	Electrode Interlayer	μ (cm^2/Vs)	V_T (V)	I_{OFF} (A)
Au	None	$1.1 \pm 1.0 \times 10^{-2}$	28.1 ± 5.7	10^{-10}
Au	Cr	$3.5 \pm 1.0 \times 10^{-3}$	31.1 ± 2.4	10^{-10}
Au	Mn	$1.1 \pm 1.2 \times 10^{-3}$	26.8 ± 5.1	10^{-10}
Au	BCP[1]	$6.7 \pm 4.3 \times 10^{-3}$	26.0 ± 2.5	10^{-8}
Au	BCP[2]	$1.6 \pm 1.3 \times 10^{-2}$	24.5 ± 2.1	10^{-10}
Ag	None	$1.1 \pm 1.3 \times 10^{-2}$	25.9 ± 3.7	10^{-9}
Ag	Cr	$8.3 \pm 7.2 \times 10^{-3}$	26.0 ± 6.4	10^{-10}
Ag	Mn	$1.0 \pm 6.4 \times 10^{-2}$	25.2 ± 5.8	10^{-10}
Ag	BCP[1]	$1.3 \pm 0.8 \times 10^{-3}$	17.2 ± 4.2*	10^{-7}
Ag	BCP[2]	$4.8 \pm 2.8 \times 10^{-3}$	24.0 ± 3.0	10^{-10}

Table 5.5: Summarized electrical properties (μ: field-effect mobility, V_T: threshold voltage, ± standard deviation) for BGTC OTFTs fabricated with F_{10}-SnPc (**3)** as the OSC and either silver (Ag) or gold (Au) primary electrodes and either Cr, Mn or BCP interlayers between the OSC and main source-drain contacts. *Notes: [1]BCP covered the entire OSC; [2]BCP covered only the electrode area of the OSC; *Value is unreliable due to high off current.*

Main Electrode	Electrode Interlayer	μ (cm^2/Vs)	V_T (V)	I_{OFF} (A)
Au	None	7.1 ±2.1 x 10^{-3}	40.8 ± 0.7	10^{-10}
Au	Cr	1.9 ± 0.8 x 10^{-3}	40.4 ± 0.7	10^{-10}
Au	Mn	9.8 ± 4.8 x 10^{-3}	39.1 ± 0.8	10^{-10}
Au	BCP[1]	2.7 ± 0.4 x 10^{-2}	36.1 ± 3.3	10^{-10}
Ag	None	5.3 ± 3.9 x 10^{-3}	37.0 ± 3.1	10^{-10}
Ag	Cr	1.7 ± 0.5 x 10^{-3}	37.1 ± 0.8	10^{-10}
Ag	Mn	6.7 ± 4.5 x 10^{-4}	36.2 ± 1.9	10^{-10}
Ag	BCP[1]	6.1 ± 2.4 x 10^{-4}	9.3 ± 12.5*	10^{-7}
Ag	BCP[2]	1.2 ± 1.9 x 10^{-2}	34.4 ± 5.2	10^{-10}

Table 5.6: Summarized electrical properties (μ: field-effect mobility, V_T: threshold voltage, ± standard deviation) for BGTC OTFTs fabricated with 246F-SnPc (**4**) as the OSC and either silver (Ag) or gold (Au) primary electrodes and either Cr, Mn or BCP interlayers between the OSC and main source-drain contacts. *Notes: [1]BCP covered the entire OSC; [2]BCP covered only the electrode area of the OSC; *Value is unreliable due to high off current.*

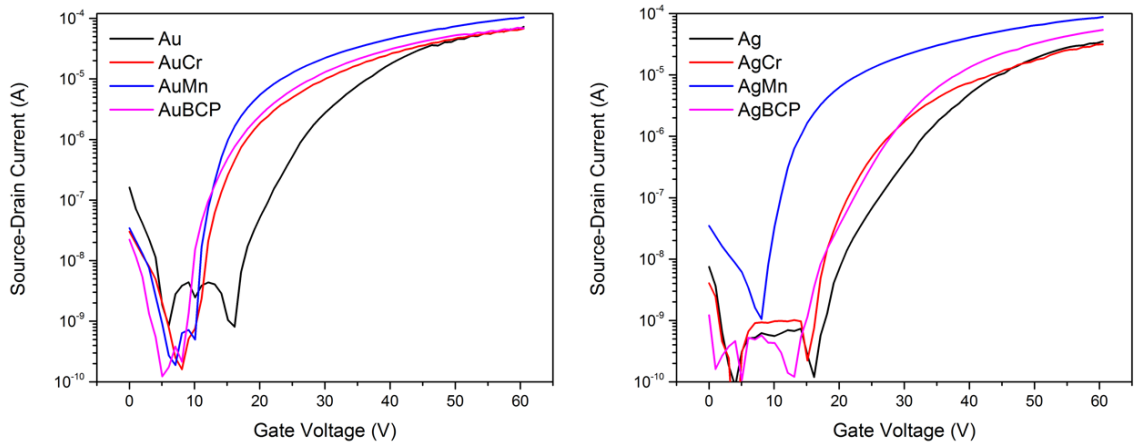

Figure 5.10: Transfer curves for F_{10}-SiPc (**1**) and various electrode configurations

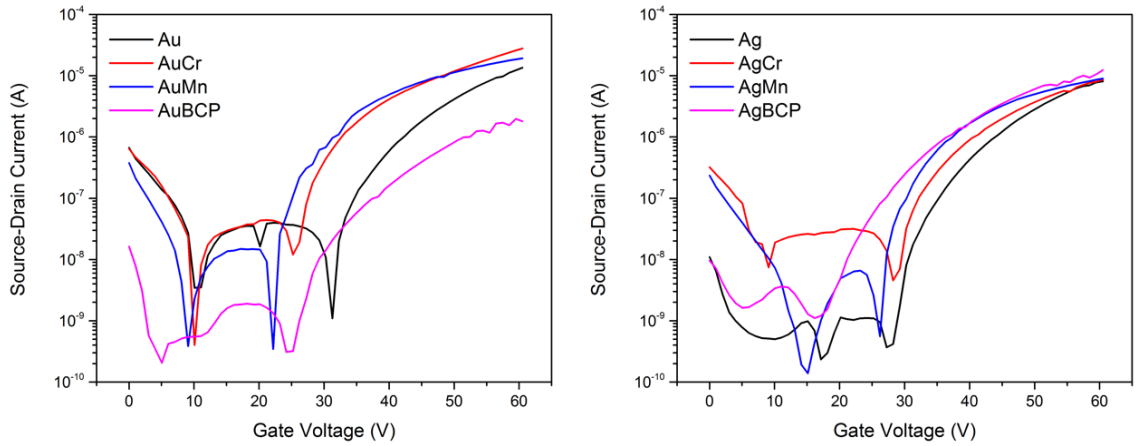

Figure 5.11: Transfer curves for 246F-SiPc (**2**) and various electrode configurations

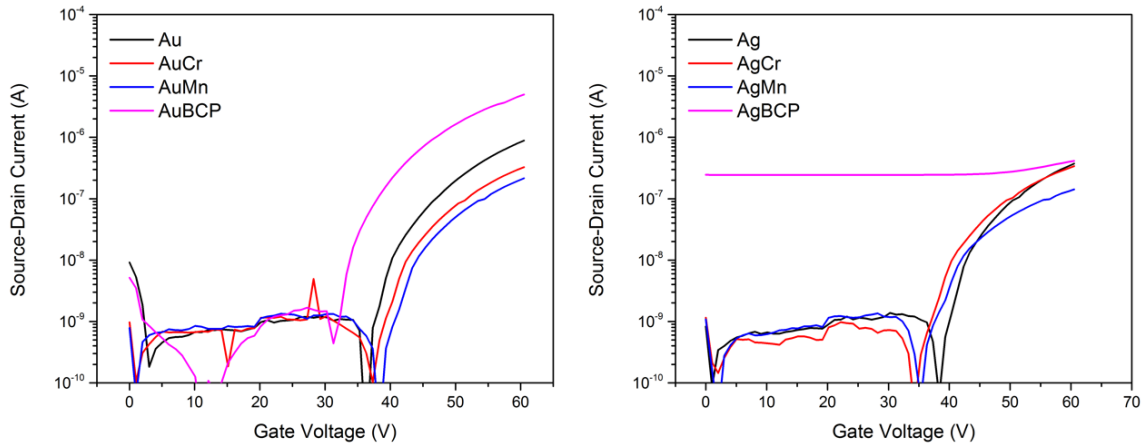

Figure 5.12: Transfer curves for 246F-SnPc (**4**) and various electrode configurations

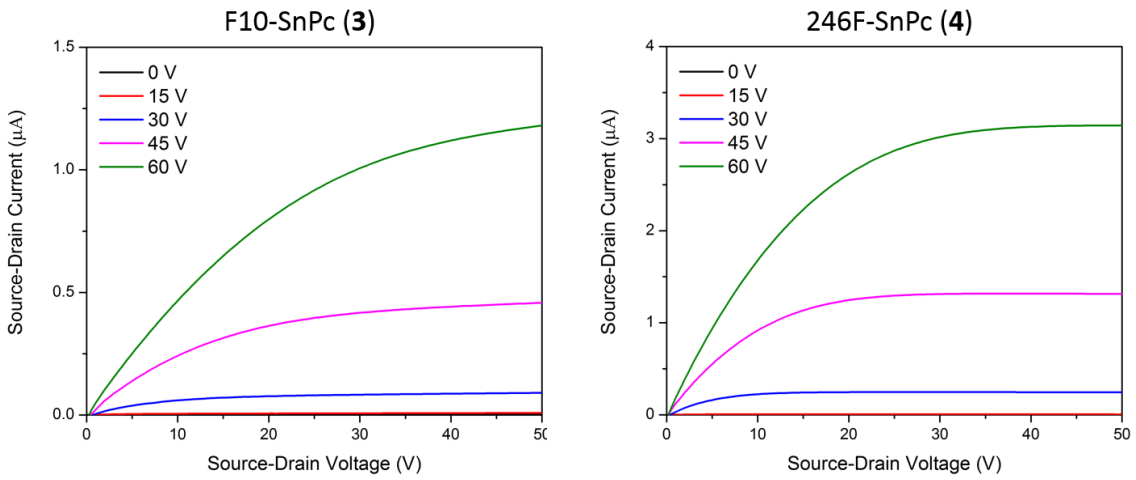

Figure 5.13: Output curves for **3** (left) and **4** (right) using Ag electrodes with a BCP interlayer in the vicinity of the electrodes. Devices were picked to match average electrical parameters.

5.6.2 Y-Function R_C Calculations

In general, OTFTs using F_{10}-SiPc (**1**) seemed to follow the same pattern as example graphs used in the YFM reference paper.[8] Figure 5.14 shows the transfer curve and transconductance (g_m) based on a 3-point smoothed derivative (with respect to V_{GS}) of the transfer curve. g_m curves down slightly, as in the L = 50 μm channel length device from the example.

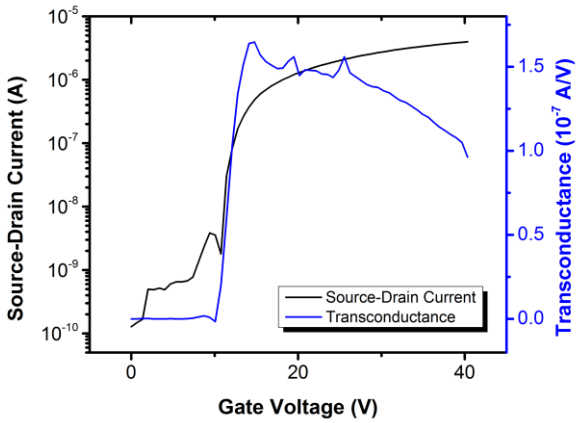

Figure 5.14: Transfer curve and transconductance as a function of V_{GS} for an example OTFT using F_{10}-SiPc (**1**) as the OSC, Au electrodes and a Mn contact interlayer.

The Y-function is calculated as $Y = \frac{I_{DS}}{\sqrt{g_m}}$ and the slope can be used to find an R_C-free mobility μ_0 and the x-intercept is the corrected V_{T0}. Figure 5.15 (left) shows the Y-function as a function of V_{GS}, a nearly straight line rising from the axis. Here $\mu_0 = 0.18$ cm^{2}V^{-1}s^{-1} and $V_{T0} = 12.1$ V. The slope of $g_m^{-\frac{1}{2}}$ with respect to $-(V_G - V_T)$ before it rises around 0 V is used to calculate the mobility attenuation factor (θ), which can be related directly to R_C if you assume negligible contributions from surface roughness and phonon scattering. Here θ = 0.009 and RC = 96000 Ω, with $R_C W = 9600$ Ωcm or 9.6 kΩcm given $W = 0.1$ cm.

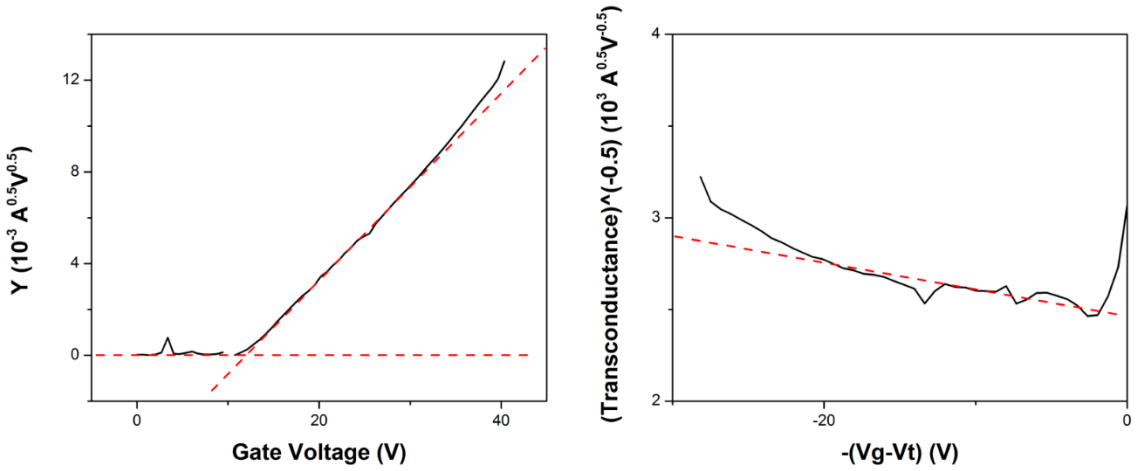

Figure 5.15: Y-function as a function of gate bias (left) and $g_m^{-\frac{1}{2}}$ plot used to calculate the mobility attenuation factor θ.

5.7 References

(1) Liu, C.; Xu, Y.; Noh, Y. Y. Contact Engineering in Organic Field-Effect Transistors. *Mater. Today* **2015**, *18* (2), 79–96.

(2) Huang, L.; Yu, B.; Song, D.; Geng, Y.; Zhu, F.; Yan, D. Tin (IV) Phthalocyanine Oxide: An Air-Stable Semiconductor with High Electron Mobility. *Appl. Phys. Lett.* **2008**, *92* (14), 143303.

(3) Song, D.; Wang, H.; Zhu, F.; Yang, J.; Tian, H.; Geng, Y.; Yan, D. Phthalocyanato Tin(IV) Dichloride: An Air-Stable, High-Performance, n-Type Organic Semiconductor with a High Field-Effect Electron Mobility. *Adv. Mater.* **2008**, *20* (11), 2142–2144.

(4) Melville, O. A.; Grant, T. M.; Mirka, B.; Boileau, N.; Lessard, B. H. Ambipolarity and Air Stability of Silicon Phthalocyanine Organic Thin-Film Transistors. *Adv. Electron. Mater.* **2019**, *5* (8), 1–7.

(5) Melville, O. A.; Grant, T. M.; Lessard, B. H. Silicon Phthalocyanines as N-Type Semiconductors in Organic Thin Film Transistors. *J. Mater. Chem. C.* **2018**, *6* (20), 5482–5488.

(6) Bittle, E. G.; Basham, J. I.; Jackson, T. N.; Jurchescu, O. D.; Gundlach, D. J. Mobility Overestimation Due to Gated Contacts in Organic Field-Effect Transistors. *Nat. Commun.* **2016**, *7*, 1–7.

(7) Lamport, Z. A.; Barth, K. J.; Lee, H.; Gann, E.; Engmann, S.; Chen, H.; Guthold, M.; McCulloch, I.; Anthony, J. E.; Richter, L. J.; DeLongchamp, D. M.; Jurchescu, O. D. A Simple and Robust Approach to Reducing Contact Resistance in Organic Transistors. *Nat. Commun.* **2018**, *9* (1).

(8) Xu, Y.; Minari, T.; Tsukagoshi, K.; Chroboczek, J. A.; Ghibaudo, G. Direct Evaluation of Low-Field Mobility and Access Resistance in Pentacene Field-Effect Transistors. *J. Appl. Phys.* **2010**, *107* (11).

(9) Liu, Z.; Kobayashi, M.; Paul, B. C.; Bao, Z.; Nishi, Y. Contact Engineering for Organic Semiconductor Devices via Fermi Level Depinning at the Metal-Organic Interface. **2010**, 2–7.

(10) Panigrahi, D.; Kumar, S.; Dhar, A. Contact Engineering for Efficient Charge Injection in Organic Transistors with Low-Cost Metal Electrodes. *Appl. Phys. Lett.* **2017**, *111* (17).

(11) Bai, Y.; Liu, X.; Chen, L.; Zhu, W. Q.; Jiang, X. Y.; Zhang, Z. L. Organic Thin Film Field Effect Transistors with MoO3 /Al Electrode and OTS/SiO2 Bilayer Gate Insulator. *AD'07 - Proc. Asia Disp. 2007* **2007**, *1*, 613–616.

(12) Xia, J.; Dong, G.; Tian, B.; Yan, Q.; Zhang, H.; Liang, X.; Peng, L. Metal Contact Effect on the Performance and Scaling Behavior of Carbon Nanotube Thin Film Transistors. *Nanoscale* **2016**, *8* (19), 9988–9996.

(13) Yi, Y.; Jeon, P. E.; Lee, H.; Han, K.; Kim, H. S.; Jeong, K.; Cho, S. W. The Interface State Assisted Charge Transport at the MoO3 /Metal Interface. *J. Chem. Phys.* **2009**, *130* (9), 1–4.

(14) Gwinner, M. C.; Pietro, R. Di; Vaynzof, Y.; Greenberg, K. J.; Ho, P. K. H.; Friend, R. H.; Sirringhaus, H. Doping of Organic Semiconductors Using Molybdenum Trioxide: A Quantitative Time-Dependent Electrical and Spectroscopic Study. *Adv. Funct. Mater.* **2011**, *21* (8), 1432–1441.

(15) Chen, F. C.; Kung, L. J.; Chen, T. H.; Lin, Y. S. Copper Phthalocyanine Buffer Layer to Enhance the Charge Injection in Organic Thin-Film Transistors. *Appl. Phys. Lett.* **2007**, *90* (7).

(16) Marmont, P.; Battaglini, N.; Lang, P.; Horowitz, G.; Hwang, J.; Kahn, A.; Amato, C.; Calas, P. Improving Charge Injection in Organic Thin-Film Transistors with Thiol-Based Self-Assembled Monolayers. *Org. Electron. physics, Mater. Appl.* **2008**, *9* (4), 419–424.

(17) Li, S.; Guérin, D.; Lmimouni, K. Improving Performance of OFET by Tuning Occurrence of Charge Transport Based on Pentacene Interaction with SAM Functionalized Contacts. *Microelectron. Eng.* **2018**, *195* (April), 62–67.

(18) Cheng, X.; Noh, Y. Y.; Wang, J.; Tello, M.; Frisch, J.; Blum, R. P.; Vollmer, A.; Rabe, J. P.; Koch, N.; Sirringhaus, H. Controlling Electron and Hole Charge Injection in Ambipolar Organic Field-Effect Transistors by Self-Assembled Monolayers. *Adv. Funct. Mater.* **2009**, *19* (15), 2407–2415.

(19) Shin, N.; Zessin, J.; Lee, M. H.; Hambsch, M.; Mannsfeld, S. C. B. Enhancement of N-Type Organic Field-Effect Transistor Performances through Surface Doping with Aminosilanes. *Adv. Funct. Mater.* **2018**, *28* (34), 1–7.

(20) Baeg, K. J.; Kim, J.; Khim, D.; Caironi, M.; Kim, D. Y.; You, I. K.; Quinn, J. R.; Facchetti, A.; Noh, Y. Y. Charge Injection Engineering of Ambipolar Field-Effect Transistors for

High-Performance Organic Complementary Circuits. *ACS Appl. Mater. Interfaces.* **2011**, *3* (8), 3205–3214.

(21) Pfattner, R.; Rovira, C.; Mas-torrent, M. Organic Metal Engineering for Enhanced Field-Effect Transistor Performance. *Phys. Chem. Chem. Phys.* **2015**, *17*, 26545–26552.

(22) Lessard, B. H.; Grant, T. M.; White, R.; Thibau, E.; Lu, Z.; Bender, T. P. The Position and Frequency of Fluorine Atoms Changes the Electron Donor/Acceptor Properties of Fluorophenoxy Silicon Phthalocyanines within Organic Photovoltaic Devices. *J. Mater. Chem. A.* **2015**, *3* (48), 24512–24524.

(23) Wang, S. D.; Minari, T.; Miyadera, T.; Tsukagoshi, K.; Aoyagi, Y. Contact-Metal Dependent Current Injection in Pentacene Thin-Film Transistors. *Appl. Phys. Lett.* **2007**, *91* (20), 1–4.

(24) Lowery, M. K.; Starshak, A. J.; Esposito, J. N.; Krueger, P. C.; Kenney, M. E. Dichloro(Phthalocyanino)Silicon. *Inorg. Chem.* **1965**, *4* (1), 128.

(25) Barrett, P. A.; Dent, C. E.; Linstead, R. P. Phthalocyanines. Part VII. Phthalocyanine as a Coordinating Group. A General Investigation of the Metallic Derivatives. *J. Chem. Soc.* **1936**, 1719–1736.

(26) Lessard, B. H.; White, R. T.; Al-amar, M.; Plint, T.; Castrucci, S.; Josey, D. S.; Lu, Z.; Bender, T. P. Assessing the Potential Roles of Silicon and Germanium Phthalocyanines in Planar Heterojunction Organic Photovoltaic Devices and How Pentafluoro Phenoxylation Can Enhance $\pi - \pi$ Interactions and Device Performance. *ACS Appl. Mater. Interfaces.* **2015**, *7* (9), 5076–5068.

Chapter 6: Overall Conclusions, Ongoing Efforts and Recommendations for Future Work

6.1 Overall Conclusions

Incorporating new organic semiconducting materials (OSCs) into organic thin-film transistors (OTFTs) continues to be an important part of their ongoing development towards commercial, medical and industrial applications. As OTFTs continue to demonstrate potential for biological and chemical sensing, printed electronics, large area electronics, and flexible electronics, they are still held back from implementation by a number of technological limitations. Issues with poor device consistency, low availability of stable n-type OSCs, high synthetic complexity, inaccurate or inconsistent reporting of parameters, and high power consumption due to low mobility, low capacitance, or high threshold voltage. The development of new OSCs must consider these issues and potential applications.

Chapter 2 explored the commercial pigment Red GG for use in OTFTs due to its exceptional low cost and high availability. Devices with μ_h of $5x10^{-5}$ $cm^2V^{-1}s^{-1}$, $I_{ON/OFF}$ of 10^{2-3} and V_T of 14 V were fabricated with some process optimization. AFM imaging and XRD characterization of the Red GG thin films helped explain the superior electrical properties of these optimized devices. The performance of these transistors was not high enough for most applications, but could be improved through the modification of the base molecule. A submitted manuscript outlined in Section 7.14 explored a few of these derivatives, and a modest performance improvement was obtained when Red GG was functionalized with a rigid phenyl substituent. Given that the family of OSCs has not been studied in OTFTs, these device baselines may serve as starting points for better devices using other Red GG derivatives.

In Chapter 3, the first OTFTs using SiPcs were reported and some structure-property relationships were established. SiPcs not only belong to the stable phthalocyanine molecular family, but also represent a group of n-type OSCs with simple synthesis and therefore large-scale production viability. In BGBC devices, bis(benzoate) silicon phthalocyanine demonstrated μ_e of 9.4×10^{-3} $cm^2V^{-1}s^{-1}$ with a V_T of 26.9 V and $I_{ON/OFF}$ of 10^{4-5}. These averaged results were achieved after a process optimization similar to Chapter 2 that included examining two other materials and

more PVD-related parameters such as deposition rate. The paper found that the combination of high substrate temperature during deposition and an OTS or ODTS surface treatment produced the best results. It also found that the larger axial substituents did not perform as well as the smaller ones, supporting the hypothesis that excessively bulky functional groups decrease the ability of SiPc molecules to pack in a way that facilitates charge transport. All of this work built a foundation for future development of SiPc-based OTFTs.

Despite the conclusion with regards to axial substitution in Chapter 2, Chapter 3 found that bis(pentafluorophenoxy) silicon phthalocyanine (F_{10}-SiPc) was superior to $SiCl_2Pc$ for OTFTs by a number of metrics, despite the much larger R groups. Indeed, F_{10}-SiPc devices deposited at 140 ºC on OTS-modified Si/SiO_2 demonstrated an average μ_e of 0.12 $cm^2V^{-1}s^{-1}$ with a V_T of 12.0 V and $I_{ON/OFF}$ of $10^{4\text{-}5}$, compared to 0.02 $cm^2V^{-1}s^{-1}$, 37.2 V and 10^5 for $SiCl_2Pc$ devices. The performance of the F_{10}-SiPc devices was strong enough that contact resistance (R_C) started to play a major role, becoming comparable to the channel resistance which tends to dominate in lower-performing devices. This was apparent in the linear region of the output curves for F_{10}-SiPc and in the channel-length dependence of μ_e. Correcting for R_C, μ_e averaged about 0.18 $cm^2V^{-1}s^{-1}$ for n = 57 devices, which is comparable to the best demonstrated n-type OSCs based on MPcs for OTFTs, and certainly within the realm of applicability. This performance was not sustained when OTFTs were characterized in air, with hole transport becoming stronger in all studied SiPcs except for $SiCl_2Pc$, which did not transport holes. This adjusting polarity of charge transport in different environmental conditions depended on the HOMO and LUMO values of the SiPcs, and could be exploited for applications where controlled ambipolarity is desirable. It could be also be considered a downside, as F_{10}-SiPc is a relatively air-instable electron conductor compared to $F_{16}CuPc$ and other n-type OSCs. As the significant bias stress in n-type OTFTs became apparent during the course of this study due to changing threshold voltage (ΔV_T), a method to minimize it by using a pulsed-gate method was borrowed from literature. This method seemed to reduce ΔV_T, increase μ_e and reduce hysteresis significantly for SiPc OTFTs, and is now used in other studies with n-type OSCs in the research group for those reasons.

High R_C and its effects on parameter reliability and device performance are a general issue in the field of OTFT development. Chapter 5 presented a method to address the issue of high R_C in SiPc OTFTs by switching to the BGTC architecture and using interlayers between the conductive metal contacts and the OSC. Mn and Cr were chosen as interlayers due to lower work

functions compared to Au, while BCP was chosen because of its established use as an electron transport layer in OPVs. F_{10}SiPc devices with Au or Ag contacts and a 10 nm Mn interlayer had superior output and transfer characteristics to those presented in Chapter 4, with measurable linear region characteristics due to the lower injection barrier. In the linear region, these OTFTs demonstrated an average μ_e of 0.14 $cm^2V^{-1}s^{-1}$, V_T between 10 – 12 V, and $I_{ON/OFF}$ of around 10^5 with a normalized contact resistance (R_CW) close to 12 kΩcm, which is impressively low for n-type OTFTs even with interlayers. The paper compares F_{10}-SiPc to 246F-SiPc and their SnPc analogues, which had not been previously published for any context. These SnPc derivatives do not perform as well as their SiPc analogues, with investigation into this difference ongoing. Despite their inferior performance, both SnPcs had some interaction with the BCP interlayer which increased their I_{OFF} in a way that was not seen for SiPcs. This externally-induced conductivity change could be exploited for sensing applications if the mechanism can be identified. Overall, this study demonstrated that high quality SiPc OTFTs with low V_T and R_C can be fabricated with unheated substrates using PVD.

Overall, this thesis contains the first reports demonstrating OTFTs using Red GG and SiPcs as OSCs. In particular, the excellent electron mobility and low threshold voltage of SiPcs, in particular F_{10}-SiPc, represents a significant contribution to the limited field of high-performance n-type OSCs. The large amount of fundamental research on process optimization, characterization conditions, electrical analysis and device design helps clarify the behavior and properties of these classes of molecules for OTFTs. I hope interest in these materials for transistors will continue with potential applications somewhere on the horizon.

6.2 Ongoing Efforts and Recommendations for Future Work

6.2.1 Exploring SiPcs

A fundamental gap in understanding from my completed research are the specific reasons for the superiority of F_{10}-SiPc over other SiPc derivatives. In order to better determine structure-property relationships, Benjamin King has been investigating BGTC devices using AgMn electrodes and a wide variety of SiPcs. So far, F_{10}-SiPc remains the best performing material, and structure-property relationships have been difficult to establish based purely on the chemical structures. We hope that more investigation into thin-film morphology will help elucidate the reasons for the superiority of this material with the hope that better materials could be synthesized.

Another issue with the SiPcs characterized so far is their relative instability in air. The LUMO levels of about -3.55 to -4.05 eV are perhaps insufficiently low to stop severe electron mobility and threshold voltage degradation when characterized in ambient conditions. Several options exist for improving the air stability of these compounds for OTFTs. Peripheral fluorination requires more complex synthesis but is being investigated between the Brusso research group and Lessard research group. Another method to stabilize the LUMO of SiPcs is to incorporate fluoroalkyl chains or more heteroatoms in the central ring structure, as discussed in Chapter 1. Despite its ability to improve n-type performance in nitrogen, manganese oxidizes easily in air and seems to hinder performance when characterized under ambient conditions. Using alternative electron-injecting interlayers such as TiO_x that do not have this innate instability may be another option to increase air stability. Finally, encapsulation can prevent access of ambient gases to the film, and has not been explored so far in the Lessard research group for OTFTs.

6.2.2 Exploring Device Design

At the beginning stages of my project I worked with polymer grafting and crosslinking, as explored in my first author paper in Section 7.1 not covered within the scope of this thesis. I originally intended to combine this work with my OTFT research, but did not end up having sufficient time. I have two ideas, one of which has had some success in experiments by Benjamin King and others. The first idea is to graft polymers onto the SiO_2 dielectric as an alternative to using an organosilane SAM. Although this concept has been demonstrated in literature before, using nitroxide-mediated polymerization (NMP) for the grafted polymers in OTFTs is novel. NMP

has several advantages in this context, providing a synthetic handle in the form a reactive end group that can be linked to the dielectric and producing low polydispersity polymers which could form more consistently sized coils on the surface for smoother coverage which is important during OSC film formation. Results so far indicate reduced V_T and exceptional stability when characterizing n-type OTFTs in nitrogen.

The other idea is to make a low-leakage, robust polymer dielectric using a two-step fabrication process. First, a thin polymer is grafted onto a gate, perhaps indium tin oxide (ITO) or Al. This polymer layer provides a slightly rough surface for a subsequently spin-cast layer to latch onto while remaining attached to the surface. This mimics the demonstrated process of spin-coating twice without the downside of dissolving the first layer partially during the second spin coat which could reduce dielectric film consistency. To make the film even more robust, the second layer could be crosslinked to itself and the first layer, ideally through a process that does not release gas. Having a thin but consistent polymer dielectric could greatly increase capacitance and could be an excellent technique in the fabrication of flexible or all-polymer OTFTs.

Chapter 7: Additional Contributions

7.1 Orthogonally Processable Carbazole-Based Polymer Thin Films by Nitroxide-Mediated Polymerization

OA Melville, B King, C Imperiale, BH Lessard

Langmuir 32 (51), 13640-13648

Publication Date: November 29, 2016

https://doi.org/10.1021/acs.langmuir.6b03920

Abstract

Cross-linking of hole-transporting polymer thin films in organic light emitting diodes (OLEDs) has been shown to increase device efficacy when subsequent layers are deposited from solution. This improvement, due to resistance of the films to dissolution, could also be achieved by covalently grafting the polymer film to the substrate. Using nitroxide-mediated polymerization (NMP), we synthesized a novel poly(9-(4-vinylbenzyl)-9H-carbazole) (poly(VBK)) copolymer which can be cross-linked and also developed two simple methods for the grafting-to or grafting-from, also known as surface-initiated polymerization, of poly(VBK) to indium tin oxide (ITO) substrates. All three of these methods produced thin films that could be orthogonally processed; that is, they resisted dissolution when the spin-coating of a subsequent layer was simulated. Similar electrochemical behavior for the poly(VBK) films was observed regardless of the technique used, suggesting that all three techniques could be used in the engineering of organic electronic devices. We expect that all three methods would be worth investigating in the solution-based assembly of OLEDs and other organic electronic devices.

Contributions

I conducted all the thin-film studies which composed the majority of this research paper, compiled the research, and wrote most of the paper (except the synthesis section). I experimented with different methods to graft polymers to an indium tin oxide (ITO) surface and from the ITO surface using an organosilane intermediary. I used electrochemistry to analyze the bulk polymers and the polymers in thin films, comparing repeated redox scans obtained using cyclic voltammetry of films produced by different methods (grafting-to, grafting-from, spin cast with crosslinking and without). I also showed that the grafted and crosslinked films were resistant to dissolution with contact angle measurements, demonstrating the potential of the films to remain intact when spin cast upon.

7.2 Organic Thin Film Transistors Incorporating Solution Processable Thieno [3, 2-b] thiophene Thienoacenes

N Rice, F Magnan, O Melville, J Brusso, B Lessard

Materials 11 (1), 8

Published: 22 December 2017

https://doi.org/10.3390/ma11010008

Abstract

Bottom-gate bottom-contact organic thin film transistors (OTFTs) were prepared with four novel star-shaped conjugated molecules containing a fused thieno[3,2-b]thiophene moiety incorporated either in the core and/or at the periphery of the molecular framework. The molecules were soluble in CS2, allowing for solution-processing techniques to be employed. OTFTs with different channel geometries were characterized in both air and vacuum in order to compare environmental effects on performance. Blending the small molecules with poly(styrene), an insulating polymer, facilitated the formation of an even semiconducting film, resulting in an order of magnitude increase in device mobility. The highest field-effect mobilities were in air and on the order of 10^{-3} cm^2/Vs for three of the four molecules, with a maximum mobility of 9.2×10^{-3} cm^2/Vs achieved for the most conjugated small molecule. This study explores the relationship between processing conditions and OTFT devices performance for four different molecules within this new family of materials, resulting in a deeper insight into their potential as solution-processable semiconductors.

Contributions

For this study, I trained the first author on OTFT fabrication and characterization, advised on analysis, and suggested using poly(styrene) for blending. I compared the performance of the devices in air and vacuum, providing a written section and figure for the paper. I also helped edit the entire paper, providing input on structure and storytelling.

7.3 The influence of air and temperature on the performance of PBDB-T and P3HT in organic thin film transistors

Samantha Brixi, Owen A Melville, Nicholas T Boileau, Benoît H Lessard

Journal of Materials Chemistry C 6 (44), 11972-11979

Published: May 9, 2018

DOI: 10.1039/C8TC00734A

Abstract

Conjugated polymers such as poly(3-hexylthiophene) (P3HT) are commonly used as semiconducting components in organic photovoltaics (OPVs) and organic thin-film transistors (OTFTs). Such devices may be exposed to oxygen or moisture in air and increased temperature during operation, potentially affecting their charge transport properties. Therefore, we produced the first reported examples of OTFTs using PBDB-T, a conjugated push–pull polymer used in high performance OPVs, and assessed their performance compared to P3HT under different environmental conditions. Drop casted and annealed bottom-gate, bottom-contact (BGBC) devices had an average mobility of 0.06 $cm^2V^{-1}s^{-1}$, an on/off current ratio of 10^4 and a desirable threshold voltage around 0 V. These OTFTs showed distinct responses to characterization at increased temperature in vacuum ($P < 0.1$ Pa) and air, with PBDB-T devices retaining their performance better than P3HT over time. These findings suggest PBDB-T has higher stability to oxidation when exposed to air than P3HT, especially at high temperatures, and therefore represent a more stable alternative for use in OTFTs and OPVs.

Contributions

I supervised the first author, training her to make and characterize devices and performing preliminary experiments with P3HT. I proposed several of the experiments in meetings, which were later fine-tuned. I heavily edited the manuscript, rewriting and restructuring a large portion of it.

7.4 Benzyl and fluorinated benzyl side chains for perylene diimide non-fullerene acceptors

Maryam Nazari, Mark Martell, Thomas A Welsh, Owen Melville, Zhe Li, Jonathan Cann, Edward Cieplechowicz, Yingping Zou, Benoit H Lessard, Gregory C Welch

Materials Chemistry Frontiers 2 (12), 2272-2276

Published: October 11, 2018

DOI: 10.1039/C8QM00487K

Abstract

The synthesis and characterization of three N-annulated perylene diimide dimers with benzyl based side-chains is reported. Benzyl, 4-fluorobenzyl, and pentafluorobenzyl groups are used as side chains at the pyrrolic N-atom position of the N-annulated perylene diimide chromophore. All three compounds were used as non-fullerene acceptors in polymer based organic solar cells. Power conversion efficiencies upwards of 5.8% were achieved for both benzyl and 4-fluorobenzyl substituted acceptors, with different donor polymers.

Contributions

I carefully fabricated and characterized transistors using the materials, sent to me from the University of Alberta, reported in the paper before and after annealing.

7.5 Synthesis of a Perylene Diimide Dimer with Pyrrolic N–H Bonds and N-Functionalized Derivatives for Organic Field-Effect Transistors and Organic Solar Cells

Marcus Vespa, Jonathan R Cann, Sergey V Dayneko, Owen A Melville, Arthur D Hendsbee, Yingping Zou, Benoît H Lessard, Gregory C Welch

European Journal of Organic Chemistry 2018 (33), 4592-4599
First published: 11 July 2018
https://doi.org/10.1002/ejoc.201801055

Abstract

This study reports on the new and optimized synthesis of an N-annulated perylene diimide dimer with functional N–H moieties. The presence of two N–H moieties renders the dimer relatively insoluble in most organic solvents. The dimer is easily functionalized with electron donating hexyl chains or electron withdrawing *tert*-butyloxycarbonyl (tBOC) groups to yield highly soluble materials. The tBOC groups can be thermally cleaved in the thin film to give the parent dimer. The N–H bonds are acidic and interact with volatile organic bases. Deprotonation results in a color change from red to blue. All compounds have utility as electron transport materials in organic field-effect transistors and green solvent, air processed organic solar cells. Electron mobilities were on the order of about $2–7 \times 10^{-6}$ cm^2/V s. Solar cell power conversion efficiency reached 2 % for those using the tBOC functionalized dimer, 3 % for those using the H-atom functionalized dimer, and 6 % for those using the hexyl chain functionalized dimer. The performance of the latter is quite impressive considering the simple materials synthesis and greener solar cell processing.

Contributions

I carefully fabricated and characterized transistors using the materials, sent to me from the University of Alberta, reported in the paper before and after annealing.

7.6 Polycarbazole-Sorted Semiconducting Single-Walled Carbon Nanotubes for Incorporation into Organic Thin Film Transistors

Nicole A Rice, William J Bodnaryk, Brendan Mirka, Owen A Melville,
Alex Adronov, Benoît H Lessard

Advanced Electronic Materials 5 (1), 1800539
First Published: November 12, 2018
https://doi.org/10.1002/aelm.201800539

Abstract

The realization of organic thin film transistors (OTFTs) with performances that support low-cost and large-area fabrication remains an important and challenging topic of investigation. The unique electrical properties of single-walled carbon nanotubes (SWNTs) make them promising building blocks for next generation electronic devices. Significant advances in the enrichment of semiconducting SWNTs, particularly via π-conjugated polymers for purification and dispersal, have allowed the preparation of high-performance OTFTs on a small scale. The intimate interaction of the conjugated polymer with both SWNTs and the dielectric necessitates the investigation of a variety of conjugated polymer derivatives for device optimization. Here, the preparation of polymer–SWNT composites containing carbazole moieties, a monomer unit that has remained relatively overlooked for the dispersal of large-diameter semiconducting SWNTs, is reported. This polymer selectively discriminates semiconducting SWNTs using a facile procedure. OTFTs prepared from these supramolecular complexes are ambipolar, and possess superior mobilities and on/off ratios compared to homo poly(fluorene) dispersions, with hole mobilities from random-network devices reaching 21 $cm^2 V^{-1} s^{-1}$. Atomic force microscopy measurements suggest the poly(carbazole)–SWNT composites form more uniform thin films compared to the poly(fluorene) dispersion. Additionally, treating the silicon dioxide dielectric with octyltrichlorosilane is a simple and effective way to reduce operational hysteresis in SWNT OTFTs.

Contributions

I assisted with editing and contributing ideas to the transistor component of the paper. I researched contact resistance and analyzed a significant amount of data to estimate contact resistance and intrinsic field-effect mobility for the semiconducting carbon nanotube transistors used in the study. I modified the OTFT characterization software to assist the primary researchers in obtaining specific desired information.

7.7 P and N type copper phthalocyanines as effective semiconductors in organic thin-film transistor based DNA biosensors at elevated temperatures

Nicholas T Boileau, Owen A Melville, Brendan Mirka, Rosemary Cranston, Benoît H Lessard

RSC advances 9 (4), 2133-2142

Published: January 15, 2019

DOI: 10.1039/C8RA08829B

Abstract

Many health-related diagnostics are expensive, time consuming and invasive. Organic thin film transistor (OTFT) based devices show promise to enable rapid, low cost diagnostics that are an important aspect to enabling increased access and availability to healthcare. Here, we describe OTFTs based upon two structurally similar P (copper phthalocyanine – CuPc) and N (hexdecafluoro copper phthalocyanine – F_{16}-CuPc) type semiconductor materials, and demonstrate their potential for use as both temperature and DNA sensors. Bottom gate bottom contact (BGBC) OTFTs with either CuPc or F_{16}-CuPc semiconducting layers were characterized within a temperature range of 25 °C to 90 °C in both air and under vacuum. CuPc devices showed small positive shifts in threshold voltage (V_T) in air and significant linear increases in mobility with increasing temperature. F_{16}-CuPc devices showed large negative shifts in V_T in air and linear increases in mobility under the same conditions. Similar OTFTs were exposed to DNA in different hybridization states and both series of devices showed positive V_T increases upon DNA exposure, with a larger response to single stranded DNA. The N-type F_{16}-CuPc devices showed a much greater sensing response than the P-type CuPc. These findings illustrate the use of these materials, especially the N-type semiconductor, as both temperature and DNA sensors and further elucidate the mechanism of DNA sensing in OTFTs.

Contributions

I trained the first author in fabrication and characterization of CuPc OTFTs, which I had previously worked on while learning to use the thermal evaporator. I made significant edits to the paper and suggested the format for illustrating changes with temperature in a way that had previously been demonstrated in Section 7.3.

7.8 Old Molecule, New Chemistry: Exploring Silicon Phthalocyanines as Emerging N-Type Materials in Organic Electronics

Nathan J Yutronkie, Trevor M Grant, Owen A Melville, Benoît H Lessard, Jaclyn L Brusso

Materials 12 (8), 1334

Published: April 24, 2019

https://doi.org/10.3390/ma12081334

Abstract

Efficient synthesis of silicon phthalocyanines (SiPc) eliminating the strenuous reaction conditions and hazardous reagents required by classical methods is described. Implementation into organic thin-film transistors (OTFTs) affords average electron field-effect mobility of 3.1 × 10^{-3} cm^2 V^{-1} s^{-1} and threshold voltage of 25.6 V for all synthetic routes. These results demonstrate that our novel chemistry can lead to high performing SiPc-based n-type OTFTs

Contributions

I fabricated and characterized all the OTFTs used in the study. I also characterized a large number of OTFTs for this project that were not included in the paper in the end.

7.9 Polyfluorene-Sorted Semiconducting Single-Walled Carbon Nanotubes for Applications in Thin-Film Transistors

B Mirka, D Fong, NA Rice, OA Melville, A Adronov, BH Lessard
Chemistry of Materials 31 (8), 2863-2872
Publication Date: April 2, 2019
https://doi.org/10.1021/acs.chemmater.8b05357

Abstract

Due to their superlative electrical and mechanical properties, single-walled carbon nanotubes (SWNTs) are capable of expanding the current scope of electronic device applications. Advancements in the selective isolation and purification of semiconducting SWNTs through the use of conjugated polymers has allowed for incorporation of high-quality SWNTs into solution-processed thin-film transistors (TFTs). In this study, we report an alternating copolymer based on fluorene and 2,5-dimethoxybenzene that is capable of selectively dispersing semiconducting SWNTs. The exceptional semiconducting SWNT purity (>99%) of the dispersion was confirmed by UV–vis and Raman spectroscopy, which exhibit negligible metallic SWNT features. TFTs fabricated with this polymer–SWNT complex exhibited maximum hole and electron mobilities of 19 and 7 $cm^2/V{\cdot}s$, respectively, with on/off ratios as high as 10^7. Device fabrication parameters including silane surface treatment, removal of excess polymer, and SWNT dispersion concentration were investigated. Evaluation of hole and electron mobilities indicates that the presence of excess polymer in the polymer–SWNT dispersion did not adversely affect device performance. Atomic force microscopy measurements showed that our polymer–SWNT dispersions were capable of forming a complete percolation pathway between electrodes, with individual SWNTs exfoliated by the polymer.

Contributions

I assisted with editing and performing contact resistance calculations and write-up.

7.10 Developing 9, 10-anthracene Derivatives: Optical, Electrochemical, Thermal, and Electrical Characterization

Mikhail Y Vorona, Nathan J Yutronkie, Owen A Melville, Andrew J Daszczynski, Kwame T Agyei, Jeffrey S Ovens, Jaclyn L Brusso, Benoît H Lessard

Materials 12 (17), 2726
Publication Date: August 26, 2019
https://doi.org/10.3390/ma12172726

Abstract

Anthracene-based semiconductors are a class of molecules that have attracted interest due to their air stability, planarity, potential for strong intermolecular interactions, and favorable frontier molecular orbital energy levels. In this study seven novel 9,10-anthracene-based molecules were synthesized and their optical, electrochemical, and thermal properties were characterized, along with their single crystal arrangement. We found that functionalization of the 9,10-positions with different phenyl derivatives resulted in negligible variation in the optical properties with minor (±0.10 eV) changes in electrochemical behavior, while the choice of phenyl derivative greatly affected the thermal stability (Td > 258 °C). Preliminary organic thin film transistors (OTFTs) were fabricated and characterized using the 9,10-anthracene-based molecules as the semiconductor layer. These findings suggest that functionalization of the 9,10-position of anthracene leads to an effective handle for tuning of the thermal stability, while having little to no effect on the optical properties and the solid-state arrangement.

Contributions

I oversaw the first author in his production and characterization of all of his OTFTs. I helped him with analysis and presentation of OTFT data.

7.11 On-the-Spot Detection and Speciation of Cannabinoids Using Organic Thin-Film Transistors

Zachary J Comeau, Nicholas T Boileau, Tiah Lee, Owen A Melville, Nicole A Rice, Yen Troung, Cory S Harris, Benoît H Lessard, Adam J Shuhendler

ACS Sensors (Published: August 27, 2019)
https://doi.org/10.1021/acssensors.9b01150

Abstract

Quality control is imperative for Cannabis since the primary cannabinoids, Δ9-tetrahydrocannabinol (THC) and cannabidiol (CBD), elicit very different pharmacological effects. THC/CBD ratios are currently determined by techniques not readily accessible by consumers or dispensaries and which are impractical for use in the field by law-enforcement agencies. CuPc- and F16-CuPc-based organic thin-film transistors have been combined with a cannabinoid-sensitive chromophore for the detection and differentiation of THC and CBD. The combined use of these well-characterized and inexpensive p- and n-type materials afforded the determination of the CBD/THC ratio from rapid plant extracts, with results indistinguishable from high-pressure liquid chromatography. Analysis of the prepyrolyzed sample accurately predicted postpyrolysis THC/CBD, which ultimately influences the psychotropic and medicinal effects of the specific plant. The devices were also capable of vapor-phase sensing, producing a unique electrical output for THC and CBD relative to other potentially interfering vaporized organic products. The analysis of complex medicinal plant extracts and vapors, normally reserved for advanced analytical infrastructure, can be achieved with ease, at low cost, and on the spot, using organic thin-film transistors.

Contributions

I advised the first author as he was learning to make and characterize OTFTs. I proposed specific experiments and analyses used in the paper including interpolating from the mobility vs. gate bias curves to estimate THC:CBD ratios, and comparing current obtained at specific inputs before and after exposure to mimic the action of an actual sensor. I made heavy edits to the paper after its first submission.

7.12 Unipolar Polymerized Ionic Liquid Copolymers as High Capacitance Electrolyte Gates for n-type Transistors

Alexander Peltekoff, Victoria E Hiller, Gregory P Lopinski, Owen A Melville, Benoît H Lessard

ACS Applied Polymer Materials

Published: October 16, 2019

https://doi.org/10.1021/acsapm.9b00959

Abstract

A series of well-defined polymerized ionic liquid (PIL) statistical and block copolymers consisting of ionic liquid monomer, 1-(4-vinylbenzyl)-3-butylimidazolium bis(trifluoromethylsulfonyl)-imide, and a non-ionic monomer, methyl methacrylate (MMA), were synthesized by nitroxide mediated polymerization (NMP) with the goal of understanding the influence of polymer structure on the thin film capacitance. Copolymer compositions were varied from 8 to 54 wt% for both statistical and block copolymers and were characterized by predictable changes in glass transition temperature (75 °C > Tg > 45 °C). When integrated into thin film capacitors, block copolymers exhibited the formation of electric double layer (EDL) at lower frequencies compared to the statistical copolymers of similar comonomer compositions. The materials which formed an EDL all produced a similar maximum double layer capacitance value, with the only difference being the frequency at which the EDL was formed. Finally, the PIL containing materials that were utilized in organic thin-film transistors (OTFTs) showed a significant reduction in operating voltage compared to the poly(MMA) baseline. These results indicate that not only composition but also polymer architecture play a vital role in the formation of an EDL and determine at which frequency the resulting OTFTs can be operated.

Contributions

I performed the characterization of the OTFTs reported in the paper with the author and provided a written analysis used by the author. I edited the section of the paper on OTFTs prior to resubmission.

7.13 Metal phthalocyanine organic thin-film transistors: changes in electrical performance and stability in response to temperature and environment

Nicholas T Boileau, Rosemary Cranston, Brendan Mirka, Owen A Melville, Benoît H Lessard

RSC Advances 9 (37), 21478-21485

Published July 10, 2019

DOI: 10.1039/C9RA03648B

Abstract

Metal phthalocyanines (MPcs) are a widely studied class of materials that are frequently used in organic thin-film transistors (OTFTs), organic photovoltaics (OPVs) and organic light emitting diodes (OLEDs). The stability of these devices and the materials used in their fabrication is important to realize their widespread adoption. Seven P-type MPcs: zinc (ZnPc), magnesium (MgPc), aluminum (AlClPc), iron (FePc), cobalt (CoPc), and titanium (TiOPc) were investigated as the semiconductors in OTFTs under varying temperatures (25 °C to 150 °C) and environmental conditions (air and vacuum, P < 0.1 Pa). Devices using the divalent MPcs (except MgPc) showed significant shifts in threshold voltage and field-effect mobility with rising temperature in both air and vacuum. AlClPc and TiOPc, on the other hand, had more stable electrical properties, making them useful for applications requiring consistent performance. Distinct variations in film morphology as determined by atomic force microscopy may explain the different thermal response between the two groups of MPcs, while thermal gravimetric analysis in air and nitrogen (N2) provides additional insight into their susceptibility to oxidation at elevated temperature. To demonstrate proof-of-concept thermal sensing under realistic operating conditions, current changes were monitored in response to temperature stimuli using two more sensitive divalent MPcs. This comparative study of the effect of central atom inclusion in MPcs, the resulting material stability and thin-film characteristics will facilitate design of future sensors and other OTFT applications.

Contributions

I made significant edits to the manuscript and advised on paper structuring.

7.14 Functionalization of Commercial Pigment Hostasol Red GG for Incorporation into Organic Thin-Film Transistors

Owen A. Melville, Trevor M. Grant, Nicole A. Rice, Bowen Wang, Benoît H. Lessard

Submitted to New Journal of Chemistry

Abstract

In the development of organic electronic devices, it is important to consider the overall cost of the carbon-based semiconductors. Many of the state-of-the-art semiconductors available today are prohibitively expensive, limiting their commercial functionality. The dye and pigment industries offer a wealth of cheap conjugated starting materials. In this study, we explored functionalizing the dye 14H-anthra[2,1,9-m,n,a]thioxanthen-14-one (Hostasol Red GG) through a simple one-pot Grignard reaction. Phenyl, primary and secondary alkyl substituents were introduced onto the parent thioxanthene benzanthrone, with 1,4-addition occurring preferentially to addition at the carbonyl for all products. The substituted Red GG derivatives were incorporated into organic thin film transistors. While the alkyl derivatives resulted in decreased device performance compared to native Red GG, transistor performance improved for the phenyl derivative. A combination of inexpensive starting materials and simple chemistry offers an abundance of possible new semiconductor targets for organic electronic devices. `

Contributions

I either performed or supervised all OTFT characterization and fabrication for this paper. I substantially edited the paper, in particular the introduction, which was originally written by Professor Lessard.